Dissertation zur Erlangung des Doktorgrades

der Fakultät für Chemie und Pharmazie

der Ludwig-Maximilians-Universität München

Precision in Time and Space: Biological Applications of FLIM in STED Multiplexing and FRET

Mariano José González Pisfil

aus

Lima, Peru

2025

Erklärung

Diese Dissertation wurde im Sinne von § 7 der Promotionsordnung vom 28. November 2011 von Herrn Christian Wahl-Schott betreut und von Herrn Martin Biel von der Fakultät für Chemie und Pharmazie vertreten.

Eidesstattliche Versicherung

Die Dissertation wurde eigenständig und ohne unerlaubte Hilfsmittel erarbeitet.

München, 23.09.2025

_____

Mariano José González Pisfil

Dissertation eingereicht am: 23.09.2025

1. Gutachter: Prof. Dr. Martin Biel

2. Gutachter: Prof. Dr. Christian Wahl-Schott

Mündliche Prüfung am: 02.12.2025

A mis padres y a mi hijo

“Silver tetradrachm coin at the Museum of Fine Arts of Lyon depicting the owl of Athena (c. 480–420 BC). The inscription "ΑΘΕ" is an abbreviation of ΑΘΗΝΑΙΩΝ, which may be translated as "of the Athenians". In daily use the Athenian drachmas were called glaukes (γλαῦκες, owls). This silver coin was first issued in 479 BC in Athens after the Persians were defeated by the Greeks.”
Extracted from Wikipedia. Marie-Lan Nguyen – “Owl of Athena” © CC BY 2.5

“Let no one be slow to seek wisdom when he is young nor weary in the search thereof when he is grown old. For no age is too early or too late for the health of the soul”

Epicurus, Letter to Menoeceus 0-14

Table of contents

1 Abbreviations and symbols

Abbreviations

AC	Alternating Coupling
DC	Direct Coupling
EV	Extracellular Vesicule
FLIM	Fluorescence Lifetime Microscopy
FPM	Fast Pattern Matching
FRAP	Fluorescence Recovery After Photobleaching
FRET	Förster Resonance Energy Transfer
GFP	Green Fluorescent Protein
HPD	Hybrid Photomultiplier Detector
IRF	Instrument Response Function
LED	Light Emitting Diode
MCP	Microchannel Plates
PIE	Pulsed Interleaved Excitation
PMT	Photomultiplier Tube
PSF	Point Spread Function
RFP	Red Fluorescent Protein
SPAD	Single-Photon Avalanche Diode
STED	Stimulated Emission Depletion
TCSPC	Time-Correlated Single Photon Counting
UV	Ultraviolet
WYSIWYG	What You See Is What You Get

Symbols (order of appearance)

c	Speed of light
λ_{em}	Wavelength of the emitted light
E_{em}	Energy of the emitted photon.
E_{FRET}	Efficiency of energy transfer
I_0	Initial fluorescence intensity immediately after excitation
I_F	Fluorescence intensity.
I_I	Incident light intensity

I_{sat}	Saturation intensity
I_{STED}	STED laser intensity
k_{FRET}	Energy transfer decay rate
k_{nr}	Non-radiative decay rate
k_r	Radiative decay rate
Q_D	Quantum yield of the donor
R_0	Förster distance
α_i	Pre-exponential factor (amplitude) for the i-th component
κ^2	Factor describing the relative dipole orientation of the donor and acceptor
τ_D	Average donor lifetime
τ_{DA}	Average lifetime of the donor under FRET
τ_i	Fluorescence lifetime for the i-th component
τ_m	Modulation depth lifetime
τ_ϕ	Phase shift lifetime
τ	Fluorescence lifetime of a molecule
τ_{Eff}	Effective lifetime
b	Path length of the sample
C	Concentration of the substrate
d	Minimum resolvable distance between two points
E	Energy of the photon
f	Linear modulation frequency
G	Real component from the Phasor plot
h	Planck's constant (6,626.10^{-34} J/s)
$I(t)$	Fluorescence intensity at time t
$J(\lambda)$	Overlap integral expressing the degree of spectral overlap between the donor emission and the acceptor absorption
k	Proportionality constant attributed to the instrument we use to measure
l	Number of exponential components
m	Modulation depth
n	Refractive index of the medium
NA	Numerical aperture
r	Distance between the donor and acceptor molecules
S	Imaginary component from the Phasor plot
t	Time elapsed since excitation

ε	Molar absorptivity
θ	Half-angle of the cone of light that enters the objective lens
λ	Wavelength of the light
υ	Frequency of light
ϕ	Phase shift
ω	Angular frequency

2 List of manuscripts

This thesis is based on the following publications, which are referred to in the text by their roman numerals (I – VI) and reprinted in the Appendix:

I. **Mariano Gonzalez Pisfil**, Sumeet Rohilla, Marcelle König, Benedikt Krämer, Matthias Patting, Felix Koberling and Rainer Erdmann
Triple-Color STED Nanoscopy: Sampling Absorption Spectra Differences for Efficient Linear Species Unmixing
2021, **The Journal of Physical Chemistry B**, 125(22), 5694-5705

II. **Mariano Gonzalez Pisfil**, Iliya Nadelson, Brigitte Bergner, Sonja Rottmeier, Andreas W. Thomae and Steffen Dietzel
Stimulated emission depletion microscopy with a single depletion laser using five fluorochromes and fluorescence lifetime phasor separation
2022, **Scientific Reports**, 12(1), 14027

III. **Mariano Gonzalez Pisfil** and Steffen Dietzel
Fluorochrome Separation by Fluorescence Lifetime Phasor Analysis in Confocal and STED Microscopy
2025, **Methods in Microscopy**, 2(1), 45-60

IV. Andrea Forero, Fabrizia Pipicelli, Sylvain Moser, Natalia Baumann, Christian Grätz, **Mariano Gonzalez Pisfil**, Michael W. Pfaffl, Benno Pütz, Pavel Kielkowski, Filippo M. Cernilogar, Giuseppina Maccarrone, Rossella Di Giaimo, Silvia Cappello
Extracellular vesicle-mediated trafficking of molecular cues during human brain development
2024, **Cell Reports**, 43(10), 114755

V. Gesine Behrens, Stephanie L. Edelmann, Timsse Raj, Nina Kronbeck, Thomas Monecke, Elena Davydova, Elaine H. Wong, Lisa Kifinger, Florian Giesert, Martin E. Kirmaier, Christine Hohn, Laura S. de Jonge, **Mariano Gonzalez Pisfil**, Mingui Fu, Sebastian Theurich, Stefan Feske, Naoto Kawakami, Wolfgang Wurst, Dierk Niessing & Vigo Heissmeyer
Roquin-1 interactions with Regnase-1 induces autoimmunity and enhances antitumor responses
2021, **Nature Immunology**, 22(12), 1563–1576

VI. Petra Vizjak, Dieter Kamp, Nicola Hepp, Alessandro Scacchetti, **Mariano Gonzalez Pisfil**, Joseph Bartho, Mario Halic, Peter B Becker, Michaela Smolle, Johannes Stigler, Felix Mueller-Planitz
ISWI catalyzes nucleosome sliding in condensed nucleosome arrays
2024, **Nature Structural & Molecular Biology**, 31(9), 1331-1340

3 Summary

Fluorescence Lifetime Imaging Microscopy (FLIM) is a powerful imaging technique that provides contrast based on the fluorescence decay time of fluorophores rather than their intensity. Although it offers clear advantages for studying complex biological processes, its adoption has historically been limited by the need for specialized hardware and advanced data analysis. Recent technological advancements, alongside increased commercial support, have significantly lowered the barrier to entry, making FLIM more accessible and practical for broader use. This thesis explores how FLIM, especially when combined with Stimulated Emission Depletion (STED) super-resolution microscopy, can be applied in diverse biological contexts using commercially available dyes and systems.

At the beginning of my doctoral research, I established a three-color STED imaging platform with pulsed interleaved excitation (PIE) and dual detection, enabling spectral separation of fluorophores. However, due to the similarity in fluorescence lifetimes among the dyes, lifetime-based unmixing was limited. To overcome this challenge, I developed a novel five-color STED imaging strategy by combining spectral information with fluorescence lifetime phasor plot analysis. This approach allowed for robust and reliable separation of fluorophores even when their emission spectra overlapped significantly and their fluorescence lifetimes differed by as little as 0.8 nanoseconds. The five-color STED imaging was achieved with a single STED depletion laser. The quantification of FLIM was implemented using the phasor plot approach which is a fit-free and intuitive analysis method which contributes to the reproducibility and ease of use of this advanced multiplexing technique.
A comprehensive, stepwise protocol was then produced of the five-color STED-FLIM microscopy, lowering the technical entry barrier and encouraging adoption of this method in routine imaging workflows across biological research fields.
The practical power of these techniques was demonstrated through a detailed investigation of extracellular vesicle (EV) uptake in neural cells. Using STED-FLIM microscopy, the study revealed that EV uptake efficiency and subcellular localization vary significantly between different neural cell types. These findings provide novel insight into EV-mediated intercellular communication during neurodevelopment, highlighting cell-type-specific trafficking and signaling mechanisms that had been largely unexplored outside the context of neurodegeneration.

Furthermore, the thesis illustrates the broad applicability of FLIM through FLIM-FRET (Förster Resonance Energy Transfer) experiments on two distinct biological systems. One study examined

the interaction between the RNA-binding proteins Roquin-1 and Regnase-1, which are key regulators of inflammatory mRNA decay and immune homeostasis. Disruption of their interaction caused marked immunological effects, including T follicular helper cell accumulation, germinal center B cell abnormalities, autoantibody production, and altered tumor-infiltrating T cell function. Another study utilized FLIM-FRET time-lapse imaging to track chromatin remodeling by the Drosophila ISWI ATPase within dense chromatin condensates. This work directly demonstrated the enzyme's ability to slide nucleosomes and remodel chromatin dynamically in vitro.

Together, these findings underscore the transformative impact of diverse fluorescence lifetime imaging microscopy techniques for dissecting intricate molecular and cellular processes. This thesis contributes both methodological innovations and biological insights, broadening the scope of fluorescence imaging in biomedical research.

Zusammenfassung

Fluoreszenzlebensdauer-Mikroskopie (FLIM nach engl. Fluorescence Lifetime Imaging Microscopy) ist eine leistungsstarke Technik, die Kontrast auf Grundlage der Fluoreszenzlebensdauer von Fluorophoren anstelle ihrer Intensität erzeugt. Trotz ihrer Vorteile für die Untersuchung biologischer Prozesse wurde eine breite Anwendung in der Vergangenheit durch die erforderliche spezialisierte Hardware und aufwändig durchzuführende Datenanalyse verhindert. Technologische Fortschritte und eine verstärkte kommerzielle Unterstützung haben diese Hürden jedoch deutlich gesenkt, sodass FLIM heute leichter zugänglich für eine breitere Anwendung ist. In der vorliegenden Arbeit wurde untersucht, wie FLIM, insbesondere in Kombination mit Stimulated Emission Depletion (STED)-Höchstauflösungsmikroskopie, in verschiedenen biologischen Kontexten eingesetzt werden kann – unter Verwendung kommerziell verfügbarer Farbstoffe und Geräte.

Zu Beginn meiner Promotionsarbeit entwickelte ich Drei-Farben-STED-Bildgebung mit PIE (*Pulsed Interleave Excitation* - Gepulste Interleave-Anregung) und dualer Detektion, die eine spektrale Trennung der Fluorophore ermöglichte. Aufgrund ähnlicher Fluoreszenz-Lebensdauern der Farbstoffe war eine lebensdauerbasierte Entmischung jedoch eingeschränkt. Um diese Einschränkung zu überwinden, entwickelte ich eine Fünf-Farben-STED-Bildgebungsstrategie, die spektrale Unterschiede mit der Information aus Fluoreszenzlebensdauer-Phasor-Plots kombiniert. Dieser Ansatz ermöglichte eine klare Trennung der Fluorophore, selbst bei stark überlappenden Emissionsspektren und nur 0,8 Nanosekunden Unterschied in der Fluoreszenzlebensdauer. Die Fünf-Farben-STED-Bildgebung konnte dabei mit nur einem STED-Abregungslaser durchgeführt werden. Für die Quantifizierung von FLIM wurde der Phasor-Plot-Ansatz verwendet, weil er eine intuitive Methode ist, die ohne Kurvenanpassung auskommt und dadurch die Reproduzierbarkeit und Benutzerfreundlichkeit erhöht.
Für diese Methode wurde auch ein detailliertes Protokoll publiziert, um die Eintrittsbarriere für die Anwendung dieser Methode zu senken.
Die Leistungsfähigkeit dieser Techniken wurde anhand der Aufnahme extrazellulärer Vesikel (EV) in neuronale Zellen demonstriert. Mithilfe der STED-FLIM-Mikroskopie konnte gezeigt werden, dass Effizienz der EV-Aufnahme und subzelluläre Lokalisation zwischen unterschiedlichen neuronalen Zelltypen stark variieren. Diese Ergebnisse lieferten neue Einblicke in die EV-vermittelte interzelluläre Kommunikation während der neuronalen Entwicklung und hoben zelltypspezifische Transport- und Signalmechanismen hervor, die außerhalb des Bereichs Neurodegeneration bislang weitgehend unerforscht waren.

Darüber hinaus zeigt die vorliegende Arbeit die breite Anwendbarkeit von FLIM im Rahmen von FLIM-FRET (Förster-Resonanz-Energie-Transfer)-Experimenten. Zwei unterschiedliche biologische Systeme wurden untersucht. Eine Studie beschäftigte sich mit der Interaktion der RNA-bindenden Proteine Roquin-1 und Regnase-1, zentralen Regulatoren des mRNA-Abbaus bei Entzündungen und der Immunhomöostase. Die Untersuchung konnte zeigen, dass eine Störung dieser Interaktion zu ausgeprägten immunologischen Effekten führt, darunter die Anreicherung von T-Follikel-Helferzellen, Auffälligkeiten der B-Zellen in Keimzentren, Autoantikörperproduktion und veränderte Funktion tumorinfiltrierender T-Zellen. Eine weitere Studie nutzte FLIM-FRET-Zeitserienmikroskopie, um Chromatin-Remodeling durch die Drosophila-ISWI-ATPase innerhalb dichter Chromatinkondensate zu verfolgen. Diese Arbeit zeigte, dass das Enzym Nukleosomen verschieben und Chromatin dynamisch in vitro umstrukturieren kann.

In der Gesamtschau verdeutlichen diese Ergebnisse die weitreichenden Möglichkeiten verschiedener Fluoreszenzlebensdauer-Bildgebungstechniken bei der Untersuchung komplexer molekularer und zellulärer Prozesse. Die vorliegende Arbeit liefert sowohl methodische Innovationen als auch neue biologische Erkenntnisse und erweitert die Einsatzmöglichkeiten der Fluoreszenzbildgebung in der biomedizinischen Forschung.

4 Introduction

4.1 Fluorescence

Fluorescence is a phenomenon that can occur when light interacts with matter. More specifically, it is a process where a substance absorbs light or other electromagnetic radiation and typically emits light of a longer wavelength. This refers to the processes of light absorption (excitation) and subsequent emission. Fluorescence has a wide range of applications, from materials sciences to forensic science passing by fluorescent paint and inks. Here, the focus will be the use of fluorescence in microscopy, and more specifically in the context of biological samples.

4.1.1 Background

For a long time, fluorescence was observed but not fully understood. The earliest known record of fluorescence is by Bernardino de Sahagún, who described in 1560 that the Aztecs knew of an infusion known as *lignum nephriticum*. People believed the infusion had medicinal properties, especially for treating kidney and bladder ailments — hence *nephriticum* (“for the kidney”). It is made from two tree species, one native to the Americas (used by the Aztecs) and another from Asia (introduced later by Spanish trade). It emits a beautiful opalescent hue depending on the incident light [1]. Other observations followed over the centuries [2-4]. However, it was only in 1845 that Sir Frederik W. Herschel precisely described the fluorescence of an object when he observed that a quinine solution exhibits a “vivid and beautiful celestial blue color” when observed at a right angle relative to the sunlight [5]. In 1852, Sir George G. Stokes conducted a more detailed study of this phenomenon using the same sample and others, including a fluorspar crystal. He coined the term "fluorescence," combining "fluorspar" and "opalescence" – *“I am almost inclined to coin a word, and call the appearance fluorescence, from fluor-spar, as the analogous term opalescence is derived from the name of a mineral”* [6]. At the beginning of the 20th century, the conceptual foundation of fluorescence microscopy was laid by Max Haitinger, who introduced the terms *Fluorochromierung* and *Fluorochrom* to describe fluorescent staining and the dyes used therein [7]. Building on this groundwork, Oskar Heimstädt (Reichert, Vienna, 1911) developed the first practical fluorescence microscope, followed shortly thereafter by Hans Lehmann (Carl Zeiss, 1913). [8-10]. Ellinger and Hirt later created "intravital microscopes" [11] for examining large and opaque living organisms using incident light instead of transmitted light. They treated organisms with fluorescent substances, used ultraviolet (UV) light for illumination, and placed filters between the objective and eyepiece to block reflected UV rays while transmitting the red-shifted fluorescent light. Fluorescent antibody labeling was introduced in

the early 1940s [12]. Later the cloning of green fluorescent protein (GFP), first isolated in 1962 [13], and the development of its spectral variants [14] have allowed for the specific labeling of proteins of interest through genetic encoding [15]. Together with the improvement of organic dyes [16] and labeling strategies [17, 18], it contributed to the boom of fluorescence microscopy at the end of the 1990's.

4.1.2 Principle of fluorescence

Fluorescent molecules, or fluorophores, are molecules that can absorb light at a specific wavelength and then re-emit light at a longer wavelength, depending on their structure. Fluorophores can be naturally occurring, like GFP, or synthetic, such as dyes like Alexa Fluor or Cy5. A subset of fluorophores, fluorochromes are fluorophores specifically designed and used for labeling and staining in biological applications. But in all cases, the process can be described using the principles of quantum mechanics.

Electrons within a molecule occupy quantized energy levels. In a simplified representation, these levels can be viewed as discrete states or steps, each associated with a specific energy value. When energy in the form of light is absorbed by the molecule, the electrons transition between energy levels. We can describe the different energy levels as the following (Figure 1):

- Ground State (S0): This is the lowest energy state of an electron in a molecule. Most electrons in a molecule are in the ground state under normal conditions.
- Excited States (S1, S2, etc.): These are higher energy states that electrons can move to when they absorb energy. The first excited state (S1) is the next higher energy level above the ground state.

When a fluorophore absorbs a photon, the energy of the photon excites an electron from the ground state (S0) to an excited state (S1 or higher). Of course, due to the quantum nature of electronic transitions, absorption spectra exhibit natural broadening effects (Doppler effect, particle collisions, vibrational and rotational effects, environment such as pH, polarity, etc.). As a result, a photon does not need to have an energy that exactly matches the energy gap between electronic states; rather, it must fall within the broadened absorption band. The energy of a photon (E) is related to its wavelength (λ) and frequency (υ) by the following equations:

$$E = h\upsilon = hc\lambda \qquad (1)$$

where,

- E is the energy of the photon.
- h is Planck's constant (6,626.10^{-34} J/s).
- υ is the frequency of the light.
- c is the speed of light (2,997.10^{8} m/s in vacuum).

- λ is the wavelength of the light.

When the electron is in the excited state, it will eventually return to the ground state. The excited electrons in the higher energy state are unstable and naturally seek to return to a lower, more stable energy level. However, instead of dropping directly back to their ground state, the electrons typically transition through a series of intermediate (S2, S1, S0), and vibrational energy states, losing small amounts of energy in the form of heat during this process and eventually reach the lowest excited state. This step is known as internal conversion or non-radiative decay.

Finally, the electron drops back to the ground state from the lowest excited state S1, and in doing so, it emits a photon. The emitted light typically has a longer wavelength – red-shifted (and thus lower energy) than the absorbed light, which is why fluorescence is observed at a red-shifted spectral range compared to the light used to excite the fluorophore.

The energy of the emitted photon (E_{em}) can be expressed as:

$$E_{em} = hc\lambda_{em} \quad (2)$$

where,

- E_{em} is the energy of the emitted photon.
- λ_{em} is the wavelength of the emitted light.

The process of fluorescence generation and the transition between energy levels can be visualize in a Jablonski diagram (Figure 1).

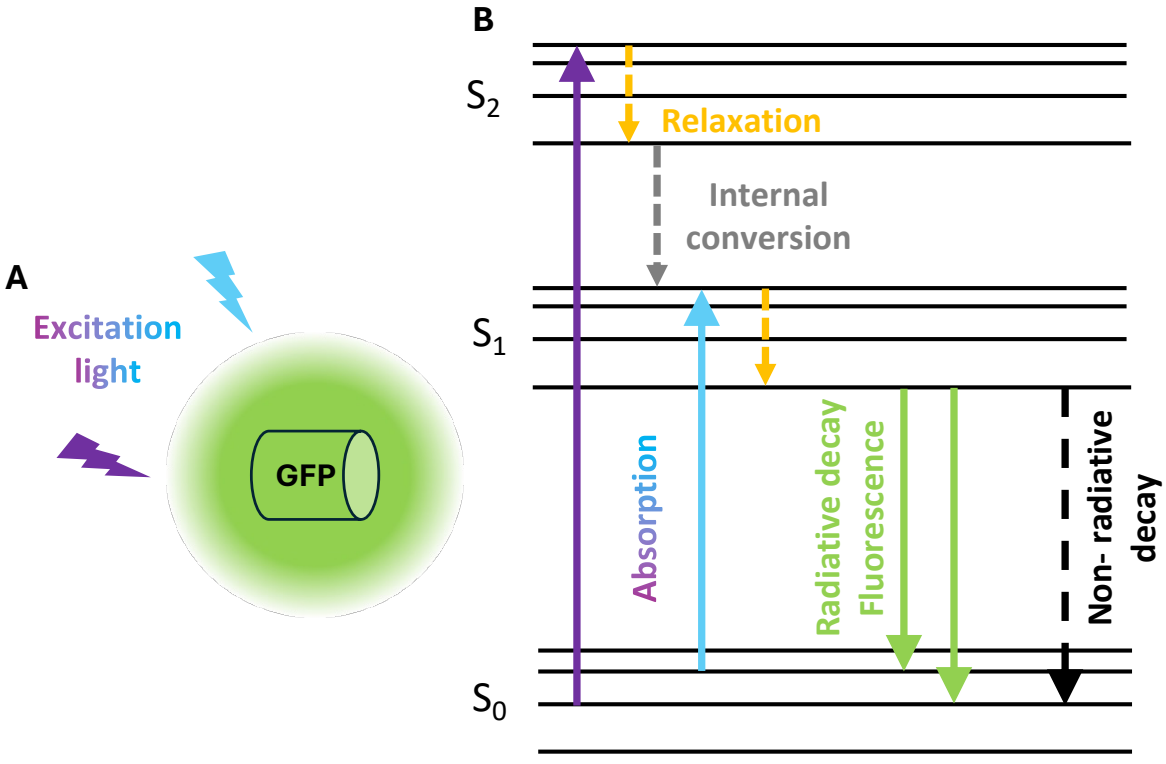

Figure 1. A: Fluorophore (GFP) excited by a light source emits a red-shifted fluorescence. B: Jablonski diagram representing the phenomenon on the left. In the diagram, the S0 and S1 states represent the ground state and the first excited state, respectively. They have many vibrational substates (simplified in the diagram) between which the electrons can jump up and down, depending on temperature. The arrows represent possible transitions. An upward arrow shows absorption (excitation), where the electron absorbs a photon and moves to a higher energy state. An arrow going downwards shows loss of energy in the form of either light (radiative decay) or heat (non-radiative processes).

The efficiency of this process is called quantum yield (Φ). It is defined as the ratio of the number of photons emitted to the number of photons absorbed.

$$\Phi = \frac{Number\ of\ photons\ emitted}{Number\ of\ photons\ absorbed} \quad (3)$$

Essentially, it tells us how effectively a fluorophore can convert absorbed light into emitted light. A quantum yield of 1 (or 100%) means that every absorbed photon results in an emitted photon, indicating perfect efficiency. Conversely, a quantum yield of 0 means that no emitted photons are produced from the absorbed photons, indicating no fluorescence. Several factors can influence the quantum yield of a fluorescent molecule, such as the molecular structure and composition. Some fluorophores have high quantum yields due to their efficient electronic transitions. Additionally, the surrounding environment, including the solvent in which the fluorescent molecule is dissolved, or if they are attached or linked to another molecule, can affect the quantum yield by offering alternative ways to dissipate the energy. Interactions with the solvent or other molecules can lead to non-radiative relaxation processes that reduce or enhance the efficiency of fluorescence. Furthermore, higher temperatures can increase non-radiative relaxation processes, thereby reducing the quantum yield [19, 20]. Conversely, lower temperatures can enhance quantum yield by minimizing photobleaching [20, 21]. Lastly, at high concentrations, fluorescent molecules can interact with each other, leading to self-quenching and a decrease in quantum yield. This phenomenon is also called concentration quenching [20]. However, many compounds are unable to emit fluorescence because they dissipate all the excess energy through nonradiative pathways. These include transferring the energy to other nearby molecules, transitioning to a nearly identical but slightly lower energy state without light emission, or undergoing chemical reactions with surrounding molecules to create new substances.

The fluorescence intensity of a uniformly fluorescent solution, as measured by a given instrument, can be expressed using an equation derived from the Lambert–Beer law:

$$I_F = kI_I\phi[1 - (10^{-\varepsilon bC})] \quad (4)$$

Where,

- I_F is the fluorescence intensity.
- k is a proportionality constant attributed to the instrument used to measure.
- I_I is the incident light intensity.

- ϕ is the quantum yield.
- ε is the molar absorptivity.
- b is the path length of the sample.
- C is the concentration of the substrate.

This means the fluorescence emission of a sample is proportional to the amount of light absorbed, the path length of the sample, the concentration of the component, and the fluorescence quantum yield. For fluorescence microscopy, a dye with a quantum yield as high as possible is desirable, because high quantum yield dyes provide brighter images, allowing for better visualization of biological samples. Over time, different labelling and imaging techniques have emerged. However, in some cases fluorescence intensity is not a reliable parameter to measure due to difficulties such as background fluorescence, staining intensities, concentration, etc. [22]. More reliable parameters to study complex samples are desirable, and fluorescence lifetime is one of the answers.

4.2 Fluorescence Lifetime Imaging Microscopy (FLIM)

Fluorescence lifetime refers to the average duration that a fluorescent molecule remains in its excited state before emitting a photon and returning to the ground state. Typically in the nanosecond range, the fluorescence lifetime is intrinsic to the fluorophore and its local environment, not of how many photons are emitted or detected. It is largely independent of the fluorescence intensity or the concentration of the fluorophore, making it a reliable parameter. However, it can be affected by its molecular environment, providing valuable insights about samples [23-26].

Many predecessors contributed to the characterization and measurement of accurate fluorophore lifetimes, but the Argentinian scientist Enrique Gaviola is considered to be the first to measure fluorescence lifetimes with modern-day precision [27, 28]. The lifetimes of Rhodamine B and Fluorescein in glycerol and water he published are remarkably close to those obtained with contemporary instruments. He named his instrument the fluorometer. Following his contributions in fluorescence during his PhD in Germany, Gaviola later achieved even greater success in astronomy, conducting fascinating research that lies beyond the scope of this thesis.

4.2.1 Principle

Mathematically, it is given by:

$$\tau = \frac{1}{k_r + \Sigma k_{nr}} \qquad (5)$$

Where,

- τ is the fluorescence lifetime of a fluorophore.

- k_r is the radiative decay rate.
- k_{nr} is the non-radiative decay rate.

Fluorescence lifetime is defined as the inverse of the decay rate shown below. It remains inherently independent of fluorophore intensity, excitation power, quantum yield, collection efficiency or fluorophore concentration, making it especially useful for more quantitative analyses compared to intensity-based methods alone. The faster any of the rates are, the shorter the lifetime of the molecule. Since fluorescence is per se a statistical phenomenon, a single decay event of a single molecule will be very rarely equal to τ. But the average decay rate of a single or a population fluorophore under given experimental conditions will always be equal to the respective lifetime.

The fluorescence lifetime of a population of molecules mathematically speaking is the fluorescence intensity $I(t)$ as a function of time after excitation. It can be described by a first order exponential decay function,

$$I(t) = I_0 e^{-t/\tau} \qquad (6)$$

where,

- I_0 is the initial fluorescence intensity immediately after excitation.
- t is the time elapsed since excitation
- τ is the fluorescence lifetime.

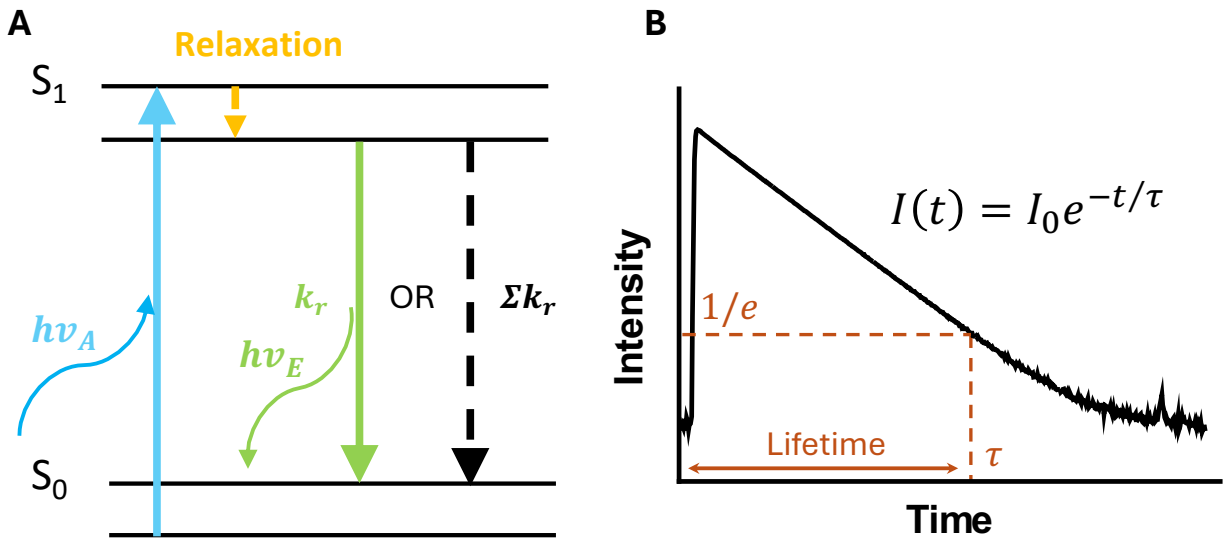

Figure 2. A: Simplified Jablonski diagram detailing the decay rates and energy absorption or emission in the form of light. B: Time histogram depicting the recording of emission intensity as a function of time for a population of fluorophores. In this case it is a measurement of a solution of ATTO 488 in water. The y-axis has a log scale, and since the decay follows an exponential pattern, it results in a straight line. The red-dotted line shows the $1/e$ value, and the average lifetime value.

An example for such a decay is shown in Figure 2. This exponential decay equation indicates that the fluorescence intensity decreases rapidly at first and then more slowly over time, reflecting the probability of photon emission as the excited electrons return to the ground state. Populations can either exhibit a mono-exponential decay of their fluorescence, or a multi-exponential. In the latter case, it remains challenging to directly associate the lifetimes with the molecular parameters of the sample. For example, non-exponential decays can result from transient quenching effects [29].

Several factors can influence fluorescence lifetime, including the chemical environment, temperature, and molecular interactions. As previously mentioned, a higher temperature generally increases the rate of non-radiative decay processes, resulting in shorter lifetimes [19]. Interactions with other molecules or quenchers can also affect fluorescence lifetime by facilitating non-radiative decay. Solvent nature as well as the pH value can affect the lifetime [24, 25]. Interaction with other molecules can quench or induce conformational changes that impact the lifetime. For example, oxygen is a common quencher that can interact with excited-state fluorophores and reduce their fluorescence lifetimes [23]. In another example, the fluorescence lifetime of NAD(P)H molecules changes depending on whether they are free or bound to a protein. In their free state, they fold, resulting in a shorter lifetime due to self-quenching. When NAD(P)H binds to a protein, it expands, which diminishes the quenching and thus increases the fluorescence lifetime [26]. Last but not least, these differences can be used to distinguish fluorophores in an imaging context instead of relying solely on spectral separation. This approach allows for an increase in the number of fluorophores per spectral channel, thereby enhancing the number of fluorophores that can be simultaneously acquired [30-33].

4.2.2 Lifetime measurement techniques

There are generally two approaches for measuring the fluorescence lifetime of a sample: time-domain techniques and frequency-domain techniques.

4.2.2.1 Time-domain technique: Time Correlated Single Photon Counting (TCSPC)

Time-domain measurements are typically performed by TCSPC.

As the name suggests, TCSPC involves recording the interval between an excitation pulse and the detection of a single emitted photon. It's akin to using a stopwatch to measure the time it takes for a photon to be emitted following the excitation pulse. Pulsed lasers usually operate between 20 megahertz (MHz) and 80 MHz. This equals to one pulse every 12.5 ns (80 MHz) or 50 ns (20 MHz). Pulse width is around 100 picoseconds, and the smaller the better to prevent the duration of the laser pulse from interfering with the recording. The repetition rate should be adjusted based on the dye's lifetime. A short repetition rate might truncate the decay and re-excite the dye before

all molecules return to the ground state, whereas a long repetition rate might unnecessarily prolong the recording time due to fewer pulses per second and, consequently, less signal collected. Hence it is important to choose the correct repetition to visualize the whole lifetime decay correctly. A good rule of thumb is to choose a pulse interval 4x – 5x as long as the lifetime measured.

Because TCSPC counts photons, it is a highly sensitive technique necessitating high-sensitivity detectors. Single-photon detectors, such as photomultiplier tubes (PMTs), microchannel plates (MCPs), single-photon avalanche diodes (SPADs), or hybrid photodetectors (HPDs), detect the emitted photons from the sample. Another essential component is the counting card, a dedicated electronic card that synchronizes the laser pulses and times the photon detections (Figure 3B). In the firsts TCSPC systems, the laser excitation pulse served as the "stop" signal for timing, and each detected photon acted as the "start" signal. Each time a photon is detected, the counting card starts a chronometer and measure the time elapsed between the detected photon and the next laser pulse. This was the case because electronics were not fast enough to respond to each laser pulse triggering the chronometer. In more recent systems, the laser pulse serves as the "start" signal, while the detected photons mark the "stop". This time interval is recorded for each photon event. This interval, known as the "time of flight", "time delay", or simply “arrival time” is compiled into a histogram (Figure 3A). The x-axis of the histogram represents the time delay, and the y-axis indicates the number of detected photons at each time delay. The resulting histogram illustrates the distribution of photon arrival times relative to the excitation pulse. Since noise is always present, there is a limit to the lifetimes that a TCSPC system can reliably measure. This limitation is reflected in the Instrument Response Function (IRF), which characterizes the system’s temporal resolution—essentially its response to an ideal, infinitely short light pulse. The IRF captures broadening and delays introduced by the detector, electronics, and laser pulse width. Accurate extraction of fluorescence lifetimes requires accounting for the IRF, as the measured decay represents a convolution of the true decay with the system response. The onset of the photon arrival histogram is determined by the IRF, which can be obtained experimentally or estimated mathematically. [34, 35]. It can be analyzed to determine the fluorescence lifetime of the sample. For TCSPC imaging approaches, typically, a confocal microscope is equipped with a pulsed laser, single-photon detectors, and a counting card (Figure 3B).

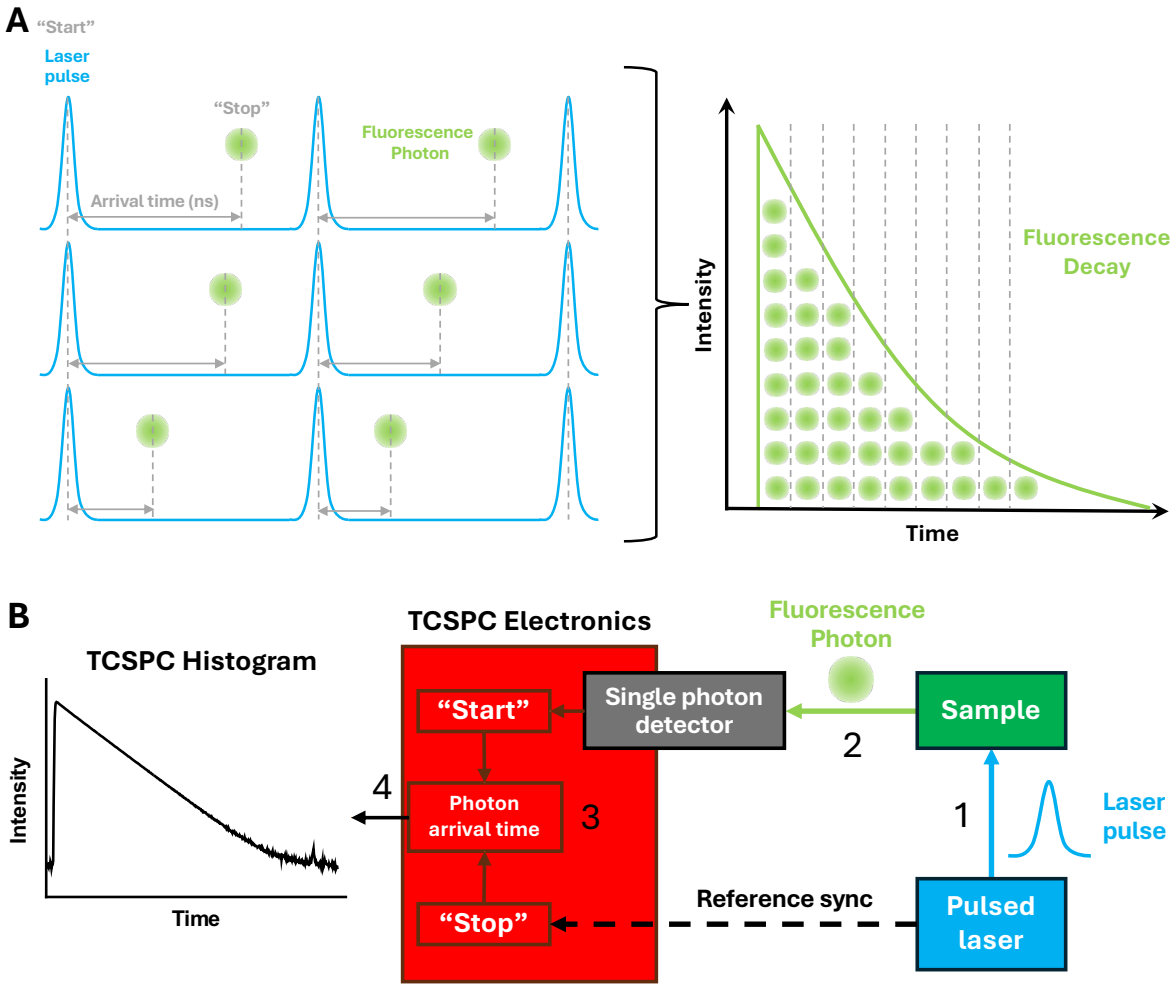

Figure 3. A: Schematic of the TCSPC process. A pulsed laser is used to excite the sample, and the arrival time of the emitted photon is measured relative to the excitation pulse, enabling time-resolved detection of fluorescence events. B: Schematic of a classic TCSPC setup. The numbers show the order in which the process unfolds.

TCSPC offers several advantages. It can detect single photons, making it highly sensitive and suitable for samples with low fluorescence yields. It also provides high temporal resolution, up to picosecond-level resolution, allowing for the study of very fast fluorescence decays. Additionally, TCSPC provides quantitative information about fluorescence lifetimes, which can be used to study molecular interactions, binding events, and environmental changes [36].

TCSPC is the technique that was applied in various incarnations for FLIM in this thesis, either on MicroTime 200 confocal microscope from PicoQuant GmbH, or an SP8 FALCON confocal microscope from Leica Microsystems GmbH.

4.2.2.2 Frequency-domain FLIM

Unlike time-domain techniques like TCSPC, which measure the time intervals between excitation and emission, frequency-domain FLIM determines lifetimes by analyzing how fluorophores respond to a modulated light source. A modulated light source is one whose intensity varies

periodically over time, typically in a sinusoidal or square-wave pattern, at high frequencies ranging from MHz to gigahertz (GHz). When this oscillating light excites the fluorophores, their emission also becomes modulated, but with a phase shift and reduced amplitude that depend on the fluorescence lifetime. By measuring these changes in phase and modulation depth, the fluorescence lifetime of the sample can be accurately calculated (Figure 4).

A typical Frequency-Domain FLIM setup includes an excitation source (modulated light source), a modulated detector, and a signal processing unit. The excitation source can be a laser or an LED, making this technique particularly suitable for widefield microscopy. It emits light in a wave pattern with a specific frequency, which is electronically controlled. The sample, labeled with fluorophores, is placed under the microscope and exposed to the modulated excitation light. A modulated detector which synchronizes with the modulation frequency of the excitation source, like a modulated camera, measures the phase shift and modulation depth of the emitted fluorescence, synchronized with the modulation frequency of the excitation light (Figure 4A).

The emitted fluorescence displays a phase shift and a change in modulation depth relative to the excitation light. The phase shift represents the time delay between the excitation modulation and the fluorescence modulation, which occurs because on average fluorescent molecules emit light after a specific period, depending on their lifetime. The modulation depth indicates the ratio of the alternating coupling (AC) component (modulated part) to the direct coupling (DC) component (steady part) of the fluorescence signal, providing information about the fluorescence decay rate (Figure 4B). The signal processing unit analyzes the detected signals to calculate the phase shift and modulation depth. The fluorescence lifetime can hence be determined in two ways in frequency-domain FLIM. One method uses the phase shift between the modulated excitation and the resulting emission signal, giving the phase shift lifetime (τ_ϕ). The other method relies on the modulation depth, which is the reduction in emission amplitude relative to the excitation, yielding the modulation depth lifetime (τ_m). For a sample with a single, mono-exponential decay, both τ_ϕ and τ_m are equal. However, in samples with multi-exponential decays, such as mixtures of fluorophores or heterogeneous environments, τ_ϕ and τ_m differ, reflecting the contribution of multiple decay components to the overall fluorescence dynamics

This contrasts with time-domain FLIM, which directly measures a single decay curve over time. In time-domain measurements, a single lifetime is obtained for mono-exponential decays, while multi-exponential decays require fitting to extract the different components. Thus, frequency-domain FLIM provides two complementary measures of lifetime from the same dataset, offering additional insight into complex fluorescence behaviors.

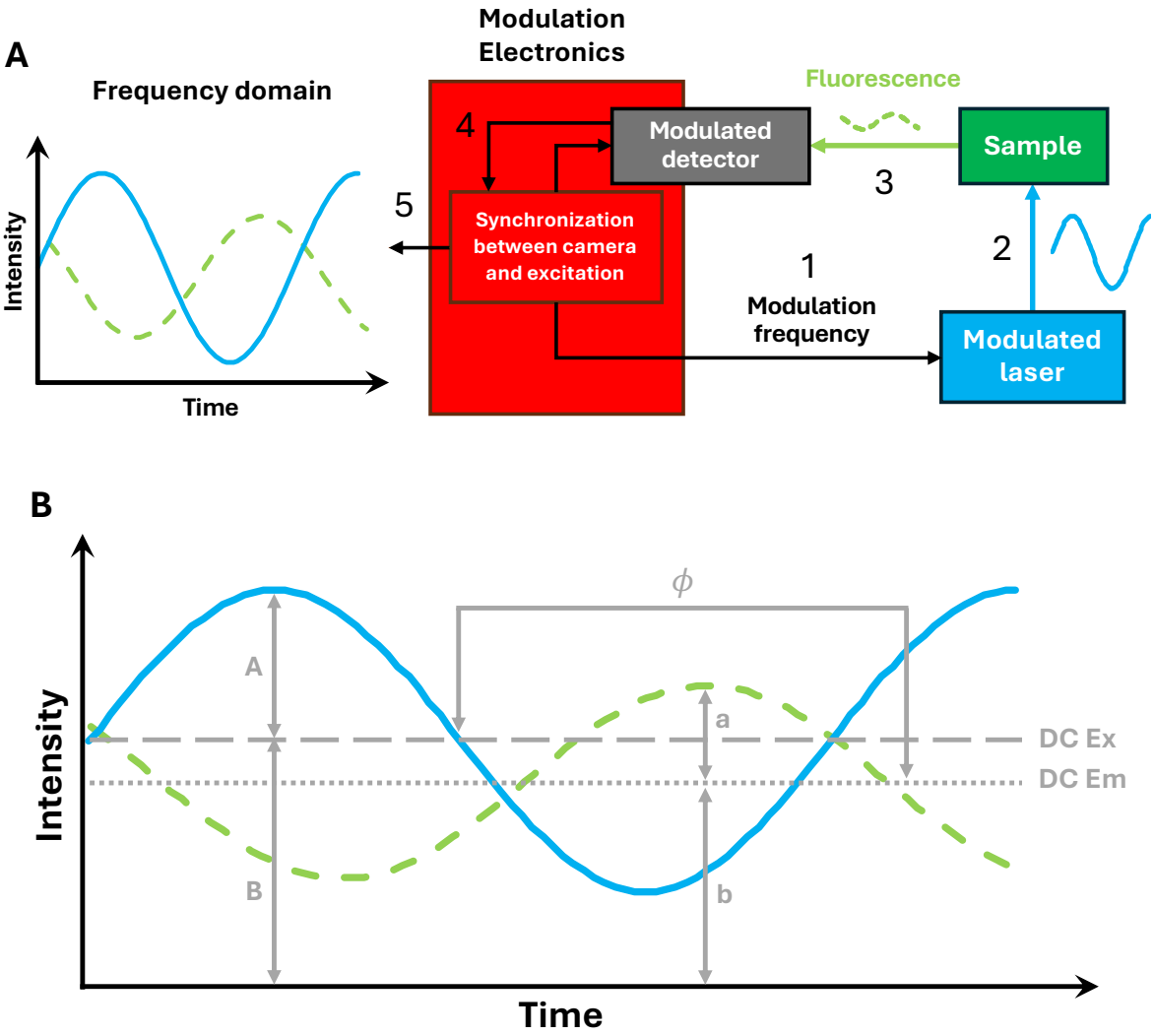

Figure 4. A: Schematics of a classic frequency-domain setup. B: Wave functions graph of a frequency domain measurement. Blue represents the excitation source, green, the emission. ϕ represents the phase shift between the two waves, whereas the ratio A+B and a+b represent the difference in modulation depth (how much the fluorescence emission signal is modulated (i.e. how much it oscillates) in response to a modulated excitation source). The numbers show the order in which the process unfolds.

The fluorescence lifetime can be derived from the phase shift and modulation depth using the following relationships:

Phase Shift Relationship:

$$\tau_\phi = \frac{tan\,(\phi)}{\omega} \qquad (7)$$

Where,

- τ_ϕ is the phase shift lifetime.
- ϕ is the phase shift.
- ω is the angular frequency ($\omega = 2\pi f$, f is the linear modulation frequency)

Modulation Depth Relationship:

$$\tau_m = \frac{1}{\omega}\sqrt{\frac{1}{m^2} - 1} \quad (8)$$

Where,

- τ_m is the modulation depth lifetime.
- m is the modulation depth: how much the fluorescence emission signal is modulated (i.e. how much it oscillates) in response to a modulated excitation source.
- ω is the angular frequency

The real lifetime of the sample is the average of the modulation and phase lifetime. Frequency-Domain FLIM offers several advantages. It can be faster TCSPC as it doesn't require detecting individual photon arrival times, making it suitable for real-time imaging and high-throughput applications. And as previously pointed out, the technique is relatively straightforward and can be implemented with standard fluorescence microscopy setups, making it accessible to many laboratories. Moreover, it is sufficiently sensitive to detect changes in fluorescence lifetime, offering valuable insights into the local environment, such as pH, ion concentration, and molecular interactions. However, it is not as sensitive or accurate as TCSPC [29].

In the context of this thesis, frequency-domain measurements are not conducted. Nevertheless, the Phasor analysis method is employed, utilizing the same principles described in this section. Therefore, it is beneficial for the reader to comprehend the Phasor analysis workflow.

4.2.3 FLIM Analysis

There are various methods for analyzing FLIM data, the two most widespread are explained here: exponential fit analysis and phasor plot.

4.2.3.1 Exponential decay fitting

As previously discussed, a fluorescence lifetime decay can be mathematically represented by a first-order exponential decay law (6). The decay curve is then fitted to an appropriate exponential model, whether single or multi-exponential, to determine the fluorescence lifetime(s). This fitting process is carried out using non-linear least-squares fitting, which aims to minimize the discrepancy between the experimental data and the respective model for mono- or multiexponential decay (Figure 5). In real biological or chemical systems, the fluorescence decay may not always conform to a single exponential pattern. Instead, it might consist of multiple decay components, each with its own distinct lifetime. This is referred to as multi-exponential decay and can be described by the following equation,

$$I(t) = \sum_{i=1}^{l} \alpha_i \, e^{-t/\tau_i} \quad (9)$$

where,

- α_i is the pre-exponential factor (amplitude) for the i-th component.
- τ_i is the fluorescence lifetime for the i-th component.
- l is the number of exponential components.

The pre-exponential factors α_i indicate the relative contribution of each lifetime component to the overall fluorescence decay. Under such challenging conditions, the effective lifetime (τ_{Eff}), a weighted average of the contributing individual lifetimes, is used in place of resolving the actual lifetime components:

$$\tau_{Eff} = \frac{\sum \alpha_i \tau_i}{\sum \alpha_i} \quad (10)$$

This approach allows for the extraction of an effective lifetime under controlled conditions, which can then be compared to the effective lifetime under a treatment condition. While it may not be the most precise method, it provides a practical and reliable means of comparison.

This method is currently the most widely used for analyzing time-domain FLIM data. It offers high precision and robustness; however, its accuracy is dependent on a substantial photon count, particularly when the decay data is complex and necessitates multiple exponential decay fits. Especially when the experimental data is deconvolved using an instrument response function (IRF) approximation during the fitting process. The IRF is a characterization of how a fluorescence lifetime imaging system responds to an infinitely short excitation pulse. It represents the broadening and distortions introduced by the laser pulse duration, the timing jitter of detectors, the electronics used for photon detection. In a typical FLIM experiment, a photon count of approximately a few thousands is commonly achieved [37]. However, this photon count is often insufficient to distinguish between a single and a double exponential decay [38]. Consequently, alternative methods for analyzing FLIM data have been developed to address this limitation.

The result of an exponential fit depends on the number of fluorescent species to which the experimental data are fitted, and thus on user input.

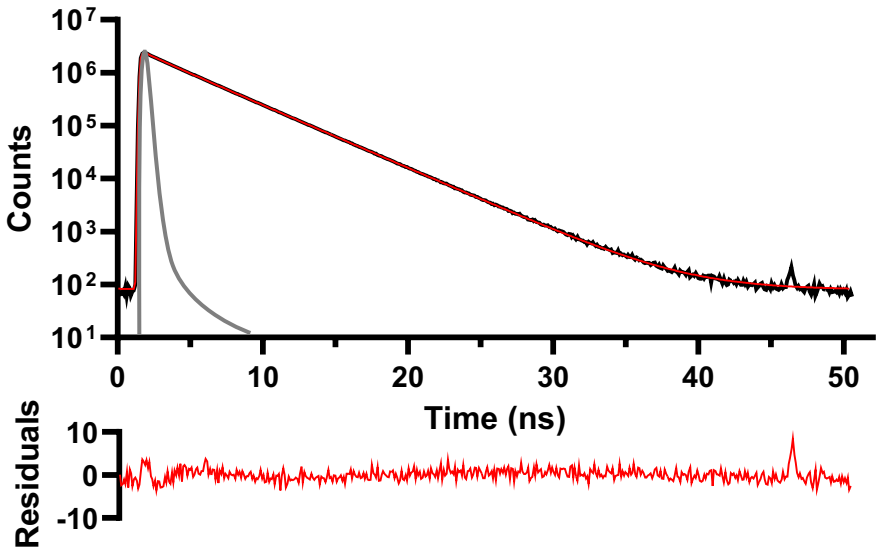

Figure 5. Example of an exponential fit. The red line represents the fitting function, while the black line depicts the recorded decay data. The Instrument Response Function (IRF) is depicted in gray. It represents the time profile of the excitation pulse as recorded by the detection system. The IRF essentially characterizes how the instrument responds to an infinitely short light pulse. In practical terms, it accounts for the finite duration of the laser pulse, the timing jitter of the detector, and any dispersion in the optical system. The IRF is used to deconvolve the recorded fluorescence decay data, allowing for more accurate determination of the fluorescence lifetime. The residuals below the histogram are defined as the differences between the recorded data and the predicted values from the model at each time point.

4.2.3.2 Phasor Plot

Unlike exponential fitting, phasor plot analysis relies purely on mathematical transformations to extract fluorescence lifetime information, offering an intuitive and efficient alternative for analyzing FLIM data. The phasor plot represents fluorescence decay data in the frequency domain, converting time-domain fluorescence decay signals into a frequency-based format. This transformation enables straightforward visualization and interpretation of complex decay behaviors. As a result, both time-domain and frequency-domain FLIM data can be analyzed using the phasor approach. Unlike traditional fitting methods that require modeling decay curves with exponential functions, the phasor plot offers a graphical, fit-free, and global representation of lifetime distributions across an image.

The fluorescence decay signal follows an exponential law (6). A phasor plot is generated by performing a normalized Fourier transform of the fluorescence decay signal at a selected modulation frequency. The transformation is expressed as:

$$\tilde{I}(\omega) = \int_0^\infty I(t) e^{-i\omega t} dt \qquad (11)$$

where,

- $\tilde{I}(\omega)$ is the complex result of the Fourier transform.
- $I(t)$ is the fluorescence intensity at time t.

- ω is the angular frequency ($\omega = 2\pi f, f$ is the laser repetition rate for TCSPC measurements).

For a decay $I(t)$ (with $t \geq 0$), the normalized complex phasor is defined as:

$$\tilde{I}(\omega) = \frac{\int_0^\infty I(t)e^{-i\omega t}dt}{\int_0^\infty I(t)\,dt} \quad (12)$$

Applying Euler's formula, $e^{-i\omega t} = \cos(\omega t) - i\sin(\omega t)$:

$$\tilde{I}(\omega) = \frac{\int_0^\infty I(t)\cos(\omega t)\,dt}{\int_0^\infty I(t)\,dt} - i\frac{\int_0^\infty I(t)\sin(\omega t)\,dt}{\int_0^\infty I(t)\,dt} \quad (13)$$

This leads to the real G and imaginary S components of the normalized transform, defined as:

$$G(\omega) = \frac{\int_0^\infty I(t)\cos(\omega t)\,dt}{\int_0^\infty I(t)\,dt}$$
$$S(\omega) = \frac{\int_0^\infty I(t)\sin(\omega t)\,dt}{\int_0^\infty I(t)\,dt} \quad (14)$$

Together, G and S define a phase vector $\vec{P}$, in the complex plane:

$$\vec{P} = (G, S) = m \cdot (\cos\phi, \sin\phi) \quad (15)$$

where,

- $m = \sqrt{G^2+S^2}$ is the modulation depth (length of the phasor vector).
- $\phi = \tan^{-1}(S/G)$ is the phase angle of the vector.

Thus, the phasor coordinates can also be written as,

$$G(\omega) = m\cos(\phi),\ \ S(\omega) = m\sin(\phi) \quad (16)$$

In phasor analysis, the G and S components represent the real and imaginary parts of the normalized Fourier transform of the fluorescence decay at a given modulation frequency ω, and they also define a vector in the complex plane. This vector-based representation provides a powerful framework for both visual and quantitative analysis of fluorescence lifetimes without the need for curve fitting. Its polar form translates complex lifetime dynamics into an intuitive geometric structure on the phasor plot, making data interpretation both elegant and accessible. (Figure 6A). Each pixel's fluorescence decay in the FLIM image is represented as a point on the phasor plot (Figure 6B). The position of each point is defined by its G and S coordinates.

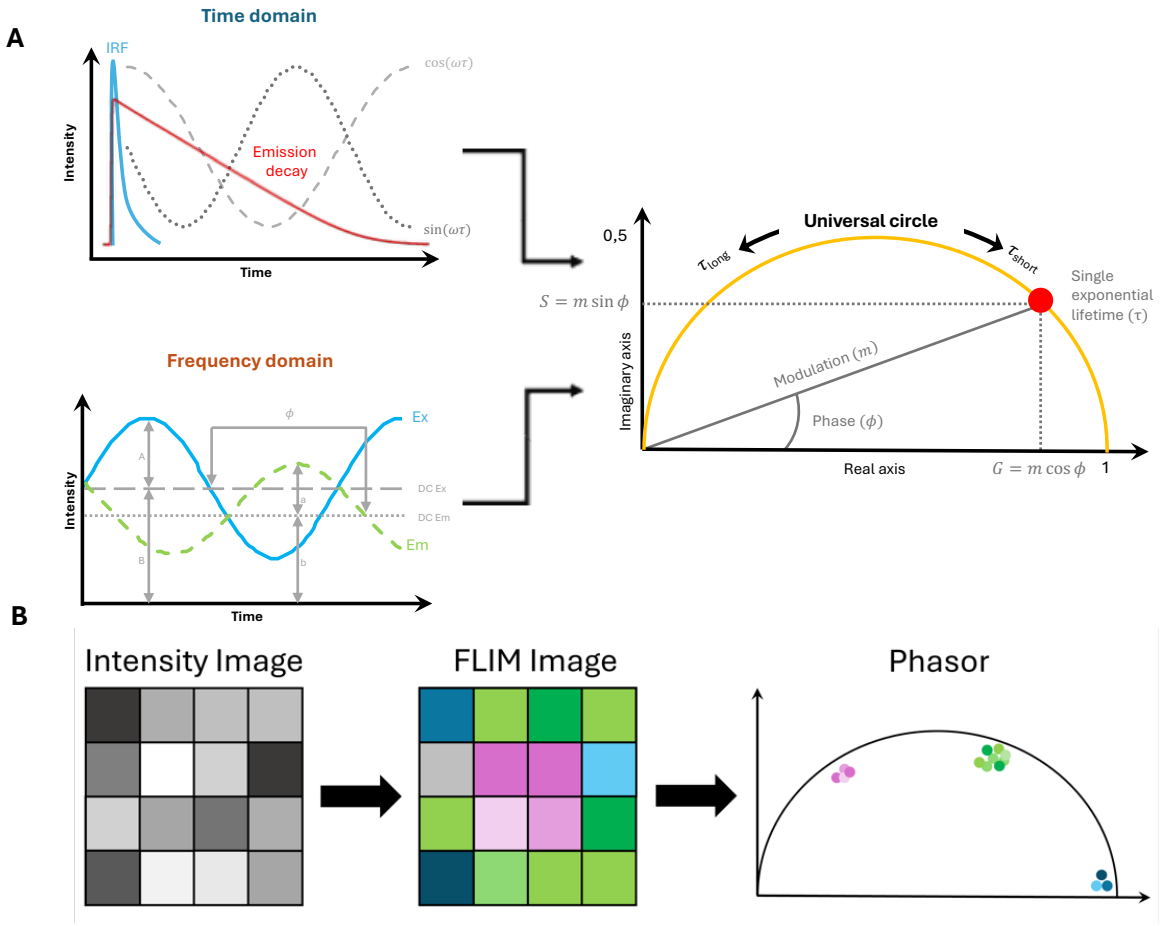

Figure 6. A: Phasor plot diagram, applicable to both time-domain and frequency-domain measurements. Single-exponential decays lie along the universal circle, where lifetimes are mapped based on their decay characteristics. Short lifetimes cluster near (1, 0), while longer lifetimes shift progressively counterclockwise toward the origin (0, 0). The coordinates in the phasor plot are computed from the Fourier transform of the time-domain fluorescence decay, with the real and imaginary components corresponding to the cosine and sine integrals, respectively. With m as the modulation (vector length) and ϕ as the phase (vector angle). B: The process outlined in Figure 6A is applied to a FLIM image. Each pixel exhibits a distinct lifetime, and based on these lifetimes, they are positioned in various regions of the phasor plot. Pixels with similar lifetimes will form clusters (B is from Gonzalez Pisfil and Dietzel. 2025).

For single exponential lifetimes, as indicated by the equations below, analytically, for $I(t) \propto \frac{1}{\tau} e^{-t/\tau}$ (normalized so $\int I(t)\, dt = 1$) the following results are obtained:

$$G = \int_0^\infty \frac{1}{\tau} e^{-\frac{t}{\tau}} \cos(\omega t)\, dt, \qquad S = \int_0^\infty \frac{1}{\tau} e^{-\frac{t}{\tau}} \sin(\omega t)\, dt \tag{17}$$

Solving the integrals:

$$G = \frac{1}{\tau} \cdot \frac{1/\tau}{(1/\tau)^2 + \omega^2}, \qquad S = \frac{1}{\tau} \cdot \frac{\omega}{(1/\tau)^2 + \omega^2} \tag{18}$$

$$G = \frac{1}{1 + (\omega\tau)^2}, \qquad S = \frac{\omega\tau}{1 + (\omega\tau)^2} \tag{19}$$

which satisfy,

$$S^2 + (G - {}^1/_2)^2 = {}^1/_4 \tag{20}$$

which indicates that all single exponential components are represented by a semicircle with its center at (½,0) and a radius of ½ on the phasor plot. This boundary is known as the "universal

circle." Points on this circle signify single exponential decays, whereas points within the circle denote multi-exponential decays. The radius of the circle is influenced by the laser angular frequency ω, i.e. repetition rate. On this semicircle, a phasor corresponding to a very short lifetime is located near the point (1,0), while a phasor representing a very long lifetime is positioned close to the point (0,0) (Figure 6A, Figure 7A & B). Absolute lifetime values can be calculated from Phasor data using the equations (7) and (8). For a mixed decay (sum of two or more exponentials), equation (19) can be rewritten as:

$$G = \sum_i \alpha_i \frac{1}{1+\omega^2\tau_i^2} \qquad S = \sum_i \alpha_i \frac{\omega\tau_i}{1+\omega^2\tau_i^2} \qquad for\ i > 1 \tag{21}$$

which produces a phasor inside the semicircle. According to equation (21), a phasor of a complex species can be decomposed as the average of multiple single exponential lifetimes τ_i. In other words, the phasor of a mixture of lifetimes is just the average of the phasors of each component, weighted by how bright (how many photons emitted) each one is. If two species with pure single exponential phasors (lying on the circle) are present, any mixture yields phasors along the straight-line segment connecting those points (Figure 7B). Likewise, three components fill the triangle defined by their three single-lifetime phasors. Thus, phasor signals falling inside the circle directly indicate multi-exponential behavior. The linear combination property means one can often visually decode fractions. For a two-component mixture, the fractional contributions correspond to the fractional distance along the line between the two pure-phasor endpoints [39]. As previously mentioned, there is a direct correspondence between the pixels in an image and their phasors on the phasor plot, determined by their decay curves. Phasors corresponding to pixels with similar lifetimes cluster in specific regions of the phasor plot. But their positions are dependent of the laser repetition rate as shown by the equation mentioned above (Figure 7A & B). This characteristic allows for the categorization of image pixels. By selecting a region of interest on the phasor plot, a reciprocal transformation can be applied, projecting the selected phasors back onto the image. This process facilitates basic image segmentation. For a more comprehensive explanation, it is recommended to consult reference [38].

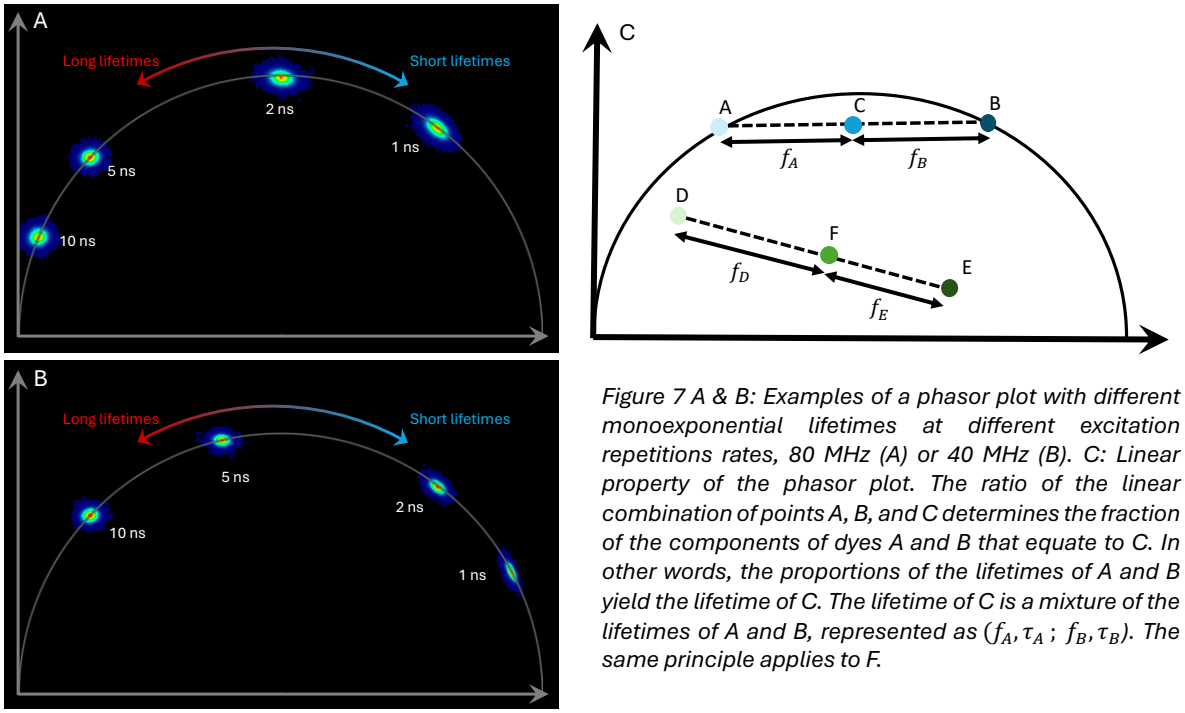

Figure 7 A & B: Examples of a phasor plot with different monoexponential lifetimes at different excitation repetitions rates, 80 MHz (A) or 40 MHz (B). C: Linear property of the phasor plot. The ratio of the linear combination of points A, B, and C determines the fraction of the components of dyes A and B that equate to C. In other words, the proportions of the lifetimes of A and B yield the lifetime of C. The lifetime of C is a mixture of the lifetimes of A and B, represented as $(f_A, \tau_A\ ;\ f_B, \tau_B)$*. The same principle applies to F.*

Owing to these properties, phasor plot analysis presents several advantages over traditional exponential fitting. One of the biggest advantages is that it is quite efficient and accurate in images with a low signal-to-noise ratio. Generally, 100 photons per pixel are enough to obtain an acceptable lifetime value [40]. It is significantly faster because it does not require iterative curve fitting. And because each molecular species or lifetime has a unique phasor, distinct lifetime populations appear as clusters in the phasor plot. This graphical clustering is used instead of explicit fitting: phasors from large data sets can be analyzed by simple rules (clustering and linear mixing) rather than iterative exponential fits. Additionally, it simplifies the analysis process since there is no need to determine the appropriate number of exponential factors for the fit. Moreover, the graphical nature of the phasor plot makes it easy to identify different lifetime components and multi-exponential decays. This approach streamlines the analysis, making it accessible to researchers with varying levels of expertise.

4.2.4 Förster Resonance Energy Transfer (FRET)

Förster Resonance Energy Transfer (FRET) is a technique that can benefit the accuracy and precision of lifetime measurements. Named after Theodor Förster who developed the theory in the mid-1940's [41], FRET involves a distance-dependent interaction between two fluorescent molecules, where energy is transferred from an excited donor fluorophore to a nearby acceptor fluorophore without emitting a photon. This non-radiative energy transfer occurs through dipole-dipole coupling and is highly sensitive to the distance between the donor and acceptor, typically taking place over distances of 1-10 nanometers, and the spectral overlap between donor

emission and acceptor absorption (Figure 8A). The process is clearly illustrated in a Jablonski diagram (Figure 8B). As such, it provides valuable insights used as a molecular ruler [42] into molecular dynamics, protein-protein interactions, and other biological processes [43-49]. This energy transfer alters both the intensity and the lifetime of the donor, which can be measured. FRET can be analyzed either by intensity-based or lifetime-based methods. Here, we will focus on the lifetime-based method known as FLIM-FRET. In the context of FRET, and based on the equation for lifetime decay (5), the average donor lifetime (τ_D) is expressed as follows,

$$\tau_D = \frac{1}{k_r + k_{FRET} + \Sigma k_{nr}} \quad (22)$$

here, k_{FRET} represents the rate of energy transfer. Due to the presence of an additional term in the denominator, the lifetime of a donor in FRET will always be shorter than in the absence of FRET. The rate k_{FRET} is highly dependent on the distance between the donor and acceptor molecules, as can be deduced from the equation,

$$k_{FRET}(r) = \frac{1}{\tau_D}\left(\frac{R_0}{r}\right)^6 \quad (23)$$

where,

- R_0 is the Förster distance (or radius), i.e. the distance at which energy transfer efficiency is 50%.
- r is the distance between the donor and acceptor molecules.

Consequently, the efficiency of energy transfer (E_{FRET}) is given by the following relationship:

$$E_{FRET} = \frac{R_0^6}{R_0^6 + r^6} \quad (24)$$

The Förster distance (R_0), typically expressed in angstroms (Å), is a crucial parameter in FRET that depends on several factors, including the spectral overlap between donor emission and acceptor absorption (Figure 8C), the quantum yield of the donor, the refractive index of the medium, and the relative orientation of the donor and acceptor transition dipoles. All these factors are reflected in the Förster distance formula,

$$R_0 = 0{,}211(\kappa^2 n^{-4} Q_D J(\lambda))^{1/6} \quad (25)$$

where,

- κ^2 is a factor describing the relative dipole orientation of the donor and acceptor.
- n is the refractive index of the medium.
- Q_D is the quantum yield of the donor.
- $J(\lambda)$ is the overlap integral expressing the degree of spectral overlap between the donor emission and the acceptor absorption.

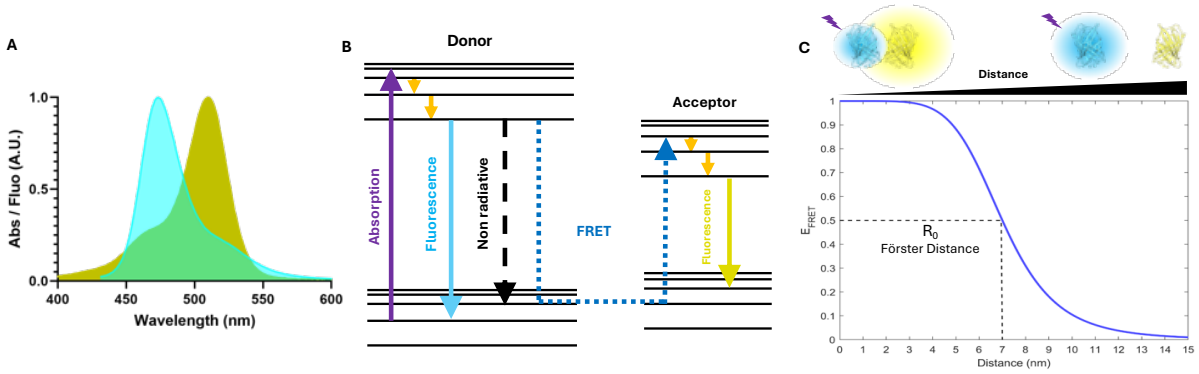

Figure 8. A: Overlap of the emission and excitation spectra of a Cyan-Yellow FRET pair. The overlap (in green of the graph) is a necessary condition for FRET to occur. B: Jablonski diagram illustrating the FRET phenomenon for a Cyan-Yellow pair. C: FRET efficiency as a function of the distance between donor and acceptor molecules, with a schematic representation positioned above the graph. The relationship is represented by a sigmoidal curve, with the Förster distance (R_0) obtained at 0.5 EFRET. This data represents a simulation of a FRET Cyan-Yellow pair with an R_0 of 7 nm (70 Å) conducted in MATLAB.

To summarize, the mechanism of FRET involves three main steps. First, the donor fluorophore absorbs a photon of light, exciting it from the ground state to an excited state. If the acceptor fluorophore is in close proximity to the excited donor, the energy is transferred non-radiatively from the donor to the acceptor through dipole-dipole coupling. Finally, the acceptor fluorophore, upon receiving the energy, gets excited and then returns to its ground state by emitting a photon. The emission wavelength of the acceptor is different from that of the donor. Unlike intensity-based FRET, where changes in intensity between the donor and acceptor are recorded, FLIM-FRET calculates only the lifetime of the donor, which is sufficient to determine the transfer efficiency,

$$E_{FRET} = 1 - \frac{\tau_{DA}}{\tau_D} \qquad (26)$$

with τ_{DA} the lifetime of the donor under FRET. Thus, measuring only the donor lifetimes in the presence and absence of the acceptor is sufficient to determine FRET efficiency. FRET data can be analyzed either with exponential fitting or phasor plot. The advantage of using FLIM-FRET is that by recording the fluorescence lifetime, the measurements are independent of random changes in intensity due to drifting, photobleaching, or sample movement. Intensity-based FRET requires extensive controls to ensure that observed changes in intensity are due to FRET and no other phenomena, such as those mentioned earlier (pH, temperature...). Moreover, since it is sufficient to observe the donor's lifetime, the acquisition and subsequent analysis are simplified, particularly when utilizing the Phasor plot. Consequently, all FRET experiments presented in this thesis utilize FLIM-FRET.

FRET is a powerful and versatile technique for studying molecular interactions and dynamics at the nanoscale. Its sensitivity to distance and non-destructive nature make it ideal for real-time monitoring of biological processes. By providing insights into protein-protein interactions,

nucleic acid hybridization, cell signaling, and molecular conformation, FRET has become an invaluable tool in biological and biochemical research. FLIM-FRET has been with success in both [48, 49] to study protein-protein interactions.

Although FLIM-FRET has been available for decades and is known for its versatility, its early use was limited by complex experimental setups and the need for custom-built systems and analysis tools. Recent advancements have significantly improved accessibility, allowing the technique to be more widely applied to answer biological questions efficiently and with high precision.

In one study (manuscript V), FLIM-FRET was used to examine the interaction between Roquin-1 and Regnase-1, two post-transcriptional regulators critical for immune homeostasis. Proximity measurements confirmed their interaction in P-bodies and, to a lesser extent, in the surrounding cytoplasm. Truncated protein variants helped define the regions responsible for binding, with no interaction detected in the nucleus, reinforcing the cytoplasmic specificity of their association. Another application (manuscript VI) demonstrated how FLIM-FRET can directly visualize nucleosome repositioning by the chromatin remodeler ISWI within dense, phase-separated condensates that mimic the crowded nuclear environment. This approach bypassed the limitations of intensity-based FRET, enabling lifetime-based detection in compact systems. Results showed that ISWI retains its remodeling activity in condensed chromatin but becomes immobilized and stiffens the structure in the absence of ATP, emphasizing ATP's dual role in catalysis and mobility. Simulations further supported a "monkey-bar" mechanism, in which ISWI remodels chromatin by sequentially interacting with adjacent nucleosomes.

4.3 Stimulated Emission Depletion (STED)

Among super-resolution techniques, STED microscopy is among those that were awarded the Nobel Prize in Chemistry in 2014. It was developed in 1994 by Stefan W. Hell and Jan Wichmann [50], and experimentally demonstrated in 1999 by Stefan W. Hell and Thomas Klar [51]. The principle of STED microscopy is based on selectively depleting the fluorescence of molecules in the periphery of the focal point, thereby reducing the effective point spread function and achieving higher resolution. Hence, unlike other Nobel Prize-winning super-resolution techniques, STED can be described as a WYSIWYG (What You See Is What You Get), or deterministic super-resolution technique – there is no need for post-processing analysis, as the image is directly available once the recording is done. Nowadays, many different super-resolution techniques have emerged, but STED and its variants have remained among the most popular due to their simplicity and the availability of STED microscopes in laboratories around the world.

4.3.1 Background

In 1873, Ernst K. Abbe discovered there is a limit to the resolution power of a microscope [52], and that limit depends on the wavelength of the light used, expressed by the following formula,

$$d = \frac{\lambda}{2n \sin(\theta)} = \frac{\lambda}{2NA} \quad (27)$$

where,

- d is the minimum resolvable distance between two points (resolution limit).
- λ is the wavelength of the light used for imaging.
- n is the refraction index in the medium between the objective lens and the sample.
- θ is the half-angle of the cone of light that enters the objective lens (also known as the numerical aperture, $NA = n\sin(\theta)$).

This equation shows that the resolution limit (d) is inversely proportional to the numerical aperture and directly proportional to the wavelength of light. Therefore, using a shorter wavelength of light and a higher numerical aperture can achieve better resolution. Abbe's formula highlights the fundamental diffraction limit imposed by the wave nature of light, which restricts the ability of optical systems to resolve details smaller than a certain size. The image of an ideal point source formed by a microscope is called the point spread function (PSF), representing how the system blurs sub-diffraction structures due to diffraction.

At the end of the 1990's, STED was the first experimentally demonstrated technique to be not limited by the diffraction barrier [51]. Resolution down to 2,4 nm have been reported [53].

4.3.2 Principle

The principle of STED microscopy relies on the phenomenon of stimulated emission, predicted by Albert Einstein [54, 55]. Stimulated emission occurs when an excited fluorophore is induced to return to its ground state by interacting with a photon of a specific wavelength. This process depletes the excited state population, creating a new photon with a frequency, polarization, and direction of travel identical to those of the incident photon (Figure 9A). This phenomenon makes STED microscopy possible. The technique involves using two spatially overlapping lasers: an excitation laser and a depletion (or STED) laser red-shifted relative to the tail of the fluorophore's emission and shaped into a doughnut-like ring around the focal point (Figure 9 B & C). The process begins with the excitation of the sample using the excitation laser, which excites the fluorophores to their excited state, similar to conventional fluorescence confocal microscopy. Then, the doughnut-shaped STED laser stimulates peripheral excited fluorophores to return to the ground state, thereby selectively reducing fluorescence outside the central minimum of the doughnut (Figure 9B). Only the fluorophores in the very center of the focal point remain in the excited state

and emit fluorescence. The resulting image has a smaller PSF, thereby increasing the resolution of the image. By selectively suppressing fluorescence in the periphery, STED achieves resolution beyond the classical diffraction limit (Figure 10).

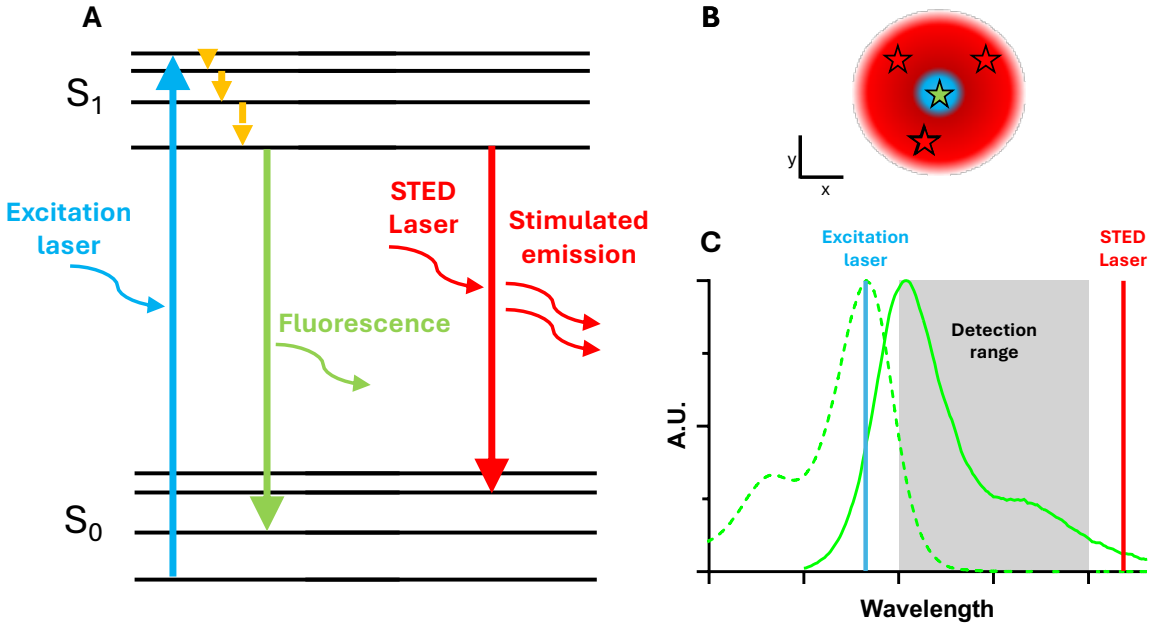

Figure 9. A: Jablonski diagram illustrating the principle of stimulated emission used in STED microscopy. In this process, the STED laser induces excited fluorophores to return to the ground state by emitting photons that match the STED laser in energy, wavelength, and thus color. This effectively depletes fluorescence in the illuminated region. B: Schematic of a STED point spread function (PSF) in XY plane showing green fluorescence preserved at the center, while surrounding fluorophores are depleted by stimulated emission from the STED laser doughnut, effectively reducing their contribution to the final image. C: Spectral positioning of the STED laser. The STED beam is typically tuned to the red tail of the fluorophore's emission spectrum. As a result, the photons generated through stimulated emission fall outside the detection window, rendering them "invisible" to the detector. This selective depletion allows only fluorophores at the very center of the excitation spot to fluoresce normally, thereby enhancing spatial resolution.

The STED resolution formula is the following:

$$d = \frac{\lambda}{2NA\sqrt{1 + {I_{STED}}/{I_{sat}}}} \qquad (28)$$

where,

- I_{STED} is the STED laser intensity.
- I_{sat} is the saturation intensity – STED laser intensity at which the fluorescence intensity drops to 50% of the initial value.

As can be seen, the formula follows an inverse square law. This means that at the beginning, for small STED laser powers, there is a significant gain in resolution. However, as the desired resolution increases, achieving further improvements becomes progressively more difficult. Typical resolutions in STED microscopy are less than 80 nanometers. However, values as low as 2.4 nanometers have also been reported [53].

STED is a single point laser scanning microscopy technique, essentially making a STED microscope an upgraded confocal microscope. The key components of a STED microscope include the excitation laser, the STED laser, a method to shape the STED laser into a doughnut, the detection system, and an appropriate fluorophore. There are various methods to shape the STED laser, with the use of a vortex phase plate being the most common. A vortex phase plate imposes a helical phase shift on the beam, ramping smoothly from 0 to 2π along a complete circle around the center of the beam (i.e., along the angular direction around the beam axis). This phase plate shapes the STED laser into a doughnut by manipulating the phase of the light waves passing through it. The phase plate introduces a phase shift in the light waves, typically by retarding them in specific regions of the beam. This phase shift causes destructive interference in the center of the beam, creating a region of zero intensity, which forms the "hole" in the doughnut. Around the central region, the phase shift results in constructive interference, leading to higher intensity light forming a ring around the periphery. By carefully designing the phase plate, the light beam is shaped into a doughnut-like ring with zero intensity at the center and high intensity around the edges.

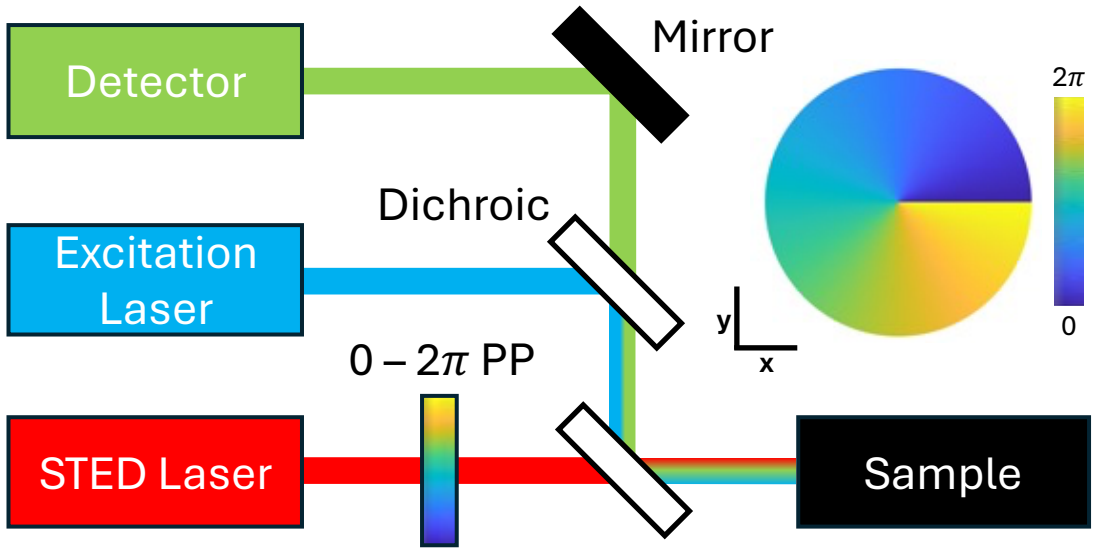

Figure 10. Simplified schematic of a STED microscope setup. The 0 – 2π phase plate (0 – 2π PP, and schematic top right) is responsible for the formation of the STED doughnut. The layout of the illumination at the sample is shown, with the star representing hypothetical fluorophores. Fluorophores affected by the STED laser emit light at the same wavelength as the STED laser and are thus "invisible" to detection. Only those fluorophores located in the center, where no STED laser light is present, are detectable, resulting in a super-resolved image. Phase plate schematic was done in MATLAB.

4.3.3 Choice of Fluorophore

The selection of a fluorophore for STED imaging is a critical decision. This choice largely depends on the available STED laser, as the STED laser must overlap with the red-shifted emission tail of the dye, as mentioned earlier. This ensures that the stimulated emission can be effectively filtered. Over the years, many fluorophores have been specially designed for STED imaging to match the three most common STED laser wavelengths: ~590 nm, ~660 nm, and ~770 nm.

However, most dyes have been developed for the ~770 nm STED laser, due to the enhanced brightness and photostability of dyes in this part of the spectrum [31, 32, 56-62]. Consequently, this thesis will focus on dyes optimized for this depletion wavelength. Live-cell STED imaging using fluorescent proteins has always posed challenges due to the high STED laser power required. However, recent advancements have made it possible to conduct such experiments with a limited number of new dyes and labelling techniques tailored for specific applications [63-67].

STED microscopy offers several key advantages. It achieves resolutions as fine as a few tens of nanometers, significantly surpassing the capabilities of conventional light microscopy, while often utilizing the same labeling strategies and dyes as those used in traditional confocal microscopy. This means there is sometimes no need for additional sample preparation, just a simple protocol adjustment to make the samples STED-ready. As a result, STED microscopy has become a widely used tool in biological research. For instance, in neuroscience, STED microscopy is employed to investigate the fine structure of synapses, neuronal networks, and the distribution of neurotransmitter receptors, offering valuable insights into brain function and neurological diseases [64, 65, 67]. In cell biology, researchers use STED to examine the organization of cytoskeletal filaments, organelles, and protein complexes at high resolution, helping to better understand cellular processes and functions[63, 65-67]. With its wide range of applications, STED microscopy has become an indispensable tool in biological research, providing detailed insights into complex biological systems.

4.3.4 Multicolor STED

In life sciences, high-resolution observation of a single structure can be beneficial, but understanding the relationships between multiple structures is often essential. This need has fueled the demand for multi-color microscopy. Since the advent of super-resolution microscopy, there has been a continuous need to visualize multiple biological structures with high resolution. Super-resolution techniques have sought to increase the number of structures that can be simultaneously imaged. Among these techniques, STED has also contributed to this endeavor. However, adapting STED for multicolor imaging has proven to be challenging. STED microscopy requires the precise alignment of two laser beams: one for exciting fluorescence and the other for quenching it via stimulated emission. This requirement complicates the imaging process for multiple fluorophores.

Initial attempts at two-color STED experiments involved using separate lasers for each fluorophore [68, 69]. While technically feasible, this approach is impractical for routine use due to the complexity of aligning two laser pairs. Consequently, shortly after new methods were

developed to achieve two-color STED microscopy, such as measuring fluorescence lifetimes [32], or employing photoswitchable fluorescent proteins [70].All the development was initially done on home-made systems. Around that time, commercial STED microscopes became available, utilizing up to three depletion laser wavelengths (592 or 595 nm, 660 nm, and 775 nm), theoretically allowing the use of fluorochromes across the entire spectral range of a confocal microscope. However, due to the alignment difficulties previously mentioned, along with the need to prevent total photobleaching of long-wavelength dyes by lower-wavelength depletion lasers and the superior performance of far-red dyes with STED [31], the 775 nm pulsed STED laser became the preferred choice. Using a single depletion laser for all fluorochromes is ideal to avoid these issues. Consequently, multi-color STED studies often rely on 775 nm depletion with near or far-red dyes.

There are few publications featuring more than three colors imaged by STED. For instance, Rönnlund et al. [71] used a scheme with two color channels, each containing two dyes or distinguishable dye conjugates. While this method was feasible in small, flat platelets, it may be challenging in larger cells due to sample drift. Another study by Stefan Hell's group demonstrated four dyes excited with 612 nm and depleted with 775 nm [59], separating the overlapping emission spectra computationally by spectral unmixing. Unfortunately, one of these dyes, KK1441, is not commercially available, limiting the scheme to three usable dyes for most researchers. Another paper from Hell's group visualized five fluorochromes by STED using a similar approach, with specific dyes imaged and bleached before uncaging additional dyes in the same spectral range, supplemented with Alexa Fluor 488 depleted with a second STED laser [72].

At the beginning of this thesis, we devised a novel approach utilizing differences in the absorption and emission spectra of fluorescent dyes with closely neighboring spectra. By exciting a pair of fluorophores with different lasers, we were able to obtain distinct emission signatures due to their varying spectra. These differences were exploited to create multicolor images in both confocal and STED modes. This approach facilitated imaging three different dyes using only one STED laser in a relatively straightforward manner. Importantly, it required no prior knowledge or reference of the dyes used. This aspect was significant because obtaining precise emission or lifetime references for individual dyes in a multi-color context is not always feasible [30].

Building on this study, we extended the number of dyes to five using a single STED laser. Recent advancements in FLIM technology have resulted in faster systems integrated with commercial confocal and STED software, making them more user-friendly, as opposed to the slow and home-made system presented in [32]. Phasor-based analysis of FLIM data, as previously described, enabled easy and rapid fluorochrome separation with lower photon numbers. Although this

method is less accurate in determining absolute lifetimes, it is effective for distinguishing different fluorochromes based on relative lifetime differences.

In subsequent work, we developed a multi-color STED-FLIM scheme using a commercial confocal system with STED and FLIM capabilities [31]. This approach minimized alignment issues by using one depletion laser (pulsed 775 nm) and one multi-wavelength excitation laser. We presented five-color STED and confocal images in only three spectral channels and suggested ways to further increase the number of colors for STED with a single depletion laser. Using commercially available fluorochrome-labeled antibodies, we demonstrated that phasor-based image analysis could effectively separate two fluorochromes by lifetime in a spectral channel. This focus was crucial for us, as we aimed to provide guidelines for creating STED images with minimal effort and cost for scientists. As commercial STED-FLIM systems become more common, more scientists have access to them, and using commercial dyes makes it more accessible for labs worldwide to produce their own STED images. I strongly support advancing research methodologies while ensuring they remain accessible to the broader scientific community.

Such advancements benefitted the project describe in manuscript IV. To investigate extracellular vesicles (EVs) uptake and cargo preservation in neural cells, the STED-FLIM imaging approach was used. The technique enabled high-resolution, multicolor imaging to track EVs localization at the nanoscale, revealing distinct uptake patterns in progenitors, neurons, and astrocytes. It also provided clear visualization of EV-associated proteins within cells, offering insights into how EV trafficking and localization vary by recipient cell type. This approach demonstrated the power of STED-FLIM for studying dynamic intercellular communication during brain development.

5 Aims of the thesis

The central focus of my thesis is to optimize FLIM in order to achieve maximal precision in both temporal and spatial dimensions. FLIM provides an additional layer of information beyond conventional fluorescence data, significantly enhancing data analysis and simplifying interpretation once the methodology is well-established. To fully exploit its potential, FLIM requires rigorous optimization and validation to demonstrate not only its technical feasibility but also its practical advantages for addressing biologically relevant questions. In this thesis, two complementary directions are pursued: the development of STED-FLIM for multicolor super-resolution imaging, and the application of FLIM-FRET for probing molecular interactions.

5.1 STED-FLIM: Multicolor Super-Resolution Imaging for Biological Applications

This part of the work aims to establish STED-FLIM as a versatile method for multicolor super-resolution imaging. The objective is to develop and optimize a three- to five-color STED multiplexing strategy based on commercially available dyes and instrumentation, and to translate this into a robust, reproducible protocol that can be broadly adopted. The optimized methodology shall then be applied to investigate extracellular vesicle uptake in neural cells, enabling high-resolution visualization of cell-type-specific localization patterns and intracellular trafficking routes. Through this approach, STED-FLIM shall be advanced as a powerful technique for multiplexed imaging in complex biological systems

5.2 Applications of FLIM-FRET Across Diverse Biological Contexts

A second aim of this thesis is to apply FLIM-FRET as a broadly adaptable technique for probing molecular interactions and dynamic processes across different biological systems. Specifically, the work shall investigate the interaction between the post-transcriptional regulators Roquin-1 and Regnase-1 within cytoplasmic P-bodies, including the identification of critical interaction domains using truncation mutants. In parallel, it shall visualize nucleosome remodeling by the ISWI ATPase within dense chromatin condensates, thereby assessing ATP-dependent remodeling activity and protein mobility. Together, these applications are designed to demonstrate the versatility of FLIM-FRET in elucidating protein interactions and chromatin dynamics within complex cellular environments.

6 Manuscripts

6.1 Triple-Color STED Nanoscopy: Sampling Absorption Spectra Differences for Efficient Linear Species Unmixing

Mariano Gonzalez Pisfil, Sumeet Rohilla, Marcelle König, Benedikt Krämer, Matthias Patting, Felix Koberling and Rainer Erdmann

2021, The Journal of Physical Chemistry B, 125(22), 5694-5705

https://doi.org/10.1021/acs.jpcb.0c11390?

This paper demonstrates a new approach using the differences in absorption spectra of fluorescent dyes with closely neighboring spectra to achieve multicolor super-resolution microscopy.

In recent years, the demand for simultaneous multicolor super-resolution in cells has grown. Each super-resolution microscopy technique has its pros and cons with respect to multicolor applications. A common problem are dyes with spectral overlap. To address this issue, a simple approach using STED super-resolution together with a commercial FLIM confocal microscope was implemented.

Using nanosecond pulsed interleaved excitation (PIE), two or more pulsed laser with the same repetition rate are delayed with a delay corresponding to the inverse of the repetition rate divided by the number of lasers used in the setup. In this case, we utilize three excitation wavelengths (595 nm, 640 nm and 660 nm) with a repetition rate of 13.33 MHz (a pulse every 75 ns), delayed by 25 ns from each other. Creating a pattern where a 595 nm pulse is followed 25 ns later by a 640 nm pulse, and 25 ns later by a 660 nm pulse. With this setup, we were able to simultaneously probe multiple spectrally overlapping fluorescent tags. These fluorescent species, ATTO 594, Abberior STAR 635P and ATTO 647N have absorption maxima as close as 13 nm. The acquired images were then analyzed and decomposed using a linear unmixing algorithm based on reference patterns, which can be identified in a 2D graph: the image correlation map (ICM). Since every dye has a unique excitation and emission spectrum, the absorption and fluorescence emission from each dye will be different and unique for each of the excitation lasers used. With the ICM, these differences can be calculated pixel-wise using all the detectors to maximize light collection. Plotting on a graph pixel-wise these intensity differences between dyes will generate unique patterns where we could identify the particular signature of each dye, and the amount of cross-talk between dyes in all channels. Thus, allowing easy identification of the single-species regions, eliminating the need to record additional reference samples. The name of this method is Fast Pattern Matching (FPM). The proposed imaging scheme demonstrates high speed and

quality species separation, even for up to three species, using established reference samples and dyes commonly employed in cellular STED imaging.

My contribution to the work was the implementation of the experimental protocol for the acquisition and the validation of technique, acquiring the images and doing the cross-talk analysis. Samples were provided by GATTAquant.

This work was done in collaboration with PicoQuant GmbH.

6.2 Stimulated emission depletion microscopy with a single depletion laser using five fluorochromes and fluorescence lifetime phasor separation

Mariano Gonzalez Pisfil, Iliya Nadelson, Brigitte Bergner, Sonja Rottmeier, Andreas W. Thomae and Steffen Dietzel

2022, Scientific Reports, 12(1), 14027

https://doi.org/10.1038/s41598-022-17825-5

This paper builds upon the previous article where a technique for three color STED was demonstrated. However, this time, the lifetime of the dyes instead of their absorption spectra was used instead to separate dyes with overlapping spectra to achieve multicolor super-resolution microscopy.

In STED microscopy, super-resolution is achieved by exciting a diffraction-limited volume and then suppressing fluorescence in its outer regions through depletion. Different approaches have been developed to increase the number of simultaneous targets imaged with different fluorochromes. One of them is using multiple depletion lasers to cover a larger spectral range. However, this can introduce misalignment and bleaching. Hence using a single depletion wavelength is preferable for multi-color analyses. This limits the number of usable spectral channels, however. In this paper, we increased the number of distinguishable colors in STED or confocal microscopy by lifetime-based separation of two dyes with similar emission spectra (i.e. in the same fluorescent channel) but different fluorescent lifetimes. Our multi-color super-resolution approach involved two fluorescent dyes in the near-red range (exc. 594 nm, em. 600-630) and two in the far-red channel (633/641-680), supplemented by a single further redshifted fluorochrome (670/701-750). We used common staining protocols and only commercially available fluorescent dyes. These dyes were all depleted using a single laser at 775 nm, effectively avoiding potential alignment issues. This strategy doubles the number of distinguishable colors not only in STED but also in confocal microscopy. Furthermore, we provide evidence that STED-FLIM with eight distinguishable colors using a single depletion laser could be feasible if suitable fluorescent dyes were identified. Additionally, we confirm that a fluorochrome's lifetime can vary depending on the molecules to which it is coupled.

My contribution involved the implementation of the method, setting up the experimental protocol for the acquisition and acquiring the images. I also handled the post-processing, including lifetime unmixing and quality control. Furthermore, I tested the overall reproducibility of the results. The samples were prepared in-house.

6.3 Fluorochrome Separation by Fluorescence Lifetime Phasor Analysis in Confocal and STED Microscopy

Mariano Gonzalez Pisfil and Steffen Dietzel

2025, Methods in Microscopy, 2(1), 45-60

https://doi.org/10.1515/mim-2024-0022

This protocol is based on a previously published manuscript (**manuscript II** in this thesis). It is a detailed and comprehensive protocol that can be adapted for different situations encountered in laboratories. We aim to offer proper guidelines so that scientists starting with STED have a solid foundation to reference for their multicolor STED images.

6.4 Extracellular vesicle-mediated trafficking of molecular cues during human brain development

Andrea Forero, Fabrizia Pipicelli, Sylvain Moser, Natalia Baumann, Christian Grätz, **Mariano Gonzalez Pisfil**, Michael W. Pfaffl, Benno Pütz, Pavel Kielkowski, Filippo M. Cernilogar, Giuseppina Maccarrone, Rossella Di Giaimo, Silvia Cappello

2024, Cell Reports, 43(10), 114755

https://doi.org/10.1016/j.celrep.2024.114755

Recent studies have increasingly recognized extracellular vesicles (EVs) as key mediators of intercellular communication within the nervous system. While much research has focused on their roles in neurodegeneration, emerging evidence highlights their functions during neurodevelopment.

This paper investigates the molecular and functional diversity of EVs throughout human brain development using iPSC-derived cerebral organoids, neural progenitor cells, neurons, and astrocytes. Utilizing mass spectrometry and high-resolution imaging, the EV cargo composition and uptake specificity across developmental stages and cell types was characterized.

The results demonstrate that EVs are highly specific in their cargo depending on their cellular origin. Neural progenitors, neurons, and astrocytes each secrete EVs with distinct proteomic signatures that evolve over time. Notably, EVs carry functionally important molecules like the transcriptional regulator YAP1, whose delivery and intracellular localization vary with the recipient cell type, indicating targeted cargo selection.

Mechanistically, the study proposes that EVs serve as active signaling units that modulate recipient cell behavior contextually, rather than passive metabolic byproducts. STED-FLIM imaging revealed cell type–dependent differences in EV uptake and localization, contributing to understanding how spatial and temporal signaling regulation occurs during early brain development. EV uptake and trafficking represent a relevant biological system where STED-FLIM imaging provides nanoscale resolution of molecular processes.

My contribution involved the implementation of the method and performing STED-FLIM super-resolution microscopy to characterize EV uptake in neural cells. I independently carried out all imaging acquisition, while collaborators handled the subsequent image analysis. Fixed neural cells were stained with DAPI and labeled with Alexa 594 or ATTO 647N depending on targeted markers. Additional labeling with DiI, ExoGlow, and RFP was applied as required by experimental conditions. This work was done in collaboration with the group of Silvia Capello at the BMC.

6.5 Disrupting Roquin-1 interactions with Regnase-1 induces autoimmunity and enhances antitumor responses

Gesine Behrens, Stephanie L. Edelmann, Timsse Raj, Nina Kronbeck, Thomas Monecke, Elena Davydova, Elaine H. Wong, Lisa Kifinger, Florian Giesert, Martin E. Kirmaier, Christine Hohn, Laura S. de Jonge, **Mariano Gonzalez Pisfil**, Mingui Fu, Sebastian Theurich, Stefan Feske, Naoto Kawakami, Wolfgang Wurst, Dierk Niessing & Vigo Heissmeyer

2021, Nature Immunology, 22(12), 1563–1576

https://doi.org/10.1038/s41590-021-01064-3

The Roquin-1 and Regnase-1 proteins play crucial roles in maintaining immune homeostasis. They bind and post-transcriptionally regulate proinflammatory messenger RNAs. Mutations in Roquin-1 disrupting this interaction and cooperative regulation of targets resulted in the induction of T follicular helper cells, germinal center B cells, and autoantibody formation. Interestingly, these mutations also enhanced the functionality of tumor-specific T cells by promoting their accumulation within the tumor and reducing expression of exhaustion markers.

My contribution to this work was on the characterization of the direct interaction between Roquin-1 and Regnase-1 and if their post-transcriptional co-regulation role is a consequence of this interaction. For that, I focused on studying the interaction in P-bodies. P-bodies are cytoplasmic granules made up of ribonucleoproteins (RNPs), mainly consisting of mRNAs that are not translated and proteins involved in mRNA degradation. A proximity assay based on FRET was performed. When the two fluorochromes are closer together than 10 nm, energy is transferred from excited GFP to mCherry: Regnase-1 was labeled with GFP, and Roquin-1 WT / Roquin-1$^{aa1\text{-}510}$ with mCherry. Both constructs were transiently transfected in cultured cells to study the interaction. A third construct, Rck-BFP (P-body marker) was also co-transfected to get spatial information. A confocal time-resolved microscope was used to perform FLIM. Mean lifetime values were calculated using curve fitting. We found that there is clear interaction of Regnase-1 and Roquin-1 in P-bodies, as well as in the rest of the cell, but to a lesser degree compared to P-bodies. A search for the minimal protein sequence responsible for the interaction in Roquin-1 was done. A cleaved form of Roquin-1 (Roquin-1$^{aa1\text{-}510}$) found in iDKO T cells was labeled with mCherry and FRET was analyzed. It was found to show partial interaction with Regnase-1, consistent with other results obtained in flow cytometry, even though it no longer localized in P-Bodies. In a last assay, a truncated form of Regnase-1 (Regnase-1$^{aa112\text{-}297}$ was labeled with GFP and tested together for FLIM-FRET with Roquin-1$^{aa1\text{-}510}$ – mCherry. Both proteins exhibited cytoplasmic localization,

but only Regnase-1$^{aa112-297}$ was present in the nucleus as opposed to Roquin-1$^{aa1-510}$. FLIM imaging showed a decrease of lifetime in the cytoplasm, synonym of interaction between the partners. Whereas in the nucleus, where only Regnase-1$^{aa112-297}$ is present, the lifetime does not change as opposed to the control. Further confirming these regions are the ones responsible of the interactions between the two partners.

I was involved implementing the method, setting up and executing the FLIM FRET protocol. I tested different conditions and validated the results for reproducibility. Additionally, I conducted the FRET analysis and the statistical evaluation of the results. I also created Fig. 5a-c.

This project was done in collaboration with the group of Vigo Heissmeyer at the BMC.

The version of this article included in this dissertation is the author's accepted manuscript. Due to copyright restrictions, the final published version cannot be reproduced here. The definitive version can be found in the following reference:
Behrens et al., (2021). "*Disrupting Roquin-1 interaction with Regnase-1 induces autoimmunity and enhances antitumor responses*." Nat Immunol 22(12): 1563-1576.

6.6 ISWI catalyzes nucleosome sliding in condensed nucleosome arrays

Petra Vizjak, Dieter Kamp, Nicola Hepp, Alessandro Scacchetti, **Mariano Gonzalez Pisfil**, Joseph Bartho, Mario Halic, Peter B Becker, Michaela Smolle, Johannes Stigler, Felix Mueller-Planitz

2024, Nature Structural & Molecular Biology, 31(9), 1331-1340

https://doi.org/10.1038/s41594-024-01290-x

In this study, it was examined how the Drosophila chromatin remodeler ISWI functions within dense chromatin environments that mimic the crowded nuclear interior. While traditional studies of nucleosome sliding focus on dilute chromatin, this work explored ISWI's activity within condensed, phase-separated nucleosome arrays.

A key methodological strength of this study was the application of FLIM-FRET to directly monitor chromatin remodeling activity in vitro. FLIM-FRET enabled precise and quantitative measurements of nucleosome repositioning within dense chromatin condensates, where traditional FRET intensity-based readouts are often confounded by fluorophore concentration and light scattering. It was possible to resolve the interaction dynamics between fluorophore-labeled nucleosomes with high temporal and spatial precision, demonstrating the capability of the technique to capture molecular events in real time and at subcellular resolution.

The results showed that ISWI retains its nucleosome sliding capability even within highly condensed chromatin. However, in the absence of ATP, ISWI stiffened the chromatin condensates and became immobilized, indicating that ATP hydrolysis is essential both for catalytic activity and for preserving dynamic behavior within dense nuclear compartments.

Furthermore, molecular dynamics simulations supported a "monkey-bar" mechanism, where ISWI moves between adjacent nucleosomes via sequential interactions, facilitating remodeling in confined environments.

This work underscores the value of FLIM-FRET in dissecting protein-nucleosome interactions. It demonstrates that FLIM-FRET is a powerful tool for probing molecular dynamics in crowded systems, offering both sensitivity and robustness beyond conventional fluorescence approaches.

In the context of this study, my contributions were centered on characterizing nucleosome sliding along DNA and evaluating the mobility of the ISWI remodeler within chromatin condensates. To assess ISWI's remodeling activity, I employed FLIM-FRET to generate and analyze time-lapse image sequences. In this experimental setup, DNA strands and nucleosomes were fluorescently

labeled with ATTO 647N and ATTO 565, respectively, forming FRET pairs. At the onset of the experiment, robust FRET signals confirmed the close spatial proximity between the DNA and nucleosomes. Upon the addition of ATP and ISWI, a marked decrease in FRET efficiency was observed, consistent with nucleosome repositioning along the DNA, a direct indication of ISWI-mediated sliding activity within dense condensates.

Additionally, I conducted Fluorescence Recovery After Photobleaching (FRAP) assays on condensates containing ISWI-GFP to investigate the remodeler's dynamic behavior under varying biochemical conditions. These experiments demonstrated that ISWI's mobility within condensates was significantly influenced by the presence of ATP, highlighting the ATP-dependence of both its catalytic activity and intra-condensate dynamics.

This project was a collaboration with the group of Felix Mueller-Planitz at the BMC.

The version of this article included in this dissertation is the author's accepted manuscript. Due to copyright restrictions, the final published version cannot be reproduced here. The definitive version can be found in the following reference:

Vizjak et al., (2024). "*ISWI catalyzes nucleosome sliding in condensed nucleosome arrays*." Nat Struct Mol Biol 31(9): 1331-1340.

7 References

1. Valeur, B. and M.N. Berberan-Santos, *A Brief History of Fluorescence and Phosphorescence before the Emergence of Quantum Theory.* Journal of Chemical Education, 2011. **88**(6): p. 731-738.

2. Clarke, E.D., *Account of a newly discovered variety of green fluor spar, of very uncommon beauty, and with remarkable properties of colour and phosphorescence.* The Annals of Philosophy, 1819. **14**(34-36): p. 2.

3. Haüy, R., *Traité de minéralogie*, in *Traité de minéralogie*, R. Haüy, Editor. 1822, Bachelier et Huzard: Paris France. p. 512.

4. Brewster, D., *XIX. On the Colours of Natural Bodies.* Transactions of the Royal Society of Edinburgh, 1834. **12**(2): p. 538-545.

5. Herschel, J.F.W., *IV. 'Αμόρφωτα, no. I.— on a case of superficial colour presented by a homogeneous liquid internally colourless.* Philosophical Transactions of the Royal Society of London, 1845. **135**: p. 143-145.

6. Stokes, G.G., *XXX. On the change of refrangibility of light.* Philosophical Transactions of the Royal Society of London, 1852. **142**: p. 463-562.

7. Freund, H., *[The role of Max Haitinger in the development of fluorescence microscopy].* Mikroskopie, 1969. **25**: p. 73-7.

8. Heimstädt, O., *Das fluoreszenzmikroskop.* Z Wiss Mikrosk, 1911. **28**(330-337): p. 14.

9. Reichert, K., *Das Fluoreszenzmikroskop.* Phys Z, 1911. **12**(1010-1011): p. 2.

10. Lehmann, H., *Das Luminszenz-Mikroskop: seine Grundlagen und seine Anwendungen*. 1913.

11. Ellinger, P. and A. Hirt, *Mikroskopische Untersuchungen an lebenden Organen*. Zeitschrift für Anatomie und Entwicklungsgeschichte, 1929. **90**(5): p. 791-802.

12. Coons, A.H., et al., *The Demonstration of Pneumococcal Antigen in Tissues by the Use of Fluorescent Antibody1*. The Journal of Immunology, 1942. **45**(3): p. 159-170.

13. Shimomura, O., F.H. Johnson, and Y. Saiga, *Extraction, Purification and Properties of Aequorin, a Bioluminescent Protein from the Luminous Hydromedusan, Aequorea*. Journal of Cellular and Comparative Physiology, 1962. **59**(3): p. 223-239.

14. Heim, R. and R.Y. Tsien, *Engineering green fluorescent protein for improved brightness, longer wavelengths and fluorescence resonance energy transfer.* Current Biology, 1996. **6**(2): p. 178-182.

15. Chalfie, M., et al., *Green Fluorescent Protein as a Marker for Gene Expression*. Science, 1994. **263**(5148): p. 802-805.

16. Terai, T. and T. Nagano, *Small-molecule fluorophores and fluorescent probes for bioimaging*. Pflügers Archiv - European Journal of Physiology, 2013. **465**(3): p. 347-359.

17. Fili, N. and C.P. Toseland, *Fluorescence and Labelling: How to Choose and What to Do*, in *Fluorescent Methods for Molecular Motors*, C.P. Toseland and N. Fili, Editors. 2014, Springer Basel: Basel. p. 1-24.

18. Van Noorden, S., *Advances in immunocytochemistry.* Folia Histochemica et Cytobiologica, 2002. **40**(2): p. 121-124.

19. Zimmermann, F.P., et al., *Fluorescence lifetime of gas-phase toluene at elevated temperatures.* Chemical Physics Letters, 2006. **426**(4): p. 248-251.

20. Liu, T., et al., *Molecular structure perspective on Temperature-Sensitive properties of rhodamine aqueous solutions.* Spectrochimica Acta Part A: Molecular and Biomolecular Spectroscopy, 2022. **275**: p. 121166.

21. Li, W., et al., *Ultra-stable and versatile widefield cryo-fluorescence microscope for single-molecule localization with sub-nanometer accuracy.* Optics Express, 2015. **23**(3): p. 3770-3783.

22. Pawley, J., *The 39 Steps: A Cautionary Tale of Quantitative 3-D Fluorescence Microscopy.* BioTechniques, 2000. **28**(5): p. 884-887.

23. Lakowicz, J.R. and G. Weber, *Quenching of fluorescence by oxygen. A probe for structural fluctuations in macromolecules.* Biochemistry, 1973. **12**(21): p. 4161-70.

24. Magde, D., G.E. Rojas, and P.G. Seybold, *Solvent Dependence of the Fluorescence Lifetimes of Xanthene Dyes.* Photochemistry and Photobiology, 1999. **70**(5): p. 737-744.

25. Nakabayashi, T., et al., *Application of fluorescence lifetime imaging of enhanced green fluorescent protein to intracellular pH measurements.* Photochemical & Photobiological Sciences, 2008. **7**(6): p. 668-670.

26. Scott, T.G., et al., *Synthetic spectroscopic models related to coenzymes and base pairs. V. Emission properties of NADH. Studies of fluorescence lifetimes and quantum efficiencies of NADH, AcPyADH, [reduced acetylpyridineadenine dinucleotide] and simplified synthetic models.* Journal of the American Chemical Society, 1970. **92**(3): p. 687-695.

27. Gaviola, E., *Die Abklingungszeiten der Fluoreszenz von Farbstofflösungen.* Annalen der Physik, 1926. **386**(23): p. 681-710.

28. Gaviola, E., *Ein Fluorometer. Apparat zur Messung von fluoreszenzabklingungszeiten.* Zeitschrift für Physik, 1927. **42**(11): p. 853-861.

29. *Frequency-Domain Lifetime Measurements*, in *Principles of Fluorescence Spectroscopy*, J.R. Lakowicz, Editor. 2006, Springer US: Boston, MA. p. 157-204.

30. Gonzalez Pisfil, M., et al., *Triple-Color STED Nanoscopy: Sampling Absorption Spectra Differences for Efficient Linear Species Unmixing.* J Phys Chem B, 2021. **125**(22): p. 5694-5705.

31. Gonzalez Pisfil, M., et al., *Stimulated emission depletion microscopy with a single depletion laser using five fluorochromes and fluorescence lifetime phasor separation.* Sci Rep, 2022. **12**(1): p. 14027.

32. Bückers, J., et al., *Simultaneous multi-lifetime multi-color STED imaging for colocalization analyses*. Optics express, 2011. **19**(4): p. 3130-3143.

33. Niehörster, T., et al., *Multi-target spectrally resolved fluorescence lifetime imaging microscopy*. Nature Methods, 2016. **13**(3): p. 257-262.

34. Rowley, M.I., et al. *Bayesian analysis of fluorescence lifetime imaging data*. in *Multiphoton Microscopy in the Biomedical Sciences XI*. 2011. SPIE.

35. Rowley, M.I., et al., *Robust Bayesian Fluorescence Lifetime Estimation, Decay Model Selection and Instrument Response Determination for Low-Intensity FLIM Imaging*. PLOS ONE, 2016. **11**(6): p. e0158404.

36. *Time-Domain Lifetime Measurements*, in *Principles of Fluorescence Spectroscopy*, J.R. Lakowicz, Editor. 2006, Springer US: Boston, MA. p. 97-155.

37. Gratton, E., et al., *Fluorescence lifetime imaging for the two-photon microscope: time-domain and frequency-domain methods*. Journal of biomedical optics, 2003. **8**(3): p. 381-390.

38. Digman, M.A., et al., *The Phasor Approach to Fluorescence Lifetime Imaging Analysis*. Biophysical Journal, 2008. **94**(2): p. L14-L16.

39. Torrado, B., L. Malacrida, and S. Ranjit, *Linear Combination Properties of the Phasor Space in Fluorescence Imaging*. Sensors, 2022. **22**(3): p. 999.

40. Leray, A., et al., *Quantitative comparison of polar approach versus fitting method in time domain FLIM image analysis*. Cytometry Part A, 2011. **79A**(2): p. 149-158.

41. Förster, T., *Energy migration and fluorescence*. Journal of Biomedical Optics, 2012. **17**(1): p. 011002.

42. Stryer, L. and R.P. Haugland, *Energy transfer: a spectroscopic ruler*. Proceedings of the National Academy of Sciences, 1967. **58**(2): p. 719-726.

43. Miyawaki, A., et al., *Fluorescent indicators for Ca2+based on green fluorescent proteins and calmodulin*. Nature, 1997. **388**(6645): p. 882-887.

44. Kraynov, V.S., et al., *Localized Rac Activation Dynamics Visualized in Living Cells*. Science, 2000. **290**(5490): p. 333-337.

45. Demarco, I.A., et al., *Monitoring dynamic protein interactions with photoquenching FRET*. Nature Methods, 2006. **3**(7): p. 519-524.

46. Wallrabe, H., et al., *Receptor Complexes Cotransported via Polarized Endocytic Pathways Form Clusters with Distinct Organizations*. Molecular Biology of the Cell, 2007. **18**(6): p. 2226-2243.

47. Bidaux, G., et al., *FRET Image Correlation Spectroscopy Reveals RNAPII-Independent P-TEFb Recruitment on Chromatin*. Biophys J, 2018. **114**(3): p. 522-533.

48. Behrens, G., et al., *Disrupting Roquin-1 interaction with Regnase-1 induces autoimmunity and enhances antitumor responses*. Nat Immunol, 2021. **22**(12): p. 1563-1576.

49. Vizjak, P., et al., *ISWI catalyzes nucleosome sliding in condensed nucleosome arrays*. Nat Struct Mol Biol, 2024. **31**(9): p. 1331-1340.

50. Hell, S.W. and J. Wichmann, *Breaking the diffraction resolution limit by stimulated emission: stimulated-emission-depletion fluorescence microscopy*. Optics Letters, 1994. **19**(11): p. 780-782.

51. Klar, T.A. and S.W. Hell, *Subdiffraction resolution in far-field fluorescence microscopy*. Optics Letters, 1999. **24**(14): p. 954-956.

52. Abbe, E., *Beiträge zur Theorie des Mikroskops und der mikroskopischen Wahrnehmung*. Archiv für Mikroskopische Anatomie, 1873. **9**(1): p. 413-468.

53. Wildanger, D., et al., *Solid Immersion Facilitates Fluorescence Microscopy with Nanometer Resolution and Sub-Ångström Emitter Localization*. Advanced Materials, 2012. **24**(44): p. OP309-OP313.

54. Einstein, A., *Strahlungs-Emission und -Absorption nach der Quantentheorie*. Deutsche Physikalische Gesellschaft, 1916. **18**: p. 318-323.

55. Einstein, A., *Zur Quantentheorie der Strahlung*. Physikalische Zeitschrift, 1917. **18**: p. 121-128.

56. Anselm, E., et al., *Oligomerization of Drosophila Nucleoplasmin-Like Protein is required for its centromere localization*. Nucleic Acids Research, 2018. **46**(21): p. 11274-11286.

57. Wegner, W., et al., *In vivo mouse and live cell STED microscopy of neuronal actin plasticity using far-red emitting fluorescent proteins*. Scientific Reports, 2017. **7**(1): p. 11781.

58. Sograte-Idrissi, S., et al., *Circumvention of common labelling artefacts using secondary nanobodies*. Nanoscale, 2020. **12**(18): p. 10226-10239.

59. Winter, F.R., et al., *Multicolour nanoscopy of fixed and living cells with a single STED beam and hyperspectral detection*. Scientific Reports, 2017. **7**(1): p. 46492.

60. Wurm, C.A., et al., *Novel red fluorophores with superior performance in STED microscopy*. Optical Nanoscopy, 2012. **1**(1): p. 7.

61. Butkevich, A.N., et al., *Fluorescent Rhodamines and Fluorogenic Carbopyronines for Super-Resolution STED Microscopy in Living Cells*. Angewandte Chemie International Edition, 2016. **55**(10): p. 3290-3294.

62. Sednev, M.V., V.N. Belov, and S.W. Hell, *Fluorescent dyes with large Stokes shifts for super-resolution optical microscopy of biological objects: a review*. Methods and Applications in Fluorescence, 2015. **3**(4): p. 042004.

63. Liu, T., et al., *Multi-color live-cell STED nanoscopy of mitochondria with a gentle inner membrane stain*. Proceedings of the National Academy of Sciences, 2022. **119**(52): p. e2215799119.

64. Arizono, M., A. Idziak, and U.V. Nägerl, *Live STED imaging of functional neuroanatomy*. Nature Protocols, 2025.

65. Calovi, S., F.N. Soria, and J. Tønnesen, *Super-resolution STED microscopy in live brain tissue.* Neurobiology of Disease, 2021. **156**: p. 105420.

66. Spahn, C., et al., *Whole-Cell, 3D, and Multicolor STED Imaging with Exchangeable Fluorophores.* Nano Letters, 2019. **19**(1): p. 500-505.

67. Nägerl, U.V., et al., *Live-cell imaging of dendritic spines by STED microscopy.* Proceedings of the National Academy of Sciences, 2008. **105**(48): p. 18982-18987.

68. Donnert, G., et al., *Two-color far-field fluorescence nanoscopy.* Biophysical journal, 2007. **92**(8): p. L67-L69.

69. Meyer, L., et al., *Dual-color STED microscopy at 30-nm focal-plane resolution*. 2008.

70. Willig, K.I., et al., *Dual-label STED nanoscopy of living cells using photochromism.* Nano letters, 2011. **11**(9): p. 3970-3973.

71. Rönnlund, D., et al., *Multicolor Fluorescence Nanoscopy by Photobleaching: Concept, Verification, and Its Application To Resolve Selective Storage of Proteins in Platelets.* ACS Nano, 2014. **8**(5): p. 4358-4365.

72. Butkevich, A.N., et al., *Photoactivatable Fluorescent Dyes with Hydrophilic Caging Groups and Their Use in Multicolor Nanoscopy.* Journal of the American Chemical Society, 2021. **143**(44): p. 18388-18393.

8 Publications

Peer-reviewed Publications

Gonzalez Pisfil, M. and Dietzel, S. (2025). "*Fluorochrome Separation by Fluorescence Lifetime Phasor Analysis in Confocal and STED Microscopy.*" Methods in Microscopy 2(1): 45-60

Forero, A., Pipicelli, F., Moser, S., Baumann, N., Gratz, C., **Gonzalez Pisfil, M.**, Pfaffl, M. W., Putz, B., Kielkowski, P., Cernilogar, F. M., Maccarrone, G., Di Giaimo, R. and Cappello, S. (2024). "*Extracellular vesicle-mediated trafficking of molecular cues during human brain development*." Cell Rep 43(10): 114755.

Napoli, M., Immler, R., Rohwedder, I., Lupperger, V., Pfabe, J., **Gonzalez Pisfil, M.**, Yevtushenko, A., Vogl, T., Roth, J., Salvermoser, M., Dietzel, S., Slak Rupnik, M., Marr, C., Walzog, B., Sperandio, M. and Pruenster, M. (2024). "*Cytosolic S100A8/A9 promotes Ca(2+) supply at LFA-1 adhesion clusters during neutrophil recruitment*." Elife 13.

Vizjak, P., Kamp, D., Hepp, N., Scacchetti, A., **Gonzalez Pisfil, M.**, Bartho, J., Halic, M., Becker, P. B., Smolle, M., Stigler, J. and Mueller-Planitz, F. (2024). "*ISWI catalyzes nucleosome sliding in condensed nucleosome arrays*." Nat Struct Mol Biol 31(9): 1331-1340.

Gonzalez Pisfil, M., Nadelson, I., Bergner, B., Rottmeier, S., Thomae, A. W. and Dietzel, S. (2022). "*Stimulated emission depletion microscopy with a single depletion laser using five fluorochromes and fluorescence lifetime phasor separation*." Sci Rep 12(1): 14027.

Behrens, G., Edelmann, S. L., Raj, T., Kronbeck, N., Monecke, T., Davydova, E., Wong, E. H., Kifinger, L., Giesert, F., Kirmaier, M. E., Hohn, C., de Jonge, L. S., **Gonzalez Pisfil, M.**, Fu, M., Theurich, S., Feske, S., Kawakami, N., Wurst, W., Niessing, D. and Heissmeyer, V. (2021). "*Disrupting Roquin-1 interaction with Regnase-1 induces autoimmunity and enhances antitumor responses*." Nat Immunol 22(12): 1563-1576.

Gonzalez Pisfil, M., Rohilla, S., Konig, M., Kramer, B., Patting, M., Koberling, F. and Erdmann, R. (2021). "*Triple-Color STED Nanoscopy: Sampling Absorption Spectra Differences for Efficient Linear Species Unmixing*." J Phys Chem B 125(22): 5694-5705.

Furlan, A., **Gonzalez Pisfil, M.**, Leray, A., Champelovier, D., Henry, M., Le Nezet, C., Bensaude, O., Lefranc, M., Wohland, T., Vandenbunder, B., Bidaux, G. and Heliot, L. (2019). "*HEXIM1 Diffusion in the Nucleus Is Regulated by Its Interactions with Both 7SK and P-TEFb*." Biophys J 117(9): 1615-1625.

Barras, A., Skandrani, N., **Gonzalez Pisfil, M.**, Paryzhak, S., Dumych, T., Haustrate, A., Heliot, L., Gharbi, T., Boulahdour, H., Lehen'kyi, V., Bilyy, R., Szunerits, S., Bidaux, G. and Boukherroub, R. (2018). "*Improved photodynamic effect through encapsulation of two photosensitizers in lipid nanocapsules*." J Mater Chem B 6(37): 5949-5963.

Bidaux, G., Le Nezet, C., **Gonzalez Pisfil, M.**, Henry, M., Furlan, A., Bensaude, O., Vandenbunder, B. and Heliot, L. (2018). "*FRET Image Correlation Spectroscopy Reveals RNAPII-Independent P-TEFb Recruitment on Chromatin*." Biophys J 114(3): 522-533.

Furlan, A., Agbazahou, F., Henry, M., **Gonzalez Pisfil, M.**, Le Nezet, C., Champelovier, D., Fournier, M., Vandenbunder, B., Bidaux, G. and Heliot, L. (2018). "*[P-TEFb and Brd4: actors of the transcription pause release as therapeutical targets]*." Med Sci (Paris) 34(8-9): 685-692.

Groux-Degroote, S., Schulz, C., Cogez, V., Noel, M., Portier, L., Vicogne, D., Solorzano, C., Dall'Olio, F., Steenackers, A., Mortuaire, M., **Gonzalez Pisfil, M.**, Henry, M., Foulquier, F., Heliot, L. and Harduin-Lepers, A. (2018). "*The extended cytoplasmic tail of the human B4GALNT2 is critical for its Golgi targeting and post-Golgi sorting*." FEBS J 285(18): 3442-3463.

Cerezo, M., Lehraiki, A., Millet, A., Rouaud, F., Plaisant, M., Jaune, E., Botton, T., Ronco, C., Abbe, P., Amdouni, H., Passeron, T., Hofman, V., Mograbi, B., Dabert-Gay, A. S., Debayle, D., Alcor, D., Rabhi, N., Annicotte, J. S., Heliot, L., **Gonzalez Pisfil, M.**, Robert, C., Morera, S., Vigouroux, A., Gual, P., Ali, M. M. U., Bertolotto, C., Hofman, P., Ballotti, R., Benhida, R. and Rocchi, S. (2016). "*Compounds Triggering ER Stress Exert Anti-Melanoma Effects and Overcome BRAF Inhibitor Resistance*." Cancer Cell 29(6): 805-819.

Sipieter, F., Cappe, B., **Gonzalez Pisfil, M.**, Spriet, C., Bodart, J. F., Cailliau-Maggio, K., Vandenabeele, P., Heliot, L. and Riquet, F. B. (2015). "*Novel Reporter for Faithful Monitoring of ERK2 Dynamics in Living Cells and Model Organisms*." PLoS One 10(10): e0140924.

Turcheniuk, K., Hage, C. H., Spadavecchia, J., Serrano, A. Y., Larroulet, I., Pesquera, A., Zurutuza, A., **Gonzalez Pisfil, M.**, Heliot, L., Boukaert, J., Boukherroub, R. and Szunerits, S. (2015). "*Plasmonic photothermal destruction of uropathogenic E. coli with reduced graphene oxide and core/shell nanocomposites of gold nanorods/reduced graphene oxide*." J Mater Chem B 3(3): 375-386.

Heinrich, P., **Gonzalez Pisfil, M.**, Kahn, J., Heliot, L. and Leray, A. (2014). "*Implementation of transportation distance for analyzing FLIM and FRET experiments*." Bull Math Biol 76(10): 2596-2626.

Other Publications

Gonzalez Pisfil M., Dietzel S. (2025). "*Fluorescence microscopy with lifetime separation*", Microscopy and Analysis 39(2): 29-31

Oral Presentations

Gonzalez Pisfil M., et al (2022, April). *Five color STED microscopy with one depletion laser and fluorescence lifetime phasor separation*, Focus on Microscopy (FOM), Online

Gonzalez Pisfil M., (2019, September). *Scanning FCS and Super-Resolution Microscopy on 2D Lipid Membranes*, 25th International Anniversary Workshop on “Single Molecule Spectroscopy and Super-resolution Microscopy in the Life Sciences”, Berlin, Germany

Gonzalez Pisfil M., et al (2018, January). *Scanning FCS and multi-species STED microscopy for diffusion studies in membranes*, Quantitative Bioimaging (QBI) conference, Göttingen, Germany

Gonzalez Pisfil M., et al (2017, October). *Multi-Species Diffusion Studies in Membranes Utilizing Scanning FCS and Super-Resolution Microscopy*, 3rd Workshop "Fluorescence correlation spectroscopy in soft matter science", Munich, Germany [also presented at Third Infinity Conference as invited speaker (2017, October). Göttingen, Germany]

Posters Presentations

Gonzalez Pisfil M., et al (2023, March). *Five color STED nanoscopy with a single depletion laser and Phasor lifetime unmixing*, Trends in Microscopy 2023, Münsingen, Germany

Gonzalez Pisfil M., et al (2019, April). *3-Color STED Nanoscopy: Linear Unmixing by Fast Pattern-Matching*, Focus on Microscopy (FOM), London, UK

Gonzalez Pisfil M., et al (2018, September). *Multi-Species Diffusion Studies in Membranes Utilizing Scanning FCS and Super-Resolution Microscopy*, 24th Workshop on Single Molecule Spectroscopy and Super-resolution Microscopy in the Life Sciences, Berlin, Germany

Gonzalez Pisfil M., et al (2015, March). *Multimodal approach to measure molecular dynamics and interactions in living cells for studies of regulation of transcription elongation phase by P-TEFb complex*, Focus on Microscopy (FOM), Göttingen, Germany

Gonzalez Pisfil M., et al (2013, May) *Measurements of molecular dynamics and interactions in living cells for studies of regulation of transcription elongation phase by P-TEFb complex*, 13th European Light Microscopy Initiative (ELMI) Meeting, Arcachon, France

Invited Speaker and Workshop Lecturer

Gonzalez Pisfil M., (2025, May). *The opportunity of a lifetime: Fluorescence Lifetime Imaging Microscopy in biological samples*, FEBS Course: Fluorescence microspectroscopy: functional imaging of biological systems, Wageningen, The Netherlands

Gonzalez Pisfil M., (2024, October). *Lecture: Multicolor imaging using lifetime phasor separation in confocal and STED microscopy*, See the Hidden: Discover more with FLIM, Online

Gonzalez Pisfil M., (2024, July). *Lecture: STED microscopy with a single depletion laser using five fluorochromes and fluorescence lifetime phasor separation*, EMBL Course: Time-resolved STED nanoscopy in life sciences, Heidelberg, Germany

Gonzalez Pisfil M., (2024, February). *Lecture: Separation of fluorochrome in the same spectral channel with FLIM in confocal and STED microscopy*, GerBI FLIM Workshop 2024 – Biomedical Center, Ludwig-Maximilians-Universität München, Munich, Germany

Gonzalez Pisfil M., (2023, July). *Lecture: STED microscopy with a single depletion laser using five fluorochromes and fluorescence lifetime phasor separation*, EMBL Course: Fluorescence Beyond Intensity, Heidelberg, Germany

Gonzalez Pisfil M., Zimmermann T. (2023, March). *Workshop: The opportunity of a lifetime: Fluorescence Lifetime Imaging Microscopy in Research, a guide from F to M*, Trends in Microscopy 2023, Münsingen, Germany

Gonzalez Pisfil M., (2023, March). *Lecture: Five Color Nanoscopy by τSTED and Phasor Lifetime Unmixing*, Advanced Fluorescence Microscopy Symposium – FLIM, FCS & *τSTED Applications - SciLifeLab*, Stockholm, Sweden

Gonzalez Pisfil M., (2022, October). *Lecture: Five Color STED with a single depletion laser and fluorescence lifetime phasor separation*, Leica Webinar, Online

Gonzalez Pisfil M., Loidolt-Krüger M. (2018, March) *Practical Session: Introduction to Micro-Time 200 - STED*, 10th Time-resolved Microscopy and Correlation Spectroscopy Course (TRMic), Berlin, Germany

Gonzalez Pisfil M., König M. (2017, March) *Practical Session: Introduction to Micro-Time 200 - STED*, *9th Time-resolved Microscopy and Correlation Spectroscopy Course (TRMic)*, Berlin, Germany

Gonzalez Pisfil M., Le Nézet C. (2016, October) *Workshop: Analyse spatio-temporelle en cellule vivante par corrélation d'image de temps de vie*, Microscopie Fonctionnelle en Biologie (MiFoBio), Seignosse, France

Gonzalez Pisfil M., Le Nézet C., (2014, October) *Workshop: FCS et FRET - FLIM : approche combinée en cellules vivantes, acquisition et analyse*, Microscopie Fonctionnelle en Biologie (MiFoBio), Seignosse, France

Gonzalez Pisfil M., Le Nézet C., (2013, December) *Workshop: Introduction to FCS measurements in live cells,* Bioimaging Advance Training (BIAT), Gif-sur-Yvette, France

9 Acknowledgment

“A journey of a thousand kilometers starts with a single step”. This quote describes the best my PhD experience. It has been a long journey of many years, with ups and downs, that finally comes to an end. Even though a doctoral thesis is considered a personal work, I did not arrive here only by myself. I would like to express my sincere gratitude to Prof. Dr. Martin Biel and Prof. Dr. Christian Wahl-Schott for providing me with the opportunity to complete my degree under their supervision, and their time, guidance, and support. I would not be here without you. I would also like to thank Dr. Steffen Dietzel whose constant encouragement and dedication over many years, played a significant role in the completion of my thesis. I would like to thank you my colleagues at the Core Facility whose nice company, knowledge, and unvaluable support has helped during all these years at the BMC. Of course, I would like to thank you all my coworkers, and collaborators who have made my daily life in the lab more enjoyable and always scientifically stimulating.

I would also like to thank my friends for providing the much-needed relaxation and enjoyable moments outside the lab. It has been an invaluable contribution to my personal life, which has also positively influenced my scientific work. ¡Gracias mi gente de Múnich, Berlín, Göttingen, Copenhague, Viena, Ámsterdam, y de otros lugares, por toda la diversión, la locura y las buenas vibras en fiestas, festivales y demás!

Desearía también agradecer a toda mi familia en el Perú, a mi hermano Sebas en Paris y sobre todo a mis padres, Nancy y Antonio por haberme criado y dado la oportunidad de llegar a donde estoy actualmente. ¡Gracias, papás! Les agradezco de todo corazón todo lo que me han dado. Siempre los tengo en mente, y nunca me olvidare de dónde vengo.

Dernièrement, je souhaiterais également remercier ma famille en France. En particulier Lisandro mon cher fils. Merci de faire partie de ma vie, et d’avoir été présent dans cette aventure en me demandant souvent « Papa, alors t’as fini ta thèse ? T’es enfin docteur ? ». Merci mon cœur, je peux enfin te dire que c’est bon, c’est fait.

To all others I could not mention individually, to friends I don’t see often, as well as to those with whom I may be distant, thank you. To everyone, you are in my thoughts, and you have undoubtedly contributed to who I am and to where I stand today.

« *Gratitude is the memory of the heart / La gratitud es la memoria del corazón / La gratitude est la mémoire du cœur* » – Jean Baptiste Massieu.

10 Appendix: Published articles

In the following, manuscripts I to VI are reprinted:

I. **Gonzalez Pisfil, et al.**, (2021). "*Triple-Color STED Nanoscopy: Sampling Absorption Spectra Differences for Efficient Linear Species Unmixing*." J Phys Chem B 125(22): 5694-5705

II. **Gonzalez Pisfil, et al.**, (2022). "*Stimulated emission depletion microscopy with a single depletion laser using five fluorochromes and fluorescence lifetime phasor separation*." Sci Rep 12(1): 14027.

III. **Gonzalez Pisfil** and Dietzel, (2025) "*Fluorochrome Separation by Fluorescence Lifetime Phasor Analysis in Confocal and STED Microscopy"*, Methods in Microscopy 2(1): 45-60

IV. **Forero et al.**, (2024). "*Extracellular vesicle-mediated trafficking of molecular cues during human brain development*." Cell Rep 43(10): 114755.

V. **Behrens et al.**, (2021). "*Disrupting Roquin-1 interaction with Regnase-1 induces autoimmunity and enhances antitumor responses*." Nat Immunol 22(12): 1563-1576.

VI. **Vizjak et al.**, (2024). "*ISWI catalyzes nucleosome sliding in condensed nucleosome arrays*." Nat Struct Mol Biol 31(9): 1331-1340.

THE JOURNAL OF PHYSICAL CHEMISTRY B
A JOURNAL OF THE AMERICAN CHEMICAL SOCIETY

pubs.acs.org/JPCB

Article

Triple-Color STED Nanoscopy: Sampling Absorption Spectra Differences for Efficient Linear Species Unmixing

Published as part of The Journal of Physical Chemistry virtual special issue "W. E. Moerner Festschrift".

Mariano Gonzalez Pisfil, Sumeet Rohilla, Marcelle König,* Benedikt Krämer, Matthias Patting, Felix Koberling, and Rainer Erdmann

Cite This: *J. Phys. Chem. B* 2021, 125, 5694–5705

Read Online

ACCESS | Metrics & More | Article Recommendations | Supporting Information

ABSTRACT: Stimulated emission depletion (STED) in confocal fluorescence microscopy enables a visualization of biological structures within cells far below the optical diffraction limit. To meet the demand in the field for simultaneous investigations of multiple species within a cell, a couple of different STED techniques have been proposed, each with their own challenges. By systemically exploiting spectral differences in the absorption of fluorescent labels, we present a novel, beneficial approach to multispecies STED nanoscopy. By using three excitation wavelengths in nanosecond pulsed interleaved excitation (PIE) mode, we probe quasi simultaneously multiple species with fluorescent labels having absorption maxima as close as 13 nm. The acquired image is decomposed into its single species contributions by application of a linear unmixing algorithm based on present reference patterns. For multispecies images containing single species regions, we introduce the image correlation map (ICM). Here, the single species regions easily can be identified in order to generate the necessary single species reference patterns. This avoids the otherwise cumbersome and artifact prone preparation and recording of additional reference samples. The power of the proposed imaging scheme persists in species separation quality at high speed shown for up to three species with established reference samples and dyes commonly used for cellular STED imaging.

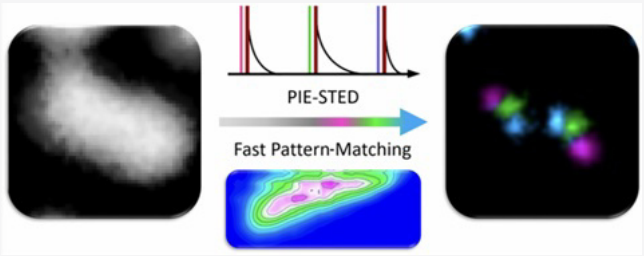

INTRODUCTION

Fluorescence super-resolution microscopy techniques have shown to be of ground-breaking impact within the life sciences since their experimental inception more than a decade ago.[1−6] Being able to visualize biological molecules and their higher-order assemblies in fixed and live cells below the diffraction limit facilitated new insights in fields such as cell biology and neurosciences.[7,8] Furthermore, with the possibility of multicolor super-resolution imaging, various biological questions could be addressed based on the discrimination of various individual components and their interactions in cells.[9−14] Nowadays, thanks to the appearance of commercial turn-key systems, super-resolving microscopes are present in many laboratories around the world easing data acquisition and analysis. Multiple super-resolving techniques are becoming standardized tools, and the demand for super-resolved images of multistained samples is constantly growing.

Among the super-resolution techniques, stimulated emission depletion (STED) microscopy has proven to be popular due to its straightforward experimental approach of tuning the observation size itself far below the diffraction limit. The acquired raw image already is super-resolved, and there is no necessity for image postprocessing. In the classical implementation of STED, a super-resolved image is obtained from a single fluorescent label with the requirements of two laser lines that are temporally and spatially overlaid and focused inside the sample: one laser line for the diffraction-limited excitation of the fluorophores and one laser line for the doughnut-shaped depletion allowing fluorescence to arise only from a sub-diffraction-limited spot. Other geometries of STED include multiple scanning beams or different illumination patterns.[15−23]

A discrimination of different fluorescent labels can be done based on differing spectral properties. The first attempts for two-species STED images used two pairs of excitation and depletion lasers.[24] Although effective, the resulting system was complex as it required an alignment of two pairs of laser lines in order to avoid a color mismatch during acquisition.[25] A further and so far simple solution is to use fluorophores having different excitation spectra but similar emission spectra, such as dyes with a long

Received: December 22, 2020
Revised: May 12, 2021
Published: May 28, 2021

https://doi.org/10.1021/acs.jpcb.0c11390
J. Phys. Chem. B 2021, 125, 5694−5705

Stokes shift.[26] The fluorophores are excited sequentially with multiple excitation lasers (line- or frame-wise) whereas a single depletion laser is used. But this approach is limited to a small number of available and STED compatible labels. In addition, color misalignments due to drifts of the setup, especially during frame alternating acquisition, have to be taken into account. A different approach for the discrimination of species is based on the utilization of another photophysical property of the fluorophores: fluorescence lifetime. Lifetime-based multicolor STED microscopy has been proven effective to help unmixing up to three dyes,[25,27] but the need of high photon numbers and prerecorded references hinders this technique's effectiveness. The latest advancements relying just on a single depletion laser for two- and even multicolor STED systems are based on linear spectral unmixing in the detection.[28,29]

Within multispecies confocal microscopy linear spectral unmixing is already widely popular. Fluorophores with similar spectral characteristics are distinguished by using their spectral fluorescence signatures which are previously recorded separately under the same experimental conditions. Based on these reference spectra, the contribution of each label in each pixel in the multicolor image can be determined. In principle, a number of detectors that equals the number of fluorophores to be unmixed is needed.[30] Still, even higher numbers of detectors are preferred, especially in multitarget biological studies.[31] For instance, in commercial confocal microscopes, spectral detectors with up to 32 channels are used.

Our presented approach is able to systematically sample, in addition to the fluorescence spectrum and the fluorescence lifetime, a third optical property, the absorption spectrum. This is advantageous if the used labels show only minor differences in their fluorescence decay characteristics or do not have acceptably separated emission spectra. Our setup, being equipped with three different excitation sources (Figure 1a), allows for quasi simultaneous absorption spectra probing via multicolor pulsed interleaved excitation (PIE, Figure 1b). The excitation toggles on a nanosecond time scale between different colored picosecond laser pulses each being accompanied by a STED laser pulse. The delayed fluorescence response, due to the fluorophores excited state lifetime, can be easily extracted by a time-gated single photon arrival time analysis. In our study, the fluorescence lifetime itself was neglected throughout the analysis.

Here, we focus on the linear unmixing procedure itself and the easy identification of suitable reference patterns. If the imaged regions contain pixels which are highly dominated by a single label species, we can straightforwardly identify these pixels in an image correlation map (ICM) representation and extract the necessary optical properties for a single species pattern without the need for the preparation and the recording of a separate single species reference sample. The used pattern-matching-based linear unmixing algorithm (fast pattern-matching: FPM) is fast, stable, and largely unsupervised. Only in the case of very similar photophysical properties of the utilized fluorophores, the identification in the ICM might need a manual optimization. As presented in the following, our method achieves successful unmixing of up to three fluorophores with reasonable residual cross-talk values.

EXPERIMENTAL SECTION

Imaging Setup. All measurements were carried out using a MicroTime 200 STED system (PicoQuant GmbH, Berlin, Germany), a time-resolved confocal microscope featuring STED super-resolution, equipped with a FLIMbee galvanometer scanner (PicoQuant GmbH, Berlin, Germany). Three

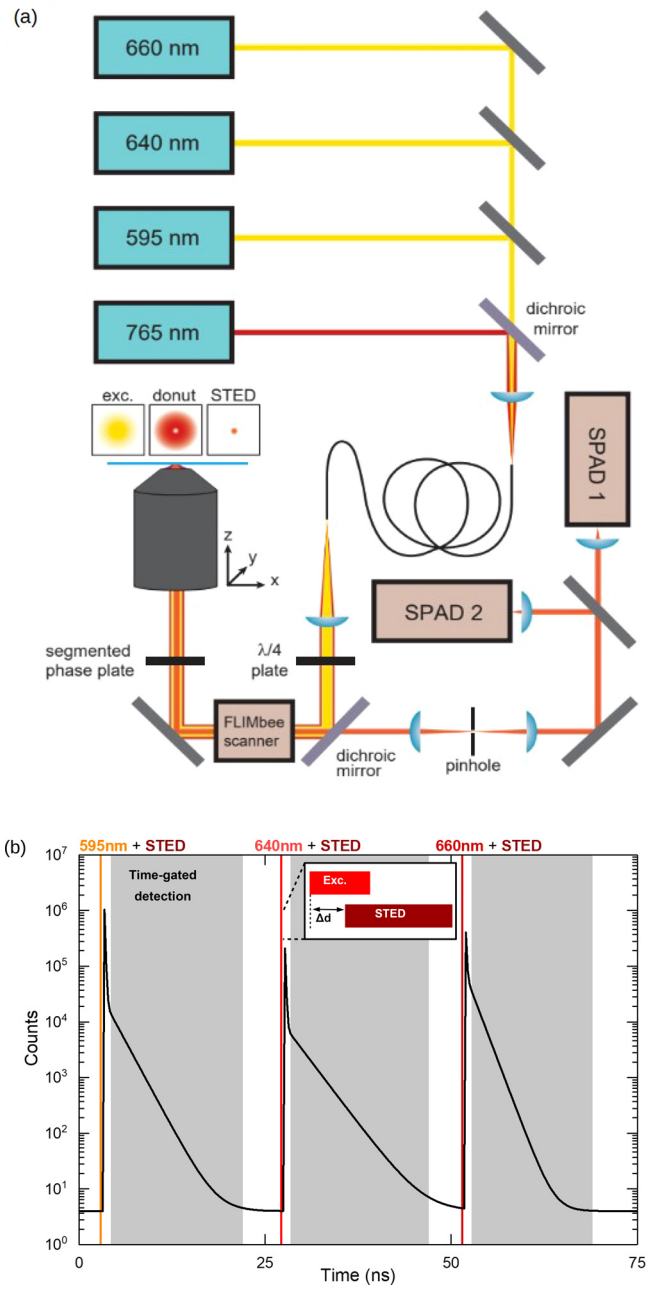

Figure 1. Experimental setup and pulsed interleaved excitation for three color STED imaging. (a) Schematics of the STED setup used: Three excitation lasers are coupled together with the STED laser into a single-mode fiber, facilitating the laser beam overlay. The excitation light was circularly polarized with a $\lambda/4$ plate before entering the FLIMbee galvanometer scanner. The STED doughnut is generated with a segmented phase-plate located below the objective. Emitted fluorescence is isolated by a dichroic mirror and then guided through a 100 μm pinhole before reaching the SPAD detectors. (b) Excitation lasers were operated in pulsed interleaved excitation (PIE) mode using electronically controlled delays between different pulsed lasers to create a specific pulse sequence. In this case, it is used to create a three color pulse cycle starting with the 595 nm laser, followed by the 640 nm laser and the 660 nm laser. Each excitation laser was set at a repetition rate of 13.3 MHz so that the time between each subset of pulses was 25 ns. A STED pulse followed each excitation pulse with a ~100 ps delay (Δ) for optimal depletion (inset).

https://doi.org/10.1021/acs.jpcb.0c11390
J. Phys. Chem. B 2021, 125, 5694−5705

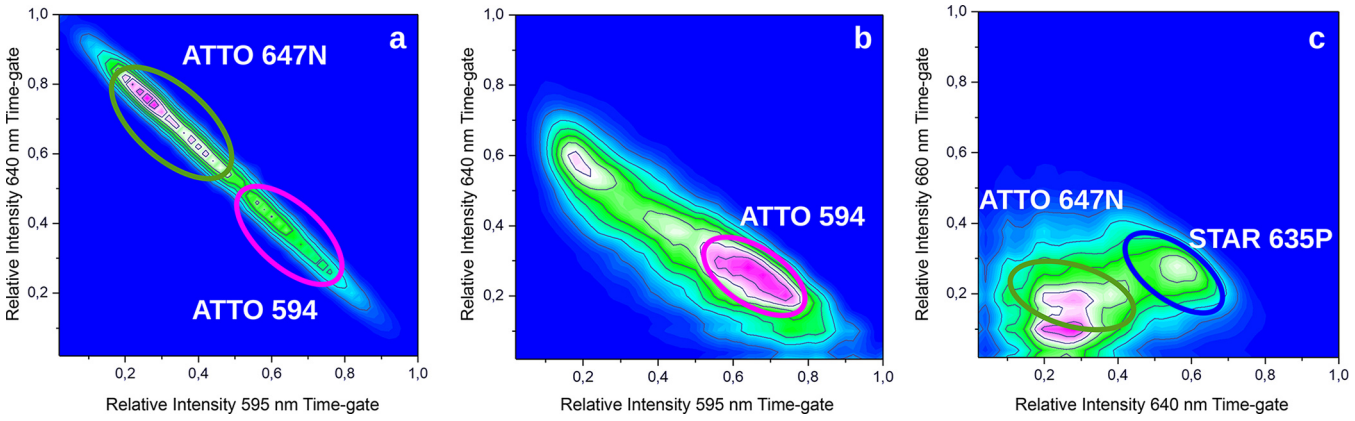

Figure 2. Intensity correlation maps (ICMs) for two and three color STED Imaging. The ICM is a 2D histogram in which two image pixel intensities are shown depending on how strong the optical response of the species was in an image pixel for two different excitation wavelengths, in our case selected via time-gates after pulsed interleaved laser (PIE) excitation. (a) ICM for the two color STED data set shown in Figure 4b with 595 and 640 nm pulsed excitation. The region of interest "ATTO 647N" encompasses pixels which contain only fluorescence from the fluorophore ATTO 647N. The photons from these pixels are used to build up the pattern to select ATTO 647N. The region of interest "ATTO 594" is used to build up the pattern for the fluorophore ATTO 594. (b and c) ICMs for the three color STED data set in Figure 5b with 595, 640, and 660 nm pulsed excitation. The ICM in part b is grouping the pixels of the recorded image based on the intensities in the time-gate after 595 nm excitation versus 640 nm excitation, and in part c, respectively, after 640 nm excitation versus 660 nm excitation. Three specific regions of interest have been selected in the ICMs (b and c) to define pixels whose photon information is used to create the patterns for the three fluorophores ATTO 594, Abberior STAR 635P, and ATTO 647N.

picosecond pulsed lasers at 595, 640, and 660 nm (LDH series, PicoQuant GmbH, Berlin, Germany) were used for the excitation. Stimulated depletion was performed with a pulsed STED laser at 765 nm (VISIR-STED,[32] PicoQuant GmbH, Berlin, Germany).[33] System layout can be seen in Figure 1a. All lasers were operated in a pulsed interleaved excitation (PIE) pattern using a PDL 828 "Sepia II" laser driver equipped with a SOM-D oscillator module (PicoQuant GmbH, Berlin, Germany). The PIE pattern consisted of either a two or a three color excitation cycle, starting with a pulse from the 595 nm laser followed by a 640 and a 660 nm pulse (the latter only in the three color imaging approach). Each excitation pulse was followed by a STED pulse with a rising edge delay of around 100 ps for optimal depletion (cf. Figure 1b). This delay was optimized electronically by temporally adjusting the pulse position for each single excitation wavelength with respect to the STED laser using the SOM-D oscillator module. The excitation lasers were operated at a repetition rate of 20 MHz for two color PIE and 13.3 MHz for three color PIE. This corresponds to a 25 ns time spacing between successive pulses in each of the presented scenarios. The repetition rate for the STED laser was set to 40 MHz, such that a STED laser pulse was generated for each excitation pulse. A whole PIE cycle lasted either 50 or 75 ns (cf. Figure 1b).

The STED and excitation lasers were coupled into the same single-mode fiber to facilitate beam overlay. The combined beams were guided to the FLIMbee scanner, which includes three galvanometer driven mirrors. The third galvanometer mirror ensures that the laser beams do not move at the microscope objective's back focal aperture. This is important when using a chromatic segmented phase-plate for generating the STED doughnut, also known as the easySTED approach.[19] Located at the back focal aperture, the phase-plate requires evenly distributed illumination powers on the four segments throughout the image scan. An EASYDOnut phase plate, 640/765 nm, (Abberior, Göttingen, Germany) was used to shape the STED laser while leaving the 640 and 660 nm excitation beams unaffected. The beam profile of the 595 nm excitation laser was slightly affected by the phase plate resulting in an asymmetrical shape of the point spread function (PSF) for the excitation wavelength 595 nm (Figure S1). Still, the quality of the point spread function (PSF) was high enough for confocal imaging. The STED performance is unaffected since the outer regions of the confocal PSF are fully removed in the STED image by fluorescence depletion initiated by the STED laser.[34] For confocal data acquisition only, the phase plate can be easily removed.

Samples were imaged through a 100× oil immersion objective (NA1.40, UPlanSApo, Olympus, Tokyo, Japan). The fluorescence was separated from backscattered illumination light by a dichroic mirror (zt595/752rpc, Chroma, Bellows Falls, VT), then passed through a 100 μm pinhole. The fluorescence beam was then spectrally split onto two Single Photon Avalanche Diodes (SPAD) (SPCM AQRH-14 TR, Excelitas Technologies, Waltham, MA) using a dichroic mirror (zt640rdc, Chroma, Bellows Falls, VT). Different emission band-pass filters were placed in front of the SPADs: a 697/58 BrightLine HC and a 664 RazorEdge long-pass for SPAD 1 (Semrock, Rochester, NY), and a 615/20 BrightLine HC (Semrock, Rochester, NY) for SPAD 2. In principle, the two SPADs could be replaced by a single SPAD with a suitable emission filter and two notch filters for the 640 and 660 nm excitation lasers, without affecting the presented results. Data acquisition was based on time-correlated single photon counting using a TimeHarp 260P[35] (PicoQuant GmbH, Berlin, Germany). Both image acquisition and data analysis were carried out with the software package SymPhoTime 64 (PicoQuant GmbH, Berlin, Germany).

The STED images were raster-scanned with a pixel dwell time of 1 ms and an image size of 4.5 μm × 4,5 μm (300 pixels × 300 pixels). Pixel size was 15 nm × 15 nm. Imaging was performed with excitation laser powers of 2−6 μW and a STED laser power of 120 mW (powers measured at the objective back focal plane). The total image acquisition times were 3 min for both confocal and STED images. No noticeable sample drift was detected during the acquisition.

https://doi.org/10.1021/acs.jpcb.0c11390
J. Phys. Chem. B 2021, 125, 5694−5705

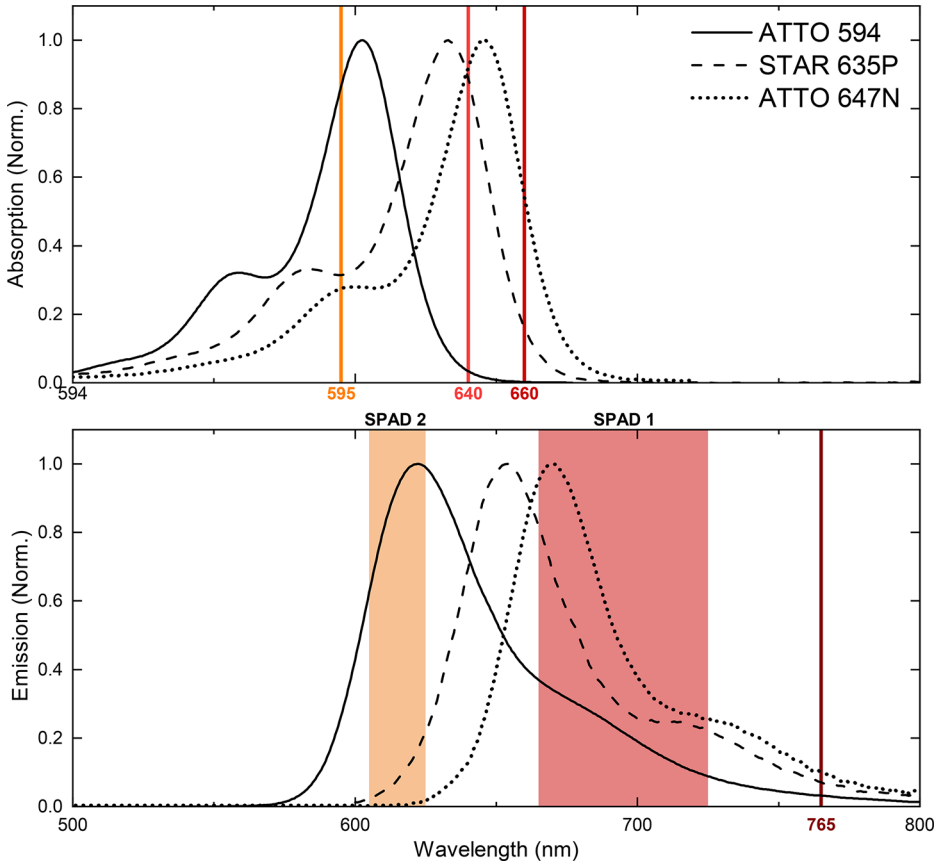

Figure 3. Excitation and emission spectra of the three fluorophores used for STED imaging. Normalized absorption (upper part) and emission (lower part) spectra. Indicated are also the spectral positions of the three laser excitation lines (595, 640, 660 nm) and the STED laser line (765 nm) as well as the spectral detection windows for the detectors SPAD 1 and SPAD 2.

Data Analysis: Image Correlation Maps for Pattern Definition and Pattern-Matching Based Linear Unmixing. Pattern-matching based unmixing allows fluorophores with different optical properties to be separated. Thus, spatial distributions of the respective fluorophores in an image can be reconstructed pixel-wise. The separation of fluorophores can be based on general differences in absorption (probed via multicolor excitation, together with the dyes' different extinction coefficients at different wavelengths: 1.2×10^{-5} M^{-1} cm^{-1} at 603 nm for ATTO 594, 1.2×10^{-5} M^{-1} cm^{-1} at 638 nm for Abberior Star 635P, and 1.5×10^{-5} M^{-1} cm^{-1} at 646 nm for ATTO 647N according to the manufacturers' documentation), in emission (probed via spectrally separated detection channels) or in variations of their fluorescence decays (via time-correlated single photon counting). In our studies, we sample the absorption spectrum with up to three different excitation wavelengths (tracked in the analysis via three time-gates, shown in Figure 1b) and the fluorescence spectrum with two detection channels. In principle, also differences in fluorescence lifetimes could be directly taken into account by splitting each current time-gate into further sections along the course of the decay. Within this study, the fluorescence decay information is neglected. Only gated STED (gSTED) is applied such that early non-super-resolving photons leading to a decreased spatial resolution are removed.[36,37]

The pattern-based species linear unmixing presented here is based on a covariant vector projection. The analysis yields, based on a linear combination of known reference patterns, the number of photons per pixel associated with the chosen patterns.[38] The patterns consist of the intensity contributions from several time-gates and/or detection channels. Any combination of time-gates can be used for the pattern differentiation. Before unmixing, the patterns are normalized. In our case, the actual time-resolved single photon information is condensed in up to six photon numbers per pixel given by the cumulated photons per time-gate (defined for each excitation pulse) and per detection channel. So one pattern of one fluorophore consists of up to six photon numbers and can be characterized by the specific ratios between the photon numbers. Alternatively, the reference patterns could be calculated from previous measurements of the single species. For the samples utilized in this publication, it is possible to derive the patterns directly from the multistained STED image data set itself. The single species patterns are generated from specific regions within the multistained images which contain only a single species. To identify and select these single species regions in a multispecies image so-called intensity correlation maps (ICMs) are used (see Figure 2). An ICM corresponds to a 2D histogram of relative pixel intensities for a chosen pair of time-gate and detector.

For the presented analysis, we used an even simpler approach pooling together the photon counts from both detection channels. This results in a reduced number of selectable ICMs and still yielded a good separation of the fluorophores investigated. The ICMs shown in Figure 2 are calculated from acquired images of a dual-stained and a triple-stained DNA origami sample. The dual-stained sample was excited with 595 and 640 nm, and Figure 2a shows the ICM for the two

https://doi.org/10.1021/acs.jpcb.0c11390
J. Phys. Chem. B 2021, 125, 5694−5705

corresponding time-gates. The triple-stained sample was excited with 595, 640, and 660 nm, and parts b and c of Figure 2 show the ICM for the time-gates applied for 595 and 640 nm excitation and the ICM for the time-gates applied for 640 and 660 nm excitation, respectively. The ICM with time-gates applied for 595 and 660 nm excitation did not supply additional information for the selection of species. The relative intensities on both axes of the ICMs are normalized to the intensity of the brightest pixel in the original gSTED image without any of the excitation time-gates applied (only the gate for gSTED is applied). So each image pixel contributes to the ICM with its sum intensity within the two considered time-gates. A gliding mean of three bins is applied in Figure 2 in order to increase histogram visibility only, and the data remain unsmoothed with a binning of 50 for each axis. The frequency of the occurrences is displayed in colors from blue (zero occurrence) via green to red (maximum occurrences). The ICM visualizes pixels with similar relative intensities in a cluster. Thus, fluorophores with different optical properties (in our case mainly in the absorption) appear in different clusters. Pixels containing a mixture of fluorophores will be mapped in the ICM in-between the clusters of the single fluorophores. The reference patterns used for the unmixing can be defined by choosing appropriate regions of interest (ROIs) encompassing characteristic clusters in the ICM. All photons contained in the pixels of one ROI are added up to obtain the reference pattern which represents the average properties of all pixels within the ROI. During the selection, in real time, the positions of the pixels chosen in the ICM are visualized in the raster-scanned image, which is a convenient way to confirm that a reasonable ROI was defined in the ICM. The unmixed photon numbers per pattern per image pixel are finally displayed as separate 2D images, showing the spatial distribution of the individual species as characterized by the chosen reference patterns. A Gaussian filter of 3×3 with $\sigma = 0.7$ was applied to all images to increase contrast and visibility.

The presented method is based on a hardware and software combination which has, to our knowledge, not previously been applied. A direct comparison with previous unmixing methods is therefore not possible. The pattern-based species linear unmixing presented here was performed using the fast pattern-matching (FPM) analysis method provided by the SymPhoTime64 software package (PicoQuant GmbH, Berlin, Germany).

Isolated Excitation Color Analysis. To assess the efficiency of the FPM analysis, a basic spectral separation approach was performed and results from both approaches were compared to each other. The basic spectral separation approach assumes that different fluorescent species can be addressed separately by exciting each with a different wavelength. This type of excitation is analog to a multiband fluorescence detection, with each detection channel being directly assigned to a different fluorescent species. To separate the fluorescence responses to the different excitation wavelengths in pulsed interleaved excitation, time-gates were applied after each excitation pulse (cf. Figure 1b). These time-gates were selected to again exclude early non-super-resolving photons in the STED images. The photons within each time-gate were summed up per image pixel and displayed as single species images for each time-gate. If each excitation laser excites just one of the fluorophores to be separated, then the time-gated images reflect the spatial distributions of these fluorophores in the images well. But if one excitation laser can excite more than one fluorophore (cf. Figure 3), then strong cross-talk between the time-gated images occurs (cf. Table 1a and 2a).

Table 1. Two Color STED Cross-Talk[a]

(a) cross-talk with isolated excitation color analysis			
		channel	
		ATTO 594	ATTO 647N
dye	ATTO 594	100	46
	ATTO 647N	26	100
(b) cross-talk with fast pattern-matching analysis			
		channel	
		ATTO 594	ATTO 647N
dye	ATTO 594	100	18
	ATTO 647N	22	100

[a]The resulting intensity of a specific fluorophore in its dedicated analysis channel is defined as 100%. The resulting intensity of a specific fluorophore in the wrong analysis channel (bleed-through) is given as percentage relative to the intensity in the dedicated analysis channel. The isolated excitation color analysis is based on the assumption of an exclusive 1:1 dedication between excitation wavelengths and species to be separated (see details in the Experimental Section).

Table 2. Three Color STED Cross-Talk[a]

(a) cross-talk with isolated excitation color analysis				
		channel		
		ATTO 594	STAR 635P	ATTO 647N
dye	ATTO 594	100	26	22
	STAR 635P	33	100	83
	ATTO 647N	38	92	100
(b) cross-talk with fast pattern-matching analysis				
		channel		
		ATTO 594	STAR 635P	ATTO 647N
dye	ATTO 594	100	11	1
	STAR 635P	17	100	9
	ATTO 647N	4	19	100

[a]The resulting intensity of a specific fluorophore in its dedicated analysis channel is defined as 100%. The resulting intensity of a specific fluorophore in the wrong analysis channel (bleed-through) is given as percentage relative to the intensity in the dedicated analysis channel.

Cross-Talk Analysis. Cross-talk calculations were performed with the isolated excitation images as well as with the images unmixed via FPM. The analysis was performed in MatLab (The Mathworks Inc., Natick, MA) using a self-written code. The tables given in Table 1 and Table 2 show in each row the fluorophore contributions to the respective analysis channel. Note that the main diagonal elements have per definition a value of 100% as it is the fluorophore contribution in the target analysis channel. Off diagonal elements depict the contribution of a given fluorophore to an "unintended" analysis channel which corresponds to cross-talk. After unmixing, in a first step, a threshold was applied to each analysis channel to eliminate background artifacts. The threshold value for all channels was set to 12.5% of the maximum pixel intensity in this individual channel. Applying this threshold, a spatial pixel mask was obtained for each channel containing all pixels with intensities above the threshold value. To calculate the amount of cross-talk, the mask from one channel was applied to an image in another

https://doi.org/10.1021/acs.jpcb.0c11390
J. Phys. Chem. B 2021, 125, 5694−5705

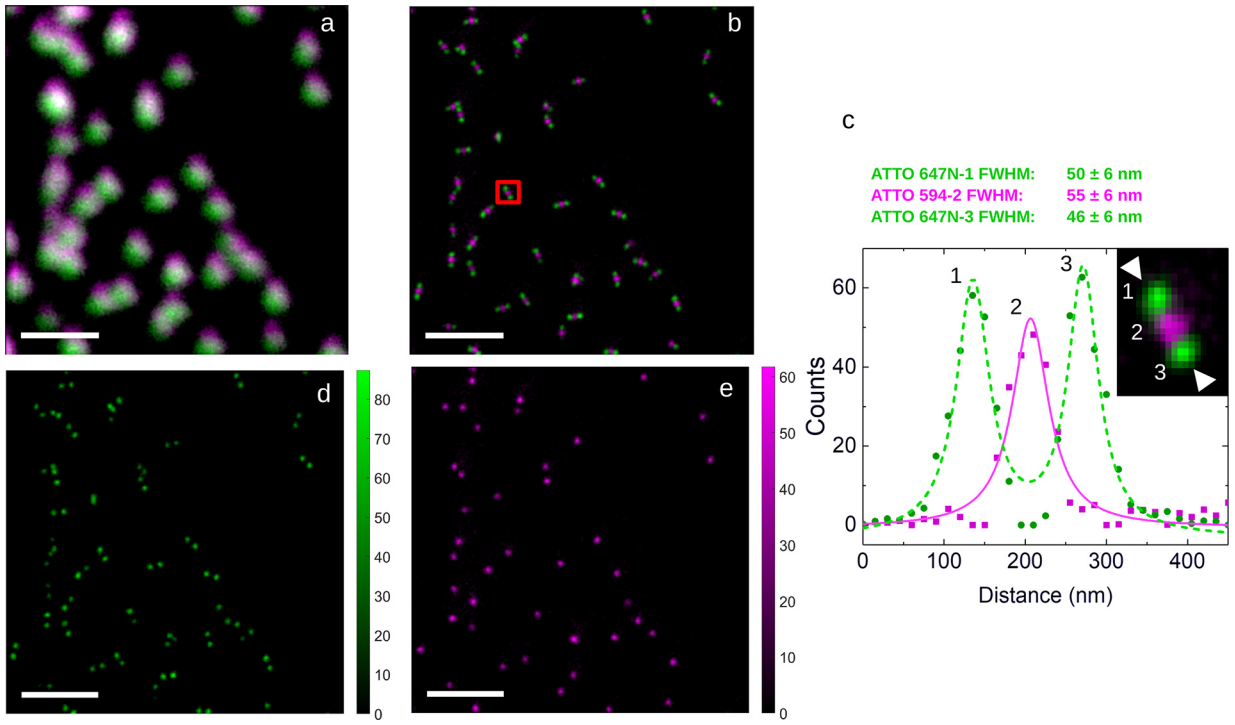

Figure 4. Two color STED imaging. Confocal (a) and corresponding STED (b) images of DNA origami labeled with two different fluorophores: ATTO 594 (magenta), and ATTO 647N (green). (c) Line profile of a DNA origami structure (red square in part b). Using a Lorentzian fit a FWHM of about 50 nm is obtained for each spot. Peak distances in part c are for ATTO 647N-1 to ATTO 594-2 70 nm, ATTO 647N-1 to ATTO 647N-3 135 nm, ATTO 594-2 to ATTO 647N-3 65 nm. Unmixed STED images of the DNA origami, showing ATTO 647N (d) and ATTO 594 (e). Species unmixing for the STED image was performed by a fast pattern-matching data analysis approach. For parts d and e, data correspond to counts after unmixing. Scale bar 1 μm.

analysis channel. Intensities per pixel belonging to the mask were then added up and divided by the total image intensity of the target channel. The result is a percentage value of how much of the total intensity from one channel is leaking into another channel. This approach was considered since high brightness differences between channels can lead to an apparently high cross-talk value even when fluorophores are properly unmixed. Since the cross-talk values represent how much of the total fluorescence of each dye is leaking into the other channels, it is a valid method to evaluate the unmixing quality. However, the limits of this approach are apparent when dealing with spatially overlapping structures.

DNA Origami. All DNA origami utilized in this study were obtained from GATTAquant (Gräfelfing, Germany). The multicolor nanorulers contain three emitting point structures each. The two color DNA origami consisted of one ATTO 594 domain sandwiched between two domains of ATTO 647N. The three color DNA origami sample featured three successive domains, each containing a single, specific dye (ATTO 594, ATTO 647N, and Abberior STAR 635P). In both samples, domain sizes were 8 × 20 nm, with the 20 nm side lying along the long axis of the ruler. The distance between adjacent domains was 70 nm, and each domain contained between 15 and 20 individual dye molecules. Individual DNA origami were immobilized on a glass coverslip by a BSA-Biotin-NeutrAvidin binding. ProLong Gold Antifade (ThermoFisher, Waltham, MA) was used as mounting medium.

RESULTS

DNA origami labeled with two and three different fluorophores were used to demonstrate the potential of the presented multicolor excitation pattern-matching based linear unmixing approach. This sample type is ideally suited as a reference material for multicolor STED imaging as it offers a wide range of customization possibilities, such as shape, fluorophore type, or numbers of emitters per domain. The three fluorophores chosen for this study (ATTO 594, ATTO 647N, and Abberior STAR 635P) can be efficiently excited at one of the three laser excitation wavelengths used (Figure 3) and have excellent characteristics for STED microscopy.[10,29,38] Since the measured fluorescence lifetimes of the labels were quite similar (between 3.3 and 3.9 ns), the lifetime information itself was neglected in our study.

In a first set of experiments, the sample consisted of individual dual-color DNA origami rods immobilized on the surface of a glass coverslip. Each rod-like origami featured one ATTO 594 domain between two ATTO 647N domains. The distance between two adjacent domains was 70 nm. The fluorophores were excited in PIE mode with two lasers (595 and 640 nm) and fluorescence was collected via two spectrally slightly differing detection channels (for the excitation with 595 nm collection of fluorescence between 605 and 625 nm, for the excitation with 640 nm collection of fluorescence between 668 and 726 nm). The time window between two subsequent excitation pulses was set to 25 ns (20 MHz repetition rate for each laser) in order to record the full fluorescence decays. Excitation powers of 2 μW per excitation laser and 120 mW for the STED laser were selected as a balanced compromise between increasing the number of detected photons and preventing the photobleaching of the fluorophores at super-resolved imaging conditions. A comprehensive description of the experimental parameters can be found in the Experimental Section.

https://doi.org/10.1021/acs.jpcb.0c11390
J. Phys. Chem. B 2021, 125, 5694−5705

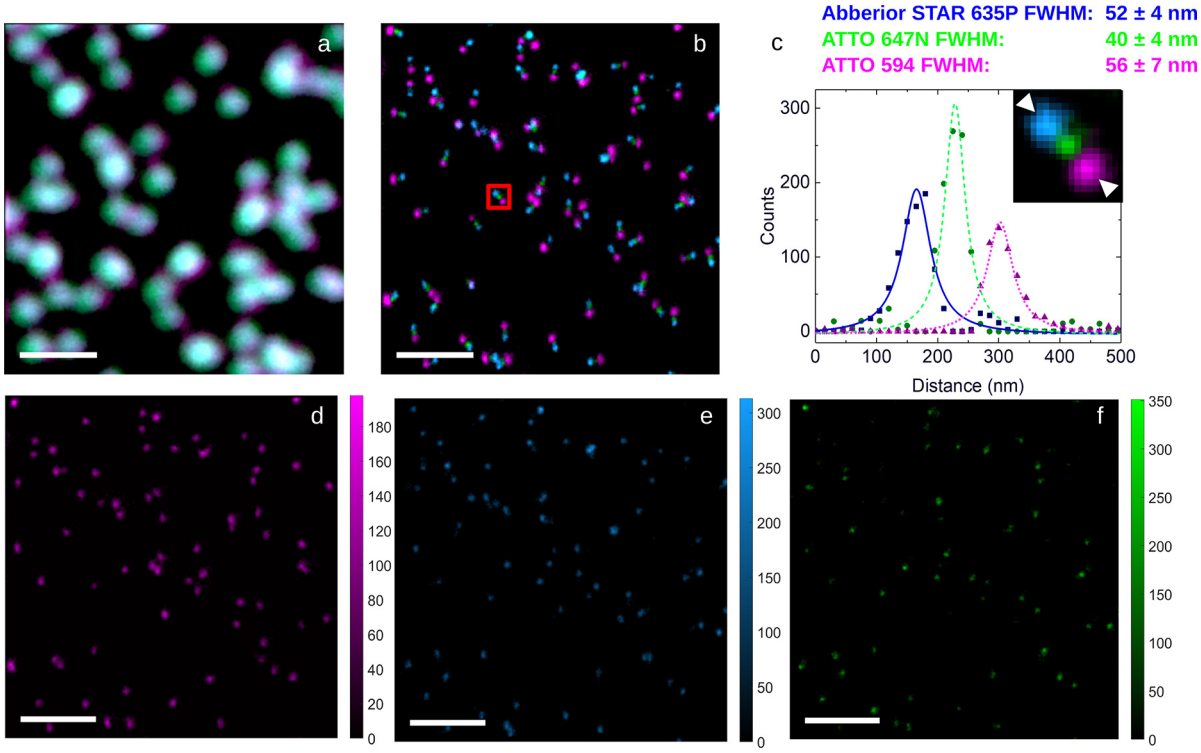

Figure 5. Three color STED imaging. Confocal (a) and STED images (b) of DNA origami labeled with three different fluorophores: ATTO 594 (magenta), ATTO 647N (green), and Abberior STAR 635P (blue). Species unmixing for the STED images was performed via fast pattern-matching. Lorentzian fitting of the peaks in the structure in the red square in part b gives a FWHM of 56 nm or less for individual spots (c). Peak distances in part c are for AbberiorStar 635P to ATTO 647N 68 nm, AbberiorStar 635P to ATTO 594 135 nm, and ATTO 647N to ATTO 594 67 nm. Unmixed STED images of DNA origami, showing ATTO 594 (d), Abberior STAR 635P (e), and ATTO 647N (f). For parts d–f, data correspond to counts after unmixing. Scale bar 1 μm.

Figure 4 shows the separation of the two types of fluorophores (ATTO 594 and ATTO 647N) under confocal and under STED imaging conditions. In the confocal data set, the subdiffraction sized origami structures are not spatially resolved, hindering the access to single species regions for a pattern-matching based extraction within the acquired images. The separation of the two species was performed using simple PIE time-gates based on the two excitation wavelengths. Figure 4a shows the unmixed image. The set PIE time-gate for 595 nm appears magenta in the confocal image, the set PIE time-gate for 640 nm appears green. In spite of the symmetric design of the origami structures, the two patterns do not fully overlap (resulting in white) in the confocal image. This is caused by the slightly asymmetrical shape of the point spread function (PSF) for the excitation wavelength 595 nm that is introduced by the STED phase plate itself (cf. Experimental Section). Without the STED phase plate the two patterns fully overlap as expected.

Under STED conditions, the single species patterns can be directly retrieved from single species regions within the multispecies STED image. The single species regions in the STED image were identified with the help of the corresponding image correlation map (ICM) (Figure 2). In the ICM, image pixels are grouped by looking at the relative intensities in different temporal, spatial and spectral excitation and emission windows. Pixels with similar intensity patterns form a cluster in the ICM. The according photon information of pixels within a cluster from one single species is extracted to define a single species pattern. The generated ICM and the selected pixel clusters used for the dual-color origami STED image are shown in Figure 2a. The cluster in the upper left (indicated by green oval) corresponds to pixels in the recorded image where contributions from ATTO 647N are dominant. Pixels with fluorescence from ATTO 647N exhibit maximum intensity when excited with the 640 nm laser and lowest intensity when excited at 595 nm (compare also absorption spectra in Figure 3). Photons from this cluster are used to create the reference pattern for ATTO 647N.

On the other hand, the pixel cluster in the lower right (magenta oval) in Figure 2a corresponds to pixels in the recorded image where contributions from ATTO 594 are dominant. In this case, higher intensities are observed upon excitation at 595 nm rather than at 640 nm. Photons from this cluster are used to create the reference pattern for ATTO 594. Of course, the generated patterns are only close to the true single species patterns due to noise and remaining cross-talk in some pixels, the latter introducing minor contributions from the undesired species. A benefit of the ICM based pixel classification and pattern generation is that photon events from both spectrally separated detectors can be pooled together to increase the photon statistics, and they still can be appropriately assigned to the respective fluorophore. This was done for ATTO 594 where most of the fluorescence is detected by the single photon avalanche diode (SPAD) 2 (due to the dichroic mirror and detection filters used), but some of its fluorescence also by SPAD 1. Once both patterns are determined, the FPM unmixing analysis is carried out (see the Experimental Section for details). The resulting FPM image with the two species unmixed is shown in Figure 4b. The three different fluorophore domains are clearly distinguishable in the unmixed image. A minor part of the DNA origami structures within the image show only one or two

https://doi.org/10.1021/acs.jpcb.0c11390
J. Phys. Chem. B 2021, 125, 5694–5705

domains which can be explained by either sample artifacts or prior photobleaching. Under STED imaging conditions, a spatial resolution better than 55 nm is achieved as inferred from 2D Lorentzian fits (Figure 4c). The separated images for the single species ATTO 647N (Figure 4d) and ATTO 594 (Figure 4e) show the power of this method. This is confirmed by the calculated channel cross-talk values (cf. Tables 1, parts a and b). Compared to an isolated excitation color approach of the same STED data set (Figure S2), FPM decreases the cross-talk of fluorophore signals by a factor of 2.5 for ATTO 594 bleeding into the ATTO 647N channel (Table 1, 18% vs 46%). This enhancement is achieved despite the rather low photon counts per pixel (approximately 60 photons in the brightest pixel). The resolution itself is mainly unaffected by the unmixing.

The multicolor excitation pattern-matching based linear unmixing approach can be extended to higher numbers of species proven by DNA origami labeled with three different fluorophores. The triple-color DNA origami rods again consist of three domains now featuring ATTO 594, Atto 647N, and Abberior STAR 635P. The single structures are immobilized on the surface of a glass coverslip. The distance between two adjacent domains again was 70 nm. The triple-color DNA origami sample was imaged by operating three excitation lasers with wavelengths at 595, 640, and 660 nm in PIE mode along with a single STED laser at 765 nm (cf. Figure 1b). Each excitation laser can excite at least two of the three fluorophores. Figure 5 shows the separation of the three fluorophores under confocal and under STED imaging conditions. Similar to the above, the separation of the three species in the confocal image was performed using simple PIE time-gates based on the three excitation wavelengths 595 nm, 640 and 660 nm. Figure 5a shows the unmixed image. Again, the asymmetrical shape of the PSF for the excitation wavelength 595 nm introduces a slight shift in the overlay of the three excitation wavelengths' PSFs. Under STED conditions, the patterns for each fluorophore were extracted using the same approach as for the dual-color DNA origami sample. In order to generate the single species patterns for the three species sample, two different ICMs have to be generated: one ICM correlates the 595 nm with the 640 nm time-gate (Figure 2b), and the other ICM used correlates the 640 nm with the 660 nm time-gate (Figure 2c). A third possible ICM, correlating the 595 nm with the 660 nm time-gate, is not used as it is very similar to the 595 nm/640 nm ICM, but with lower photon counts in the 660 nm time-gate. From the three fluorophores, only ATTO 595 is excited efficiently at 595 nm. Therefore, the reference pattern for ATTO 594 is extracted from the 595 nm/640 nm ICM (Figure 2b). Pixels with fluorescence from ATTO 595 exhibit maximum intensity when excited with the 595 nm laser, the fluorophore is not excited efficiently at 640 nm (compare also absorption spectra in Figure 3) showing lower intensity in the 640 nm time-gate (cluster within magenta oval). Extracting the remaining two patterns for ATTO 647N and Abberior STAR 635P is more challenging. As can be seen from the 640 nm/660 nm ICM, the clusters are not well-separated due to the similar spectral properties and resulting cross-talks. The overlap is mainly caused by the efficient excitation of both the fluorophores Abberior STAR 635P and ATTO 647N with the 640 and 660 nm lasers. Since Abberior STAR 635P has a higher quantum yield (90% vs 65%, Atto-Tec GmbH and Abberior GmbH), we can assign the cluster in the upper right corner in Figure 2c to Abberior STAR 635P (blue oval). This assignment is further confirmed by checking the location of pixels associated with Abberior STAR 635P domains in the acquired intensity image. One of the outer two domains already is assigned to ATTO 594, the other outer domain is known to contain Abberior STAR 635P. Selecting a pixel cluster for ATTO 647N is even more challenging, since pixels associated with it lie close to the main diagonal of the ICM plots. The pattern for ATTO 647N was selected in Figure 2c, because excitation at 660 nm is the most efficient for this fluorophore (green oval). The overall higher relative intensities within the 660 nm time-gate for Abberior STAR 635P are due to the higher quantum yield of this fluorophore compared to ATTO 647N. The reference patterns extracted from these three ICM regions allow the three components to be unmixed using FPM in a similar way as described for the two species DNA origami. The resulting three species separation under STED conditions is shown in Figure 5b. The three different fluorophore domains are clearly distinguishable for most of the origami structures in the unmixed image. The investigated triple-color origami were fully customized for these measurements and represented a novel sample class at the time of the measurements. Hence, a part of the DNA origami structures within the image show only one or two domains which can be explained by sample artifacts. Under STED imaging conditions, a resolution of 40 nm for ATTO 647N, 52 nm for Abberior STAR 635P, and 56 nm for ATTO 594 was achieved (all calculated from 2D Lorentzian fits, Figure 5c). This makes it possible to clearly distinguish the three fluorophore domains in the DNA origami. Unmixing by FPM proves to be very good and efficient, as can be seen in the unmixed images for the individual fluorophores: ATTO 594 in Figure 5d, Abberior STAR 635P in Figure 5e, and ATTO 647N in Figure 5f. Compared to an isolated excitation color approach of the same STED data set (Figure S3), FPM decreases the cross-talk of fluorophore signals significantly. With the isolated excitation color approach rather high cross-talk values between fluorophores occur. Values reach up to 92% for ATTO 647N into the Abberior STAR 635P channel (Table 2a) due to the strongly overlapping absorption spectra and close excitation wavelengths. Thanks to FPM, an up to 9-fold decrease in the cross-talk (for Abberior STAR 635P into the ATTO 647N channel) is achieved, thus significantly improving the quality of the multispecies STED images.

DISCUSSION

We present the combination of multicolor PIE in conjunction with a fast pattern-matching (FPM) analysis as a spectrally based image unmixing method. Probing small differences mainly in the fluorophore absorption spectra complements the recently proposed multispecies STED imaging schemes exploiting differences in emission spectra and fluorescence decay characteristics.[26,29] Mostly, multicolor microscopy relies on differences in the fluorophore emission spectra. Primarily, the fluorescent labels are selected such that their spectral overlap is minimized. Furthermore, at least one detector with suitable cutoff or band-pass filter is required per fluorophore. Under confocal conditions, such an approach is suitable for performing imaging with more than three different fluorescent species.[30,31] This is, however, not well suited for STED microscopy since the wavelength of the depletion laser must fit into the emission tail of each fluorophore for the depletion effect to take place, while none of the absorption spectra should even slightly overlap with the STED wavelength in order to avoid re-excitation.[1] As a consequence, with only one STED laser available, the different fluorophores will exhibit overlapping emission spectra. Thus,

https://doi.org/10.1021/acs.jpcb.0c11390
J. Phys. Chem. B 2021, 125, 5694−5705

obtaining images with high resolution and contrast coupled with acceptable low cross-talk values is a rather challenging task.

Different approaches have been developed in the past to overcome this limitation: the implementation of more than one STED laser,[10,25,39] the usage of long Stokes shift fluorophores,[26,40] or spectral unmixing.[29] The implementation of more than one STED laser leads to a complex optical system. System alignment and maintenance become challenging, and additional postprocessing image registration protocols might be necessary.[41] The second spectral STED imaging window is typically opened at shorter wavelengths (such as excitation in-between 450 and 520 nm and STED with 590 nm). But STED dyes in this spectral window are typically less efficient and the shorter STED wavelength can cause significant photodamage in biological specimens (especially in vivo) due to higher absorption coefficients when moving toward blue wavelengths.[42] The usage of long Stokes shift fluorophores is a certain compromise to circumvent a second, blue-shifted STED wavelength and still being able to excite further fluorophores in a different spectral window. But for these dye candidates, the overall photon efficiency is less as compared to the well-established STED fluorophores in the red wavelength range.[43] In addition, appropriate care and effort must be taken again (considering chromatic corrections and individual beam steering and focusing) in order to overlay multiple laser foci which are widely spread over the visible spectrum (e.g., 435, 488, 532, 620 nm).[26] A pure spectral unmixing approach using only spectral emission information was recently shown with up to four fluorophores with their emission maxima being separated by about 25 nm each spanning from 627 to 701 nm.[29] On the one hand, sufficient spectral spacing of the fluorophores is needed to enable reasonable spectral unmixing. On the other hand, a sufficient STED efficiency concerning the emission tail of the most blue-shifted fluorophore as well as a negligible re-excitation by the STED laser concerning the absorption spectrum of the most red-shifted fluorophore have to be ensured. In order to quantify the re-excitation and take it into account in the image analysis, a second image scan with only the STED laser was performed, exposing the sample to twice the STED laser dose.

To avoid the above-mentioned limitations, we concentrate on an approach which utilizes a single STED laser excitation in the red wavelength regime. This restriction allows, in combination with the easySTED method,[19] the laser alignment and system maintenance to be simplified. Our primary focus lies on taking full advantage of combining the easySTED method with a multicolor multiplexing in the excitation properties of the fluorophores. Using this approach, we are able to add valuable information about absorption differences of the fluorophores to the spectral unmixing analysis, which allows us to sacrifice separability in the emission by just using one or two spectrally slightly separated emission detection windows as compared to four channels in other approaches.[29] Following this, the spacing of the fluorophore emission peaks can be decreased (on average 19 nm between 626−664 nm, cf. Figure 3). The closer positions of the fluorophore spectra ensure no visible STED re-excitation of the most red-shifted fluorophore (ATTO 647N) and still a good STED efficiency in the emission tail of the most blue-shifted fluorophore (ATTO 594). For ATTO 647N, we measured a resolution of 40 nm. In the same origami, a resolution of 56 nm was measured for ATTO 594 (Figure 5c). Since in our setup the same depletion power is applied to each fluorophore, the obtained resolution will be different for each type of fluorophore due to their varying depletion efficiencies. In simple terms, the closer the STED laser wavelength is to the emission peak of the STED dye, the more efficient is the depletion process,[1] although other intrinsic properties of each dye may also play a role in their depletion efficiency.

As an alternative to common line sequential imaging for three color excitation multiplexing,[26] we implemented a multicolor pulsed interleaved excitation (PIE). This is the method closest to true simultaneous multicolor excitation, avoiding artifacts caused by moving structures or disappearing (blinking, photobleaching) fluorophores on longer time scales. Of course, concerning STED exposure and the number of total STED pulses being seen by the sample, there is mainly no difference whether one toggles after each single excitation pulse in-between colors (PIE) or whether this takes place per pixel, per line or even per frame.

Image unmixing based on reference patterns in the spectral or lifetime domain has already been used for unmixing purposes in STED microscopy.[26,29,38] The main challenges are (I) to find a suitable set of fluorophores combined with a probing scheme to enable a data collection with sufficient differences between the fluorophore reference patterns, (II) to record these reference patterns unambiguously under relevant conditions, and (III) to conduct the unmixing in a stable and straightforward way.

(I) Since the development of new STED dyes has been focused on the red spectral range in the past[25,42−45] multilabel STED works best at the red edge of the visible spectrum. This leads to spectrally closely overlapping fluorophores. We overcome this situation by using a multicolor excitation scheme to also probe differences in the absorption spectra (Figure 1b and Figure 3).

(II) Due to the achieved STED resolution we are, for the presented origami samples, even in the multicolor image itself able to identify regions that contain only a single fluorophore species. They can be used to define the individual single species reference patterns. The straightforward identification of correct regions is guided by image correlation maps which locate image pixels based on their individual photon information in a 2D map. Clusters of pixels with similar photon properties can be easily identified and selected in order to create a specific reference pattern for a single species. Due to the ICM there is neither a need of detailed prior knowledge of the sample's structural features nor a requirement for a cumbersome procedure to manually select multiple regions of interest in the image itself. Because the ICMs contain photons from all pixels in the whole image, selecting a pattern based on a region of interest in the ICM offers the highest available photon statistics and thereby quality for this reference pattern. Of course, a prior knowledge about the fluorophore properties is helpful to correctly discriminate between the single fluorophore based regions in an ICM and regions in the ICM that contain pixels with contributions from several species in the fluorescence or STED image. Using the ICM helps the user to easily identify the single fluorophore pixels and to select the correct reference patterns even in complex scenarios, such as multispecies images. A multistep multilabeling procedure can specifically modify the labels' fluorescent properties in the final multilabeled sample by changes in the local environment. To re-enact these relevant conditions in a single labeled

https://doi.org/10.1021/acs.jpcb.0c11390
J. Phys. Chem. B 2021, 125, 5694−5705

reference sample is sometimes difficult, sometimes impossible, and can have a major impact on the extracted reference pattern, the unmixing and the final separability achieved. If one has single species domains in the multispecies image, like in our STED case, the ICM allows the user to easily generate the necessary reference patterns for the unmixing without the need of additional single species reference samples.

(III) The defined reference patterns are then used in a linear combination to yield fluorescence contributions of each reference pattern per pixel in the image (cf. Experimental Section). Contrary to the unmixing algorithm proposed by Winter et al.,[29] our decomposition algorithm is mainly unsupervised and needs no manually guided iterative fine-tuning for a new set of fluorophores. With up to three different excitation wavelengths and two spectrally separated detection channels, each pattern consists of up to six parameters to be determined per reference pattern. This limited number of parameters allows for fast data analysis. For the image in Figure 5b, with 300 pixels × 300 pixels containing in total 3.3 million photons, the FPM decomposition with three reference patterns takes 3 seconds.

To quantify the degree of separation achieved we determined the residual cross-talk values for image regions where only a single species is present (see Experimental Section for details). Our approach is compared to an isolated excitation color analysis that mimics the basic multicolor approach assuming well-spaced emission (or in our case absorption spectra) and which can be probed with well-separated spectral windows and be addressed with well-separated excitation wavelengths. However, in the case of strongly overlapping spectra of STED-compatible fluorophores at the red edge of the visible spectrum, this approach leads to unacceptably high spectral cross-talk values. With FPM, as compared to the isolated excitation color analysis, a significant improvement in the amount of cross-talk was achieved with less than 20% residual cross-talk even in the three color images (Table 2). This residual cross-talk is as good as reported in previous multispecies STED publications; see, e.g., the maximum of 16% for a three color sample in Winter et al.[29] By also taking the differences in the absorption spectra into account, we were even able to clearly separate fluorophores with only a 13 nm difference in their peak emission wavelength as compared to recommended not less than 20 nm by Winter et al.[29] Due to the increased STED resolution in comparison to confocal imaging, it was possible to resolve the structures given by the fluorescent domains on the origami. The quality is illustrated in the line profiles in Figure 4c and Figure 5c, where the length of the whole structure was found to be 136 and 135 nm from peak to peak of the outer dots, respectively. These values match up well with the manufacturer's specifications (140 nm). An analysis of several images yielded very similar results (data not shown).

Photobleaching is a relevant issue in STED microscopy and was also observed in our experiments. In multicolor STED imaging, this problem can even become more complex due to each dye's different photobleaching rate. To decrease limitations induced by photobleaching, our approach can be, in principle, easily be combined with newly developed STED techniques that reduce photobleaching.[15,16,46]

We have demonstrated that by using just one depletion wavelength and by exploiting the differences in the STED dyes' absorption spectra, up to three fluorophores can be effectively unmixed. By using the fluorescence lifetime as an additional parameter it is possible to further increase the number of fluorophores and the unmixing quality.[25,27,38] This aspect was not explored in this paper as the fluorescence lifetimes of the fluorophores used here were quite similar (3.9 ns for ATTO 594, 3.3 ns for Abberior STAR 635P, and 3.5 ns for ATTO 647N). Still, the FPM method used is capable of taking differences in the photon arrival time histograms, as a consequence of different excited state lifetimes, into account. Due to the pattern-matching approach, the individual fluorescence decays do not have to be described analytically (for example by exponential tail fitting), but they are just recorded as references in parallel with the spectral properties. Without the need of iterative decay fitting but with the possibility to give stable results even with limited photon statistics per pixel, the pattern-matching analysis is again for this modality the superior approach in STED imaging.

Finally, we expect our approach to be easily applied to biological specimen and even useful for live-cell measurements, since it depends only on the appropriate selection of fluorescent labels with significant differences in their absorption spectra. The labels used in this study have already been used successfully in cells, including live-cell STED measurements.[6,9,10,29,38,47−49] Also, further suitable red dyes are already established for these kind of measurements (SiR and CF680R).[29] With only 15 to 20 fluorescent molecules per subdiffraction sized domain on our origami structures, the number of labeled molecules was quite low. As the label concentration in fixed cells is usually much higher, we expect that our approach will yield similar or even better results in cells.

CONCLUSION

The presented approach of fast pattern-matching (FPM) integrates well with STED microscopy and does not require additional steps beside a multicolor PIE-mode acquisition. A simple turn-key system equipped with a single STED laser, a set of different pulsed excitation sources, and two detectors is enough to obtain multicolor STED images with just a single image scan. As our FPM image decomposition is a purely postprocessing step, implementing it into existing acquisition and analysis routines is easily possible. If the quasi simultaneous multicolor probing is not mandatory (because the sample is fixed and system drift is no issue), one could even operate the excitation lasers in line or frame interleaved mode to generalize the approach. Our FPM-based spectral unmixing of the three utilized fluorophores ATTO 594, Abberior Star 635P and ATTO 647N can in principle also be extended by adding a fourth red-shifted fluorophore (e.g., CF680R[29]). In addition, the FPM approach can be taken one step further by including fluorescence decay information into the unmixing process. We expect that this should enable the method to be applied to even more than four fluorophores while using only two detectors, provided that the fluorophores are carefully chosen with regard to their fluorescence lifetimes. As an example, one could add the dye SiR to the mixture of three fluorophores used within the presented study, as it has a significantly shorter lifetime (2.7 ns).[45] The remaining challenge of all pattern-matching techniques is to extract proper reference patterns, either from separate samples or by manual selection of single species regions in the multispecies image. However, the latter subjective choice is prone to introduce a bias in the unmixing algorithm. In the future, this issue could be addressed by including machine

https://doi.org/10.1021/acs.jpcb.0c11390
J. Phys. Chem. B 2021, 125, 5694−5705

learning algorithms (e.g., k-means clustering algorithms) to find the best set of single species clusters in an ICM.

■ ASSOCIATED CONTENT

Supporting Information

The Supporting Information is available free of charge at https://pubs.acs.org/doi/10.1021/acs.jpcb.0c11390.

Figure S1: Point spread functions for the excitation wavelengths 595 nm, 640 nm, and 660 nm, and for the STED wavelength 765 nm (PDF)

Figure S2: Isolated excitation color approach of the two color STED data set (PDF)

Figure S3: Isolated excitation color approach of the three color STED data set (PDF)

■ AUTHOR INFORMATION

Corresponding Author

Marcelle König − *PicoQuant GmbH, 12489 Berlin, Germany;* orcid.org/0000-0002-9697-4859; Email: koenig@picoquant.com

Authors

Mariano Gonzalez Pisfil − *PicoQuant Innovations GmbH, 12489 Berlin, Germany; Department of Biology, Molecular Biophysics, IRI Life Sciences, Humboldt-Universität zu Berlin, 10115 Berlin, Germany*

Sumeet Rohilla − *PicoQuant Innovations GmbH, 12489 Berlin, Germany; Department of Internal Medicine/Infectious Diseases and Respiratory Medicine, Charité − Universitätsmedizin Berlin, corporate member of Freie Universität Berlin, Humboldt-Universität zu Berlin, and Berlin Institute of Health, 10117 Berlin, Germany*

Benedikt Krämer − *PicoQuant GmbH, 12489 Berlin, Germany*

Matthias Patting − *PicoQuant GmbH, 12489 Berlin, Germany*

Felix Koberling − *PicoQuant GmbH, 12489 Berlin, Germany*

Rainer Erdmann − *PicoQuant GmbH, 12489 Berlin, Germany*

Complete contact information is available at: https://pubs.acs.org/10.1021/acs.jpcb.0c11390

Author Contributions

M.G.P. and M.K planned the experiments. M.G.P. carried out all experiments and analyzed the data. B.K. provided support with regards to the used microscope hardware while M.G.P., S.R. and M.P. contributed toward the data analysis software. M.G.P., M.K. and F.K. wrote the main manuscript together and M.G.P. prepared all figures. R.E. secured funding for the project and was in charge of the overall direction, outline and planning. The manuscript was reviewed by all authors.

Notes

The authors declare the following competing financial interest(s): RE has a financial interest in PicoQuant and PicoQuant Innovations. He is a founder of the companies and also serves as General Director. The other authors are or were employed at PicoQuant or PicoQuant Innovations.

The data sets and analysis generated during the current study are available from the corresponding author on reasonable request.

■ ACKNOWLEDGMENTS

This project has received funding from the European Union's Framework Programs for Research and Innovation Horizon 2020 (2014−2020) under the Marie Skłodowska-Curie Grant Agreement No. 675512 (BE-OPTICAL) and No. 675332 (BITMAP).

■ REFERENCES

(1) Hell, S. W.; Wichmann, J. Breaking the diffraction resolution limit by stimulated emission: stimulated-emission-depletion fluorescence microscopy. *Opt. Lett.* **1994**, *19*, 780−782.

(2) Klar, T. A.; Hell, S. W. Subdiffraction resolution in far-field fluorescence microscopy. *Opt. Lett.* **1999**, *24*, 954−956.

(3) Betzig, E.; Patterson, G. H.; Sougrat, R.; Lindwasser, O. W.; Olenych, S.; Bonifacino, J. S.; Davidson, M. W.; Lippincott-Schwartz, J.; Hess, H. F. Imaging Intracellular Fluorescent Proteins at Nanometer Resolution. *Science* **2006**, *313*, 1642−1645.

(4) Gustafsson, M. G. L. Nonlinear structured-illumination microscopy: Wide-field fluorescence imaging with theoretically unlimited resolution. *Proc. Natl. Acad. Sci. U. S. A.* **2005**, *102*, 13081−13086.

(5) Rust, M. J.; Bates, M.; Zhuang, X. Sub-diffraction-limit imaging by stochastic optical reconstruction microscopy (STORM). *Nat. Methods* **2006**, *3*, 793−795.

(6) Willig, K. I.; Kellner, R. R.; Medda, R.; Hein, B.; Jakobs, S.; Hell, S. W. Nanoscale Resolution in GFP-Based Microscopy. *Nat. Methods* **2006**, *3*, 721−723.

(7) Han, R.; Li, Z.; Fan, Y.; Jiang, Y. Recent Advances in Super-Resolution Fluorescence Imaging and Its Applications in Biology. *J. Genet. Genomics* **2013**, *40*, 583−595.

(8) Sahl, S. J.; Hell, S. W.; Jakobs, S. Fluorescence nanoscopy in cell biology. *Nat. Rev. Mol. Cell Biol.* **2017**, *18*, 685−701.

(9) Yu, Y.; Jans, D. C.; Winblad, B.; Tjernberg, L. O.; Schedin-Weiss, S. Neuronal Aβ42 is enriched in small vesicles at the presynaptic side of synapses. *Life Science Alliance* **2018**, *1*, No. e201800028.

(10) Meyer, S. A.; Ozbay, B. N.; Restrepo, D.; Gibson, E. A. Super-resolution imaging of ciliary microdomains in isolated olfactory sensory neurons using a custom STED microscope. *Proc. SPIE* **2014**, 104−111.

(11) Lakadamyali, M.; Babcock, H.; Bates, M.; Zhuang, X.; Lichtman, J. 3D Multicolor Super-Resolution Imaging Offers Improved Accuracy in Neuron Tracing. *PLoS One* **2012**, *7*, No. e30826.

(12) Galiani, S.; Waithe, D.; Reglinski, K.; Cruz-Zaragoza, L. D.; Garcia, E.; Clausen, M.; Schliebs, W.; Erdmann, R.; Eggeling, C. Super-resolution Microscopy Reveals Compartmentalization of Peroxisomal Membrane Proteins. *J. Biol. Chem.* **2016**, *291*, 16948−16962.

(13) Bottanelli, F.; Kromann, E. B.; Allgeyer, E. S.; Erdmann, R. S.; Wood Baguley, S.; Sirinakis, G.; Schepartz, A.; Baddeley, D.; Toomre, D. K.; Rothman, J. E.; et al. Two-colour live-cell nanoscale imaging of intracellular targets. *Nat. Commun.* **2016**, *7*, 10778.

(14) Neumann, D.; Bückers, J.; Kastrup, L.; Hell, S. W.; Jakobs, S. Two-color STED microscopy reveals different degrees of colocalization between hexokinase-I and the three human VDAC isoforms. *PMC Biophys.* **2010**, *3*, 4.

(15) Heine, J.; Reuss, M.; Harke, B.; D'Este, E.; Sahl, S. J.; Hell, S. W. Adaptive-illumination STED nanoscopy. *Proc. Natl. Acad. Sci. U. S. A.* **2017**, *114*, 9797−9802.

(16) Staudt, T.; Engler, A.; Rittweger, E.; Harke, B.; Engelhardt, J.; Hell, S. W. Far-field optical nanoscopy with reduced number of state transition cycles. *Opt. Express* **2011**, *19*, 5644−5657.

(17) Curdt, F.; Herr, S. J.; Lutz, T.; Schmidt, R.; Engelhardt, J.; Sahl, S. J.; Hell, S. W. isoSTED nanoscopy with intrinsic beam alignment. *Opt. Express* **2015**, *23*, 30891−30903.

(18) Harke, B.; Ullal, C. K.; Keller, J.; Hell, S. W. Three-Dimensional Nanoscopy of Colloidal Crystals. *Nano Lett.* **2008**, *8*, 1309−1313.

(19) Reuss, M.; Engelhardt, J.; Hell, S. W. Birefringent device converts a standard scanning microscope into a STED microscope that also maps molecular orientation. *Opt. Express* **2010**, *18*, 1049−1058.

(20) Rönnlund, D.; Xu, L.; Perols, A.; Gad, A. K. B.; Eriksson Karlström, A.; Auer, G.; Widengren, J. Multicolor Fluorescence Nanoscopy by Photobleaching: Concept, Verification, and Its Application To Resolve Selective Storage of Proteins in Platelets. *ACS Nano* **2014**, *8*, 4358−4365.

(21) Osseforth, C.; Moffitt, J. R.; Schermelleh, L.; Michaelis, J. Simultaneous dual-color 3D STED microscopy. *Opt. Express* **2014**, *22*, 7028−7039.
(22) Wildanger, D.; Rittweger, E.; Kastrup, L.; Hell, S. W. STED microscopy with a supercontinuum laser source. *Opt. Express* **2008**, *16*, 9614−9621.
(23) Bingen, P.; Reuss, M.; Engelhardt, J.; Hell, S. W. Parallelized STED fluorescence nanoscopy. *Opt. Express* **2011**, *19*, 23716−23726.
(24) Donnert, G.; Keller, J.; Wurm, C. A.; Rizzoli, S. O.; Westphal, V.; Schönle, A.; Jahn, R.; Jakobs, S.; Eggeling, C.; Hell, S. W. Two-Color Far-Field Fluorescence Nanoscopy. *Biophys. J.* **2007**, *92*, L67−L69.
(25) Bückers, J.; Wildanger, D.; Vicidomini, G.; Kastrup, L.; Hell, S. W. Simultaneous multi-lifetime multi-color STED imaging for colocalization analyses. *Opt. Express* **2011**, *19*, 3130−3143.
(26) Sidenstein, S. C.; D'Este, E.; Böhm, M. J.; Danzl, J. G.; Belov, V. N.; Hell, S. W. Multicolour Multilevel STED nanoscopy of Actin/Spectrin Organization at Synapses. *Sci. Rep.* **2016**, *6*, 26725.
(27) Gorlitz, F.; Hoyer, P.; Falk, H. J.; Kastrup, L.; Engelhardt, J.; Hell, S. W. A STED Microscope Designed for Routine Biomedical Applications. *Progress In Electromagnetics Research* **2014**, *147*, 57−68.
(28) Tønnesen, J.; Nadrigny, F.; Willig, K. I.; Wedlich-Soldner, R.; Nägerl, U. V. Two-Color STED Microscopy of Living Synapses Using A Single Laser-Beam Pair. *Biophys. J.* **2011**, *101*, 2545−2552.
(29) Winter, F. R.; Loidolt, M.; Westphal, V.; Butkevich, A. N.; Gregor, C.; Sahl, S. J.; Hell, S. W. Multicolour nanoscopy of fixed and living cells with a single STED beam and hyperspectral detection. *Sci. Rep.* **2017**, *7*, 46492.
(30) Zimmermann, T.; Rietdorf, J.; Pepperkok, R. Spectral Imaging and Its Applications in Live Cell Microscopy. *FEBS Lett.* **2003**, *546*, 87−92.
(31) Dickinson, M. E.; Bearman, G.; Tille, S.; Lansford, R.; Fraser, S. E. Multi-Spectral Imaging and Linear Unmixing Add a Whole New Dimension to Laser Scanning Fluorescence Microscopy. *BioTechniques* **2001**, *31*, 1272−1278.
(32) Schönau, T.; Siebert, T.; Härtel, R.; Eckhardt, T.; Klemme, D.; Lauritsen, K.; Erdmann, R. Pulsed picosecond 766 nm laser source operating between 1−80 MHz with automatic pump power management. *Proc. SPIE* **2013**, 38−42.
(33) König, M.; Reisch, P.; Dowler, R.; Krämer, B.; Tannert, S.; Patting, M.; Clausen, M. P.; Galiani, S.; Eggeling, C.; Koberling, F. ns-time resolution for multispecies STED-FLIM and artifact free STED-FCS. *Proc. SPIE* **2016**, 85−93.
(34) Göttfert, F.; Wurm, C. A.; Mueller, V.; Berning, S.; Cordes, V. C.; Honigmann, A.; Hell, S. W. Coaligned Dual-Channel STED Nanoscopy and Molecular Diffusion Analysis at 20 nm Resolution. *Biophys. J.* **2013**, *105*, L01−L03.
(35) Wahl, M.; Röhlicke, T.; Rahn, H.-J.; Erdmann, R.; Kell, G.; Ahlrichs, A.; Kernbach, M.; Schell, A. W.; Benson, O. Integrated multichannel photon timing instrument with very short dead time and high throughput. *Rev. Sci. Instrum.* **2013**, *84*, 043102.
(36) Vicidomini, G.; Schönle, A.; Ta, H.; Han, K. Y.; Moneron, G.; Eggeling, C.; Hell, S. W. STED Nanoscopy with Time-Gated Detection: Theoretical and Experimental Aspects. *PLoS One* **2013**, *8*, No. e54421.
(37) Moffitt, J. R.; Osseforth, C.; Michaelis, J. Time-gating improves the spatial resolution of STED microscopy. *Opt. Express* **2011**, *19*, 4242−4254.
(38) Niehörster, T.; Löschberger, A.; Gregor, I.; Kraemer, B.; Rahn, H.-J.; Patting, M.; Koberling, F.; Enderlein, J.; Sauer, M. Multi-target spectrally resolved fluorescence lifetime imaging microscopy. *Nat. Methods* **2016**, *13*, 257−262.
(39) Mehedi, M.; Smelkinson, M.; Kabat, J.; Ganesan, S.; Collins, P. L.; Buchholz, U. J. Multicolor Stimulated Emission Depletion (STED) Microscopy to Generate High-resolution Images of Respiratory Syncytial Virus Particles and Infected Cells. *Bio-protocol* **2017**, *7*, No. e2543.
(40) Beater, S.; Holzmeister, P.; Lalkens, B.; Tinnefeld, P. Simple and aberration-free 4color-STED - multiplexing by transient binding. *Opt. Express* **2015**, *23*, 8630−8638.
(41) Hebisch, E.; Wagner, E.; Westphal, V.; Sieber, J. J.; Lehnart, S. E. A protocol for registration and correction of multicolour STED superresolution images. *J. Microsc.* **2017**, *267*, 160−175.
(42) Wegner, W.; Ilgen, P.; Gregor, C.; van Dort, J.; Mott, A. C.; Steffens, H.; Willig, K. I. In vivo mouse and live cell STED microscopy of neuronal actin plasticity using far-red emitting fluorescent proteins. *Sci. Rep.* **2017**, *7*, 11781.
(43) Sednev, M. V.; Belov, V. N.; Hell, S. W. Fluorescent dyes with large Stokes shifts for super-resolution optical microscopy of biological objects: A review. *Methods Appl. Fluoresc.* **2015**, *3*, 042004.
(44) Wurm, C. A.; Kolmakov, K.; Göttfert, F.; Ta, H.; Bossi, M.; Schill, H.; Berning, S.; Jakobs, S.; Donnert, G.; Belov, V. N.; et al. Novel red fluorophores with superior performance in STED microscopy. *Optical Nanoscopy* **2012**, *1*, 7.
(45) Butkevich, A. N.; Mitronova, G. Y.; Sidenstein, S. C.; Klocke, J. L.; Kamin, D.; Meineke, D. N. H.; D'Este, E.; Kraemer, P.-T.; Danzl, J. G.; Belov, V. N.; et al. Fluorescent Rhodamines and Fluorogenic Carbopyronines for Super-Resolution STED Microscopy in Living Cells. *Angew. Chem., Int. Ed.* **2016**, *55*, 3290−3294.
(46) Spahn, C.; Grimm, J. B.; Lavis, L. D.; Lampe, M.; Heilemann, M. Whole-Cell, 3D, and Multicolor STED Imaging with Exchangeable Fluorophores. *Nano Lett.* **2019**, *19*, 500−505.
(47) Wildanger, D.; Medda, R.; Kastrup, L.; Hell, S. W. A compact STED microscope providing 3D nanoscale resolution. *J. Microsc.* **2009**, *236*, 35−43.
(48) Eggeling, C.; Ringemann, C.; Medda, R.; Schwarzmann, G.; Sandhoff, K.; Polyakova, S.; Belov, V. N.; Hein, B.; von Middendorff, C.; Schönle, A.; et al. Direct observation of the nanoscale dynamics of membrane lipids in a living cell. *Nature* **2009**, *457*, 1159−1162.
(49) Pellett, P. A.; Sun, X.; Gould, T. J.; Rothman, J. E.; Xu, M.-Q.; Corrêa, I. R., Jr; Bewersdorf, J. Two-color STED microscopy in living cells. *Biomed. Opt. Express* **2011**, *2*, 2364−2371.

https://doi.org/10.1021/acs.jpcb.0c11390
J. Phys. Chem. B 2021, 125, 5694−5705

scientific reports

Check for updates

OPEN

Stimulated emission depletion microscopy with a single depletion laser using five fluorochromes and fluorescence lifetime phasor separation

Mariano Gonzalez Pisfil, Iliya Nadelson, Brigitte Bergner, Sonja Rottmeier, Andreas W. Thomae & Steffen Dietzel✉

Stimulated emission depletion (STED) microscopy achieves super-resolution by exciting a diffraction-limited volume and then suppressing fluorescence in its outer parts by depletion. Multiple depletion lasers may introduce misalignment and bleaching. Hence, a single depletion wavelength is preferable for multi-color analyses. However, this limits the number of usable spectral channels. Using cultured cells, common staining protocols, and commercially available fluorochromes and microscopes we exploit that the number of fluorochromes in STED or confocal microscopy can be increased by phasor based fluorescence lifetime separation of two dyes with similar emission spectra but different fluorescent lifetimes. In our multi-color FLIM-STED approach two fluorochromes in the near red (exc. 594 nm, em. 600–630) and two in the far red channel (633/641–680), supplemented by a single further redshifted fluorochrome (670/701–750) were all depleted with a single laser at 775 nm thus avoiding potential alignment issues. Generally, this approach doubles the number of fully distinguishable colors in laser scanning microscopy. We provide evidence that eight color FLIM-STED with a single depletion laser would be possible if suitable fluorochromes were identified and we confirm that a fluorochrome may have different lifetimes depending on the molecules to which it is coupled.

In the life sciences, highly resolved images of a single structure can be helpful in some cases, but often it is necessary to know where one structure is in relation to another or several others. This generates a demand for multi-color super-resolution microscopy. Commercially available stimulated emission depletion (STED) microscopes have up to three depletion laser wavelengths, 592 or 595, 660 and 775 nm. This theoretically allows usage of fluorochromes over the full spectral range of a confocal microscope. However, in the experience of others[1] and ourselves, dyes depleted with a 592 or 660 nm continuous wave laser tend to bleach fast, compared to some that can be depleted with the pulsed 775 nm laser. This is also reflected by the relatively small number of fluorochromes typically used in STED microscopy (see following examples). Further technical obstacles for usage of several depletion lasers are the need to align those lasers very precisely to allow meaningful super-resolution multi-color colocalization studies and total photobleaching of long wavelength dyes by the lower wavelength depletion laser. Therefore, ideally only one depletion laser is used for all fluorochromes[2]. And indeed, multi-color STED studies tend to apply only 775 nm depletion using near or far red dyes[1–8].

Publications with more than three colors imaged by STED are scarce. We found two that used four distinguishable fluorochromes[5,9]. Rönnlund et al. applied a scheme with two color channels where two dyes or distinguishable dye conjugates were in each color channel (ATTO 647N & Dylight650; Alexa Fluor 594 coupled to antibody and phalloidin). After an initial scan, one in each channel was specifically photobleached. While this was feasible in small and flat platelets (thrombocytes), it may be difficult in larger cells, e.g. due to sample drift. The 2017 study from the group of Stefan Hell, who invented STED microscopy, excited four dyes with 612 nm and depleted with 775 nm in fixed cells. They used the fluorochromes ATTO 594 (max exc./em 601/627), Abberior STAR 635P (633/654), KK1441 (661/679), and CF680R (680/701)[5], dyes with heavily overlapping emission

Core Facility Bioimaging and Walter-Brendel-Centre of Experimental Medicine, Biomedical Center, Ludwig-Maximilians-Universität München, Großhaderner Straße 9, 82152 Planegg-Martinsried, Germany. ✉email: dietzel@lmu.de

spectra which they separated computationally by mathematical spectral unmixing. The anti-stokes excitation[10,11] of CF680R by the STED beam was subtracted prior to the unmixing. A 'residual crosstalk' between channels of up to 20% remained in a selected image. Unfortunately, one of these dyes, KK1441, does not seem to be commercially available, neither easily replaceable, thus limiting the number of usable dyes from this scheme for most researchers to three. Another paper from Stefan Hell's group visualized five fluorochromes by STED with an approach similar to the Rönnlund-study: Abberrior STAR 580 and 635P where imaged and bleached before uncaging two other dyes in the same spectral range, supplemented with Alexa Fluor 488 depleted with a second STED laser [12]. A prior inspection of all signals in confocal mode is not possible in this approach. Both groups performed their experiments on custom-built microscope systems, indicating a talent and preference for microscope building, which in the case of the average life scientist who wants to examine biological questions is usually not given.

A further approach to multi-color STED used up to four primary antibodies with single strand DNA labels (~ 10 nucleotides) to which complementary DNA oligonucelotides bound transiently[13,14]. One of the four complementary DNA strands was perfused over the sample and washed out before the next strand was applied. This approach theoretically allows unlimited numbers of labels. Potential problems are z-drift or shift between recordings (in particular if several fields of view were to be recorded), the long time periods needed for each image (about 20 min per color in fast variants[15]), and the inability to make permanent samples. The need to conjugate the DNA oligonucelotides to the primary antibodies and the impossibility to preselect multiple labeled areas of interest through the eyepiece or with an overview scan may further deter life scientists from this approach.

A combination of STED with fluorescence lifetime imaging (FLIM) to separate fluorochromes was first published in 2011, also by the group of Stefan Hell[2]. They separated ATTO 647N and KK114[6] (later commercialized as Abberior STAR Red, according to the company's web site) by lifetime and used ATTO 590 as a third color with a second STED beam. Since with FLIM separated fluorochromes the photons of two dyes are recorded simultaneously, any drift or misalignment issues are excluded by design. However, a decade ago FLIM equipment was slow and difficult to operate compared to a confocal microscope. In addition, classical curve fitting analysis to separate dyes by lifetime requires high numbers of photons[16], which are typically difficult to achieve in STED microscopy of biological samples. Curve fitting for dye separation faces another problem: while many dyes may exhibit a single exponential lifetime free in solution, when coupled to antibodies or other targeting molecules they can obtain additional lifetime components. Two fluorochromes with bi-exponential behavior would thus present four lifetime components, rendering classic exponential decay fitting more complex[16]. With increased number of lifetime components the number of required photons and thus imaging time increases, making this approach difficult to combine with STED.

Accordingly, we found only three other papers, one of them also from the Hell group[17], describing the use of FLIM to increase the number of fluorochromes in multi-color STED. In confocal microscopy, separation of five fluorochromes excited by the same laser line was demonstrated by a mixture of spectral and FLIM separation[16]. Another study made use of cross labelling antibodies to create new lifetime species via Förster resonance energy transfer (FRET), later unmixed by the same spectral FLIM separation approach[18]. However, for high precision color separation a commercially not available spectral detector was used in both studies and the applied pattern matching for color separation requires relatively high photon numbers, at least if structures are overlapping[16,19]. The method was also applied to STED, but here the separation of only two dyes in a single color channel was demonstrated on images with 5000–10,000 photons in the brightest pixels[16].

Complementing fluorescence lifetime and emission spectra, utilization of the absorption spectra was suggested for multi-color STED[19], but so far the number of fluorochromes was limited to three.

Recent advances in FLIM technology brought faster systems which are fully integrated with commercial confocal and STED software and thus much more user friendly and easier to operate by life scientists. In addition, the development of phasor based analysis of FLIM data[20–22] reached a point where it allows easy and fast fluorochrome separation with substantially lower photon numbers when compared to curve fitting if background is present[23]. Applicability with low photon numbers is important since in STED, due to the depletion of fluorochromes and much smaller pixels compared to typical confocal microscopy, in a given time span the number of detected photons per pixel is low. Phasor analysis with low photon numbers will not determine absolute lifetimes with the same accuracy as curve fitting with high photon numbers. Furthermore, most fluorochromes show a multi-exponential decay and the various lifetimes of a multi-exponential decay cannot be separated in phasor analysis; they will result in a mean lifetime in the phasor plot. However, to separate different fluorochromes by phasor analysis, only relative lifetime differences between two dyes are needed. We therefore revisited the multi-color FLIM-STED approach and combined it with phasor analysis.

We used a commercial confocal system with STED and FLIM capabilities to develop a multi-color FLIM-STED scheme with one depletion laser (pulsed 775 nm) and one multi-wavelength excitation laser, thus minimizing alignment issues. Only commercially available fluorochrome-labeled antibodies, phalloidin and wheat germ agglutinin (WGA) were used. Fixation and staining were performed by typical immunofluorescence protocols and are thus easily reproducible by other life scientists. We show for biological samples that phasor based image analysis can very well separate two fluorochromes by lifetime in a spectral channel. We demonstrate five color STED and five color confocal images in only three spectral channels. We also suggest avenues to further increase the number of colors for STED with a single depletion laser.

Results

Five color STED microscopy. We performed FLIM-STED with five fluorochromes using one depletion laser and three spectrally separated channels, each with a fitting excitation wavelength. Two of the channels carried two spectrally similar fluorochromes that were separated by phasor lifetime analysis (Fig. 1). Fixed HeLa cells were stained in the far red channel with Abberior STAR 635P coupled to a secondary anti-rabbit antibody

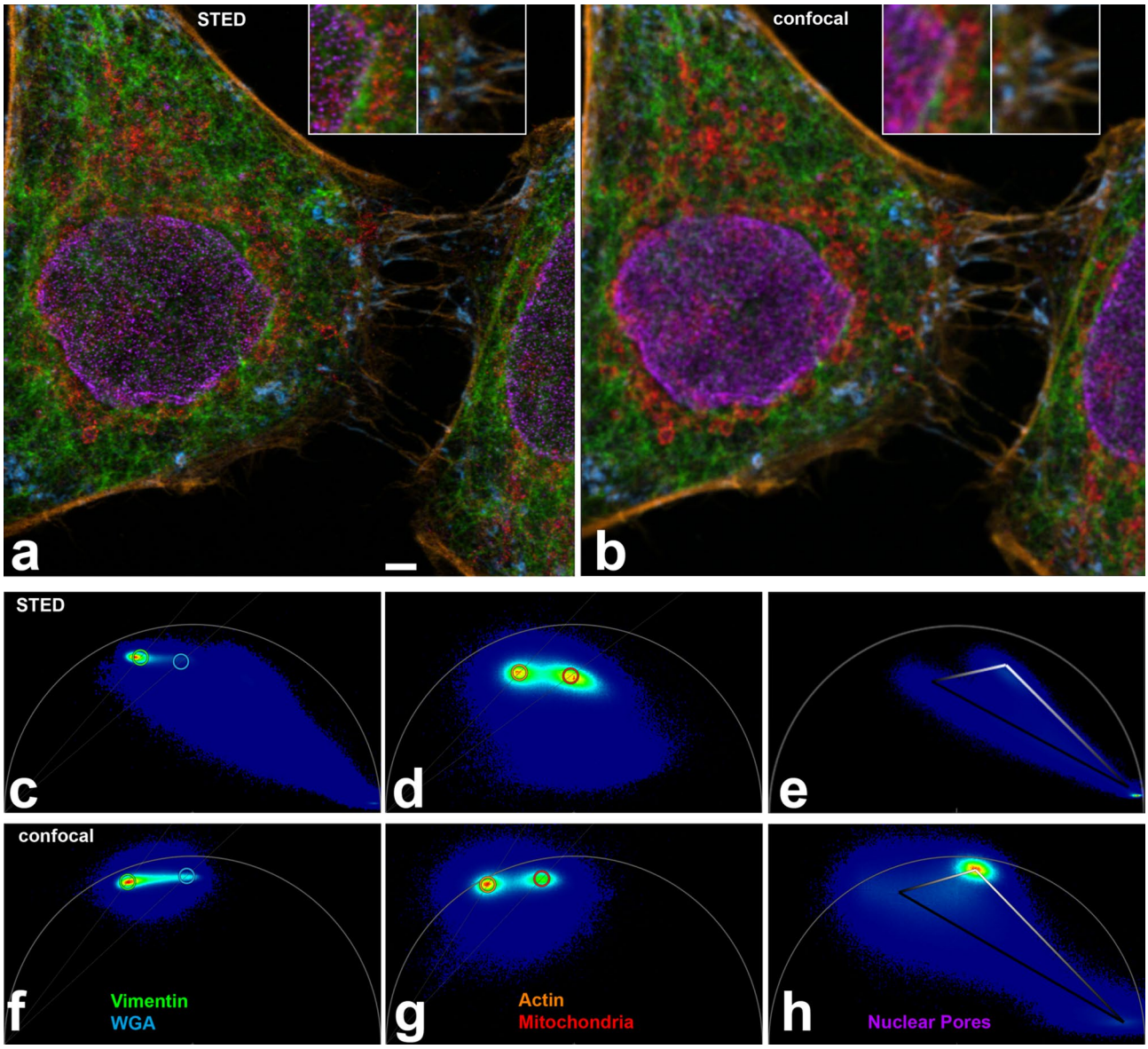

Figure 1. (**a**) Five color FLIM-STED phasor separated image. Insets show two areas doubled in size. Raw images had 1516, 1213, and 542 photons in the brightest pixels in the near red, far red and CF680R channels. Scale bar 2 µm. (**b**) Corresponding phasor separated FLIM confocal image with the same pixel size (25 nm). (**c**–**h**) Phasor plots from STED (**c**–**e**) and confocal (**f**–**h**) raw images corresponding to (**a**, **b**). Near red channel (**c**, **f**, 600–630 nm), far red channel (**d**, **g**, 641–680 nm) and 701–750 nm channel (**e**, **h**) are shown. In phasor plots, each image pixel is positioned according to its lifetime behavior. Pixels with monoexponential decay will be on the semi-circle (called 'universal circle'), those with multiexponential decay towards the inside. Short lifetimes are to the right, long lifetimes to the left, the scale is non-linear. Note that the lifetime distribution in phasor plots in STED is shifted to the right, reflecting shorter lifetimes. For nuclear pores, the confocal phasor plot (**h**) shows pixels with crosstalk from the far red channel (compare **g**) while the STED phasor plot (**e**) shows in addition strong reflection of the 670 nm excitation in the lower right corner (zero lifetime), since no notch filter was available to suppress it.

(Tau 2.2 ns) to detect mitochondrial outer membrane protein TOMM20 and with ATTO 647N coupled to phalloidin (Tau 3.2 ns) which delineates the actin cytoskeleton. Excitation was at 633 nm, detection at 641–680 nm. All lifetimes are given for confocal images.

The near red color channel (594 nm, 600–630 nm) was populated with Alexa Fluor 594 coupled to a secondary anti-chicken antibody (Tau 2.6 ns) to visualize the cytoskeletal filament vimentin and WGA-CF594 (Tau 1.8 ns). WGA is a lectin that has a high affinity for sialic acid and N-acetylglucosamine moieties of glycoproteins and glycolipids; thus it stains the plasma membrane[24–26].

In the third spectral channel, CF680R labeled a secondary anti-mouse antibody (Tau 1.7 ns) to detect nuclear pores and was excited with the longest available wavelength, 670 nm (detection 701–750 nm). Sequential scanning of the three channels allowed to minimize bleed-through of fluorochromes to neighboring spectral channels

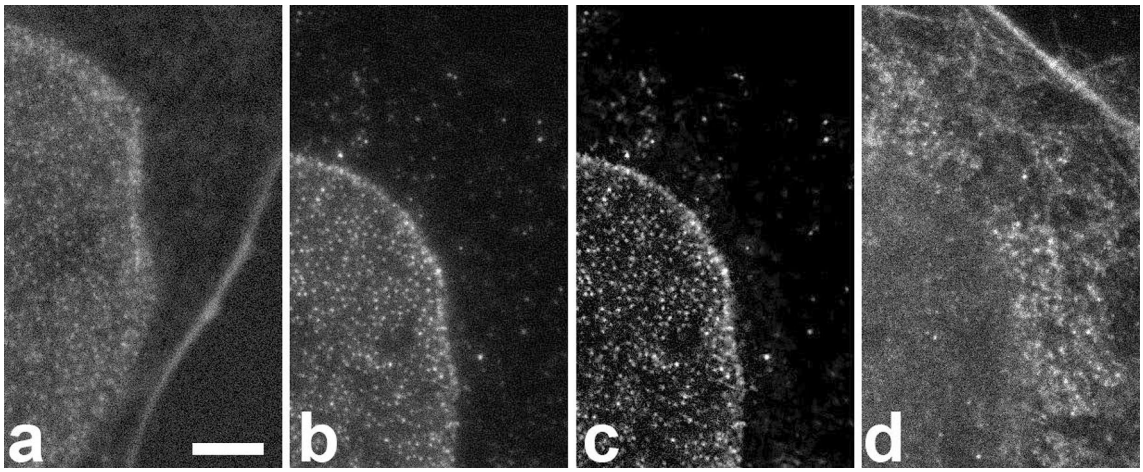

Figure 2. Crosstalk of far red dyes into the CF680R nuclear pore channel is observed with 670 nm excitation but not with 685 nm. Scale bar 2 µm for all images. (**a**) Excitation of a five color sample with 670 nm. The detection window was 701–750 nm. This raw image prior to Tau-STED processing shows substantial crosstalk from ATTO 647N (actin staining, strong fiber in the image from bottom to right) while Abberior STAR 635P (mitochondria) crosstalk is hardly above background. (**b**) Excitation of a different cell with 685 nm on another microscope shows no sign of crosstalk from other dyes. A haze around the nuclear pores is due to anti-stokes excitation of CF680R by the depletion beam. (**c**) The same image after Tau-STED processing which removed the anti-Stokes contribution. (**d**) Raw image of the area shown in (**b**, **c**) in the far red channel with actin and mitochondrial staining, demonstrating the presence of both structures and their fluorochromes.

and to adapt the STED laser power. By the latter, we could avoid the strong anti-stokes excitation of CF680R by the 775 nm STED beam that was previously described[5] (Fig. 1a,b).

Phasor based lifetime separation of two fluorochromes in the same color channel in STED images (Fig. 1c–e) revealed excellent partitioning (Fig. 1a). Visual comparison with confocal images of likewise acquisition (Fig. 1b,f–h) revealed significant resolution improvement.

In raw images of the CF680R channel, it was obvious that a substantial cross talk from ATTO 647N and to a much lesser extent from Abberior STAR 635P was present, when excitation was performed with 670 nm (Fig. 2a). In our routine procedure, this unwanted signal was efficiently eliminated by a Tau-STED approach implemented in the software, making use of the large differences in fluorescence lifetimes (1.2 vs 2.0 and 3.5 ns). For testing purposes, we could generate a few images on a microscope that allowed longer excitation wavelengths. With 685 nm excitation, clear raw images of nuclear pores were obtained without noticeable ATTO647N or Abberior STAR 635P contribution (Fig. 2b–d).

Orange as an additional spectral channel. A new probe for the orange channel (exc. ~550, em. 560–600), SPY555-actin, for which the manufacturer's material suggested that it could be depletable with 775 nm, became available during the course of this study. This was indeed the case in our experiments (Fig. 3). The super-resolution effect was clearly detectable, suggesting that this spectral range could be used as a fourth spectral channel in STED with 775 nm depletion, with two additional dyes, separable from each other by lifetime, if suitable fluorochromes were available.

STED causes a shortening of fluorescence lifetimes compared to confocal images. When comparing phasor plots of STED and confocal images, it was obvious that the average lifetimes of all dyes were substantially shortened in STED, compared to confocal images (Fig. 1c–h). Fluorochrome molecules that stay longer in the excited state are more likely to undergo stimulated depletion while those with a very short residence time in the excited state may have already emitted a short-lifetime fluorescence photon before stimulated depletion occurred[27,28]. Accordingly, we too observed that lifetime was inversely related to STED laser power.

The shortening of the lifetimes makes phasor separation for STED images (Fig. 1c–e) more demanding than for confocal images (Fig. 1f–h), since the absolute difference between lifetimes of two fluorochromes also becomes smaller. The lifetime of a fluorochrome in STED depends on its depletability by the wavelength of the STED beam and the beam's intensity and shape. STED lifetime in any specific experiment is thus difficult to predict. This suggests a trial-and-error approach to identify new dye pairs in the same color channel suitable for FLIM-STED, starting with fluorochromes that are reported to have big lifetime differences and that show low photobleaching in STED conditions.

Two colors with a single fluorochrome: lifetime depends on the binding partner. When testing various combinations of stainings for this study, a combination of two antibodies labeled with either Abberior STAR 635P or ATTO 647N showed more similar lifetimes for both dyes compared to the experiment presented

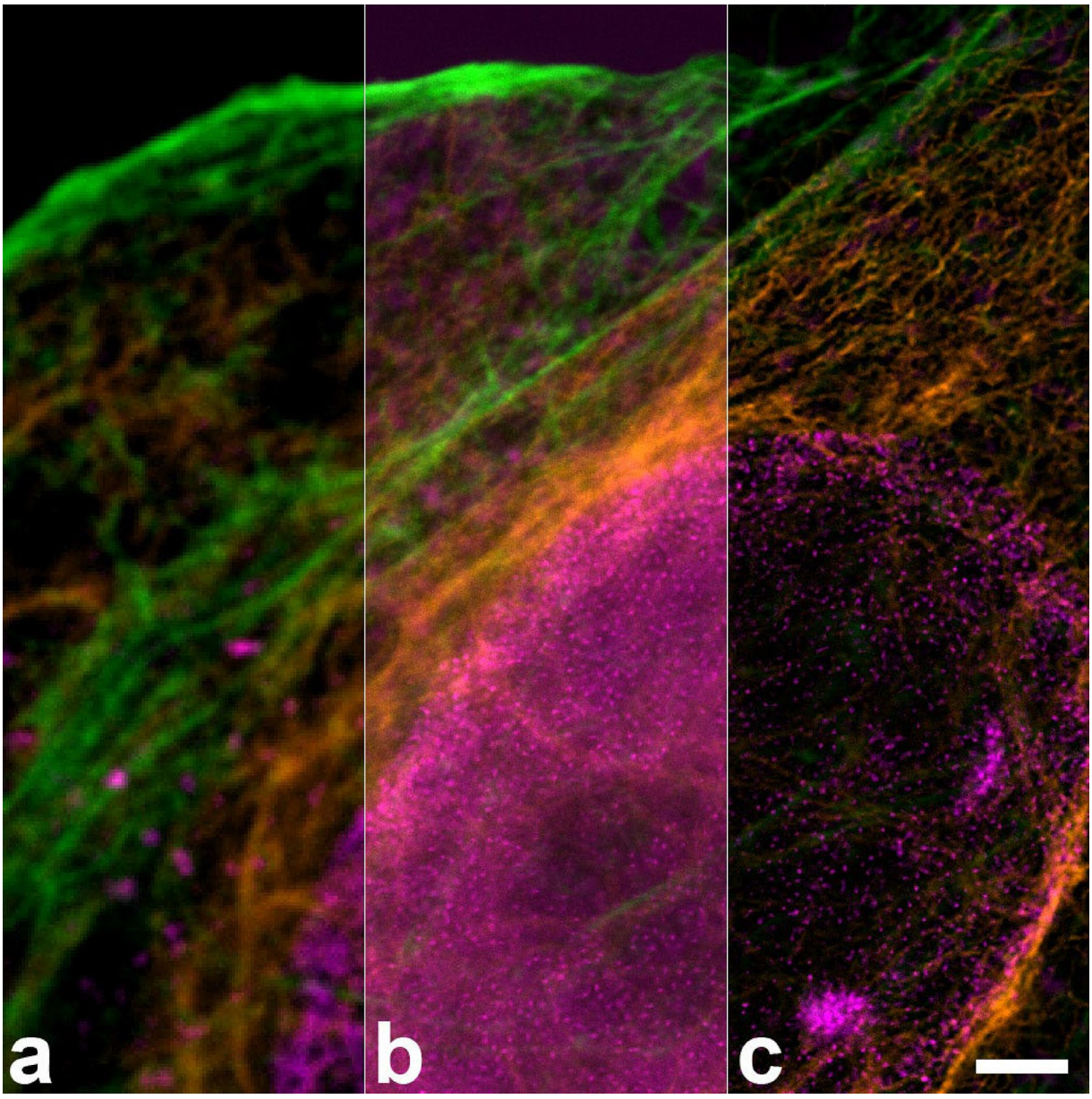

Figure 3. Three color image with spectrally separated SPY555-actin (green) and antibody stainings against vimentin (Alexa Fluor 594, orange) and nuclear pores (CF680R, magenta), all depleted with 775 nm. (**a**) confocal, (**b**) STED (**c**) Tau-STED. This dye combination could be supplemented with e.g. Abberior STAR 635P to obtain four spectrally separable fluorochromes. Scale bar: 2 µm. The three original full images are shown in Supplemental Fig. 1.

above where ATTO 647N was coupled to phalloidin. In STED images, the two antibody conjugated dyes could not be separated sufficiently by the phasor approach.

Different lifetimes of these two dyes and others, depending on their conjugation partner, were described previously[2,16]. In our hands, the lifetime differences induced by different conjugation partners (antibody or phalloidin) of Abberior STAR 635P or ATTO 647N were sufficient for discrimination of the two conjugates by phasor based separation in confocal images but did not lead to optimal results in STED, due to the generally shortened STED lifetimes. We performed double stainings with the same fluorochrome (either Abberior STAR 635P or ATTO 647N) coupled to both, an antibody and to phalloidin (Fig. 4). For both dyes, phasor analysis of confocal images allowed separation of phalloidin and antibody conjugates. In this sample, Abberior STAR 635P coupled to phalloidin had a lifetime of 3.4 ns, but only 2.3 ns when coupled to an anti-chicken antibody to detect vimentin (Fig. 4a; lifetimes determined on the phasor overlay of five images). Lifetime for ATTO 647N was measured as 3.6 ns when coupled to phalloidin but as 2.5 ns when coupled to an anti-mouse antibody to detect nuclear pores (Fig. 4b; lifetimes from phasor overlay of three images). Thus in both cases, the phalloidin coupled dye had a 0.7–0.9 ns longer lifetime than the antibody coupled one, a sufficient difference for phasor based separation in

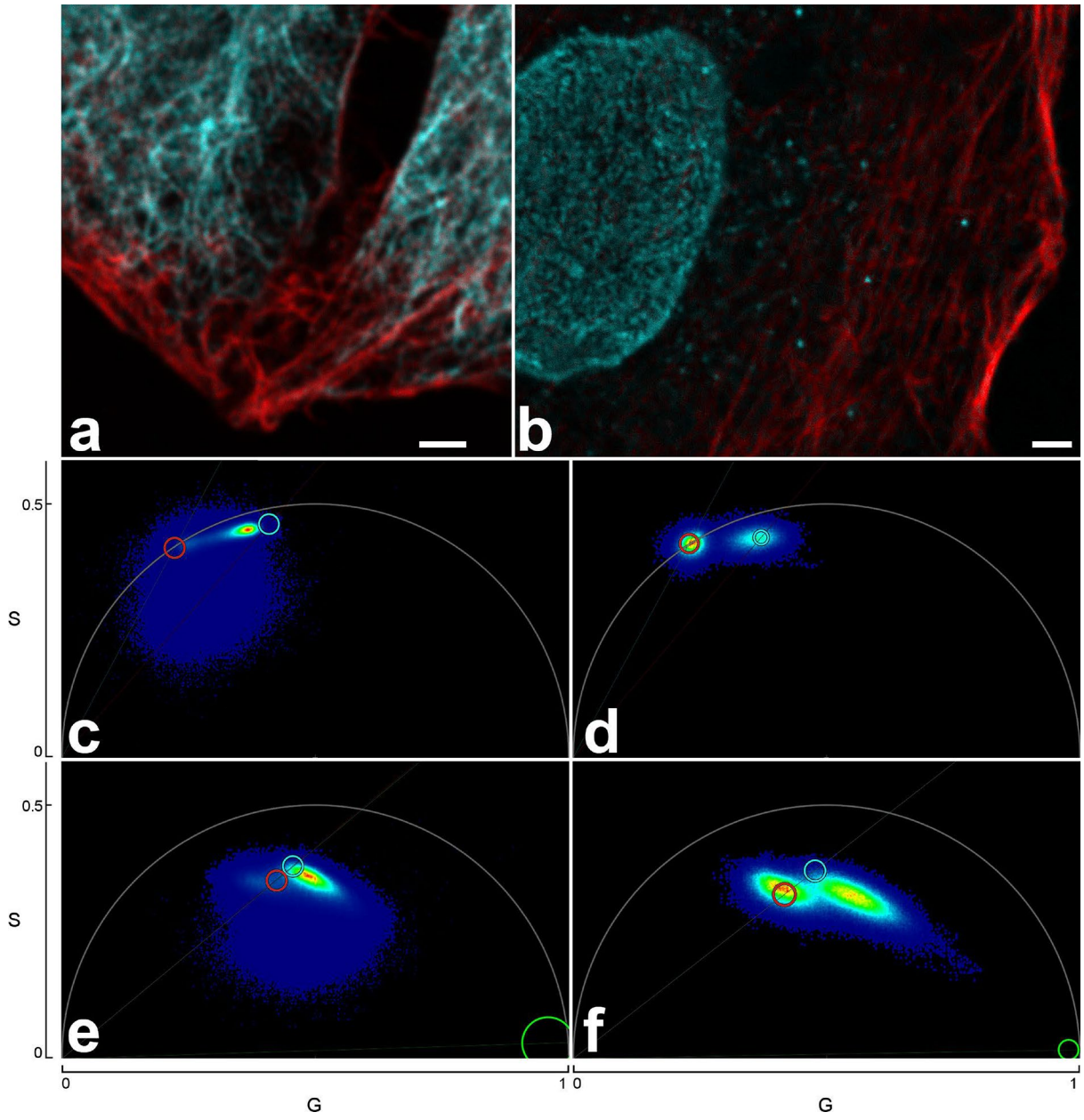

Figure 4. Fluorochromes have different lifetimes when coupled to antibodies or to phalloidin. (**a**) Confocal image of Abberior STAR 635P coupled to an antibody delineating vimentin (cyan) and to phalloidin (actin staining; red) and subjected to phasor based lifetime separation. (**b**) Confocal image of ATTO 647N coupled to phalloidin (actin staining, red) and an antibody (nuclear pores, cyan. Both confocal images show good separation of the two stained structures. Scale bars 2 µm. (**c**, **d**) Phasor plots for the complete raw images of (**a**, **b**). The actin coupled dyes have longer lifetimes (left cloud, red circle) compared to their antibody-conjugated versions (right cloud, cyan circle). (**e**, **f**) Phasor plots of respective STED images show that the lifetime differences are much reduced, due to the depletion effect causing a shorter average lifetime. Therefore, despite inclusion of a background component (green circle at G = 1, S = 0), separation of STED images was not satisfying and resulting images are not shown. Cyan and red circles indicate the best possible positions for separation of the two species. In (**e**, **f**) the right-hand clouds contain the pixels with antibody label derived photons, but they also contain substantial amounts of actin label derived photons. To compensate for this the circles were positioned next to the clouds.

confocal images (Fig. 4c,d). In STED images, however, the lifetimes and the difference between them decreased so that a phasor based separation did not achieve a satisfying quality.

Three fluorochromes were not satisfactory discriminated by phasor plot separation. In an attempt to further increase the number of fluorochromes per color channel, we performed a triple staining with two secondary antibodies labeled with either Abberior STAR 635 visualizing vimentin or with Alexa Fluor

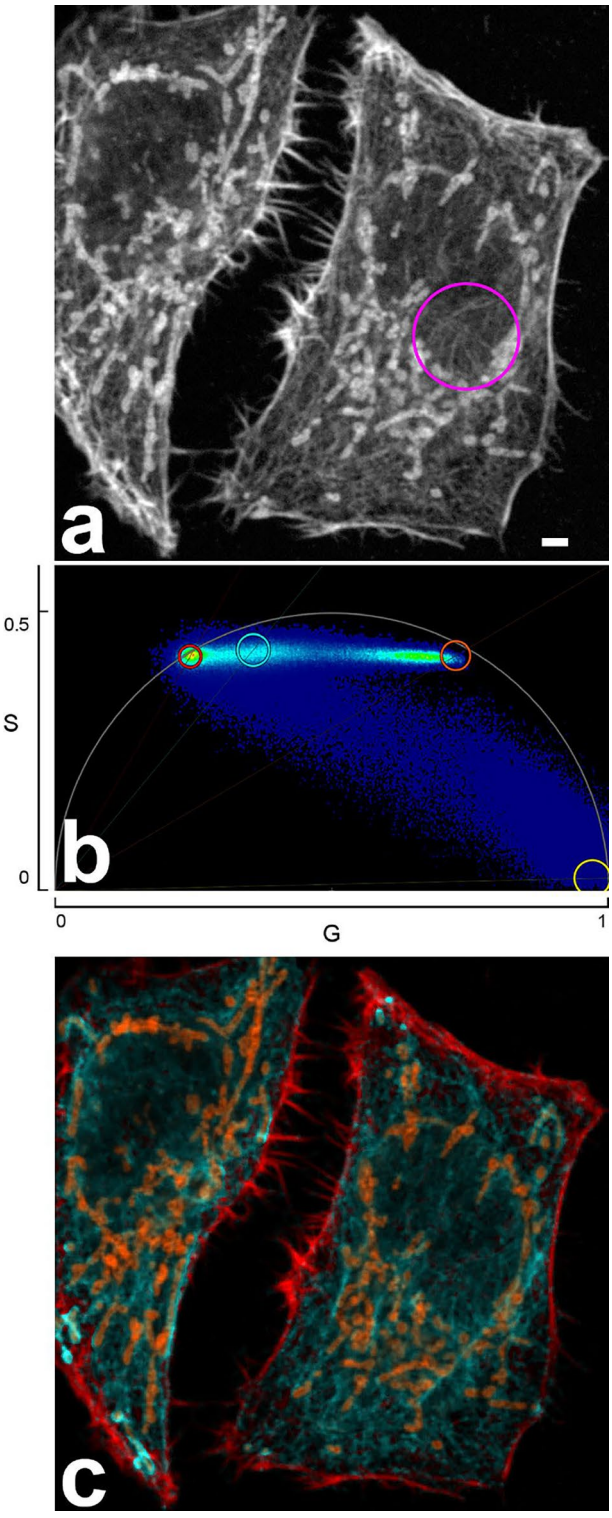

Figure 5. Three fluorochromes in the same spectral range with different lifetimes cannot be separated with high quality by the phasor approach. (**a**) Confocal raw image with Abberior STAR 635P labeled vimentin, Alexa Fluor Plus 647 labeled mitochondria and ATTO 647N labeled actin. Scale bar 2 µm. Magenta circle highlights some delicate vimentin fibers. (**b**) Phasor plot of this image. The lifetime components are indicated by circles: ATTO 647N-actin red, Abberior STAR 635P-vimentin cyan, Alexa Fluor 647-mitochondria orange. A background component (yellow circle) was also included for phasor separation to suppress noise. In pixels with a low photon count, noise from reflection and other sources will determine the average lifetime of the pixel, making it likely to be sorted with the background component. (**c**) Phasor separated image, same color code. Note the poor preservation of delicate vimentin fibers in the circle in (**a**). The respective pixels were not correctly assigned to the vimentin channel.

Plus 647 visualizing mitochondrial outer membrane, while the actin cytoskeleton was delineated by phalloidin-ATTO 647N (Fig. 5a). Vimentin, mitochondria and actin filaments form longitudinal structures that cross each other within a cell. Although the lifetimes of these dyes were quite different (Tau = 2.0, 1.2, and 3.5 ns, respectively), already in confocal images it turned out that three dyes could not be separated satisfactory by our current phasor approach (Fig. 5b,c). While some components were split up correctly into the respective channels, finer details got lost and possibly misallocated. For many image pixels it was impossible to distinguish whether their signals and average lifetime were made up by the dye with the intermediate lifetime, or by a mixture of the long and short lifetime dyes or both (Fig. 5b).

A separation of three (Fig. 5c) or even more currently available dyes might be successfully performed when a certain amount of crosstalk can be tolerated, or if differently labeled structures do not overlap in space. However, it does not appear to be an advisable strategy for subcellular high resolution colocalization studies. In such studies, a successful separation of a third dye could potentially be possible if it had a very different pattern in the phasor plot, e.g. with a lifetime of over 10 ns. Then three or four fluorochromes might be arranged in a triangle or trapezoid in the phasor plot, not a line. This was shown for unusual, monoexponential dyes in solution[29] and for autofluorescence and Second Harmonic Generation of Collagen[30]. However, typical commercial fluorochromes have a lifetime below 4 ns and are thus relatively close to each other in the phasor plot.

3D-stacks and fluorescence lifetime. We investigated whether our FLIM-STED approach can be applied to record 3D-stacks of images. We found that measured lifetimes change within the stack when moving from coverslip to deeper sample regions. A strong decrease of the average pixel lifetime towards the coverslip was found for CF680R-labeled nuclear pores, where we could not suppress reflection of the excitation beam with a suitable notch filter. The explanation that reflection was key in this case was supported by the observation that for CF680R-labeled nuclear pores the effect was also observed in confocal images. Since lifetimes were evaluated pixel-wise and reflected photons have a lifetime of zero, photons reflected at the coverslip surface shift the average lifetime of a pixel to smaller values.

No lifetime shift in confocal images located towards the coverslip surface was observed for near red and far red dyes, where notch filters were available to suppress reflection. Still, in STED images lifetimes changed with distance to the coverslip (Fig. 6). We assume that differences in the refractive index between coverslip and mounting medium and/or increasing refractive index mismatch with increasing depth induced shape changes of the depletion donut, thus causing the observed effect. The effect was large enough that phasor based lifetime separation would have to be performed for each z-position separately, rendering 3D recordings difficult.

Estimate of resolution improvement. In the five color STED images, all five labeled targets showed substantial resolution improvement when visually compared to confocal images (Fig. 1). To obtain an estimate of resolution improvement, we applied Fourier ring correlation (FRC) to matching STED and confocal images. FRC works unsupervised and is thus unbiased by selection of individual structures for analysis. A disadvantage is that image areas with no or no small structures will generate a low resolution value and thus skew the average value of an image to higher, worse resolution values that do not represent the best resolution achieved in an image. FRC, however, does allow an unbiased comparison of two conditions such as confocal and STED. Five confocal and five STED five-color image sets were analyzed (Supplemental Fig. 2). The average FRC-calculated resolution values for confocal images for the five different fluorochromes were between 276 and 305 nm. The corresponding average FRC values for STED were between 97 (WGA-CF594) and 136 nm (ATTO 647N, actin label), indicating a resolution improvement by a factor of ~ 2.5.

Crosstalk in 5 color FLIM-STED. For biological questions such as colocalization or non-colocalization of two proteins, it is important to assess how much of a given signal spills over to the neighboring channels and contaminates the obtained images, an effect known as crosstalk or bleed-through. In our study, 'neighboring' refers to spectral neighbors as well as to the two lifetime channels detected in one spectral channel. For the near red and far red spectral channel, we did not observe lifetime components from spectral neighbors in the phasor, suggesting limited spill-over.

We compared two channels by evaluating photon numbers in a region of interest (ROI) determined by thresholding of the whole image. The ROI had strong signals in the 'home' channel but no structure of the neighboring channel was present, e.g. a strong vimentin signal in the vimentin channel (home) but no mitochondrial signal in the mitochondrial channel (neighbor). For the given example, the ROI was obtained by creating a mask using a high threshold to the vimentin signal but subtracting a mask generated with a rather low threshold on the mitochondrial image, including high to low signals (low threshold; see "Methods" for details).

Sample preparations may have vastly different staining intensities in different channels. When comparing biological images, the spillover from neighbors should be set in relation to signal intensity to determine whether the spillover is problematic or not. To this regard, we calculated a "contribution" value in which bleed-through is normalized by the relative staining intensities of the signals in both channels (see "Methods"). Contribution may hence be reduced by changes to the staining procedure, such as different antibody concentrations or switching labels for individual cellular targets.

To determine which amount of crosstalk can be expected in purely spectrally separated color channels, we first analyzed a STED experiment with only three, spectrally separated fluorochromes: Alexa Fluor 594 (vimentin), Abberior STAR 635P (mitochondria), and CF680R (nuclear pores) (Fig. 7a). Eleven image sets with three images each were evaluated (Fig. 7b). The average contribution was up to around 20%.

This evaluation also shows a clear limitation of the cross-talk determination in multi-color samples: the second highest value of 21.6% contribution was obtained for CF680R-labeled nuclear pore spillover into the

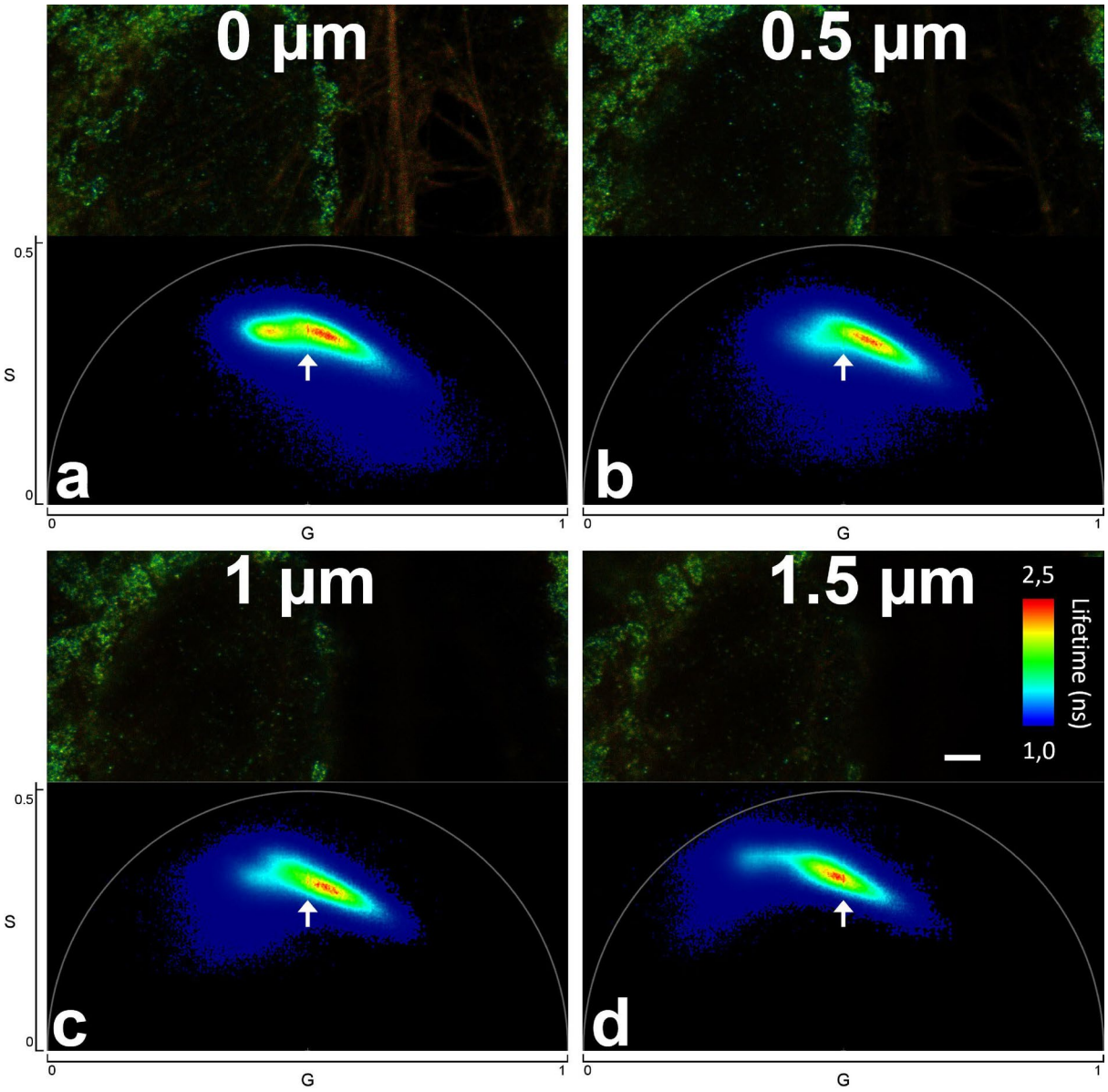

Figure 6. Fluorescence lifetime changes with distance to the coverslip. Parts of raw images of the far red channel from a five color sample at different sample depths (scale bar 2 µm) and their respective phasor plots. The color in the microscopic images codes the average lifetime of the pixels. (**a**) is near to the coverslip, (**b**–**d**) each 0.5 µm further into the sample. The arrows over the phasor plots always point to the same position. Near the coverslip in (**a**), ATTO 647N labeled phalloidin produces a separate peak to the left in phasor plot that dwindles further into the sample due to the reduced amount of actin at higher sample depths. Note the movement of the Abberior STAR 635P contribution in the phasor plot (major peak) relative to the arrow.

Alexa Fluor 594-labeled vimentin channel. Clearly, strong spillover of CF680R into the near red channel is physically impossible and the observed phenomenon is due to biological overlap of the two structures. The brightest nuclear pore signal at the edge of the nuclei is in close proximity of a strong component of the vimentin around the nucleus. Despite the measures described above, such effects cannot be excluded in biological samples. All values are therefore an upper estimate. Actual crosstalk will be equal to or less than the obtained values. Other average contribution values ranged from 9.4 to 22.5% (Fig. 7b).

In five color FLIM-STED images described above (Fig. 1a), average contribution values from 21 image sets were between 1.7 and 14.9% (Fig. 8). Notably, the distributions of the four contributions between lifetime separated channels from the same spectral channel (Abberior STAR 635P-labeled mitochondria versus ATTO 647N-labeled phalloidin-actin and CF594-labeled WGA staining versus Alexa Fluor 594 labeled vimentin) were well within the range for contributions between spectrally separated channels (Fig. 8). Again, the highest contribution mean value was obtained for CF680R-labeled nuclear pore contribution into Alexa Fluor 594-labeled vimentin. As above, we contribute this solely to biological overlap, not to physical spillover of photons to the near red channel. We conclude that crosstalk between lifetime separated images is well within the range of crosstalk

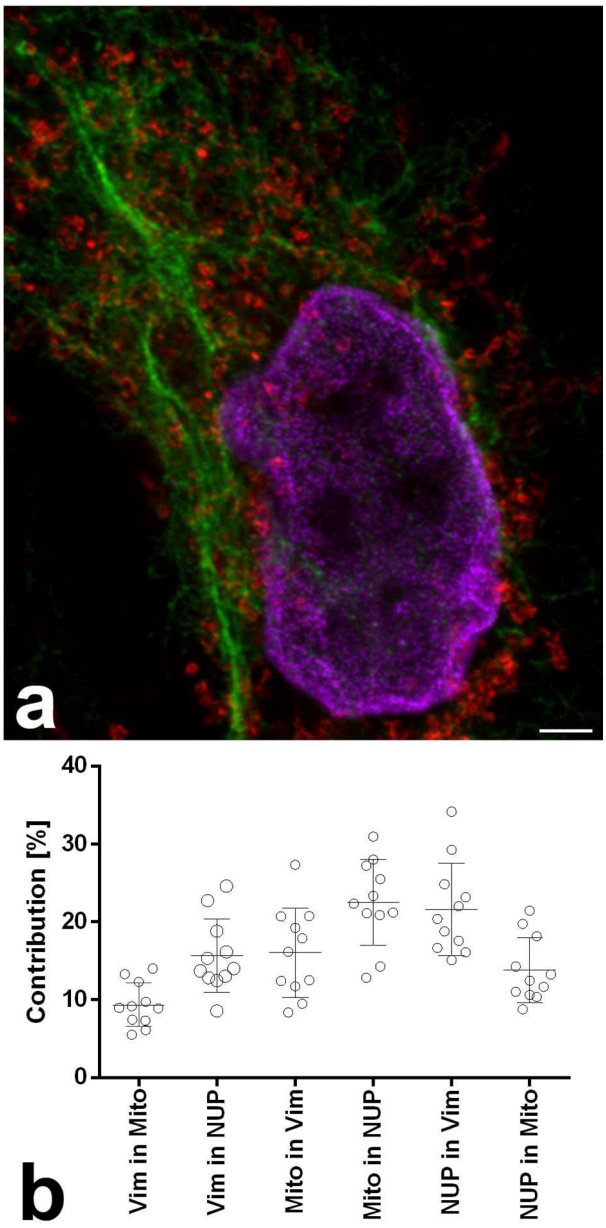

Figure 7. STED with three spectrally separated colors and corresponding crosstalk to other channels. (**a**) Example color overlay of the three channels. Vimentin Alexa Fluor 594 (green), mitochondria Abberior STAR 635P (red), and nuclear pores CF680R (magenta). Scale bar 2 µm. (**b**) Contribution chart, n = 11 image sets.

between spectrally separated channels. Non-normalized bleed-through values and an example are shown in Supplemental Figs. 3 and 4, respectively.

Discussion

We here show that two fluorochromes per spectral channel can be separated in STED and confocal microscopy if their lifetime is sufficiently different. Exploring this, we generated multi-color FLIM-STED images with five colors from three spectral channels, all depleted with 775 nm laser light. We also demonstrate that a fourth spectral channel can be used with 775 nm depletion. Provided two fluorochromes with suitable lifetimes could be identified for each of those spectral channels, eight color STED with a single depletion line would be possible. Long stokes shift dyes with excitation around 500 nm or less, but emission in the red spectral range, might further increase the number of distinguishable labels for a single depletion wavelength.

Already with five colors, we had difficulties to find independent labeling pathways. Typically, labeling of cellular targets occurs with primary antibodies from mouse or rabbit and then secondary antibodies from goat or donkey, which are labeled with the fluorochrome of choice. For some targets, primary antibodies from different animals such as chicken, hamster or rat are available, but these are rare compared to the wealth of rabbit and mouse primaries.

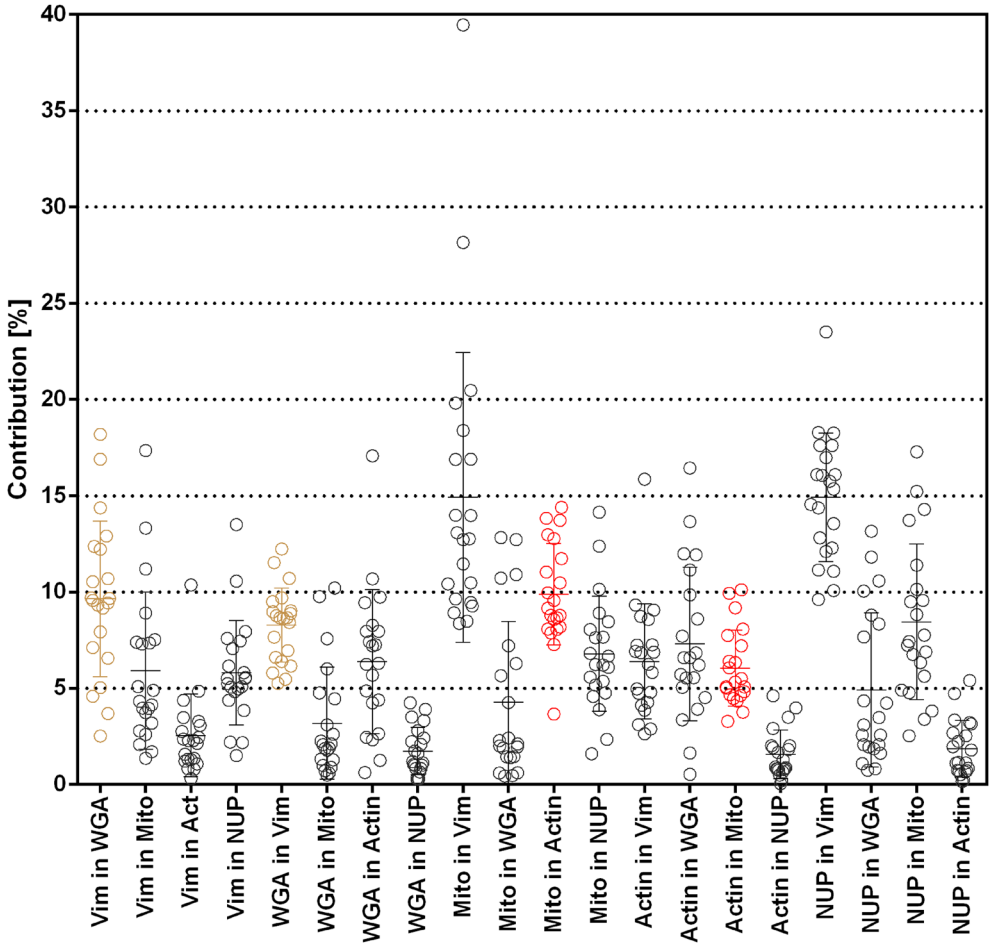

Figure 8. Contribution values for spectrally and lifetime separated signals in five color FLIM-STED images, n = 21 image sets. Channels generated by phasor separation from the same raw images are shown in the same color, all others in black. Note that "contribution" is normalized to signal intensities (see "Methods"). The non-normalized bleed-through is shown in Supplemental Fig. 3.

With sufficient budget and experience, primary antibodies could be directly labeled with the desired fluorochrome thus avoiding the problem of limited numbers of species. From a theoretical point of view, this is also desirable since it decreases the distance from the fluorochrome to the actual target, potentially improving the achievable resolution. However, it also decreases signal intensity since several polyclonal secondary antibodies can bind to one primary, multiplying the number of fluorochrome molecules.

Exploiting monoclonal primaries and subtype specific secondary antibodies would increase the number of labeling options. In our study we had to resort to polyclonal commercial secondary antibodies conjugated to fluorochromes, limiting the number of targets we could detect with antibodies from a certain host species to one. We used mouse, rabbit and chicken primaries detected with secondaries from a goat or donkey. These were supplemented with fluorochrome labeled molecules binding directly to cellular targets: WGA-CF594, phalloidin coupled to ATTO 647N or Abberior STAR 635P or SPY555-actin.

Apart from the problem of antibody labeling strategies, it is obvious that the fluorochromes that were available to us were not perfect for lifetime separation in STED imaging. Our choices were in particular limited when it came to antibody labels since the two photostable dyes we used in the far red channel, Abberior STAR 635P and ATTO 647N, have more similar lifetimes when coupled to antibodies. We could separate Alexa Fluor 647 and ATTO 647N antibody labeled signals in STED (unpublished), however, during STED acquisition Alexa Fluor 647 bleached dramatically in our samples.

We hope that the possibilities of multi-color FLIM-STED and multi-color FLIM confocal microscopy, together with the advent of respective equipment in many labs, will increase the importance that fluorochrome developers will grant to the lifetime of their dyes and influence future developments accordingly. In general, dyes with a very short lifetime < 1 ns will be poor STED dyes, since they will emit a large part of their fluorescence before the depletion effect can take place. Photostable dye pairs with lifetimes above 1 ns and a difference in lifetime of 1 ns or more would be promising candidates, e.g. one lifetime between 1 and 2 ns and one lifetime above 3 ns when coupled to antibodies. Due to our limited resources, we were not able to test further commercially available dyes and it is quite possible that some of them constitute good FLIM-STED pairs when conjugated to antibodies.

For the life science researcher who needs only two or three colors for a STED experiment, it appears to be easiest to use spectrally separable dyes with little spectral crosstalk such as CF680R, Abberior STAR 635P and either CF594 or Alexa Fluor 594. SPY555-actin could be used in combination with those fluorochromes. When additional structures need to be labeled, FLIM-STED provides an avenue to extend the number of distinguishable fluorochromes. Even with three or fewer fluorochromes when no lifetime separation is required, FLIM can improve STED resolution: the depletion laser extinguishes long lifetimes in the donut crest area, and the remaining fluorescence from this area can be filtered out based on its short lifetime[27,31]. A principle we applied here on FLIM-STED images.

Methods

Cell culture and fluorescence stainings. HeLa-Kyoto cells were kindly provided by Sandra Hake (now Institute for Genetics, Justus-Liebig-Universität Gießen). Cells were passaged twice per week in Dulbecco's Modified Eagle Medium (DMEM) high glucose, supplemented with Penicillin and Streptomycin and 10% fetal calf serum and grown in an incubator at 37 °C with 5%CO_2. For microscopy, cells were grown on uncoated 15 mm diameter high precision coverslips (170 µm ± 5–10 µm (Marienfeld Superior, Paul Marienfeld GmbH, Lauda-Königshofen,Germany, or Hecht Assistant, Glaswarenfabrik Karl Hecht GmbH, Sondheim vor der Rhön, Germany)) in a 10 cm Petri dish for 24 h.

Live cells staining with wheat germ agglutinin (WGA) CF594 conjugate (Biotium, 29,023–1, Stock 1 mg/ml in H2O, diluted 1:500 in medium) was performed for 10 min in the incubator. Prestained cells were washed twice in PBS. All specimens were fixed with 4% formaldehyde in PBS made from a methanol-free 16% stock solution (Thermo Fisher Scientific, # 28908). Washing and fixing solutions were prewarmed to 37 °C but the 10 min fixation period was at room temperature. Fixed samples were stored in PBS at 4 °C until usage. WGA would stain internal membranes and nuclear pores in fixed cells, and sometimes had a tendency to redistribute to those targets after live cell staining during subsequent antibody incubations. WGA thus gave variable results in different samples.

Permeabilization was on ice with PBS/0.25% Triton X-100 for 6 min followed by washing in PBS and incubation for 30 min at room temperature in blocking solution, PBS/5% heat inactivated normal goat serum or bovine serum albumin. Primary antibodies were diluted in blocking solution and incubated either over night at 4 °C or for 45–60 min at 37 °C in a humid chamber. Following three washes with PBS/0.1% Triton X-100, coverslips were rinsed in PBS and incubated with secondary antibodies diluted in blocking solution in a humid chamber for 90 min at room temperature or for 45–60 min at 37 °C. Three washes in PBS/0.1% Triton X-100 followed. Staining with phalloidin was after a postfixation step with 1% formaldehyde in PBS for 10 min for 45 min at room temperature and followed by another postfixation step, followed by 3 washes with PBS. Coverslips with stained cells were mounted to a glass slide with 7 µl Fluoromount-G (Invitrogen, 00-4958-02). They were sealed with nail polish within 10 min after mounting. Air drying of the cells was carefully avoided during the whole procedure.

Antibodies and fluorophore conjugates. The following antibodies were used at the respective concentrations: Primary: Chicken IgY anti-vimentin polyclonal, Invitrogen, PA1-10003, 1:1000; rabbit anti-TOMM20 polyclonal, Sigma, HPA011562, 1:200; mouse anti-NUP107 monoclonal (39C7); Invitrogen, MA1-10031, 1:100. Secondary: Goat anti-chicken IgY (H + L) cross-adsorbed, Alexa Fluor Plus 594, polyclonal, Invitrogen Thermo Fisher A32759, 1:500-1–1000; goat anti-rabbit Abberior STAR 635P, polyclonal, Abberior, 2-0012-007-2, 1:200; Goat anti-rabbit IgG Alexa Fluor Plus 647, polyclonal, Invitrogen Thermo Fisher, A32733, 1:200; Goat anti-mouse IgG ATTO 647N polyclonal, Rockland 610-156-121S, 1:50; donkey anti-mouse IgG CF680R, polyclonal, Sigma-Aldrich, SAB4600207, 1:200. Phalloidin ATTO 647N conjugate, ATTO-TEC, AD 647 N-81, 1:2000; Abberior STAR 635P phalloidin, Abberior 2-0205-007-0, 20 µg dissolved in 1.77 ml Methanol and diluted 1:400.

Microscopy. Images were recorded at the Core Facility Bioimaging of the Biomedical center, LMU München. STED was performed on a TCS SP8 WLL STED 3X FALCON from Leica Microsystems CMS, Mannheim, Germany with a 100 × 1.4 oil immersion "STED white" objective and SMD hybrid photodetectors. The white light laser allowed to pick any wavelength between 470 and 670 nm for excitation. It was pulsed at 80 MHz with a pulse width of 200 ps. To minimize crosstalk, color channels were recorded in frame sequential mode. A 2D-STED donut was applied, originating from a 775 nm 80 MHz Laser with 650 ps pulse width. Pulse delay between the two lasers was set to 200 ps. Typical STED images were recorded with 21—26 nm pixel size at 400 Hz e.g. for Fig. 1 with 1552 × 1552 pixels with a pixel dwell time of 1.04 µs and a pinhole of 0.93 AU@580 nm. 20 times accumulation for confocal and 100 times accumulation for STED was applied, except for z-stacks (Fig. 6) where 40 accumulations were used for STED. Relative laser intensities were typically 9% at 594 nm excitation (~ 36 µW) with 30% STED power (~ 102 mW), 12% @ 633 (~ 55 µW) with 15% STED (~ 50 mW), and 10% @ 670 (~ 38 µW) with 10% STED (34 mW). Absolute values were extrapolated from measurements with a power meter with a 10 × 0.3 air objective and 100% laser power. Recording of a STED image with 1552 × 1552 pixels and all three spectral ranges with 100 accumulations each took about 13 min. No drift was observed during the acquisition.

Samples for which only confocal FLIM images were taken were recorded on a Leica TCS SP8 WLL MP DIVE Falcon (funded by the Deutsche Forschungsgemeinschaft, INST 86/1909-1). For images with 685 nm excitation, a STELLARIS 8 STED FALCON system was kindly made available by Leica Microsystems at their demo labs in Mannheim, Germany.

Phasor based lifetime separation. Each pixel from the microscopic image is represented by a single dot in the phasor plot, positioned according to its average lifetime. Areas in the plot where dots accumulate are

rainbow color coded with blue for low occurrence to red for high accumulation of dots. Lifetime is an intrinsic characteristic of every dye in a given environment, leading to a specific phasor pattern. For an image with two fluorochromes with different lifetimes the phasor plot will typically reveal three scenarios: (1) pixels containing only the shorter lifetime dye, (2) pixels containing only the longer lifetime dye and (3) pixels containing a mixture of both. Phasor plot location of pixels containing only one dye will correspond to the location obtained with single stained samples. Pixels with a mixture of both dyes will be located along a line between the patterns of the individual dyes. Their position will depend on the mix of the components from both dyes. This is where the "linear property" of the phasor is powerful: the ratio of the linear combination determines for each image pixel the fraction of the components of the two dyes.

The Leica LAS X software version 4.1.1.23273 (Stellaris) was used for phasor analysis on a separate workstation post acquisition. Using the tools provided in the software, areas identified to contain the phasor pattern of single dyes were selected, and a linear separation was done by the software using the linear property of the phasor plot. In this software, the references for the separation are the center of circles which are defined by clicking on the phasor plot. The radius of the cursor has no effect on the analysis. A different strategy was applied to images of nuclear pores labeled with CF680R, to suppress ATTO 647N bleed-through, reflection, and the anti-Stokes excitation by the depletion laser. A phasor based filter was applied called Tau STED in the software (see below). This was possible since only one color needed to be extracted. As shown in Fig. 1h, a zero intensity ruler of triangular shape was placed both on the reflection (bottom right corner of the phasor plot) and ATTO 647N bleed-through pattern (center left angle) to filter them, to only keep the CF680R signal. Images were subsequently saved and exported. As a result, a separate image for each labeled structure was obtained. Obviously, a reasonable lifetime separation of two labels is possible only if their lifetime is sufficiently different, resulting in sufficiently distanced phasor plot distributions.

Tau STED applies filtering of pixels based on their phasor signature instead of discarding an arbitrary part of the photons in the whole image as in gated STED[27,28] or SPLIT-STED which uses a continuous depletion laser [31]. Background from laser reflection and autofluorescence with typically short lifetimes and low resolution photons coming from dye molecules that emitted before being depleted by the STED laser can be filtered out, while keeping as much information as possible. Within the STED depletion pattern, a diffraction-limited doughnut, intensity is not equally distributed. Since depletion results in a shorter average lifetime of the remaining fluorescence[28], a certain lifetime distribution is created from the uneven distribution of the depletion laser intensity. This distribution determines the STED trajectory in the phasor plot. Once this STED trajectory is established, it is possible to distinguish photons that are a result of the STED process from any other photon contributions. The photon contributions not correlated to the STED trajectory can be tagged as noise and thus be separated from the signal of interest, as explained above. Based on the characteristics of the fluorochrome undergoing STED, a filter can be applied to single out long lifetime signals within the STED trajectory that more likely originate from the donut center and thereby contribute to a highly resolved image. This solves the problems of reflection and low resolution photons (short lifetimes) and crosstalk (different behavior of different dyes) that can be seen in typical STED multicolor experiments. The accuracy of such determination, as in all lifetime-based approaches, is photon budget dependent.

The low photon numbers typical for STED images are an additional challenge even in the phasor approach. Typical filtering strategies to improve phasor cloud accuracy often fail in these regimes. The use of a complex wavelet filter[32] both within Tau STED and the phasor separation described above allow to work on the typical STED imaging regimes without a need to further increase the available photons.

The lifetime of fluorochromes was determined by interactively selecting the most intense spot of the corresponding phasor signature (pixel cloud in the phasor) and reading the lifetime from the software display. This interactive procedure was surprisingly reproducible: When three different operators selected the center of a cloud, the obtained values differed only in the second decimal place (delta < 0.033 ns; n = 5). Since we only give the first decimal place in this article, this value can be regarded as robust. The lifetimes of the dyes in the five color FLIM-STED experiment were determined on a phasor overlay of ten image sets, to avoid chance results in single images.

No deconvolution was applied, since deconvolution algorithms assume a Gaussian distribution of noise. Such a distribution cannot be assumed as a given, after phasor based separation of fluorochromes. Further resolution increase might be achieved if adapted deconvolution algorithms were available.

Only linear intensity adjustments were applied to images presented in figures.

Fourier ring correlation. The Fiji-Plugin NanoJ-SQUIRREL[33] was used for Fourier ring correlation. Complete FLIM-separated images were analyzed, without creating subregions (one block per image). Confocal and STED images were from the exact same sample region, recorded directly after each other and matched in pixel size.

Crosstalk analysis. This analysis was performed in Fiji[34] version 1.53f51 and Microsoft Excel. For each set of five images generated by phasor separation (or of three images with the three color experiment), first a common region for background measurement was identified which contained no structures. In each of the channels, the respective average background value was subtracted from the original image, leading to the background corrected image (bgc-image). Only then further analysis was performed, to avoid that results would be influenced by different background intensities in different channels.

In multi-color samples it is difficult to accurately quantify crosstalk, since a spatial overlap of differently labeled biological structures, like two crossing filaments, might falsely be interpreted as channel crosstalk. With such samples, it is therefore advisable to focus on areas in which one structure is strongly labeled but no structures

of the labels in other channels are present. To achieve this, for each of the channels, a high threshold was applied to the complete bgc-image such that only intense signals were above it, creating a mask. Often this threshold was near the 97th-intensity percentile. Next, a low threshold was applied to the bgc-image such that all signals from the structures that were supposed to be in that image were above it. It was typically between the 50 and 70 percentile. All images within a set were compared pairwise: to determine crosstalk from a 'home channel' to a 'neighboring channel', the high threshold mask from the home channel was taken and the low threshold mask from the neighboring channel was subtracted. For the remaining region of interest (ROI), intensity was measured in both channels and the mean value exported in a csv file.

Bleed-through of the home channel into the neighboring channel was determined in Microsoft Excel as intensity in the ROI in the neighboring channel divided by the intensity in the ROI in the home channel (Supplemental Figs. 3 and 4). To obtain the contribution value (Figs. 7b and 8), the bleed-through value was normalized by multiplication with the ratio (home/neighbor) of the 99th intensity percentiles of the whole images. A desirable low "contribution" can accordingly be achieved either by low bleed-through or by high intensity of the home channel signal. Graphs, means and standard deviation values were produced in Graphpad Prism 6.01.

Data availability

Image data will be made available by the corresponding author on reasonable request.

Received: 13 April 2022; Accepted: 1 August 2022
Published online: 18 August 2022

References

1. Wegner, W. *et al.* In vivo mouse and live cell STED microscopy of neuronal actin plasticity using far-red emitting fluorescent proteins. *Sci. Rep.* **7**, 11781. https://doi.org/10.1038/s41598-017-11827-4 (2017).
2. Bückers, J., Wildanger, D., Vicidomini, G., Kastrup, L. & Hell, S. W. Simultaneous multi-lifetime multi-color STED imaging for colocalization analyses. *Opt. Express* **19**, 3130–3143. https://doi.org/10.1364/OE.19.003130 (2011).
3. Anselm, E., Thomae, A. W., Jeyaprakash, A. A. & Heun, P. Oligomerization of Drosophila Nucleoplasmin-Like Protein is required for its centromere localization. *Nucleic Acids Res.* **46**, 11274–11286. https://doi.org/10.1093/nar/gky988 (2018).
4. Sograte-Idrissi, S. *et al.* Circumvention of common labelling artefacts using secondary nanobodies. *Nanoscale* **12**, 10226–10239. https://doi.org/10.1039/d0nr00227e (2020).
5. Winter, F. R. *et al.* Multicolour nanoscopy of fixed and living cells with a single STED beam and hyperspectral detection. *Sci. Rep.* **7**, 46492. https://doi.org/10.1038/srep46492 (2017).
6. Wurm, C. A. *et al.* Novel red fluorophores with superior performance in STED microscopy. *Opt. Nanosc.* https://doi.org/10.1186/2192-2853-1-7 (2012).
7. Sednev, M. V., Belov, V. N. & Hell, S. W. Fluorescent dyes with large Stokes shifts for super-resolution optical microscopy of biological objects: A review. *Methods Appl. Fluoresc.* **3**, 042004. https://doi.org/10.1088/2050-6120/3/4/042004 (2015).
8. Butkevich, A. N. *et al.* Fluorescent rhodamines and fluorogenic carbopyronines for super-resolution STED microscopy in living cells. *Angew. Chem. Int. Ed. Engl.* **55**, 3290–3294. https://doi.org/10.1002/anie.201511018 (2016).
9. Rönnlund, D. *et al.* Multicolor fluorescence nanoscopy by photobleaching: Concept, verification, and its application to resolve selective storage of proteins in platelets. *ACS Nano* **8**, 4358–4365. https://doi.org/10.1021/nn406113m (2014).
10. Vicidomini, G., Moneron, G., Eggeling, C., Rittweger, E. & Hell, S. W. STED with wavelengths closer to the emission maximum. *Opt. Express* **20**, 5225–5236. https://doi.org/10.1364/OE.20.005225 (2012).
11. Chiu, L. D. *et al.* Protein expression guided chemical profiling of living cells by the simultaneous observation of Raman scattering and anti-Stokes fluorescence emission. *Sci. Rep.* **7**, 43569. https://doi.org/10.1038/srep43569 (2017).
12. Butkevich, A. N. *et al.* Photoactivatable fluorescent dyes with hydrophilic caging groups and their use in multicolor nanoscopy. *J. Am. Chem. Soc.* **143**, 18388–18393. https://doi.org/10.1021/jacs.1c09999 (2021).
13. Wang, Y. *et al.* Rapid sequential in situ multiplexing with DNA exchange imaging in neuronal cells and tissues. *Nano Lett.* **17**, 6131–6139. https://doi.org/10.1021/acs.nanolett.7b02716 (2017).
14. Beater, S., Holzmeister, P., Lalkens, B. & Tinnefeld, P. Simple and aberration-free 4color-STED-multiplexing by transient binding. *Opt. Express* **23**, 8630–8638. https://doi.org/10.1364/OE.23.008630 (2015).
15. Schueder, F. *et al.* Universal super-resolution multiplexing by DNA exchange. *Angew. Chem. Int. Ed. Engl.* **56**, 4052–4055. https://doi.org/10.1002/anie.201611729 (2017).
16. Niehörster, T. *et al.* Multi-target spectrally resolved fluorescence lifetime imaging microscopy. *Nat. Methods* **13**, 257–262. https://doi.org/10.1038/nmeth.3740 (2016).
17. Görlitz, F. *et al.* A STED microscope designed for routine biomedical applications. *Progress Electromagnet. Res.* **147**, 57–68 (2014).
18. Rohilla, S., Kramer, B., Koberling, F., Gregor, I. & Hocke, A. C. Multi-target immunofluorescence by separation of antibody cross-labelling via spectral-FLIM-FRET. *Sci. Rep.* **10**, 3820. https://doi.org/10.1038/s41598-020-60877-8 (2020).
19. Gonzalez Pisfil, M. *et al.* Triple-color STED nanoscopy: Sampling absorption spectra differences for efficient linear species unmixing. *J. Phys. Chem. B.* **125**, 5694–5705. https://doi.org/10.1021/acs.jpcb.0c11390 (2021).
20. Malacrida, L., Ranjit, S., Jameson, D. M. & Gratton, E. The phasor plot: A universal circle to advance fluorescence lifetime analysis and interpretation. *Annu. Rev. Biophys.* **50**, 575–593. https://doi.org/10.1146/annurev-biophys-062920-063631 (2021).
21. Digman, M. A., Caiolfa, V. R., Zamai, M. & Gratton, E. The phasor approach to fluorescence lifetime imaging analysis. *Biophys. J.* **94**, L14-16. https://doi.org/10.1529/biophysj.107.120154 (2008).
22. Redford, G. I. & Clegg, R. M. Polar plot representation for frequency-domain analysis of fluorescence lifetimes. *J. Fluoresc.* **15**, 805–815. https://doi.org/10.1007/s10895-005-2990-8 (2005).
23. Leray, A. *et al.* Quantitative comparison of polar approach versus fitting method in time domain FLIM image analysis. *Cytometry A* **79**, 149–158. https://doi.org/10.1002/cyto.a.20996 (2011).
24. Hiller, G. & Weber, K. Golgi detection in mitotic and interphase cells by antibodies to secreted galactosyltransferase. *Exp. Cell Res.* **142**, 85–94. https://doi.org/10.1016/0014-4827(82)90412-8 (1982).
25. Kramer, R. H. & Canellakis, E. S. The surface glycoproteins of the HeLa cell. Internalization of wheat germ agglutinin-receptors. *Biochim. Biophys. Acta* **551**, 328–348. https://doi.org/10.1016/0005-2736(89)90010-2 (1979).
26. Virtanen, I., Ekblom, P. & Laurila, P. Subcellular compartmentalization of saccharide moieties in cultured normal and malignant cells. *J. Cell Biol.* **85**, 429–434. https://doi.org/10.1083/jcb.85.2.429 (1980).
27. Vicidomini, G. *et al.* STED nanoscopy with time-gated detection: Theoretical and experimental aspects. *PLoS ONE* **8**, e54421. https://doi.org/10.1371/journal.pone.0054421 (2013).

28. Vicidomini, G. *et al.* Sharper low-power STED nanoscopy by time gating. *Nat. Methods* **8**, 571–573. https://doi.org/10.1038/nmeth.1624 (2011).
29. Vallmitjana, A. *et al.* Resolution of 4 components in the same pixel in FLIM images using the phasor approach. *Methods Appl. Fluoresc.* **8**, 035001. https://doi.org/10.1088/2050-6120/ab8570 (2020).
30. Ranjit, S. *et al.* Imaging fibrosis and separating collagens using second harmonic generation and phasor approach to fluorescence lifetime imaging. *Sci. Rep.* **5**, 13378. https://doi.org/10.1038/srep13378 (2015).
31. Lanzano, L. *et al.* Encoding and decoding spatio-temporal information for super-resolution microscopy. *Nat. Commun.* **6**, 6701. https://doi.org/10.1038/ncomms7701 (2015).
32. Wang, P. *et al.* Complex wavelet filter improves FLIM phasors for photon starved imaging experiments. *Biomed. Opt. Express* **12**, 3463–3473. https://doi.org/10.1364/BOE.420953 (2021).
33. Culley, S. *et al.* Quantitative mapping and minimization of super-resolution optical imaging artifacts. *Nat. Methods* **15**, 263–266. https://doi.org/10.1038/nmeth.4605 (2018).
34. Schindelin, J. *et al.* Fiji: An open-source platform for biological-image analysis. *Nat. Methods* **9**, 676–682. https://doi.org/10.1038/nmeth.2019 (2012).

Acknowledgements

We thank Luis Alvarez (Leica Microsystems, Mannheim, Germany) for providing access to a Leica STELLARIS system with 685 nm excitation and for helpful discussions. We thank the Deutsche Forschungsgemeinschaft for funding of a Leica SP8 FALCON system (INST 86/1909-1).

Author contributions

S.D. conceived the study, designed it with support from M.G.P. and A.T., and wrote the manuscript. B.B. and S.R. prepared samples and recorded images, supervised by A.T., M.G.P. and S.D. M.G.P. recorded images and performed the phasor based separation. I.N. developed the crosstalk-contribution Fiji macros supervised by S.D. All authors contributed to the final manuscript.

Funding

Open Access funding enabled and organized by Projekt DEAL.

Competing interests

The authors declare no competing interests.

Additional information

Supplementary Information The online version contains supplementary material available at https://doi.org/10.1038/s41598-022-17825-5.

Correspondence and requests for materials should be addressed to S.D.

Reprints and permissions information is available at www.nature.com/reprints.

Publisher's note Springer Nature remains neutral with regard to jurisdictional claims in published maps and institutional affiliations.

Tutorial

Mariano Gonzalez Pisfil and Steffen Dietzel*

Fluorochrome separation by fluorescence lifetime phasor analysis in confocal and STED microscopy

https://doi.org/10.1515/mim-2024-0022
Received November 11, 2024; accepted February 20, 2025;
published online March 7, 2025

Abstract: In fluorescence microscopy, discrimination of fluorochromes in multi-color labeling was originally based on the emission spectrum only, then on emission and distinct excitation wavelengths. With the advent of faster and easier to use fluorescence lifetime imaging microscope (FLIM) systems, an additional, third level of discriminating fluorochromes becomes feasible. In this tutorial, we describe how to separate two fluorochromes, one with shorter and one with longer fluorescence lifetime, in a single spectral channel. The separation is done with the help of a phasor diagram of the lifetime information. We applied the method on images made by confocal or stimulated emission depletion (FLIM-STED) microscopy but it is transferable to other FLIM methods. This approach works with considerable less photons than separation by curve fitting. Images can be recorded at speeds comparable to normal confocal or STED microscopy. One shown example has two spectral channels with two fluorochromes each, plus another neighboring color channel in which spectral bleed-through and reflection is corrected by lifetime properties. All fluorochromes as well as the hard- and software used are commercially available. Lifetime separation generally may double the number of fluorochromes that can be used in fluorescence microscopy.

Keywords: fluorescence lifetime imaging (FLIM); multi-color fluorescence microscopy; confocal; STED; phasor; time-correlated single-photon counting (TCSPC)

***Corresponding author: Steffen Dietzel**, Core Facility Bioimaging and Institut für Kardiovaskuläre Physiologie und Pathophysiologie, Biomedical Center, Ludwig-Maximilians-Universität München, 81252 Planegg-Martinsried, Germany; and Biomedical Center, Großhaderner Str. 9, 81252 Planegg-Martinsried, Germany, E-mail: dietzel@lmu.de.
https://orcid.org/0000-0001-5725-3242
Mariano Gonzalez Pisfil, Core Facility Bioimaging and Institut für Kardiovaskuläre Physiologie und Pathophysiologie, Biomedical Center, Ludwig-Maximilians-Universität München, 81252 Planegg-Martinsried, Germany; and Biomedical Center, Großhaderner Str. 9, 81252 Planegg-Martinsried, Germany

1 Introduction: multi-color fluorescence microscopy

Typically, the microscopist in the life sciences wants to find out where something is in relation to something else. To do so, at least two structures must be visible, ideally labelled with two clearly distinguishable dyes. Fluorescence microscopy has the advantage that labeled structures stand out above a dark background. Fluorochromes targeted to a structure of interest are a light source in the sample itself so that even small amounts of targets can be detected. Historically, the number of different targets that could be detected and distinguished from each other in a given sample was always technically limited by the number of fluorochromes that could be discriminated in a sample. Section 1.1 describes the steps in the development of multi-color fluorescence microscopy while Section 1.2 introduces separation of fluorochromes by phasor analysis of their lifetime.

1.1 Development of multi-color fluorescence microscopy

1.1.1 Level 1: fluorochrome discrimination only by emission

A first level of fluorochrome discrimination in multi-color fluorescence microscopy was achieved already in the first half of the 20th century. Staining with plant extracts or chemically produced dyes would, for example, distinguish fat and myelin sheaths or cell nuclei and plasma by their emission color [1]. At the time only UV-light was used for excitation, but the emission of various fluorochromes ranged from blue to red. The invention of immunofluorescence in 1942 [2] allowed in its further development to label virtually any structure of interest. It took another 15 years until the first experiment using two antibodies labeled with different fluorochromes was described [3], a distinction of two bacteria species: “By using the rhodamine B labeled antibody simultaneously with a different antibody labeled with fluorescein isocyanate, they were able to

differentiate between two organisms of unlike antigenic composition in the same smear preparation, one organism appearing red-orange and the other yellow-green when viewed in the ultraviolet microscope" [4]. The term ultraviolet microscope again points to UV excitation of all dyes.

1.1.2 Level 2: fluorochrome discrimination by excitation and emission

Johan Sebastiaan Ploem's work on dichroic mirrors in the 1960ies [5], [6] led to the development of epifluorescence microscopes with quickly exchangeable filter cubes, one for each color channel. From 1974 on Ernst Leitz GmbH produced the PLOEMOPAK 2 for four filter cubes in a rotatable turret, each cube containing a dichroic mirror, excitation and emission filter [7], a design that is, with more cubes, essentially still in use today.

A second level of color separation was reached since every color channel now not only had a distinct emission range but also a distinct excitation. The new microscopes allowed to selectively excite orange-red fluorochromes such as TRITC with green light, avoiding simultaneous excitation and bleed-through of the green FITC [8]. A review from 1989 stated that fluorescence microscopes now generally came with filters for green and red fluorescence [9].

By technical refinements, in 1996 six spectrally separable fluorochromes could be used in fluorescence *in situ* hybridization (FISH) experiments detected with widefield fluorescence microscopy (Dapi, FITC, Cy3, Cy3.5, Cy5, Cy7; [10], [11]), a number that was increased to eight shortly after with DEAC (cyan) and Cy5.5 in addition to the above [12] (overview in Ref. [13]).

1.1.3 Level 1 and 2 in confocal microscopy

Confocal microscopes provide better contrast than "normal" or widefield fluorescence microscopes. In the 1980ies and early 1990ies, however, they were limited in excitation lines. Thus level-1-type two-color confocal microscopy with a single excitation line was an option, again the fluorochromes distinguished only by emission [14], as half a century earlier in widefield fluorescence microscopy. Post-acquisition cross-talk compensation was advised. Using separate laser lines was considered preferable though and had been demonstrated in the early 1990ies for two colors with Argon (488 nm) and Helium–Neon-Lasers (543 or 633 nm) or with an Argon–Krypton laser (488, 567 and 647 nm) and using three lines was considered desirable and technically feasible [14]. Thus, confocals soon reached level 2 multicolor fluorescence microscopy. In the late 1990ies, indeed confocals typically had 3 excitation wavelengths. The number of laser lines and thus spectrally separated fluorescent channels kept increasing: In the early 2000s, a well-equipped confocal microscope could have five laser lines, 405, 488, 561, 594 and 633 nm [13]. Thus, including Dapi (405 exc.) five fluorochromes could be recorded without spectral bleed-through under ideal conditions.

More could be used if bleed-through in the original image was accepted and corrected by post acquisition cross-talk compensation, now called linear unmixing or spectral unmixing: If the number of fluorescent channels is as big or bigger than the number of fluorochromes, then the signal can be computationally moved to the channel "where it belongs", based on single fluorochrome controls ([15], reviewed in Ref. [16]). For example, Alexa 488 and Alexa 514 or Alexa 633 and Cy5 could be separated [13]. In flow cytometry this approach is still known as compensation [17].

Another decade later, due to a wider range of excitation laser lines towards longer wavelengths, even more fluorescence channels became available. With the 670 nm of a white light laser (WLL) in the Leica SP8, dyes such as Alexa 680 or CF680R can be excited. The WLL in its successor, the Leica Stellaris 8, allows excitation up to 790, opening up additional channels. Current confocal microscopes from other major suppliers can be equipped with single line lasers with 730 nm (Zeiss) or 730 and 785 nm (Nikon and Evident, formerly Olympus), according to their marketing material.

1.1.4 Fluorochrome recycling

To further increase the number of detectable targets, various approaches have been applied to erase fluorescent signals after recording and provide one or many additional rounds of labeling with the same fluorochromes as in round 1. ReFISH [18], DNA-PAINT [19] and other flow labeling approaches [20], as well as bleaching fluorochromes before addition of new labels [21], [22] are based on this concept (reviewed in Ref. [23]). A common disadvantage of these approaches is that no permanent samples can be generated and a certain time span will pass with each round before the new labels are ready for recording. While this concept theoretically raises the number of potential labels to infinity, from the view point of fluorescence microscopy we do not consider this concept as an additional level.

1.1.5 Level 3: fluorochrome discrimination by lifetime

Fluorochromes are distinguishable from each other not only by their spectral properties but also by their fluorescence

lifetime: the average time it takes upon excitation to emit the fluorescence photon [24], [25]. This allows for a third level of fluorochrome discrimination in multi-color fluorescence microscopy. For fluorochromes that are typically used in fluorescence microscopy, the lifetime is between 0.5 and 5 ns [25]–[28]. Fluorescence lifetime imaging (FLIM) was used for Förster Resonance Energy Transfer (FRET) [29] and environmental measurements such as local Calcium ion concentrations already in the 1990ies [30]. In 1992 also the potential of lifetime to discriminate between fluorochromes in confocal imaging was recognized [31] and later the same year fluorescence from a sample was separated in two images based on lifetime [32] in a proof of concept study. The two images were simply showing two time intervals, one below 0.9 ns showing mostly chlorophyll fluorescence and one above 0.9 ns showing mostly FITC fluorescence. Obviously, chlorophyll and FITC easily can be separated spectrally and indeed spectrally separated images were shown as control. Computational separation by curve fitting or phasor was beyond the technology of the time and clearly FITC fluorescence was also present in the short-lifetime-window.

To our knowledge the first computational separation by different lifetimes of dyes in the same color channel was published in 1999 [33]. It appears, however, that in the following two decades only very few reports showed separation of fluorescent species by lifetime into separate images [26], [34]–[37]. The advantage of a computational separation is that, highly simplified, those photons emitted from the longer lifetime dye in the first nanosecond are also assigned to the correct image. Not only fluorochromes, but also different components of the autofluorescence of skin were successfully separated [38].

1.2 Separating fluorochromes by lifetime phasor analysis

While lifetime separation was initially performed by curve fitting, the promotion of phasor based lifetime analysis [39] opened the possibility to apply this technique to separate fluorochromes with different lifetimes, an approach applied by several groups [28], [36], [40]–[43].

We initially got interested into color separation by lifetime because of constrains of STimulated Emission Depletion (STED) superresolution microscopy. In confocal microscopy, the excitation light in the focal plane is concentrated to a small, diffraction limited area. In STED a “donut” of depletion light is placed around the center of this area so that the fluorochromes in this depletion light are stimulated to emit at the depletion wavelength and not in the spectral region in which the fluorescent signal is recorded [44]. The wavelength of the depletion laser has to be within the emission spectrum of the fluorochrome used and for practical reasons, as to not spectrally overlap with the collected fluorescence, it should be towards the upper end of the emission spectrum. This fundamentally limits the number of spectrally separable fluorochromes that can be distinguished with a single depletion laser line. Additional depletion lasers can be implemented but this introduces two difficulties. First, the depletion lasers have to be aligned correctly down to a few nanometers to avoid chromatic mismatch in the superresolved images. Second, due to their strong power output, shorter wavelength depletion lasers will likely bleach longer wavelength fluorochromes so that the sample is destroyed during recording. Therefore, it is best if all colors can be recorded with a single depletion laser line.

This put the option to distinguish fluorochromes not only by color but also by lifetime in our focus. With this approach, we were able to image five fluorochromes with 775 nm depletion only. We separated CF594 and Alexa 594 in the near red channel, Abberrior Star 635P and ATTO647N in the far-red channel and recorded CF680R in an even longer wavelength channel [40]. We also showed separation of respective confocal images (Figure 1). In general, two fluorochromes can be distinguished in a color channel, provided their lifetime is sufficiently different. In this tutorial we describe how to perform lifetime separation with the help of the phasor diagram, an intuitive way to display the lifetime information of an image.

2 Materials and methods

2.1 Sample preparation

Fixation methods and staining protocols do not differ from normal immunostaining procedures and therefore are not described in detail.

2.1.1 Labelling

We performed antibody labeling of HeLa cells grown on coverslips with primary and secondary antibodies. With many targets this quickly gets complicated because most available primary antibodies are from rabbit or mouse and thus may limit the number of detectable antigens. Fluorescence labeling of primary antibodies by either fluorochrome conjugation or via preincubation with fluorochrome labeled nanobodies or similar approaches may alleviate this problem but we did not test this approach for lifetime color separation. Fluorochrome labeling of primary

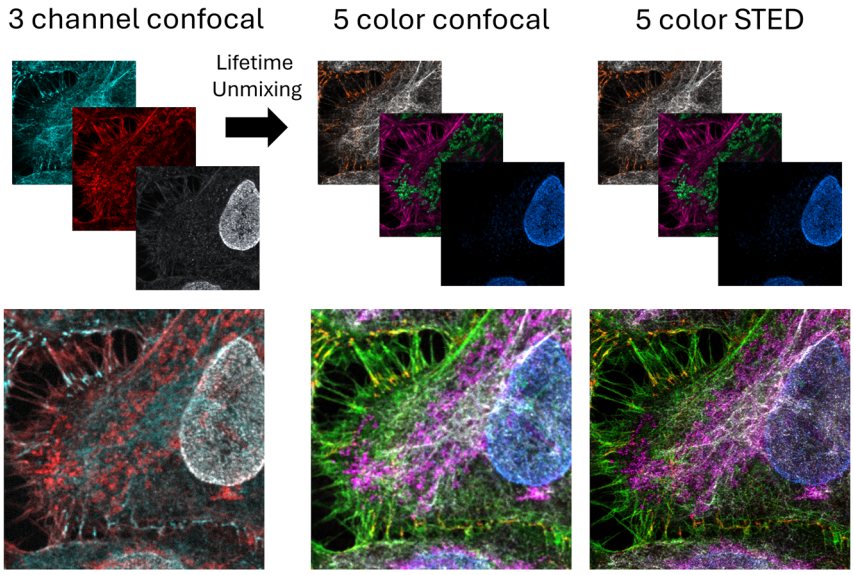

Figure 1: Summary showing how 5-color confocal and STED images were generated from 3 fluorescent channels with lifetime information. From each of the first two confocal channels, two lifetime images were extracted (not shown). Those grayscale images, each representing one fluorochrome, were pseudocolored with different hues, here orange (WGA CF594) and white (antibody detection of vimentin with Alexa Fluor Plus 594) or magenta (actin detected with phalloidin ATTO647N) and green (antibody detection of mitochondria with Abberior Star 635P). The third confocal channel (antibody detection of nuclear pores with CF670R) was cleared up from spectral bleed-through and noise using lifetime features to produce the image of the fifth fluorochrome (blue). The five images were then overlaid (bottom). The same procedure was applied to STED images, the 3 channel STED images are not shown.

antibodies may result in weaker signals since no amplification by a second layer takes place. Other staining methods such as fluorescence *in situ* hybridization (FISH) should also work, but again we have no experience with this.

For lifetime separation, we found that we can cleanly separate two fluorochromes per channel from each other, but not more [45], see Section 3.2 for detailed discussion. We were successful with the fluorochromes as listed in Table 1 in a five color sample (Figure 1). While the highest available excitation wavelength in our systems, 670 nm, that we used for CF680R also excites the dyes in the far-red channel (ATTO647N and AS635P), the lifetime of CF680R was short enough, so that it could be separated from the other fluorochromes by lifetime [40] (Figures 7 and 9).

Table 1: Fluorochromes and what they were attached to in the five color sample.

Channel	Label 1	Label 2
Near red	CF594-wheat germ agglutinin	Alexa Fluor Plus 594 goat-anti-chicken antibody
Far red	Abberior Star 635P goat-anti-rabbit antibody	ATTO-647N – Phalloidin
670 nm exc	CF680R-donkey-anti-mouse antibody	

Staining with WGA-CF594 (10 min; Biotium, 29023-1) was performed on live cells to limit the staining to the cell surface. Otherwise WGA also labels additional glycosylated proteins such as internal membrane proteins and nuclear pores. WGA sometimes redistributes during further steps, giving generally variable staining results. Fixation was for 10 min in 4 % formaldehyde in PBS. Air drying was carefully avoided at all times to preserve structural integrity. Postfixation with 1 % formaldehyde in PBS for 10 min was performed to minimize diffusion of fluorochromes in the sample [40]. Five color sample, primary antibodies: Chicken IgY anti-vimentin polyclonal (Invitrogen, PA1-10003, diluted 1:1,000 in Blocking solution); Rabbit anti-TOMM20 polyclonal (Sigma, HPA011562, 1:200); Mouse anti-NUP107 monoclonal (39C7) (Invitrogen, MA1-10031, 1:100). Fluorochrome coupled secondary antibodies: Goat anti-chicken IgY (H + L) cross-adsorbed, Alexa Fluor Plus 594, polyclonal, (Invitrogen Thermo Fisher A32759, 1:500–1:1,000); Goat anti-rabbit Abberior STAR 635P, polyclonal (Abberior, 2-0012-007-2, 1:200); Donkey anti-mouse IgG CF680R, polyclonal (Sigma-Aldrich, SAB4600207, 1:200). Staining with phalloidin ATTO647N conjugate (ATTO-TEC, AD 647N-81, 1:2,000) was after the secondary antibody. For further details see [40].

In confocal images Alexa Fluor Plus 647 could be well separated from ATTO647N (Figure 4) or Abberior Star 635P,

but in STED it bleached fast. For the two-color sample, phalloidin-ATTO647N and the primary anti-TOMM20 antibody were as above, the latter was detected with a polyclonal Alexa Fluor 647 Plus-labeled goat-anti-rabbit antibody (Invitrogen Thermo Fisher, A32733).

2.1.2 Good samples for microscopy

The mounting medium plays an important role in the optical path: most mounting media for slide-coverslip samples have a refraction index lower than coverslip glass. Therefore, spherical aberration is introduced into the optical path. With increasing distance from the coverslip this has an increasing negative impact not only on resolution but also on fluorescence intensity since the produced fluorescence photons are smeared over a larger volume rather than kept in a tight and therefore bright point spread function [46]. Therefore, wherever possible, the object of interest should be sitting on the cover slip and not on the glass slide.

Our samples were mounted in Fluoromount G (Invitrogen, 00-4958-02). This mounting medium does not harden and thus avoids shrinkage of the sample, an effect that is counterproductive for high resolution microscopy. We seal the samples around the edge of the coverslip with transparent nail polish.

The thickness of the coverslip should be 0.17 mm, as indicated on the barrel of most objectives. This is the thickness for which the optical correction of the objective is calculated. Deviations also cause spherical aberrations. Unfortunately, most coverslips are thinner than that. The widely spread “number 1” or “#1” thickness is 0.14–0.17 mm and thus usually too thin. Better options are #1.5 (0.16–0.18 mm) and #1.5H (0.165–0.175 mm). Hecht-Assistent, Marienfeld and others provide such coverslips.

2.1.3 The actual lifetimes of fluorochromes in a sample

The lifetimes of fluorochromes depend on their chemical structure but also on their environment. Some companies now provide the lifetime of their fluorochromes free in solution. This is an improvement but still merely a rough indicator what the lifetime will be in the final sample. The same fluorochrome can have different lifetimes depending on the binding partner such as antibodies or other molecules [26], [41]. A striking example are the lifetimes of ATTO647N and Abberior Star635P when bound to either antibodies or phalloidin, a molecule that binds to actin fibers. For both dyes, the lifetime changes with the binding partner so strongly that we could successfully separate the actin signal from the antibody target by lifetime, although only a single fluorochrome was used [40]. Lifetime is likely to be different in different mounting media. It also varies somewhat in repeated, similar lab experiments. In essence, the lifetime and the difference in lifetime for a given pair of fluorochromes to be separated in a given spectral channel must be confirmed under actual sample conditions.

2.1.4 Conditions for successful lifetime unmixing

We found that for separation by lifetime, a lifetime difference of 0.8 ns between two dyes (measured by confocal microscopy under actual sample conditions, see previous section) is sufficient for both, confocal and STED microscopy. With a difference of 0.8 ns separation typically works well even if the labeled targets show close proximity in space. In STED images, due to application of the STED beam the lifetime of a fluorochrome is significantly shortened. (The position in the phasor diagram shifts in direction of the lower right corner, see Section 2.3.1, Figures 2 and 3, compare Figure 6A and B). This means that for two dyes also the actual difference between the lifetimes is shorter than in confocal images. Therefore, in STED the required difference in lifetime measured by confocal FLIM is bigger than for separation in confocal images. Thus, for confocal microscopy differences smaller than 0.8 ns should be sufficient for successful separation, but we did not explore the limit. Since the actual lifetime in STED varies with the power of the depletion beam, no reasonable value can be given for a “Lifetime in STED”. All lifetime values given in this article were measured in the confocal mode.

2.2 Image recording

2.2.1 Microscopes

The imaging procedures in this protocol were established on two Leica Microsystems TCS SP8 WLL FALCON systems

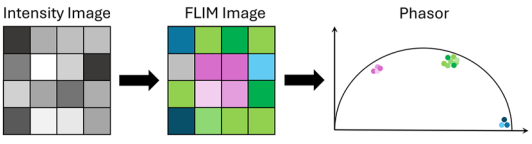

Figure 2: Schematic drawing showing the relationship between the intensity grayscale image (left), the FLIM image (center) and the phasor plot (right). With a lifetime capable microscope, in addition to the intensity image, the lifetime image can be recorded, where every pixel has an average lifetime value. From these values a phasor can be created. Pixels with similar long lifetimes (pink), similar intermediate lifetimes (green), and similar short lifetimes (blue) will form clusters on the phasor plot.

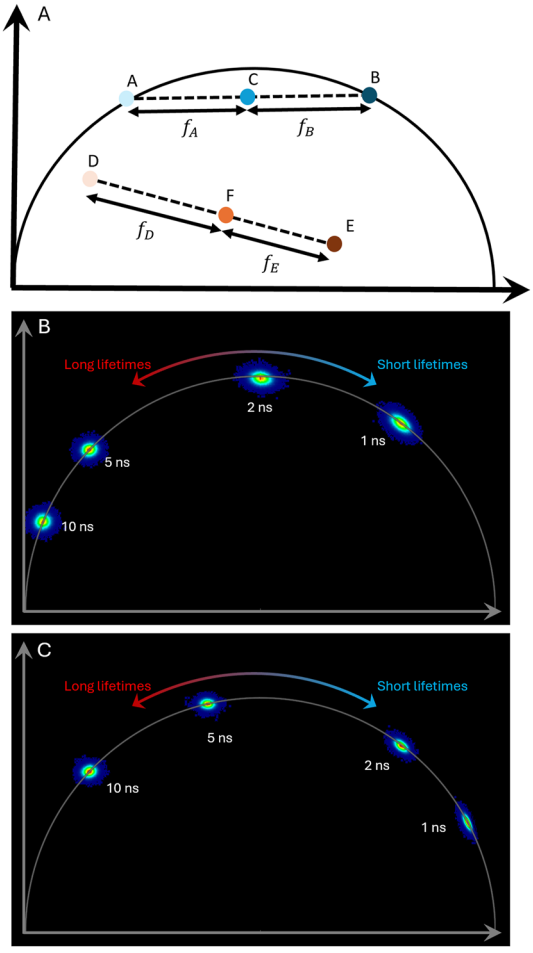

Figure 3: Phasor, behind the scenes. (A) Points A-C-B show the situation with two fluorochromes with different lifetimes, both with single exponential decay (points A and B). Pixels containing both fluorochromes will be positioned on the line between points A and B, for example at C. The length of fA and fB is directly related to the ratio of the two fluorochromes in the respective pixel. D-F-E show the respective situation when the two fluorochromes do not have a monoexponential decay. (B) Phasor plot with multiple monoexponential lifetimes (simulated data). Monoexponential lifetimes are located on the universal circle (semi-circle), with short lifetimes towards the right and long lifetimes towards the origin (left bottom corner). Multi-exponential lifetimes are located inside the circle. The scaling of lifetimes is not linear and depends on the repetition rate of the laser. This plot reflects the situation with 80 MHz repetition. The same distribution is achieved with 40 MHz and a harmonic setting of 2 (compare Figure 4E and F). (C) As in B, but with a repetition rate of 40 MHz (and no increase of the harmonic).

with linear scanning mode. These systems perform time-correlated single-photon counting (TCSPC) to determine fluorescence lifetimes. One, a mixed confocal and multi-photon setup, is based on an upright DM8. The other SP8 is based on an inverted DMi8 stand and has STED super resolution capabilities with a pulsed 775 nm depletion laser. We expect our fluorochrome separation approach to work with FLIM systems from other manufacturers as well but we did not have the opportunity to test it.

Our two systems have the following characteristics: A pulsed white light laser (WLL) allows to pick any wavelength between 470 and 670 nm for one-photon excitation. 80 MHz repetition rate with 200 ps pulse width. In confocal mode the repetition rate can be reduced to 40 or 20 MHz if desired. In STED mode the repetition rate is slaved to the 80 MHz of the depletion laser. Detection windows are spectrally freely definable with 1 nm steps due to the detectors being behind a prism. Single molecule detection hybrid photodetectors (“SMD-HyDs”) allow high single photon count rates due to short dead times. FLIM is also possible with “normal” HyDs, but SMD-HyDs are selected for low noise and allow higher count rates (1 count per pulse as opposed to 0.5 per pulse), according to the manufacturer. On the STED system, the STED donut originates from a 775 nm 80 MHz Laser with 650 ps pulse width. NA 1.4 Plan Apo oil immersion objectives were used, a 63× on the upright system and a 100× “STED white” objective on the STED system.

2.2.2 Imaging parameters for confocal and STED

2.2.2.1 Sequential recording and image settings

The two-color sample with Alexa Fluor 647 Plus and ATTO647N was recorded with excitation of 0.5 % laser power at 633 nm (≈3 µW at the sample plane), emission window 650–800 nm with two detectors in tandem at 650–668 nm and 668–800 nm. Two detectors in tandem allow to record twice as many photons per second without saturation compared to a single detector. Lower excitation power and a single detector would have worked but would have taken longer. Data from both detectors were combined to obtain a single intensity and FLIM image. We used a scan speed of 200 Hz (lines per second) and set the frame accumulation to 50 to obtain optimal image contrast, although fluorochrome separation is already possible with a single frame (Figure 4).

When selecting excitation wavelengths for neighboring channels care should be taken that a wavelength with a high excitation of the desired fluorochromes but a low excitation of spectrally neighboring fluorochromes is selected. For the five color confocal and STED sample (Figures 1, 6, and 7), three frame-sequential sequences were recorded to minimize spectral crosstalk in the following order (775 nm depletion only in STED mode):

1. exc. 5 % at 670 nm (≈17 µW)/em. 700–750 nm/775 nm STED at 5 % (≈17 mW)
2. exc. 6 % at 633 nm (≈28 µW)/em. 640–680 nm/775 nm STED at 20 % (≈68 mW)

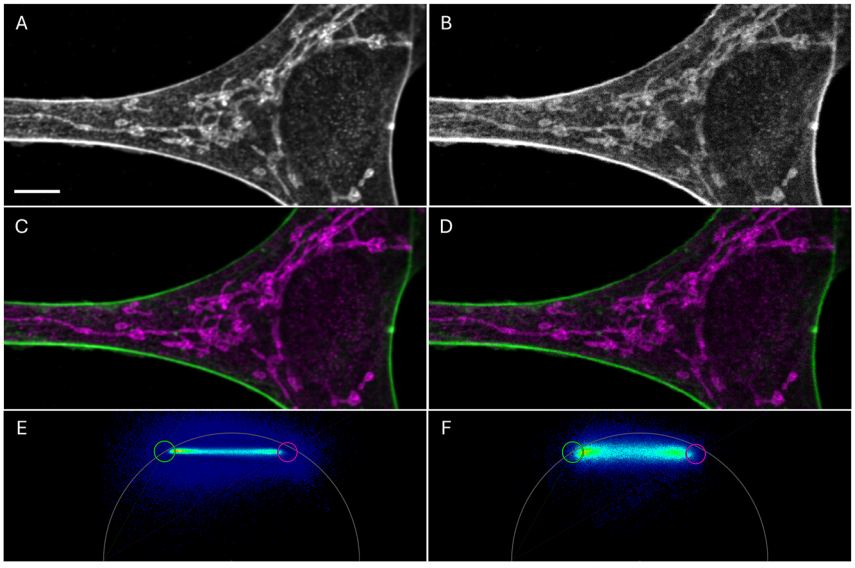

Figure 4: Confocal images of a cell labeled with ATTO647N-phalloidin (actin skeleton, green, lifetime 3.1 ns) and Alexa 647 Plus TOMM20 (mitochondria; magenta, lifetime 2.0 ns). The images were generated from 50 accumulated frames (A, C, E) or with just one frame (B, D, F). Note the signal to noise difference. (A–B) Intensity image with an average number of photons in the bright actin filaments of 7,500 in A and 120 in B and in the dimmer mitochondrial signals 2,500 in A, 60 in B. Scale bar 5 µm. (C–D) Actin and mitochondrial signals were separated in two grayscale images, false color coded and overlaid. (E–F) Phasor plot used for the color separation of C and D, respectively. Repetition rate was 40 MHz and the harmonic was set to 2, so the phasor plot appears like an 80 MHz phasor plot. Threshold values (see main text) were 100 and 1 photons, respectively. For circles see main text and next figure.

3. exc. 3 % at 594 nm (≈12 µW)/em. 600–630 nm/775 nm STED at 30 % (≈102 mW)

The sequences move from longest to shortest excitation wavelength to minimize bleaching. Particularly for STED recordings where the 775 nm depletion causes some anti-stokes excitation of the longer wavelength dyes this is important. If available use notch filters for every excitation and STED laser wavelength to minimize the contribution of reflection. Before recording, the fully integrated FLIM module must be started within the Leica software so that not only the intensity image but also the lifetime information is recorded.

For the examples above, we used a scan speed of 400 Hz (lines per second) for the five-color sample and 200 Hz for the two-color sample. With the respective software control, we set frame accumulation for confocal FLIM images to 20.

2.2.2.2 More frames for STED images

In STED we increased frame accumulation to 100. For truly point-like signals, both STED and confocal imaging should result in the same signal intensity (number of photons) when the beams are centered on the structure, because all of the signal originates from a point that is in the center of the STED donut anyway. For signals from extended structures such as fibers, however, depletion will reduce the signal intensity, because signal from neighboring parts of the structure is suppressed, the detection volume is smaller.

Other influences are introduced by the scanning process: In STED, pixels sizes are typically smaller, in our case linearly about 3× smaller. (∼25 nm, compared to ∼75 nm in confocal). If all other settings are kept the same this results in a ∼3× shorter pixel dwell time and thus 3× less photons per pixel. On the other hand, the scan lines are 3× closer together so that light from a given structure is recorded more often and thus additional photons are collected.

In practice, we observe that more frame accumulation is required in FLIM-STED compared to confocal images to detect a reasonable number of photons in pixels with signals.

2.2.2.3 Further parameters for a STED recording

To record STED images we typically apply the following additional parameters: Pinhole at 0.93 AU@580 nm. This helps to increase the Signal to Background ratio. Optimized pulse delay between the WLL and STED depletion laser was determined to be at 200 ps in our system. The correct delay timing is important to maximize the STED effect: If the depletion pulse comes too early it has no effect, if it comes too late, many photons are already emitted before depletion can occur. In both cases total signal will be brighter than in the optimal scenario. Hence, the timing can be optimized

for lowest intensity = strongest depletion. Pixel size was 21–26 nm. Image size will depend on zoom factor and number of pixels used.

With these parameters, recording of a STED image with 1,552 × 1,552 pixels and all three sequences with 100 accumulations each takes about 13 min.

2.2.2.4 Pulse rate in confocal images

For confocal imaging, the pulse rate can be reduced from 80 to 40 or 20 MHz. 80 MHz translate into one pulse every 12.5 ns. For fluorochromes with average lifetimes of several nanoseconds, a rather small but noticeable fraction of photons will thus be detected only after the next pulse (in the next cycle) and thus result in a measured lifetime that is slightly shorter than the actual lifetime. However, for separation purposes the exact measured lifetimes do not matter, the lifetimes of different fluorochromes just have to be different enough.

Reduced pulse rates also result in respectively less collected photons per second, increasing overall imaging time to reach the same image quality. For fluorochrome separation by lifetime, 40 or 80 MHz pulse rates deliver good results for many samples.

2.3 Image analysis: lifetime unmixing via phasor for confocal and STED images

2.3.1 Background: the phasor of lifetime images

A phasor diagram is a graphical representation of the lifetimes found in a given image in a polar plot, based on the sine-cosine transforms of frequency domain information. Thus, the phasor is also called “polar plot” by some authors [47], [48]. TCSPC provides time domain information however, so that a Fourier transformation is performed to obtain the frequency domain data. A description of phasors in FLIM and how they are mathematically generated can be found in Ref. [39]. In the following we explain how a phasor represents the FLIM image as a foundation for the lifetime separation in the next section.

In this section, the term “pixel” always refers to a pixel in the confocal or STED image (and not the phasor plot image). Each pixel is represented by a single dot in the phasor plot, positioned according to the average lifetimes of the present fluorochromes (Figures 2 and 3B, C). Lifetime is an intrinsic characteristic of every fluorochrome in a given environment, leading to a specific phasor pattern. In phasors from microscopic images, many pixels will be represented in neighboring positions in the phasor plot since they have similar lifetime components (Figure 4E and F). Areas in the plot where dots lie on top of each other are color coded. In our plots (from the Leica LAS X software) a rainbow color code with blue for low occurrence to red for high accumulation of dots is used.

For an image with two fluorochromes with different lifetimes a phasor plot will show three scenarios: pixels containing only the longer lifetime dye (region A or D in Figure 3A). Pixels containing only the shorter lifetime dye (Region B or E). And pixels containing a mixture of both (region C or F). Phasor plot locations of pixels containing only one dye will correspond to the location obtained with single stained samples. Pixels with a mixture of both dyes will be located along a line between the positions of the individual dyes. This is where the “linear property” of the phasor is powerful: The exact position of the pixel in the phasor is defined by the fraction of the components of the two dyes (Figure 3A, fA, and fB). Hence, from the position of the pixel in the phasor diagram, the percentages of its photons belonging to dye A and dye B can be extracted.

An advantage of the phasor plot is that, as opposed to curve fitting, for its generation there is no need to choose parameters from a range of possibilities such as the number of expected lifetime species. The phasor diagram is based only on mathematical calculations, no fitting is required: The same data will always generate the same phasor plot. Avoiding the fitting procedure which requires user input makes the technique more robust. Thus the phasor is a powerful tool for lifetime analysis with its robustness and ease of use among its biggest advantages.

2.3.2 Separation of fluorochromes by phasor analysis

Image analysis was performed with Leica LAS X software version 4.1.1.23273 which we installed on a separate computer. This is not the version that comes with the SP8 (LAS X 3.X) but the variant for the SP8 successor “Stellaris”. It contains an extended, user friendly suite of tools for phasor lifetime analysis. A “separate”-button makes unmixing procedures easier, compared to the 3.X version. We have trained users without previous FLIM experience and they became quickly autonomous for their lifetime analysis. LAS-X 4 installation files were kindly provided by Leica Microsystems CMS. License dongles appear to be compatible between the 3.X and 4.X versions.

2.3.2.1 Parameters

To achieve an acceptable phasor unmixing, as a rule of thumb at least 100 photons per pixel should be collected in those regions that contain fluorescence signal (Figure 4B and D). One can obtain results with dimmer images, but results may vary depending on other parameters, such as background and overlap between labelled structures.

An unfiltered phasor plot is generated using every pixel in the image: Pixels with only a few photons of background noise are also displayed and may confuse the clarity of the data presentation. They can be suppressed by estimating the background intensity (in number of photons) and entering this number as threshold in the software. Pixels with a photon number below threshold will then not be displayed in the phasor. This is recommended. In LAS X, there is a threshold menu in the phasor menu. The highest value that can be entered is 100 photons, typically we apply around 20–50.

STED images, including FLIM-STED images, typically have low photon numbers per pixel, leading to unfavorable signal-to-noise ratios that can impede the extraction of information from phasor data. To enhance data visualization and improve analysis and interpretation, filters can be applied to the image before calculating the phasor. Traditionally, median filters have been used in phasor analysis to tackle this issue. However, median filters degrade high spatial frequency FLIM information, particularly affecting edges of features, puncta, or any fine structures. We recommend using a wavelet filter instead, if available. Wavelet filtering preserves said features and is thus beneficial when working with low photon numbers [49].

The lifetime distribution and dynamic range of the phasor depends on the repetition rate of the pulsed laser used. The higher the repetition rate, the further to the left the positions for given lifetimes will move. Ideally, the lifetimes of a given image should be in the central range of the phasor because then the distance between different lifetimes will be largest. For lifetimes between 1 and 4 ns a repetition rate of 40 MHz or 80 MHz is well suitable (Figures 3B, C and 4E, F).

If for some reason an image has to be recorded with a rather low repetition rate, the phasor can be adjusted by applying a harmonic value of 2 or higher (see legend to Figure 4B). In a Fourier Transform, a periodic waveform can be decomposed into a series of sinusoidal waves. The fundamental frequency is the lowest frequency of the waveform, and the harmonics are the higher frequencies that are integer multiples of this fundamental frequency. Adjusting the harmonic number alters the harmonic wave that the respective lifetime is multiplied by. For very short lifetimes, the regions of interest on the phasor plot are situated in

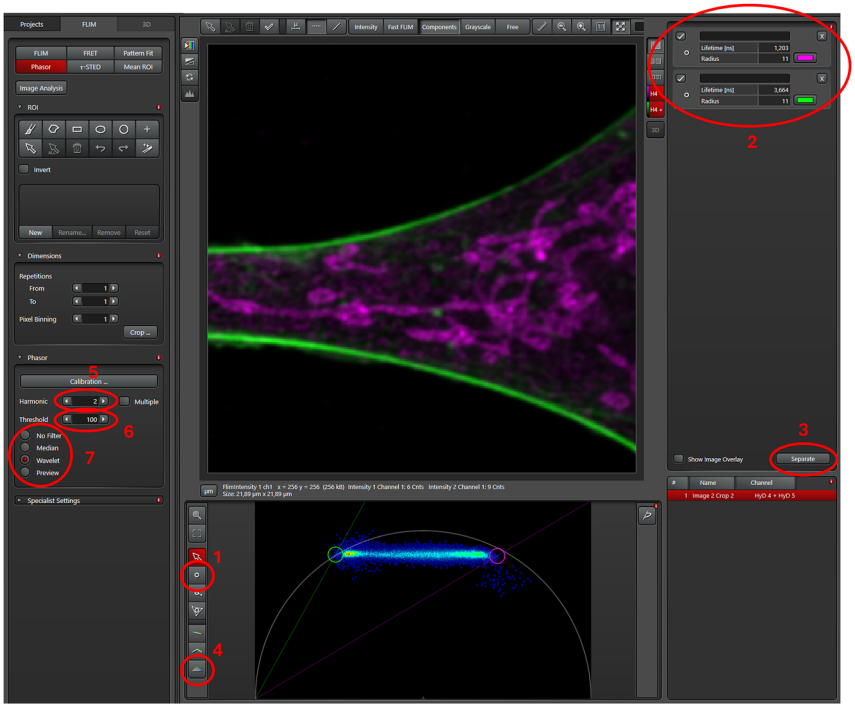

Figure 5: User interface of the FLIM window of the LAS X software. Only a part of the cell from the previous figure is shown and represented in the phasor. Using the “draw cursor” tool (ROI 1), two areas slightly outside of phasor signature of the single dye lifetimes are marked (circles). Depending on the labelling intensities, the locations can be either seen clearly (like here) or not. Single color references can be used as control to determine the phasor signature of said dye for later use. The lifetime of the two circle-cursors and the assigned pseudocolors are displayed at the top right corner (ROI 2). When satisfied with all settings, a click on the separate button (ROI 3) starts the phasor based unmixing. The final two unmixed images are displayed. Once the images are saved, they can be exported as 16-bit tiff files. The triangle tool for more complex unmixing (see Figures 7 and 9) is below the “draw cursor” tool (ROI 4). The harmonic, threshold and phasor filter can be changed as needed on the left (ROI 5, 6 and 7, respectively).

the lower right corner (blue in Figure 2). By increasing the harmonic number the visualization of these regions is expanded and shifted closer to the middle of the universal circle (Figure 3B and C). This results in a more convenient visualization of the data, with larger distances between the values. For more details see [39].

2.3.2.2 Separation of two fluorochromes by lifetime

Figure 4 shows a cell where the actin skeleton (green) and mitochondria (magenta) were labeled with dyes with similar spectral properties but different lifetimes. In the intensity image (A, B) the two fluorochromes cannot be distinguished, but a good separation by lifetime was achieved (C, D). The phasors are shown in E, F.

Using the tools provided in the Leica software, areas identified to contain the pattern of single dyes were selected in the phasor plot (Figure 5), and a linear separation was conducted (see Figure 5 legend for details). The software makes use of the linear property of the phasor plot. The algorithm takes the centers of two circles (Figures 4E, F and 5) which are defined by clicking on the phasor plot as the single dye references for the separation. The centers of the circles define the maximal and minimal lifetimes for the separation. Having them positioned outside the actual distribution makes sure that no signal pixel is outside the defined range of lifetimes thus "saturation" does not occur. The radius of the circles has no effect on the analysis. Figure 5 shows a screenshot of the software's user interface. Results are shown in Figure 4C and D and for a different sample in Figure 6.

Separated images were saved and exported. Pseudocoloring and overlay to obtain final images as in Figure 1 bottom was performed in a different software, Fiji or Imaris.

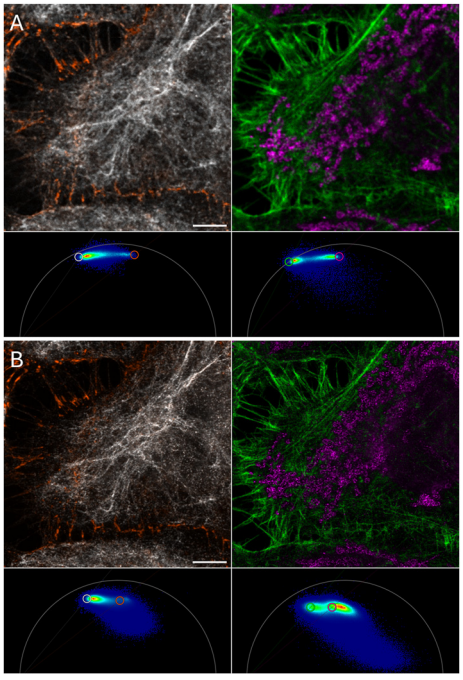

Figure 6: Five-color sample, unmixing of sequences with two fluorochromes, based on the displayed phasor plot. (A) Confocal images. (B) STED images. Left: vimentin in white (Alexa Fluor 594, lifetime 2.6 ns) and WGA in orange (CF594, 1.7 ns). Right: phallodin labeled actin fibers green (ATTO647N, 3.5 ns) and mitochondria in magenta (Aberrior Star 635P, 2.0 ns). In the STED phasor plots, due to the stimulated depletion, the photophysics is more complex than usual. Hence the different positioning of the cursors in STED phasors. In STED phasors, the "top left" fraction of each fluorochrome's signature contain the most informative pixels (see main text and Figure 8) and the curser is set to represent those. This different positioning is only applicable to STED phasors. Confocal images were separated as described above. Scale bar 5 µm.

2.3.2.3 Removing bleed-through, autofluorescence and reflected photons

The phasor can also be used to filter non-desirable contributions from spectral bleed-through or autofluorescence. In Figure 7A, ATTO647N–Phalloidin bleeds through to the CF680R channel: Actin fibers are dim but clearly recognizable, e.g. in the top left quadrant of this confocal image. The ATTO647N label was quite strong and still somewhat excited at 670 nm which was used for CF680R. Excitation with 680 nm would be more suitable [40] but was not available on the SP8 systems. Since no notch filter was available to suppress reflection of 670 nm, the recorded image also contained considerable amounts of reflected photons with 0 ns lifetime. Pixels containing only reflected photons are represented at the lower right corner of the phasor plot (Figure 7C). However, most of them are below the set threshold value (see above). Note that compared to Figures 4 and 5 the ATTO647N distribution is elongated in the phasor, towards the bottom right corner. The intensity of this bleed-through signal is close to background levels. The respective pixels thus contain a considerable percentage of reflected photons, hence the elongation towards the bottom right corner.

Lifetimes of ATTO 647N (3.5 ns) and CF680R (1.5 ns) were sufficiently different from each other and from the reflected photons (0 ns) to separate them (Figure 7B). Image filtering was done using a tool in the shape of a triangle (Figure 7C; see Figure 5, ROI 4 for tool location in the software). The triangle tool is suitable if three components are present from which only one is to be kept. This tool uses a lifetime gradient based on the phasor coordinates and assigns an intensity value to the pixels depending on their position on the phasor, hence to their lifetime (see Figure 9 for detailed explanation).

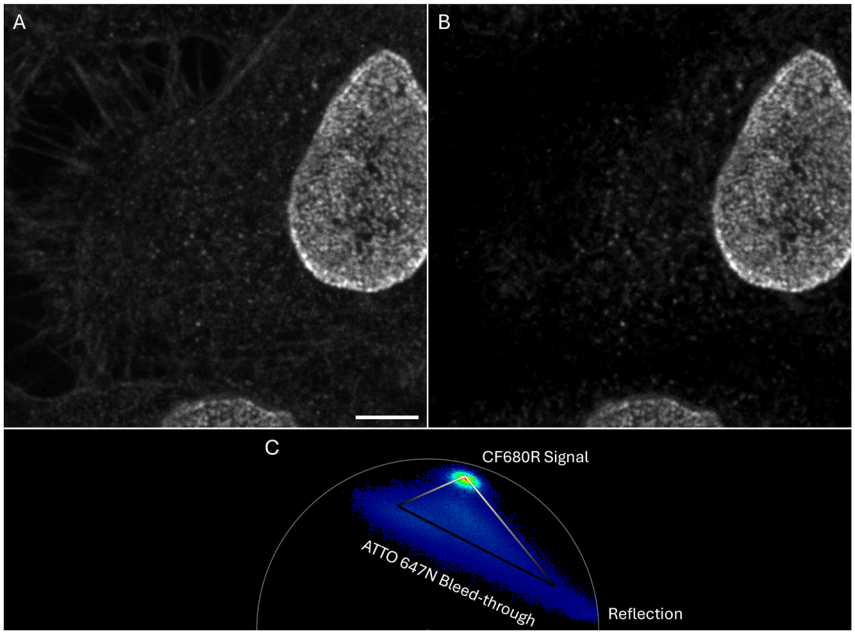

Figure 7: Confocal images of cells with labeled nuclear pores (CF680R-NUP107; lifetime 1.5 ns) and bleed-through from ATTO647N-phalloidin (3.5 ns). Only the CF680R-channel of the 5-color sample is shown. Filtering of the ATTO647N and reflection is performed with the phasor. (A) Raw intensity image where the actin filaments can clearly be seen (ATTO647N bleed-through). (B) Filtered image where the ATTO647N contribution is eliminated. (C) Phasor used to generate the filtered image. See Figure 9 for explanation of the triangle. Scale bar 5 µm.

2.4 Image analysis: Tau-STED and STED-anti-stokes excitation

Resolution in STED images can be improved by lifetime approaches such as "gated STED" which during acquisition discards all photons with very short lifetimes, e.g. <0.5 ns, since this "gate" contains fluorescence photons emitted before depletion took effect as well as reflected photons [50]. SPLIT-STED is another example. It uses fluorophore lifetime dynamics under CW-STED conditions (depletion with continuous wave laser) to effectively differentiate photons emitted from the central region (not affected by depletion) and from the outer edges of the excitation (affected by depletion) [51].

In contrast to gated STED, a fully lifetime capable system can use lifetime also post acquisition to improve the resolution and achieve the best possible result. The depletion laser modifies the photo dynamics of the population of fluorophores that it affects, including their average lifetime. The lifetime modification depends on the local depletion light intensity. Since the STED doughnut is a Gaussian beam, its intensity is uneven across the PSF. This leads to variable average lifetimes, depending on the exact position of the fluorophores (Figure 8). This displaced, elongated distribution of average lifetimes (compared to confocal) can be seen and characterized in the phasor (compare Figure 6A and B, compare Figures 7C with 9C).

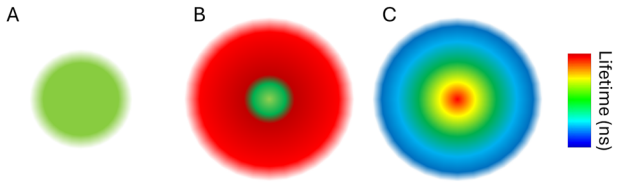

Figure 8: Lifetime in STED. (A) Scheme of the Gaussian excitation. (B) STED depletion profile (red) over the excitation leads to a smaller sampling volume. (C) Schematic representation of the lifetime distribution across the STED point spread function. The fluorescence lifetime is shortened more where the depletion is stronger. In the center, the fluorescence lifetime is the same as in the absence of STED.

τSTED ("Tau-STED") is a name Leica gave to a proprietary algorithm that applies background correction and filtering of pixels based on their phasor signature [52]. The current version works best if a spectral channel contains one desired fluorochrome. A vector can be drawn in the phasor plot (right edge of triangle in Figure 9C) to separate pixels with photons mostly unaffected by the depletion process (longer lifetimes) from pixels with many depletion affected photons (shorter lifetimes, compare Figure 8C). In addition, those pixels that do not correlate with the drawn vector can be identified as containing noise and filtered out (see legend to Figure 9). This approach addresses issues of reflection, low-resolution photons (short lifetimes), and crosstalk (different behavior of different dyes) commonly seen in STED

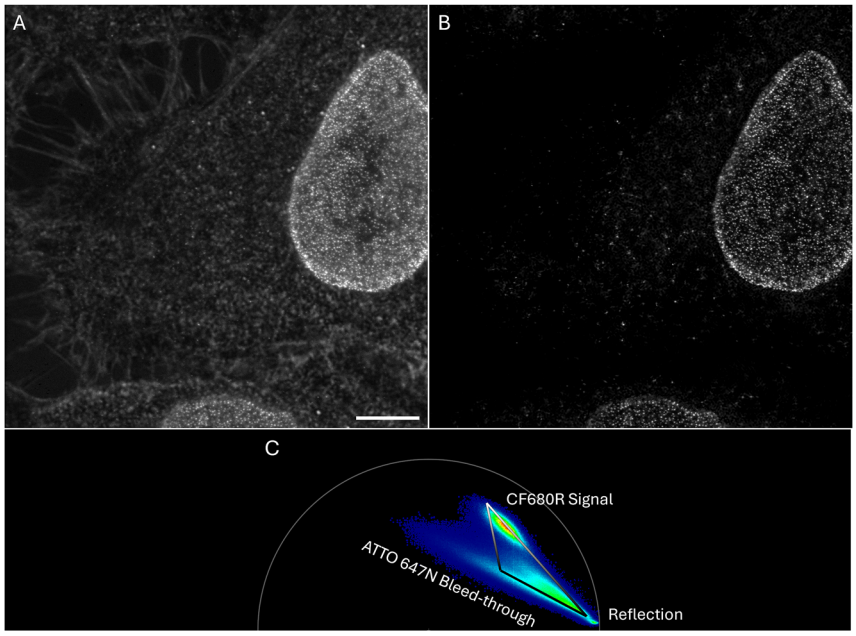

Figure 9: τSTED example. Fluorochromes and labels as in Figure 7 but note the improved spatial resolution. (A) Raw STED image. (B) τSTED corrected image. (C) Phasor plot of image (A) used for the τSTED correction shown in (B). The various contributions to the phasor plot can be easily identified. The top part of the right edge of the triangle represents the pixels with the desired CF680R signals. Pixels at the top corner of the triangle have 100 % intensity (meaning intensity in the final image (B) is the same as in the original image (A)). In current τSTED-phasors, the two lower corners of the triangle always represent zeros, meaning pixels at those corners and on the line between them (zero line) are black in (B). For all other pixels, the intensity in the final image (B) (between 0 and 100 % of the intensity in (A)) is linearly dependent on the distance to the triangle's top corner and to the zero line (compare Figure 3A). Scale bar 5 µm.

multicolor experiments. The accuracy of this determination, as with all lifetime-based approaches, depends on the available photon budget.

For the spectral channel in our five color STED images containing the CF680R antibody staining of nuclear pores, the τSTED function in LAS X was used (Figure 10). After activating Expert mode (see Figure 10) the phasor appears in the bottom right corner of the user interface. With the "Draw color coding triangle" tool (ROI 2 bottom) a triangle was placed on the phasor (Figures 9C and 10) and the τSTED image was generated (Figure 9B).

The triangle tool (and not the line tool) was used because in this particular case the strong ATTO 647N Phalloidin staining in the neighboring spectral channel caused crosstalk into the CF680R channel. However, ATTO 647N and CF680R have different lifetimes. ATTO 647N is distributed in a very elongated cluster, since this bleed-through signal is weak and close to the background level (see above). Thanks to the lifetime difference, the phasor signatures of theses dyes are in different positions on the phasor plot. Reflection and low resolution photons were also filtered out to obtain a crosstalk and background corrected image (Figure 9B). See legend to Figure 9 for details.

In the case shown here, expert mode was used because of the complexity of the sample. For a spectral channel with only a single fluorochrome with minimal bleed-through, the "τSTED" mode (ROI 1, center), is sufficient. In this mode, the software predicts what would be the best trajectory, and applies it automatically.

The generated image should be saved before export.

3 Results and discussion

3.1 Phasor based separation by lifetime

We demonstrated that two fluorochromes per spectral channel can be separated in confocal (Figures 4 and 6A) and STED microscopy (Figure 6B) if their lifetime is sufficiently different. Exploiting this, we generated multi-color confocal and FLIM-STED images with five colors from only three spectral channels (Figure 1). In our previous publication we demonstrated that the remaining bleed-through between lifetime separated images is well in the range of spectrally separated images [40]. Lifetime separated images can thus have the same quality as spectrally separated images. Others have shown that phasor based separation is also possible

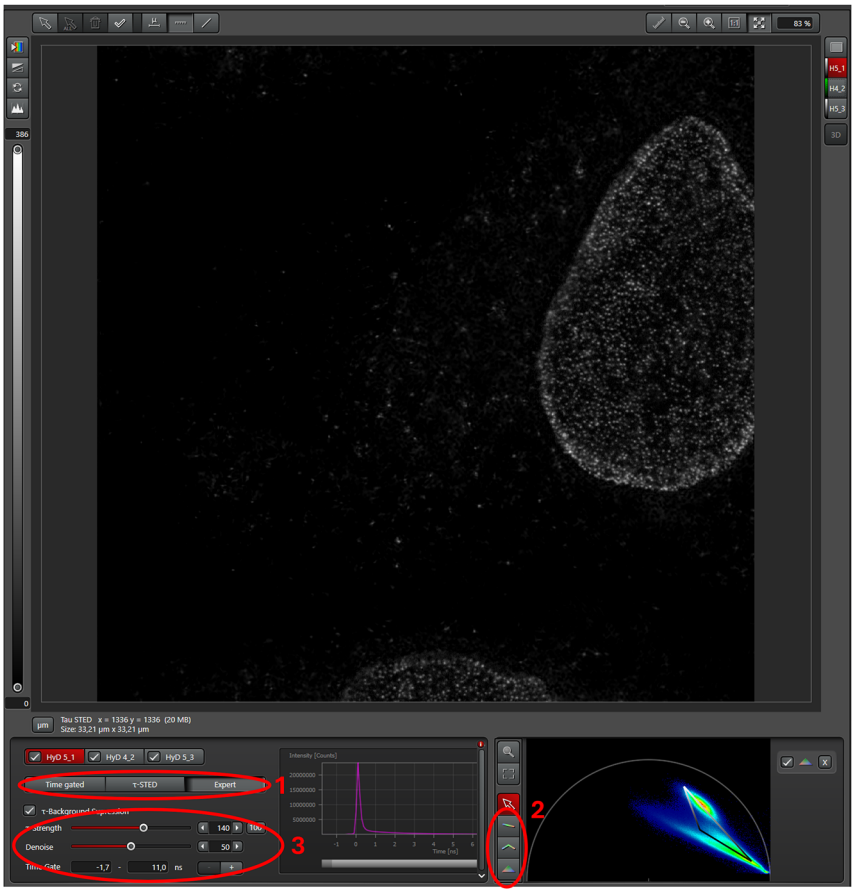

Figure 10: User interface of the τSTED part of the LAS X software. The expert mode shown here is needed only for complex samples (see main text) and activated at ROI 1. Else the τ-STED-mode can be used. As explained at Figure 5, either a line or a triangle tool (ROI 2) can be used for lifetime filtering. Here the triangle tool was applied to filter out ATTO647N bleed-through, noise and reflections (see Figure 9 and main text). Different parameters for the strength of the filtering are in ROI 3. Typically, they can be left at the default values. With increased τ-Strength values, more weight is given to long-lifetime signals. The physical limit is set by the photon budget and signal-to-noise ratio. See [52] for further information. Once the τSTED image is generated it should be saved by clicking "Save image" on the bottom left corner of the FLIM window (surrounding the window shown here) or by right click on the image. It can be exported as 16-bit tiff file.

in image-scanning microscopy [42] (ISM), an approach were the confocal pinhole is replaced with an array detector to avoid loss of light while obtaining optimal confocal resolution [53].

Color separation by phasor analysis is feasible with much smaller numbers of photons (Figure 4B, D, and F) than separation by curve fitting, because the phasor is more accurate to calculate the average lifetime of multi-exponential decays with low photon counts and SNR [48]. With curve fitting, two fluorochromes with multiexponential decay would further increase the complexity with their additional exponential components. For more components more photons are needed for an accurate fit. Hence phasor analysis is superior for lifetime unmixing with small photon numbers.

We would like to point out that all procedures were performed with commercially available fluorochrome-coupled antibodies or other reagents, commercial hardware and software. We have the hope that the above detailed protocols will help to motivate others to use these procedures in their own multi-color fluorescence experiments.

3.2 Separating more than two fluorochromes by lifetime?

The procedure described above works well with spectral channels containing two fluorochromes with different lifetimes (Figures 4 and 6). An obvious question is whether more than two fluorochromes can be separated by lifetimes. We tried this with Abberior STAR 635P on antibodies, Alexa Fluor Plus 647 labeled antibodies and ATTO 647N-Phalloidin (lifetimes of 2.0, 1.2, and 3.5 ns) [40]. While any two of this set could be separated, separation of all three, while possible, resulted in loss of detail and thus suboptimal image quality. The technical problem that arose was that the lifetime

position of the three fluorochromes in the phasor plot more or less formed a line. Any pixel in the middle of the line could correspond to either a mixture of the dyes with the longest and the shortest lifetime, or a significant contribution of the dye with the intermediate lifetime. Under such conditions, a good separation only would be possible if the fluorochromes would label spatially separated and identifiable structures such as nuclear speckles versus cell membranes. But then also a single fluorochrome would do.

Successful separation of three fluorescent species based on the phasor plot was reported by others, however [41], [54]. In these cases the positions of the three fluorescent species formed a triangle in the phasor plot. Thus, a unique solution could be identified for each phasor position. In one case lifetimes were 3.71, 3.05 and 2.14 ns, with the 2.14 ns lifetime coming from a tri-exponential decay and thus a position away from the universal circle so that the three phasor positions indeed formed a triangle despite the small lifetime differences [41]. While generally good separation was shown, close inspection of pictures with overlapping structures (e.g. their Fig. S31D) reveal some separation artifacts though. Qdot 585 (longest lifetime), Bodipy TMR (intermediate lifetime), and AF555 (shortest lifetime; in other reports this dye is called Alexa Fluor 555 or Alexa 555), all coupled to antibodies were also successfully separated [54]. The actual lifetimes were not given in this report, but other publications give around 0.7 ns for antibody bound AF555 [26] and 19.5 ns for free Qdot 585 [55].

A separation of four fluorochromes using the phasor plot was also reported [56]. Transformation of the phasor plot to higher harmonics (Figure 3B and C) resulted in additional equations so that a unique solution for four components could be determined. Respective lifetimes covered a wide range: 12, 3.8, 1.4 and 0.6 ns. Since currently commercially available labels on antibodies do not exceed 5 ns (to our knowledge), it currently may be difficult to perform this approach with immunostained samples.

3.3 Conclusion: recommendations for multi-color fluorescence

It currently seems easiest to first explore the possibilities of spectral separation of a given instrument, in particular since spectral separation is broadly available. We successfully used six spectrally different colors on our confocal SP8 systems, five excited with the white light laser (470–670 nm) plus DAPI excited with 405 nm. New systems may allow even more spectrally separable fluorochromes. For projects where the spectral options are exhausted, either because more fluorochromes are needed or because of special constrains such as a single STED depletion laser, we recommend to apply separation of two fluorochromes with different lifetimes in a given spectral channel. We could show that such a separation works with as little bleed-through as spectral separation [40]. In the future, dyes with a wider range of lifetimes may become available allowing the separation of even more than two fluorochromes per spectral channel in standard experiments with commercial dyes.

In practice, for experiments with primary and secondary antibodies, the number of labels will not be limited by the number of separable fluorochromes but by the number of species from which primary antibodies are available. This limitation can be circumvented by the use of self-labeled primary antibodies at the expense of additional work and costs and labeling intensity.

Acknowledgments: We thank our colleagues at the Core Facility Bioimaging for their practical support and many helpful discussions. We thank the Deutsche Forschungsgemeinschaft for funding the upright Leica SP8 FALCON FLIM microscope, grant INST 86/1909-1. We thank Leica Microsystems for providing an offline version of the Stellaris LAS-X software with FLIM analysis.
Research ethics: Not applicable.
Informed consent: Not applicable.
Author contributions: All authors have accepted responsibility for the entire content of this manuscript and approved its submission.
Use of Large Language Models, AI and Machine Learning Tools: None declared.
Conflict of interest: The authors state no conflict of interest.
Research funding: This work was supported by the Deutsche Forschungsgemeinschaft by funding the upright Leica SP8 FALCON FLIM microscope, grant INST 86/1909-1.
Data availability: Not applicable.

References

[1] M. Haitinger, *Fluorescenzmikroskopie Ihre Anwendung in der Histologie und Chemie*, Leipzig, Akademische Verlagsgesellschaft, 1938, p. 108.
[2] A. H. Coons, H. J. Creech, R. N. Jones, and E. Berliner, "The demonstration of pneumococcal antigen in tissues by the use of fluorescent antibody," *J. Immunol.*, vol. 45, no. 3, pp. 159—170, 1942.
[3] A. M. Silverstein, W. C. Eveland, and J. D. Marshall, Jr., "Rapid identification of organisms with fluorescent antibodies of contrasting colors. (Abstract.)," in *Bacteriological Proceedings, The Society of American Bacteriologists*, cited after Riggs et al., 1958, 1957, p. 147.
[4] J. L. Riggs, R. J. Seiwald, J. H. Burckhalter, C. M. Downs, and T. G. Metcalf, "Isothiocyanate compounds as fluorescent labeling

agents for immune serum," *Am. J. Pathol.*, vol. 34, no. 6, pp. 1081—1097. 1958.
[5] J. S. Ploem, "The use of a vertical illuminator with interchangeable dichroic mirrors for Fluorescence microscopy with incident light," *Zeitschr. Wiss. Mikroskopie*, vol. 68, no. 3, pp. 129—42, 1967.
[6] J. S. Ploem, "Die Möglichkeit der Auflichtfluoreszenzmethoden bei Untersuchungen von Zellen in Durchströmungskammern und Leightonröhren, Xth Symposium d. Gesellschaft f. Histochemie 1965," *Acta Histochem.*, vol. 7, pp. 339—343, 1967.
[7] R. C. Nairn and J. S. Ploem, "Moderne Immunfluoreszenzmikroskopie und ihre Anwendung in der klinischen Immunologie," *Leitz Mitt. Wiss. Techn.*, vol. 6, no. 3, pp. 91—95, 1974.
[8] G. Cox, "The Ploem fluorescence microscope," in *Fundamentals of Fluorescence Imaging*, G. Cox, Ed., Singapore, Jenny Stanford Publishing Pte. Ltd., 2019, pp. 35—47.
[9] F. H. Kasten, "The origins of modern fluorecence microscopy and fluorescent probes," in *Cell Structure and Functions by Microspectrofluorometry*, E. Kohen, Ed., San Diego, California, Academic Press, Inc, 1989, pp. 3—50.
[10] M. R. Speicher, S. Gwyn Ballard, and D. C. Ward, "Karyotyping human chromosomes by combinatorial multi-fluor FISH," *Nat. Genet.*, vol. 12, no. 4, pp. 368—375, 1996.
[11] E. Schröck, *et al*., "Multicolor spectral karyotyping of human chromosomes," (in eng), *Science*, vol. 273, no. 5274, pp. 494—497, 1996.
[12] J. Azofeifa, *et al*., "An optimized probe set for the detection of small interchromosomal aberrations by use of 24-color FISH," *Am. J. Hum. Genet.*, vol. 66, no. 5, pp. 1684—1688, 2000.
[13] J. Walter, *et al*., "Towards many colors in FISH on 3D-preserved interphase nuclei," *Cytogenet. Genome Res.*, vol. 114, nos. 3—4, pp. 367—378, 2006.
[14] T. C. Brelje, M. W. Wessendorf, and R. L. Sorenson, "Multicolor laser scanning confocal immunofluorescence microscopy: practical application and limitations," *Methods Cell Biol.*, vol. 70, pp. 165—244, 2002.
[15] M. E. Dickinson, G. Bearman, S. Tille, R. Lansford, and S. E. Fraser, "Multi-spectral imaging and linear unmixing add a whole new dimension to laser scanning fluorescence microscopy," *Biotechniques*, vol. 31, no. 6, pp. 1272—1278, 2001.
[16] T. Zimmermann, "Spectral imaging and linear unmixing in light microscopy," *Adv. Biochem. Eng. Biotechnol.*, vol. 95, pp. 245—265, 2005.
[17] G. Szaloki and K. Goda, "Compensation in multicolor flow cytometry," *Cytometry A*, vol. 87, no. 11, pp. 982—985, 2015.
[18] S. Muller, M. Neusser, and J. Wienberg, "Towards unlimited colors for fluorescence in-situ hybridization (FISH)," *Chromosome Res.*, vol. 10, no. 3, pp. 223—232, 2002. .
[19] R. Jungmann, C. Steinhauer, M. Scheible, A. Kuzyk, P. Tinnefeld, and F. C. Simmel, "Single-molecule kinetics and super-resolution microscopy by fluorescence imaging of transient binding on DNA origami," *Nano Lett.*, vol. 10, no. 11, pp. 4756—4761, 2010.
[20] M. Glogger, *et al*., "Synergizing exchangeable fluorophore labels for multitarget STED microscopy," *ACS Nano*, vol. 16, no. 11, pp. 17991—17997, 2022.
[21] S. M. Lewis, *et al*., "Spatial omics and multiplexed imaging to explore cancer biology," *Nat. Methods*, vol. 18, no. 9, pp. 997—1012, 2021.
[22] W. Schubert, *et al*., "Analyzing proteome topology and function by automated multidimensional fluorescence microscopy," *Nat. Biotechnol.*, vol. 24, no. 10, pp. 1270—1278, 2006.
[23] T. Semba and T. Ishimoto, "Spatial analysis by current multiplexed imaging technologies for the molecular characterisation of cancer tissues," *Br. J. Cancer*, vol. 131, no. 11, pp. 1737—1747, 2024.
[24] J. R. Lakowicz, "Fluorescence lifetimes and quantum yields," in *Principles of Fluorescence Spectroscopy*, 3rd ed. New York, NY, USA, Springer Science+Business Media, LLC, 2006, ch. 1.4, pp. 8—12.
[25] M. Y. Berezin and S. Achilefu, "Fluorescence lifetime measurements and biological imaging," *Chem. Rev.*, vol. 110, no. 5, pp. 2641—2684, 2010.
[26] T. Niehörster, *et al*., "Multi-target spectrally resolved fluorescence lifetime imaging microscopy," *Nat. Methods*, vol. 13, no. 3, pp. 257—262, 2016.
[27] H. Brismar, O. Trepte, and B. Ulfhake, "Spectra and fluorescence lifetimes of lissamine rhodamine, tetramethylrhodamine isothiocyanate, Texas red, and cyanine 3.18 fluorophores: influences of some environmental factors recorded with a confocal laser scanning microscope," *J. Histochem. Cytochem.*, vol. 43, no. 7, pp. 699—707, 1995.
[28] M. S. Frei, B. Koch, J. Hiblot, and K. Johnsson, "Live-cell fluorescence lifetime multiplexing using synthetic fluorescent probes," *ACS Chem. Biol.*, vol. 17, no. 6, pp. 1321—1327, 2022.
[29] P. I. Bastiaens and A. Squire, "Fluorescence lifetime imaging microscopy: spatial resolution of biochemical processes in the cell," *Trends Cell Biol.*, vol. 9, no. 2, pp. 48—52, 1999.
[30] J. R. Lakowicz, H. Szmacinski, and M. L. Johnson, "Calcium imaging using fluorescence lifetimes and long-wavelength probes," *J. Fluoresc.*, vol. 2, no. 1, pp. 47—62, 1992.
[31] C. G. Morgan, A. C. Mitchell, and J. G. Murray, "Prospects for confocal imaging based on nanosecond fluorescence decay time," *J. Microsc.*, vol. 165, no. 1, pp. 49—60, 1992.
[32] E. P. Buurman, *et al*., "Fluorescence lifetime imaging using a confocal laser scanning microscope," *Scanning*, vol. 14, no. 3, pp. 155—159, 1992.
[33] R. Pepperkok, A. Squire, S. Geley, and P. I. Bastiaens, "Simultaneous detection of multiple green fluorescent proteins in live cells by fluorescence lifetime imaging microscopy," *Curr. Biol.*, vol. 9, no. 5, pp. 269—272, 1999.
[34] M. Elangovan, R. N. Day, and A. Periasamy, "Nanosecond fluorescence resonance energy transfer-fluorescence lifetime imaging microscopy to localize the protein interactions in a single living cell," *J. Microsc.*, vol. 205, no. Pt 1, pp. 3—14, 2002.
[35] M. Wahl, F. Koberling, M. Patting, H. Rahn, and R. Erdmann, "Time-resolved confocal fluorescence imaging and spectroscopyy system with single molecule sensitivity and sub-micrometer resolution," *Curr. Pharm. Biotechnol.*, vol. 5, no. 3, pp. 299—308, 2004.
[36] F. Fereidouni, K. Reitsma, and H. C. Gerritsen, "High speed multispectral fluorescence lifetime imaging," *Opt. Express*, vol. 21, no. 10, pp. 11769—11782, 2013.
[37] J. Bückers, D. Wildanger, G. Vicidomini, L. Kastrup, and S. W. Hell, "Simultaneous multi-lifetime multi-color STED imaging for colocalization analyses," *Opt. Express*, vol. 19, no. 4, pp. 3130—3143, 2011.

[38] W. Becker, *et al*., "Fluorescence lifetime images and correlation spectra obtained by multidimensional time-correlated single photon counting," *Microsc. Res. Tech.*, vol. 69, no. 3, pp. 186—195, 2006.
[39] M. A. Digman, V. R. Caiolfa, M. Zamai, and E. Gratton, "The phasor approach to fluorescence lifetime imaging analysis," *Biophys. J.*, vol. 94, no. 2, pp. L14—L16, 2008.
[40] M. Gonzalez Pisfil, I. Nadelson, B. Bergner, S. Rottmeier, A. W. Thomae, and S. Dietzel, "Stimulated emission depletion microscopy with a single depletion laser using five fluorochromes and fluorescence lifetime phasor separation," *Sci. Rep.*, vol. 12, no. 1, p. 14027, 2022.
[41] M. S. Frei, M. Tarnawski, M. J. Roberti, B. Koch, J. Hiblot, and K. Johnsson, "Engineered HaloTag variants for fluorescence lifetime multiplexing," *Nat. Methods*, vol. 19, no. 1, pp. 65—70, 2022.
[42] G. Tortarolo, *et al*., "Compact and effective photon-resolved image scanning microscope," *Adv. Photonics*, vol. 6, no. 1, pp. 016003-1—016003-12, 2024.
[43] L. Wang, *et al*., "Phasor-FSTM: a new paradigm for multicolor super-resolution imaging of living cells based on fluorescence modulation and lifetime multiplexing," *Light Sci. Appl.*, vol. 14, no. 1, p. 32, 2025.
[44] S. W. Hell, "Toward fluorescence nanoscopy," *Nat. Biotechnol.*, vol. 21, no. 11, pp. 1347—1355, 2003.
[45] Q. S. Hanley, V. Subramaniam, D. J. Arndt-Jovin, and T. M. Jovin, "Fluorescence lifetime imaging: multi-point calibration, minimum resolvable differences, and artifact suppression," *Cytometry*, vol. 43, no. 4, pp. 248—260, 2001. .
[46] A. Egner and S. W. Hell, "Aberrations in confocal and multi-photon fluorescence microscopy induced by refractive index mismatch," in *Handbook of Biological Confocal Microscopy*, J. B. Pawley, Ed., 3rd ed. New York, NY, Springer Science+Business Media, LLC, 2006, ch. 20, pp. 404—413.
[47] C. Buranachai, J. P. Eichorst, K. W. Teng, and R. M. Clegg, "Fluorescence lifetime imaging in living cells," in *Fundamentals of Fluorescence Imaging*, 1st ed. G. Cox, Ed., Singapore, Jenny Stanford Publishing Pte. Ltd., 2019, pp. 209—252.
[48] A. Leray, C. Spriet, D. Trinel, R. Blossey, Y. Usson, and L. Heliot, "Quantitative comparison of polar approach versus fitting method in time domain FLIM image analysis," *Cytometry A*, vol. 79, no. 2, pp. 149—158, 2011.
[49] P. Wang, F. Hecht, G. Ossato, S. Tille, S. E. Fraser, and J. A. Junge, "Complex wavelet filter improves FLIM phasors for photon starved imaging experiments," *Biomed. Opt. Express*, vol. 12, no. 6, pp. 3463—3473, 2021.
[50] G. Vicidomini, *et al*., "Sharper low-power STED nanoscopy by time gating," *Nat. Methods*, vol. 8, no. 7, pp. 571—573, 2011.
[51] L. Lanzano, I. Coto Hernandez, M. Castello, E. Gratton, A. Diaspro, and G. Vicidomini, "Encoding and decoding spatio-temporal information for super-resolution microscopy," *Nat. Commun.*, vol. 6, p. 6701, 2015.
[52] L. A. J. Alvarez, U. Schwarz, L. Friedrich, J. Foelling, F. Hecht, and M. J. Roberti, "Application note: pushing STED beyond its limits with TauSTED," *Nat. Methods*, vol. 18, no. 6, 2021.
[53] I. Gregor and J. Enderlein, "Image scanning microscopy," *Curr. Opin. Chem. Biol.*, vol. 51, pp. 74—83, 2019.
[54] M. K. Rahim, *et al*., "Phasor analysis of fluorescence lifetime enables quantitative multiplexed molecular imaging of three probes," *Anal. Chem.*, vol. 94, no. 41, pp. 14185—14194, 2022.
[55] S. H. Ko, K. Du, and J. A. Liddle, "Quantum-dot fluorescence lifetime engineering with DNA origami constructs," *Angew Chem. Int. Ed. Engl.*, vol. 52, no. 4, pp. 1193—1197, 2013.
[56] A. Vallmitjana, A. Dvornikov, B. Torrado, D. M. Jameson, S. Ranjit, and E. Gratton, "Resolution of 4 components in the same pixel in FLIM images using the phasor approach," *Methods Appl. Fluoresc.*, vol. 8, no. 3, p. 035001, 2020.

Cell Reports

CellPress
OPEN ACCESS

Article

Extracellular vesicle-mediated trafficking of molecular cues during human brain development

Andrea Forero,[1,2,11] Fabrizia Pipicelli,[1,3,11] Sylvain Moser,[1,3] Natalia Baumann,[4] Christian Grätz,[5] Mariano Gonzalez Pisfil,[6] Michael W. Pfaffl,[5] Benno Pütz,[1] Pavel Kielkowski,[7] Filippo M. Cernilogar,[8,9] Giuseppina Maccarrone,[1] Rossella Di Giaimo,[1,10,*] and Silvia Cappello[1,2,12,*]

[1]Max Planck Institute of Psychiatry, Munich, Germany
[2]Division of Physiological Genomics, Biomedical Center (BMC), Faculty of Medicine, Ludwig Maximilian University (LMU), Munich, Germany
[3]International Max Planck Research School for Translational Psychiatry, Munich, Germany
[4]Department of Basic Neurosciences, University of Geneva, Geneva, Switzerland
[5]Division of Animal Physiology and Immunology, Technical University of Munich, Freising, Germany
[6]Core Facility Bioimaging and Walter-Brendel-Centre of Experimental Medicine, Biomedical Center, Ludwig Maximilian University, Munich, Germany
[7]Department of Chemistry, Ludwig Maximilian University, Munich, Germany
[8]Division of Molecular Biology, Biomedical Center (BMC), Faculty of Medicine, Ludwig Maximilian University, Munich, Germany
[9]Department of Science and Technological Innovation, University of Piemonte Orientale, Alessandria, Italy
[10]Department of Biology, University of Naples Federico II, Naples, Italy
[11]These authors contributed equally
[12]Lead contact
*Correspondence: digiaimo@unina.it (R.D.G.), silvia.cappello@bmc.med.lmu.de (S.C.)
https://doi.org/10.1016/j.celrep.2024.114755

SUMMARY

Cellular crosstalk is an essential process influenced by numerous factors, including secreted vesicles that transfer nucleic acids, lipids, and proteins between cells. Extracellular vesicles (EVs) have been the center of many studies focusing on neurodegenerative disorders, but whether EVs display cell-type-specific features for cellular crosstalk during neurodevelopment is unknown. Here, using human-induced pluripotent stem cell-derived cerebral organoids, neural progenitors, neurons, and astrocytes, we identify heterogeneity in EV protein content and dynamics in a cell-type-specific and time-dependent manner. Our results support the trafficking of key molecules via EVs in neurodevelopment, such as the transcription factor YAP1, and their localization to differing cell compartments depending on the EV recipient cell type. This study sheds new light on the biology of EVs during human brain development.

INTRODUCTION

The events that organize brain structure during development include neurogenesis, cell migration, and axon projection and guidance.[1–3] In this dynamic context, cell-to-cell communication is an essential process influenced by factors including cell morphology, adhesion molecules, the local extracellular matrix (ECM), and secreted vesicles.[4–6] Extracellular signals are required during development to establish precise cell numbers, unique cell types, and specific cell migration patterns, positions, and functions.[7–10]

Extracellular vesicles (EVs) are small particles in the brain extracellular environment that have gained interest due to their potential in diagnostics and therapeutics in neurodevelopmental disorders.[11] EVs are secreted by all cells and are classified mostly as exosomes and microvesicles based on their size, composition, and origin. While exosomes are generally smaller (30–200 nm) and released by the fusion of multivesicular bodies with the plasma membrane, microvesicles (of much variable size, 100–1000 nm) are directly shed by the outward blebbing of the plasma membrane.[12] Vesicles travel long distances within and outside of cells, thus impacting crosstalk at several levels and sites. Although EVs are key players in extracellular environment composition, few studies have focused on their functional role during brain development. Studies have shown that neural stem cells release Prominin-1 via EVs,[13] while retinal stem cells release EVs containing developmental transcription factors (TFs), microRNA, and membrane proteins that regulate gene expression in developing mouse and human retinal organoids.[14,15] Neurons and astrocytes *in vitro* have also been shown to secrete EVs containing varied cargoes, such as the L1 adhesion molecule and specific subunits of the glutamate receptor.[16,17] EVs also have physiological and pathological functions, for instance, directing neuronal differentiation and regulating synapse formation in healthy neurons,[16,18,19] as well as in neurodevelopmental disorders such as cortical malformations and autism spectrum disorder.[7,20,21] Recent studies support that EVs can act as carriers of ECM components such as Tenascin C[22,23] and, therefore, regulate cell growth, differentiation, and migration by transporting ECM remodeling cargoes like matrix

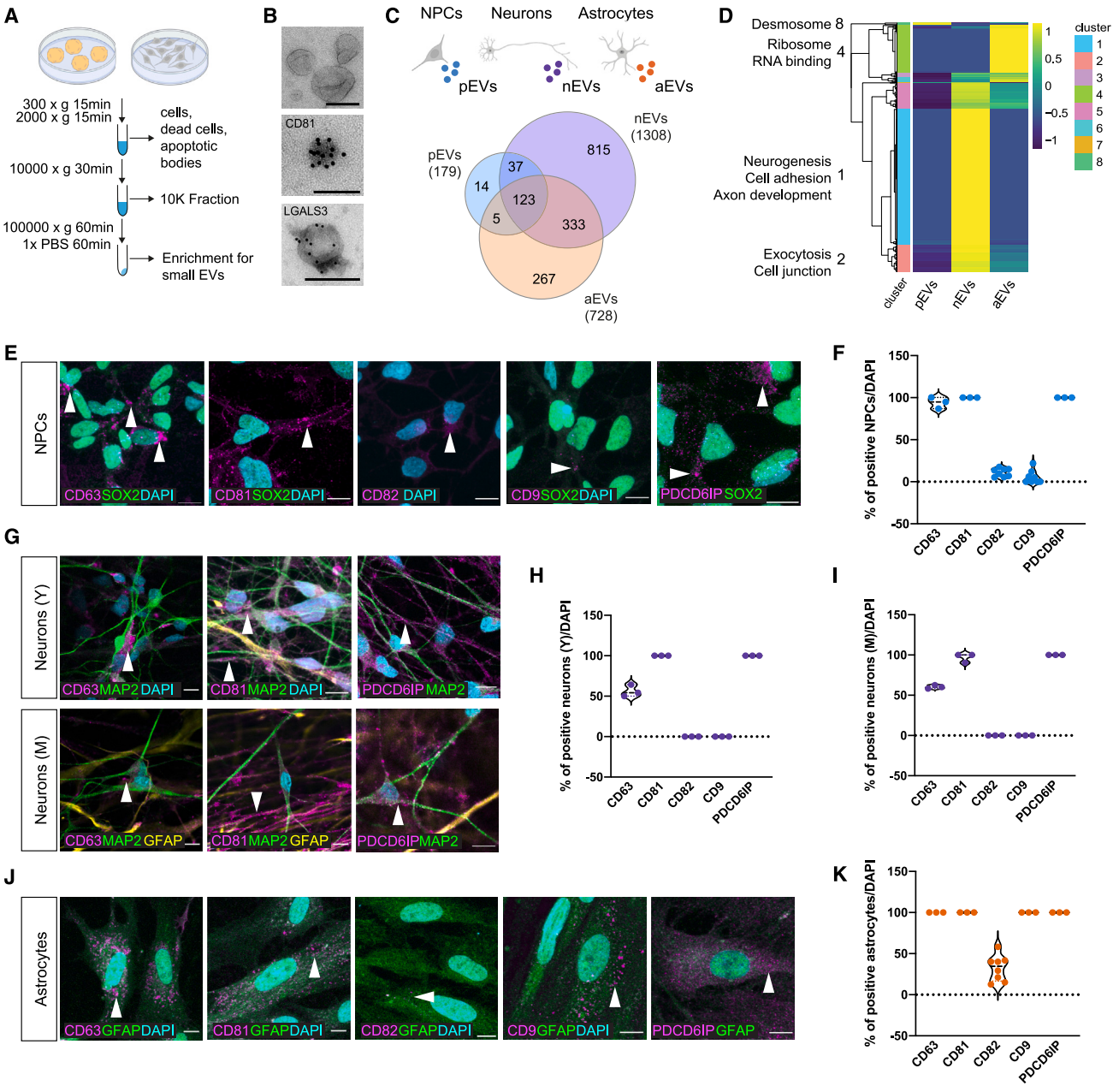

Figure 1. Isolation and cell-type-specific characterization of EVs

(A) Schematic of EV isolation protocol by differential ultracentrifugation. Cell and EVs are generated from control line C1.

(B) Immuno-electron micrographs of CD81 and LGALS3 in EVs collected from CO conditioned media. Scale bar: 100 nm.

(C) Schematic of EVs secreted by 2D cell populations, NPCs (neural progenitor cells; pEVs, blue), neurons (nEVs, purple), and astrocytes (aEVs, orange) (top), and Venn diagram of proteins detected in pEVs, nEVs, and aEVs (bottom).

(D) Heatmap showing hierarchical clusters of proteins detected in pEVs, nEVs, and aEVs. GO enrichments of clusters are displayed. EVs were collected from the conditioned media of 3–5 different wells of cells in culture.

(E) CD63, CD81, CD82, CD9, and PDCD6IP immunostaining in NPCs (SOX2+, green) (arrowheads). DAPI, cyan. Scale bar: 10 μm.

(F) Quantification of $CD63^+$, $CD81^+$, $CD82^+$, $CD9^+$, and $PDCD6IP^+$ NPCs. Violin plots show the median and interquartile range. Every dot refers to a field of view, each from a different differentiation (biological replicates), n = 3–8 per condition.

(G) CD63, CD81, and PDCD6IP immunostaining in young (Y) neurons (MAP2+, green) (top) and mature (M) neurons (MAP2+, green and GFAP+, yellow) (bottom) (arrowheads). DAPI, cyan. Scale bar: 10 μm.

(H) Quantification of $CD63^+$, $CD81^+$, and $PDCD6IP^+$ neurons(Y). Violin plots show the median and interquartile range. Every dot refers to a field of view, each from a different differentiation (biological replicates), n = 3 per condition.

(legend continued on next page)

metalloproteinases that can alter depositions of different collagen types.[24] Moreover, annexin-enriched osteoblast-derived EVs act as an extracellular site of mineral nucleation in developing stem cell cultures.[25] However, most of these studies have focused on EV content at a single time point in a two-dimensional (2D) cell culture environment.

Here, we present insight into EV release, composition, uptake, and function across varying neural cell types and developmental stages. For this purpose, we use two human brain models: human induced pluripotent stem cell (iPSC)-derived neural cells in 2D monolayer cultures and a 3D model of human brain development, namely cerebral organoids (COs).

RESULTS

EV protein content varies among neural cell types

We hypothesized that during brain development, different cell types secrete vesicles enriched with cell-type-specific proteins. To investigate this, we first isolated a mixed population of small EVs (Figure S1A), containing both exosomes and small microvesicles, from the secreted fraction (culture medium) of 2D monolayer cultures enriched in human iPSC-derived neural progenitor cells (NPCs), neurons, and astrocytes. EV isolation was conducted by differential ultracentrifugation,[26,27] and we further characterized EVs by nanoparticle tracking analysis (NTA) and immunoelectron microscopy with transmembrane (CD81) and intraluminal (LGALS3) markers (Figures 1A, 1B, and S1A). We then profiled the protein content of EVs isolated from our 2D neural cultures by mass spectrometry (Figures 1C, 1D, and S1B; Table S1). The results of the protein profiling validated our EV purification protocol, in accordance with the guidelines provided by the International Society for Extracellular Vesicles.[28] Standard positive EV markers (CD63, TSG101, and PDCD6IP) were present in all our samples, while negative markers (CYC1 and GOLGA2) were undetectable (Figure S1C). The relative abundance of EV proteins was confirmed by western blot (WB) on independent samples (Figure S1D).

Our results showed that the three populations of human iPSC-derived neural cells grown in 2D share less than 8% of the total EV proteins (Figure 1C). EVs from NPCs (pEVs) were the least diverse (in total protein number), with less than 1% of the EV proteins being unique for this cell type (Figures 1C and 1D, cluster 8). On the contrary, neurons exhibited the most unique protein content in EVs (nEVs; Figures 1C and 1D, clusters 1 and 2), suggesting that neurons make extensive use of EVs for cellular crosstalk, as previously shown.[29] Among nEV proteins, we identified an enrichment in proteins linked to neurogenesis, cell adhesion, and axon development. The RNA catabolic process and ribonucleoprotein complex (Figure 1D, cluster 4) were enriched in astrocyte EVs (aEVs). We further performed an immunohistochemical analysis of common EV markers, mainly tetraspanins (CD63, CD81, CD82, CD9) and PDCD6IP, in our 2D neural cultures due to their role in EV biogenesis, specifically cargo loading.[30] We observed some markers being ubiquitously expressed (CD63, CD81, and PDCD6IP), while others presented a more restrictive pattern of expression among different cell types. For instance, CD82 and CD9 were the least abundant overall, limited to a small percentage of NPCs and astrocytes, while absent in both young (Y; 4 weeks in culture) and mature (M; 10 weeks in culture) neurons (Figures 1E–1K). These results are congruent with the expression of these common EV markers among diverse cell types as shown by single-cell RNA sequencing (RNA-seq) analysis of COs (Figures S2A and S2B), which identified CD63, CD81, and PDCD6IP as generally expressed proteins and CD82 and CD9 as enriched in subclasses of neural progenitors. Together, our data show that varying combinations of EV markers are present in different neural cell types, suggesting certain cell-type specificity in EV biogenesis. However, this heterogeneity in EV marker expression is not sufficient to provide insight into the differential loading of EV proteins among the cell types here studied. Therefore, our cell-type-specific proteomic analysis highlighted the release of EVs from different neural cell types loaded with common as well as unique proteins, suggesting the heterogeneity of EVs during human brain development.

EV protein content varies through CO developmental stages

We then investigated EV protein composition using a more complex model system, human iPSC-derived COs, which display a temporal progression similar to that observed in the human fetal brain and not present in our 2D model systems. We performed a systematic proteomic analysis of EVs at different developmental stages in COs (days 15–360; Figure 2A). This analysis was conducted on different batches of organoids derived from a single control cell line, C1, since our aim was to observe changes in EV protein composition at different time points and overcome genetic background variability. We detected a total of 3,791 proteins, with substantial heterogeneity (number of detected proteins) at the different time points (Figures 2B and 2C; Table S1; validation by WB in Figure S3A). The unique protein content for each developmental stage was associated with cell cycle and RNA splicing (day 15), intracellular transport and mitochondrial membrane (day 40), ribosome biogenesis and mitochondrion (day 200), and locomotion, secretion, neuron part, and cell motility (day 360) (Figure 2C). 6.8% of EV proteins were shared across all the developmental stages, including those involved in cell junctions and secretory functions (Figures 2B and 2C). The EV protein difference across CO development suggests unique EV signatures and variety. The total number of EV proteins from 3D COs was strongly increased compared to 2D cultures, suggesting a higher variety in the 3D model system (Figure 2D; Table S1). Day 15 COs are mainly composed by neural progenitors (Figure S3D), while neurons start to be detected

(I) Quantification of $CD63^+$, $CD81^+$, and $PDCD6IP^+$ neurons(M). Violin plots show the median and interquartile range. Every dot refers to a field of view, each from a different differentiation (biological replicates), $n = 3$ per condition.

(J) CD63, CD81, CD82, CD9, and PDCD6IP immunostaining in astrocytes (GFAP+, green) (arrowheads). DAPI, cyan. Scale bar: 10 μm.

(K) Quantification of $CD63^+$, $CD81^+$, $CD82^+$, $CD9^+$, and $PDCD6IP^+$ astrocytes. Violin plots show the median and interquartile range. Every dot refers to a field of view, each from a different differentiation (biological replicates), $n = 3–8$ per condition.

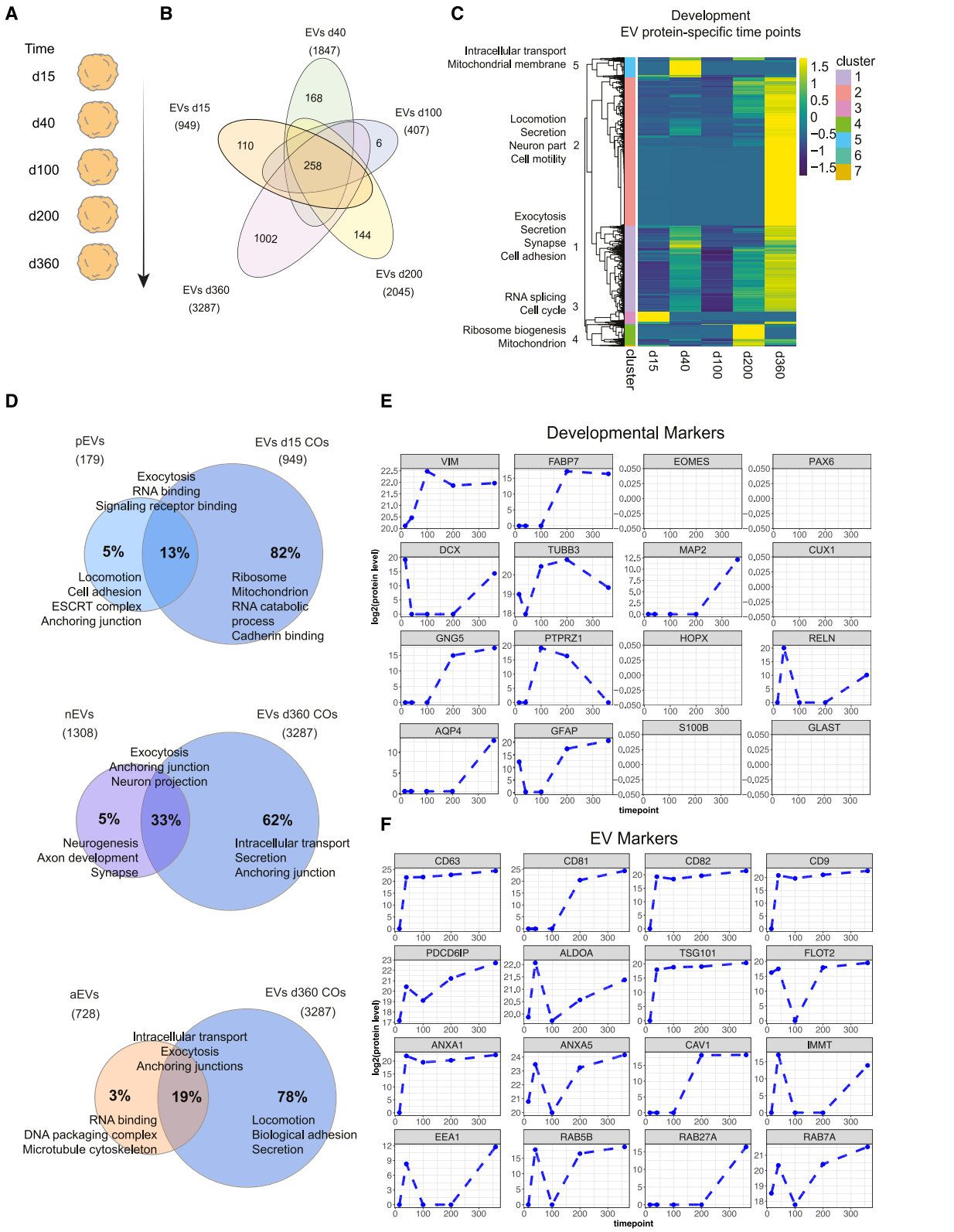

(legend on next page)

only at day 20 (where PAX6 and NESTIN+ progenitor cells are surrounded by very few Doublecortin (DCX)+ neuroblasts; Figure S3E); therefore, we compared pEVs in 2D and 3D day 15 COs. 3D day 360 COs consist of different cell types, including M neurons/astrocytes; therefore, we compared EVs from M astrocytes (aEVs) and M neurons (nEVs) with EVs from day 360 COs. The number of proteins varied greatly, and the enriched Gene Ontology (GO) terms suggest that the 3D environment, composed by a higher heterogeneity of cell types, contributes to EV secretion (Figure 2D). To verify that the shared fraction of proteins between 2D and 3D were not cell-type dependent, we compared the protein content of pEVs and day 15 COs generated from 2 different iPSC lines (Figures 2D and S2C). The results show similar content of shared proteins in the two lines (13% and 17%; Figures 2D and S2C). To assess if the secretion of proteins via EVs followed their physiological pattern of expression in cells, development-associated proteins that were identified in EVs were compared with their cellular gene expression[31] and localization in intracellular vesicles (IVs). Surprisingly, EV proteins did not match gene expression strictly, and their trajectories did not always follow cellular compartmentalization in IVs (Figures 2E, S3B, and S3C), indicating a regulated loading of protein cargo to be released via vesicles. Alternatively, the 3D tissue could interfere with the release of EVs into the medium compared to 2D monolayer cultures. For example, markers for apical radial glia, like VIM and FABP7, already highly expressed early on and throughout development, are secreted in EVs with a comparable dynamic (Figures 2E, S3B, and S3C). Typical markers for basal radial glia, a cell type normally appearing around day 50 in COs, were enriched at different stages in EVs, with PTPRZ1 peaking at day 100 and GNG5 at day 200. Early neuronal markers were detected in EVs, and while DCX peaked at day 15, RELN was strongly enriched at day 40 (Figure 2E). M neuronal markers also exhibited distinctive patterns: TUBB3 was persistently secreted in EVs, while MAP2 was only secreted after 200 days. Glial genes, like AQP4, GFAP, S100B, and GLAST, consistently show an enrichment in the latest stages of CO development, compatible with the process of gliogenesis following neurogenesis. On the contrary, some of the TFs typically expressed in progenitors and neurons during development were not detected in EVs (PAX6, EOMES, HOPX; Figures 2E, S3B, and S3C), suggesting a selective mechanism of protein loading into vesicles. We next examined common EV markers (Figure 2F) and identified unique developmental expression trajectories suggesting EV heterogeneity. Specific microvesicle markers (ANXA1, ANXA5, CAV1, and IMMT) or exosome markers (EEA1, RAB27A, RAB5B, and RAB7A)[32] also displayed a different pattern of secretion during development, suggesting a time- or cell-type-regulated secretion (Figure 2F). Together, our results show a dynamic change in the protein content loading and secretion of EVs depending on the developmental stage and cell type. Moreover, a more complex environment (3D) is associated with increased EV heterogeneity.

EV uptake dynamics is cell-type dependent

Since our proteomic analysis in both 2D neural cultures and 3D COs confirmed heterogeneity in EV protein content, we hypothesized heterogeneity also in the dynamics of EV uptake by receiving cells. To assess this, we collected and fluorescently labeled EVs from our neural cell populations previously described (pEVs, nEVs(Y), nEVs(M), and aEVs; Figures 3A–3C and S4A). Because RFP-labeled NPCs in a microfluidic chamber released RFP+ pEVs that traveled to MAP2+ neurons (Figure S4B), we applied RFP+ or DiI+ EVs directly to our neural cell populations and observed that the uptake mechanism varies between cell types. First, we examined the preferential uptake of each cell type for the different types of EVs by quantifying the percentage of cells positive for donor EVs. NPCs displayed a preference for nEV uptake, both from Y and M neurons, compared to pEVs and aEVs (Figure 3D). Interestingly, while Y neurons uptake both pEVs and aEVs indistinctly, M neurons preferentially uptake EVs released by astrocytes (Figure 3E). Astrocytes appeared to also internalize both pEVs and nEVs, with a higher uptake for M nEVs (Figure 3F). Therefore, EVs generated by the same cell type show a different uptake in recipient cell types. pEVs preferentially target Y neurons, their physiological partners during development (Figure S4C). Similarly, nEVs from Y neurons are internalized mainly by NPCs, while nEVs from M neurons target astrocytes more, a cell type they are more in communication with (Figure S4D). aEV uptake is primarily conducted by neurons (Figure S4E). We also quantified the number of EVs taken up by individual cells (particles per soma) and identified that while most cell types presenting low EV uptake also present low uptake by their individual cells, there are some instances, such as in the uptake of pEVs by NPCs, in which only 26.13% of NPCs uptake pEVs; these cells uptake, on average, 38.90% pEVs per cell compared to 18.70% nEVs (Figures S4F–S4H). We next investigated EV cellular localization following uptake in different cell types using super-resolution microscopy and Imaris 3D rendering (Oxford Instruments). Treatment of NPCs with EVs led to the detection of EVs in their cytoplasm and, more interestingly, their nucleus (Figures 3A and S4I). Both Y and M neurons appeared to internalize EVs in their soma. Additionally, using super-resolution microscopy stimulated emission depletion (STED), we confirmed the docking of EVs along the membrane of neurons at discrete locations, suggesting receptor-mediated signaling

Figure 2. Developmental characterization of EVs

(A) Schematic of analyzed developmental stages in COs. d, day. COs and EVs are generated from control line C1.

(B) Venn diagram of EV proteins at all developmental stages. d, day.

(C) Heatmap showing hierarchical clusters of EV proteins at different time points. GO enrichments of clusters are displayed. EVs were collected from the conditioned media of 15 cm Petri dishes containing 20–30 COs; EVs from different time points were collected from at least 3 different batches of COs.

(D) Venn diagram indicating the percentage of unique and common proteins secreted by NPCs and 15 day COs (top), neurons (8–10 weeks differentiation) and 360 day COs (middle), and astrocytes and 360 day COs (bottom). Functional annotations of GO enrichments of each protein group are shown.

(E) Temporal trajectories of the expression of developmental markers in EVs at different stages.

(F) Temporal trajectories of EV marker expression in EVs at different stages.

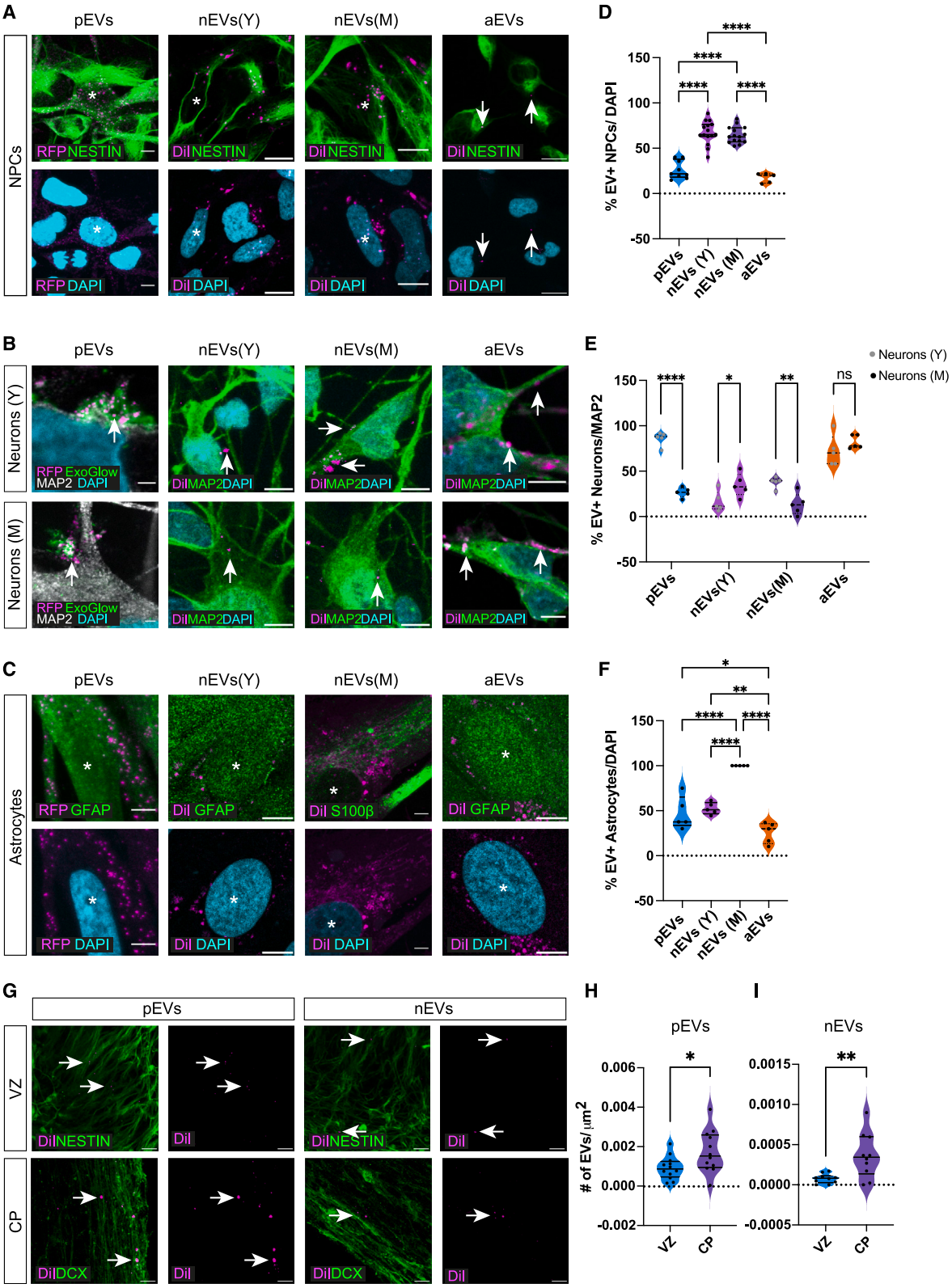

(legend on next page)

(Figures 3B and S4J). Finally, in astrocytes, we detected the uptake of EVs to the cytoplasm; however, these were not transported to the nucleus of the cells as observed in NPCs (Figures 3C and S4K). Alternatively, EVs could fuse by direct contact with the membrane of the receiving cells and induce a cellular response without being phagocytosed.[33]

We then analyzed EV uptake in COs (day 40), focusing on pEVs and nEVs(M) since these COs mainly consist of a ventricular zone (VZ) composed of progenitors and a developing cortical plate (CP) composed of maturing neurons (Figure 3G). Similar to what we observed in the 2D cultures, pEVs are preferentially localized in the CP area compared to VZ progenitors (Figure 3H). nEVs(M) are also localized mainly to the CP; however, their position is more proximal to the VZ and could therefore also be interacting with intermediate progenitors (Figures 3G and 3I).

Together, these data indicate that the mechanism by which EVs interact with recipient cells in both 2D and 3D environments varies, and therefore certain EVs, and naturally their content, could potentially have a higher impact on a specific cell type. In particular, each cell type favors EVs from other cell types compared to self-generated EVs. Moreover, each cell type preferentially takes up EVs secreted by cells that, in physiological conditions, share the same environment. For example, while NPCs mainly take up EVs coming from Y neurons, astrocytes rather favor EVs released by M neurons. Furthermore, the cellular localization of EVs in the recipient cells is distinctly cell-type specific: mostly nuclear in NPCs, membrane bound in neurons, and cytoplasmic in astrocytes, implying that the same EV could have a different signaling mechanism in each target cell.

EVs exert a brain-region-dependent signaling function

Intrigued by the idea that EV content is dependent on cell type and extracellular environment, we investigated whether EVs released from diverse donor cells may have a differential signaling function on recipient cells. For this purpose, we generated ventrally and dorsally patterned forebrain COs (vCOs and dCOs).[34,35] vCOs resemble the ventral telencephalon composed mainly of the ganglionic eminences, which give rise to various types of interneurons, while dCOs resemble the dorsal telencephalon, more specifically, the cerebral cortex. Knowing that 3D organoids are a more suitable model to generate the heterogeneity and diversity of EVs, we used brain-region-specific organoids as different sources of EVs. Thus, we profiled EV proteins from vCOs (vEVs) and dCOs (dEVs) (Figure 4A; Table S1; validation by WB in Figure S5A). vEVs and dEVs shared 62.5% of the total proteins. While vEVs only had a small fraction of unique proteins (2.5%), dEVs contained 35% of unique proteins, showing a greater heterogeneity and suggesting that dorsal and ventral cells make distinct use of EV-mediated communication (Figure 4A). Cell adhesion and motility proteins were enriched in vEVs, while RNA, microRNA (miRNA), and chromatin binding were the main functions for dEV proteins (Figure 4B; Table S1). Among the unique proteins, typical patterning-related proteins were transported either in vEVs (SHH) or dEVs (WNT3A) (Figure 4C). An essential molecular motor (KIF1A) and other proteins associated with neurodevelopmental disorders (RELN) were specific or enriched in vEVs or dEVs (Figure 4C). Single-cell RNA-seq of vCOs and dCOs indicated a similar patterned expression of SHH and KIF1A compared to their EV expression (Figures S5B and S5C). On the contrary, TUBB6 and CHD8 showed a broader RNA expression but a patterned EV protein load (Figures 4C, S5B, and S5C). Interestingly dEVs contained 84 TFs, including TFs fundamental during neurogenesis (examples in Figure 4D; Table S1), while vEVs only contained 50, 48 of which were shared with dEVs. The levels of TFs loaded into EVs did not strictly correspond with their expression levels (Figures S5B and S5C), suggesting a regulated secretion of TFs by specific cell types. To dissect if EVs, and particularly the TFs contained in EVs, have a functional role during cellular crosstalk, we investigated transcriptional changes on cells exposed to EVs. We performed RNA-seq analysis on NPCs acutely treated (12 h) with vEVs and dEVs (Figure 4E). The NPC transcriptome was significantly altered upon EV treatment, particularly upon treatment with dEVs compared to vEVs

Figure 3. EV uptake dynamics in 2D neural cell cultures and 3D COs

Cells and COs are generated from control line C1. EVs are from C1 and an RFP-labeled line (see below).

(A) Immunostaining indicating the uptake of pEVs, nEVs(Y), nEVs(M), and aEVs (magenta) by NPCs (NESTIN+). Asterisks indicate EV receiving cells, and arrows point to EVs detected in cells. DAPI, cyan. Scale bars: full image, 10 μm; close-up, 5 μm.

(B) Immunostaining indicating uptake of pEVs, nEVs(Y), nEVs(M), and aEVs (magenta) by Y (top) and M (bottom) neurons (MAP2+). Arrows point to EVs detected in cells. DAPI, cyan. Scale bars: full image, 10 μm; close-up, 1 μm.

(C) Immunostaining indicating uptake of pEVs, nEVs(Y), nEVs(M), and aEVs (magenta) by astrocytes (GFAP+ or S100b+). Asterisks indicate EV receiving cells. DAPI, cyan. Scale bars: full image, 10 μm; close-up, 5 μm.

(D) Quantification of EV+ NPCs following treatment with pEVs, nEVs(Y), nEVs(M), and aEVs. Data are represented as mean and ±SEM. Every dot refers to a field of view; $n = 9$ (pEVs), $n = 15$ (nEVs(M)), $n = 15$ (nEVs(Y)), and $n = 5$ (aEVs). Statistical significance is based on a one-way analysis of variance (ANOVA); $^{****}p < 0.0001$.

(E) Quantification of EV+ neurons(Y) and neurons(M) following treatment with pEVs, nEVs(Y), nEVs(M), and aEVs. Data are represented as mean and ±SEM. Every dot refers to a field of view; $n = 5$ (pEVs), $n = 5$ (nEVs(M)), $n = 5$ (nEVs(Y)), and $n = 5$ (aEVs). Statistical significance is based on a one-way ANOVA; $^{*}p < 0.05$, $^{**}p < 0.01$, $^{****}p < 0.0001$, and ns, not significant.

(F) Quantification of EV+ astrocytes following treatment with pEVs, nEVs(Y), nEVs(M), and aEVs. Data are represented as mean and ±SEM. Every dot refers to a field of view; $n = 5$ (pEVs), $n = 5$ (nEVs(M)), $n = 5$ (nEVs(Y)), and $n = 5$ (aEVs). Statistical significance is based on a one-way ANOVA; $^{*}p < 0.05$, $^{**}p < 0.01$, and $^{****}p < 0.0001$.

(G) Immunostaining indicating the uptake of pEVs and nEVs(M) (magenta) in the ventricular zone (VZ; NESTIN+) and cortical plate (CP; DCX+) of d40 COs. Arrows point to EVs detected in each region. Scale bar: 100 μm.

(H) Quantification of pEVs detected in the VZ (NESTIN+) and CP (DCX+) of day 40 COs. Data are represented as mean and ±SEM. Every dot refers to a field of view; $n = 12$ per condition. Statistical significance is based on a Student's t test; $^{*}p < 0.05$.

(I) Quantification of nEVs (M) detected in the VZ (NESTIN+) and CP (DCX+) of day 40 COs. Data are represented as mean and ±SEM. Every dot refers to a field of view; $n = 10$ per condition. Statistical significance is based on a Student's t test; $^{**}p < 0.01$.

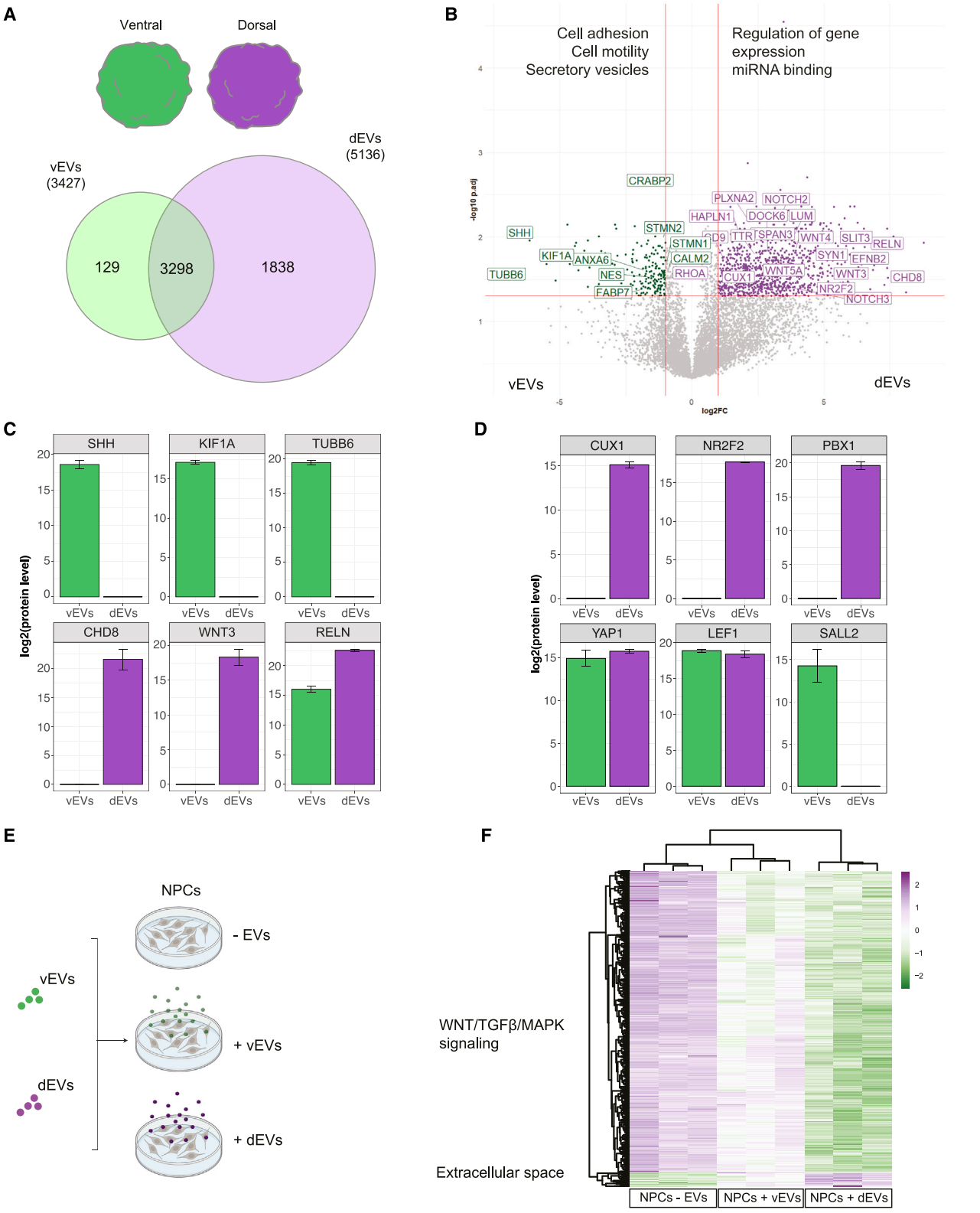

(legend on next page)

(Figure 4F; Table S1). Interestingly, GO terms associated with patterning pathways (e.g., WNT and transforming growth factor β [TGF-β] signaling[36]) were found to be dysregulated in the recipient NPCs. In addition, downstream target genes were differentially expressed according to the type of donor EVs (Figures S5D and S5E). To confirm if these transcriptional changes are due to the differential uptake of vEVs vs. dEVs in NPCs, we conducted an EV uptake assay, which showed no differences in the uptake of these two types of EVs by receiving NPCs (Figure S5D). We can therefore attribute the changes in transcription following differential EV treatment (vEVs vs. dEVs) to the varying content trafficked by each type of EV and not by a difference in their uptake.

Taken together, these results indicated that different cell fate trajectories, for example, excitatory vs. inhibitory, lead to specialized signaling mediated by EVs.

TFs transported via EVs have a signaling function on recipient cells

To identify if some of the transcriptional changes observed in NPCs exposed to EVs were caused by TFs contained in vEVs and dEVs, we analyzed the expression of their targets. BIRC5 (target of YAP1), ECT2 and RACGAP1 (targets of CUX1), and HEY1 and HEY2 (targets of NR2F2) were significantly altered according to the TF enrichment in the patterned EVs (Figures 5A, S5E, and S5F). Since YAP1 is known to be highly expressed in NPCs[37] and is secreted by NPCs via EVs at early stages of human development (Figure 5B), we tested if we could track its journey from secretion to uptake. To achieve this, donor NPCs were first transfected with a FLAG-YAP1 plasmid, then EVs containing FLAG-YAP1 were collected from their medium and used to treat recipient NPCs, which do not express FLAG-YAP1 (Figures 5C and 5F). Immunostaining with FLAG and YAP1 antibodies performed in the recipient NPCs exposed to the FLAG-YAP1 EVs revealed the presence of FLAG in the cytoplasm and nucleus of these cells (Figures 5D and 5E) with a preferential nuclear localization (arrowheads). Increased YAP1 immunofluorescence (IF) intensity was detected in the nucleus (defined by yellow outlines) of receiving cells compared to treatment with control EVs (Figures 5G and 5H). Finally, to evaluate if the higher nuclear levels of YAP1 in recipient cells also led to a physiological response, we assessed proliferation in the recipient cells 72 h following EV treatment (Figure 5I). As expected, we observed an increase in the percentage of KI67+ proliferating cells, providing evidence for a functional role of YAP1 transported via EVs (Figures 5J and 5K). Altogether, these data support not just the trafficking of TFs via EVs but their physiological effect on recipient cells. Nevertheless, we were intrigued by the question of whether the breakdown of the nuclear envelop occurring during mitosis contributed to the transport of EVs into the nuclei of NPCs. We particularly focused on the trafficking of EVs within NPCs, following our observation that this is the only cell type with nuclear uptake of EVs (Figure 3A). To assess this idea, we performed live-cell imaging of NPCs, whose nuclei were labeled with a DNA dye (NucSpot 488) and treated with fluorescently labeled EVs. We imaged cells for 24 h and analyzed them at three stages: pre-mitotic, mitotic, and post-mitotic, based on chromatin condensation (Figure 5L). We observed that out of the 39 mitotic cells identified, 20 of them (51.3%) internalized EVs (EV+ cells) (Figure 5M). At a pre-mitotic stage, 20% of them presented EVs localized within the DNA (Figure 5M). In the post-mitotic daughter cells (DCs), we observe an increase to 80% of the cells with EVs within the nucleus, colocalizing with the DNA staining (Figure 5N). Together, these data suggest that EVs play a role during neurodevelopment, as they contain many regulators, such as TFs, that can be translocated from cell to cell, reach the nucleus, and lead to functional transcriptional changes in receiving cells.

DISCUSSION

In this study, we characterized the developmental-, regional-, and cell-type-specific protein composition of EVs in human neural cells using both a 2D culture system and 3D COs, highlighting the specific function of EVs in physiological conditions. We isolated a mixture of small EVs due to the challenges of isolating specific subtypes of EVs, as exosomes and microvesicles share common markers and sizes.[28] We aimed at identifying cell-type-specific EV markers for NPCs, neurons, and astrocytes, similarly to the work presented in previous studies.[17,38] However, our results emphasize the heterogeneity of EVs and how their composition widely varies through time. EVs collected from COs clearly show that EV protein content does not strictly follow RNA expression, nor protein packaging within IVs, pointing toward a regulated dynamic process in EV protein loading that changes at different developmental stages. This is not surprising, as protein levels do not always reflect RNA expression for different reasons, including protein turnover, stability, degradation, and compartmentalization.[33] Intriguing is the comparison between IVs and EVs, which highlights the heterogeneous intracellular trafficking of vesicles. Therefore, we consider that the EV protein

Figure 4. Brain-region-dependent signaling function of EVs

COs and EVs are generated from control lines C1 and C3.

(A) Schematic of brain-region-specific COs, vCOs (ventral, green) and dCOs (dorsal, purple) (top), and Venn diagram of vCO EV (vEV) and dCO EV (dEV) proteins (bottom).

(B) Volcano plot of protein level of vEVs and dEVs from 40-day-old COs, plotting the negative log10 q-values (false discovery rate [FDR]) of all proteins against their log2 fold change (dEVs vs. vEVs). Significantly expressed proteins ($q < 0.05$) are labeled (vEVs, green; dEVs, purple). GO enrichments are shown. EVs were collected from the conditioned media of 15 cm Petri dishes containing 20–30 COs.

(C) Bar plots showing the expression of brain-region-specific markers in vEVs and dEVs. Data are represented as mean ± SD of technical replicates. $n = 2$ control (CTRL) lines and 2 EPM1 lines.

(D) Bar plots showing the expression of transcriptions factors in vEVs and dEVs. Data are represented as mean ± SD of technical replicates. $n = 2$ CTRL lines and 2 EPM1 lines.

(E) Schematic of acute treatment (12 h) of NPCs with brain-region-specific CO EVs (vEVs, ventral, green; dEVs, dorsal, purple).

(F) Heatmap showing differentially regulated genes in NPCs after treatment with vEVs and dEVs vs. no EV treatment. $n = 3$ replicates per condition.

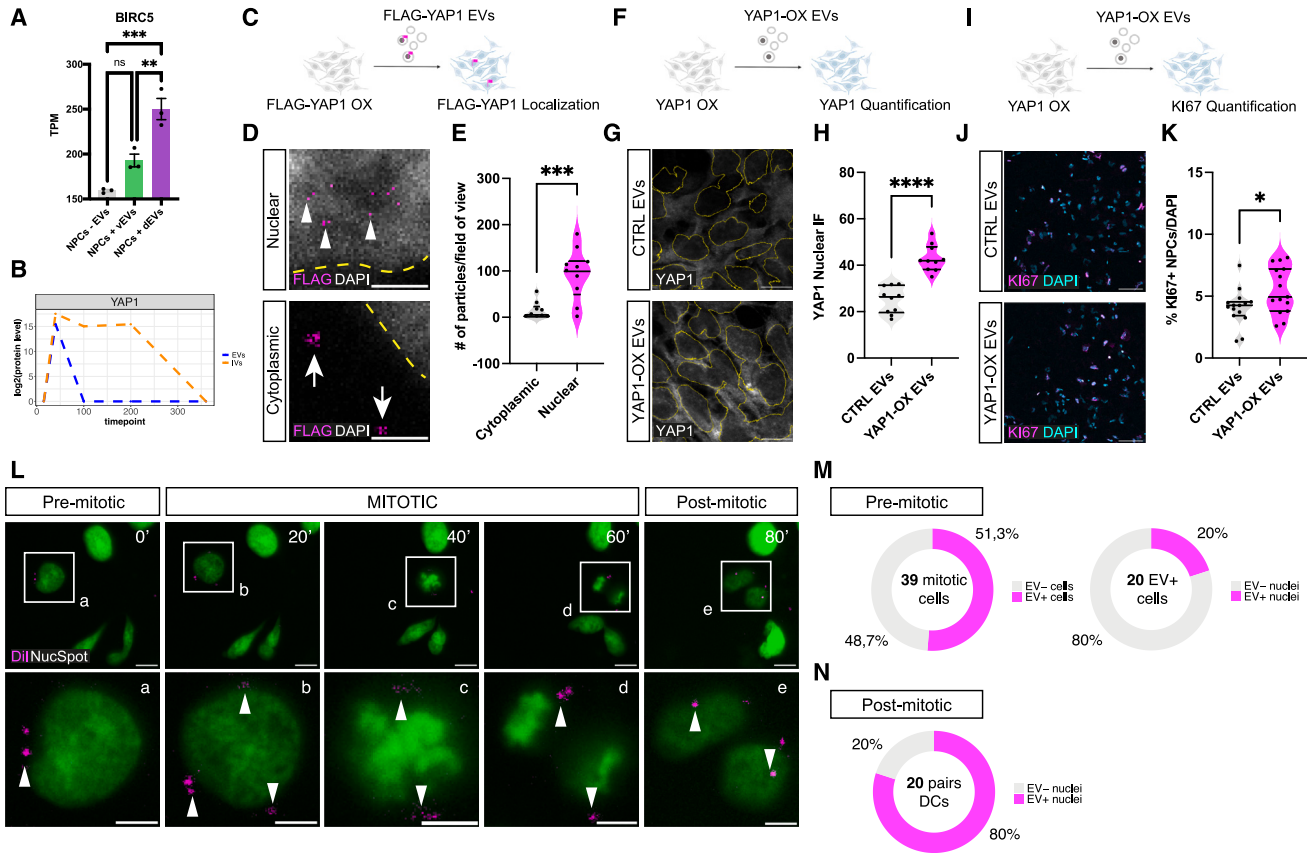

Figure 5. Trafficking of transcription factors via EVs in recipient cells

Cells and EVs are generated from control line C1.

(A) Bar plot showing the expression (TPM [transcripts per million]) of BIRC5 in NPCs after treatment with no EVs, vEVs, and dEVs. Data are represented as mean and ±SEM. $n = 3$ (per condition). Statistical significance is based on a one-way ANOVA; $^{**}p < 0.01$ and $^{***}p < 0.001$.

(B) Temporal trajectory of YAP1 expression in EVs and IVs at different stages of CO development.

(C) Schematic of treatment with FLAG-YAP1 EVs derived from FLAG-YAP1-overexpressing (FLAG-YAP1-OX) NPCs for the localization of FLAG-YAP1 in receiving NPCs.

(D) Immunostaining indicating uptake of FLAG-YAP1 EVs (magenta) by NPCs (nuclear, top; cytoplasmic, bottom) with a yellow outline delimiting the cell nuclei. Arrowheads point to EV localization in the nucleus, and arrows point to EV localization in the cytoplasm. DAPI, gray. Scale bars: 1 μm.

(E) Quantification of the number of particles (FLAG+) detected in NPCs following treatment with FLAG-YAP1 EVs in the nucleus vs. cytoplasm. Data are represented as mean and ±SEM. Every dot refers to a field of view; $n = 10$ (nuclear) and $n = 9$ (cytoplasmic). Statistical significance is based on a Student's t test; $^{***}p < 0.001$.

(F) Schematic of treatment with YAP1-OX EVs derived from YAP1-OX NPCs for the quantification of YAP1 nuclear expression in receiving NPCs.

(G) Immunostaining of YAP1 in NPCs treated with YAP1-OX EVs with a yellow outline delimiting the cell nuclei. DAPI, cyan. Scale bars: 10 μm.

(H) Quantification of nuclear YAP1 fluorescence intensity (FI) detected in NPCs following treatment with YAP1-OX EVs vs. treatment with control EVs. Data are represented as mean and ±SEM. Every dot refers to a field of view; $n = 10$ (per condition). Statistical significance is based on a Student's t test; $^{****}p < 0.0001$.

(I) Schematic of treatment with YAP1-OX EVs derived from YAP1-OX NPCs for the quantification of proliferative marker Ki67 in receiving NPCs.

(J) Immunostaining of KI67 (magenta) in NPCs treated with YAP1-OX EVs. DAPI, cyan. Scale bar: 100 μm.

(K) Quantification of KI67+ NPCs following treatment with YAP1-OX EVs vs. treatment with control EVs. Data are represented as mean and ±SEM. Every dot refers to a field of view; $n = 10$ (per condition). Statistical significance is based on a Student's t test; $^{****}p < 0.0001$.

(L) Time sequence images of EV uptake (DiI, magenta) by NPC nuclei stained with NucSpot (green) in pre-mitotic, mitotic, and post-mitotic stages. Arrowheads point to EV localization. Scale bars: full image, 10 μm; close-up, 5 μm.

(M) Quantification of pre-mitotic EV uptake by NPCs. Left: percentage of mitotic cells (39 cells) that were EV+ or EV−; right: percentage of EV+ mitotic cells (20 cells) that had EV+ nuclei or EV− nuclei.

(N) Quantification of post-mitotic EV uptake by NPCs. Percentage of pairs of daughter cells (DCs) that had EV+ nuclei or EV− nuclei.

composition is highly dependent on the state of the cell and the environment in which it is developing, as shown by the trajectory of developmental markers. Our results present the first evidence that providing a 3D environment during development is critical for building heterogeneous EVs, therefore emphasizing the contribution of tissue complexity to the landscape of EVs in the extracellular space. An increased number of proteins in EVs at late developmental stages could depend on higher cellular heterogeneity, the presence of M and active neurons, or cell death.

Our data indicate that different cell types use specific mechanisms to receive signals from EVs. These differences in composition and uptake may be responsible for a unique cell-specific crosstalk during brain development. Small EVs (exosomes and microvesicles)[39] partially overlap in size and share many extracellular surface markers, making the identification of specific subtypes not trivial.[40] In addition, they can trigger a response based on the different docking mechanisms and localization in the recipient cells.[33] For example, EVs can bind receptors to the surface of the cell, fuse their membrane, and release the content intracellularly or be internalized by different mechanisms (micropinocytosis, phagocytosis, clathrin-mediated endocytosis, lipid rafts, etc.).

While EVs from donor cells were not selectively loaded with classic transmembrane proteins associated with EVs, recipient cells showed preferential affinity with EVs from cells that were developmentally more related (e.g., NPCs and Y neurons or astrocytes and M neurons). Moreover, the cellular localization of EVs in recipient cells (e.g., nuclear in NPCs, cytoplasmic in astrocytes, and plasma membrane in neurons) indicates specific mechanisms of uptake, suggesting that EVs secreted from the same cell type can trigger different responses in different recipient cells. It was recently reported that the cellular response to EVs is highly dependent on the EV dose used during treatment.[41] Since the dosage of our EV treatment was comparable among cells, it would therefore be of relevance to manipulate the EV dosage used during our EV treatment assays to see if this modifies the pattern of uptake so far observed.

Within proteins loaded into EVs, we focus attention on the trafficking of signaling molecules and TFs. Our data show that not all TFs are transported in EVs; however, some that are relevant for human brain development, such as YAP1, are being loaded and trafficked between cells and exert a physiological function on the receiving cells. This is congruent with previous results showing the transfer of TFs in EVs derived from embryonic stem cells,[42] retinal progenitor cells,[14] and disease models of Alzheimer's disease[43] and various cancers.[44,45] However, these results also highlight the specificity of the proteins trafficked by various cell types. For instance, while a study observed the transport of PAX6 and SOX2 in retinal progenitor EVs, we do not detect these TFs in our EV samples.

Additionally, we observed the transport of EVs to the nucleus of recipient NPCs during mitosis and their localization within the nucleus in the descendant DCs. This is a process we identify as being unique for NPCs but that occurs independent of the origin of the EVs, whether they are derived from NPCs, neurons, or astrocytes. Previous studies have shown that EVs can be engulfed in the nucleus of cancer cells by nuclear envelope invaginations.[46,47] Therefore, these data point toward a mechanism within proliferating cells for the transport and incorporation of EVs within the nucleus. A new, interesting avenue would be to decipher which cytoskeletal components are relevant for this mechanism, as it is known that microtubules, actin, and intermediate filaments are the intracellular highways for EV transport.[48,49]

In conclusion, we provide novel insights into a physiological cell non-autonomous mechanism relevant for human brain development. For the first time, we present a detailed analysis supporting that although EVs present protein heterogeneity dependent on cell type and developmental stages, their biogenesis and release is a regulated process that does not strictly correspond with cellular gene expression. We also highlight the transport of physiologically functional molecules, such as TFs. Taken together, our results shed new light on the complexity of cellular crosstalk that plays a critical role in the regulation of neurodevelopmental processes.

Limitations of the study

A notable limitation of our study is the use of COs to model brain development. While COs represent a significant advance in neuroscience research and offer a more realistic model of human brain development compared to conventional cell cultures, they fall short in replicating the intricate complexity and maturity of the human brain. Specifically, COs typically mirror early developmental phases and may lack the extensive structural and functional organization observed in a fully matured brain. It is also noteworthy that COs lack important cues coming from either missing cell types (e.g., microglia) or missing signals (e.g., cerebrospinal fluid and blood vessels). Therefore, experiments carried out with an *in vivo* model system would be important to further validate our results. Additionally, in this study, we have mostly focused on NPCs to demonstrate that EVs have a role in neurogenesis. However, a more complex system containing a more heterogeneous population of cells would be crucial to provide additional evidence of crosstalk between different cell types.

RESOURCE AVAILABILITY

Lead contact

Further information and requests for resources and reagents should be directed to and will be fulfilled by the lead contact, Prof. Dr. Silvia Cappello (silvia.cappello@bmc.med.lmu.de).

Materials availability

This study did not generate new unique reagents.

Data and code availability

- RNA-seq and single-cell RNA-seq data have been deposited at the Gene Expression Omnibus under GEO: GSE197252 and GSE202874, respectively. The mass spectrometry proteomics data have been deposited to the ProteomeXchange Consortium via the PRIDE[50,51] partner repository with the dataset identifier PXD028438.
- This paper does not report original code.
- Any additional information required to reanalyze the data reported in this paper is available from the lead contact upon request.

ACKNOWLEDGMENTS

We thank I. Miinalainen, M. Ködel, C. Cruceanu, C. Turk, S. Zünd, S. Dietzela, and P. Gressens for technical help and critical discussions. We are grateful to all the members of the Cappello, Nguyen, Baulac, Jabaudon, and Baffet labs for the exciting scientific exchange and development of novel ideas over the past few years. This project is supported by ERA-Net E-Rare (HETEROMICS | 01GM1914), the European Union (ERC Consolidator Grant, ExoDevo | 101043959), the Fritz Thyssen Stiftung, the DFG (CA1205/4-1-RU1232/7-1), Italian Ministry of Foreign Affairs and International Cooperation (MAE02035442023-11-16), FRA2022_lineaB_EXOCSTB_Di_Giaimo, and the Munich Cluster for Systems Neurology (SyNergy).

AUTHOR CONTRIBUTIONS

Conceptualization, S.C. and R.D.G.; methodology, R.D.G., F.P., A.F., G.M., P.K., S.M., C.G., M.W.P., and M.G.P.; investigation, S.C., R.D.G., F.P., A.F., N.B., and F.M.C.; visualization, S.C., F.P., A.F., S.M., B.P., and M.G.P.; funding acquisition, S.C.; supervision, S.C., R.D.G., and G.M.; writing – original draft, S.C.; writing – review & editing, S.C., R.D.G., F.P., and A.F.

DECLARATION OF INTERESTS

The authors declare no competing interests.

STAR★METHODS

Detailed methods are provided in the online version of this paper and include the following:

- KEY RESOURCES TABLE
- EXPERIMENTAL MODEL AND STUDY PARTICIPANT DETAILS
  - Cell lines
- METHOD DETAILS
  - IPSC generation and maintenance
  - Generation of RFP-labelled iPSC lines
  - Generation of unpatterned human cerebral organoids
  - Generation of dorsally- and ventrally- patterned human cerebral organoids
  - NPC, neuron and astrocyte cultures
  - FLAG-YAP1 overexpression and EV exchange
  - EV and IV collection and analysis
  - EV uptake assay in 2D cell cultures
  - EV uptake assay in sectioned COs
  - Immunohistochemistry
  - Imaging
  - Microfluidics chamber
  - Proteomic analysis
  - Validation of proteomic results with automated western blot
  - Single-cell RNA-sequencing
  - Bulk-RNA-sequencing
  - RNAseq analysis
- QUANTIFICATION AND STATISTICAL ANALYSIS
  - Quantification of EV markers in cell types
  - Quantification of EV uptake by cell types
  - Quantification of EV uptake by CO sections
  - Proteomic statistical analysis
  - RNAseq statistical analysis
  - Enrichment analysis

SUPPLEMENTAL INFORMATION

Supplemental information can be found online at https://doi.org/10.1016/j.celrep.2024.114755.

Received: November 22, 2023
Revised: July 3, 2024
Accepted: August 29, 2024
Published: September 19, 2024

REFERENCES

1. Taverna, E., Gotz, M., Huttner, W.B., Siripala, A.D., Welch, M.D., Azzarelli, R., Kerloch, T., Pacary, E., Morgan, D.O., Croft, D.R., et al. (2007). The cell biology of neurogenesis: toward an understanding of the development and evolution of the neocortex. Cell *135*, 465–502. https://doi.org/10.1146/annurev-cellbio-101011-155801.
2. Heng, J.I.T., Chariot, A., and Nguyen, L. (2010). Molecular layers underlying cytoskeletal remodelling during cortical development. Trends Neurosci. *33*, 38–47. https://doi.org/10.1016/j.tins.2009.09.003.
3. Rakic, P. (2009). Evolution of the neocortex: a perspective from developmental biology. Nat. Rev. Neurosci. *10*, 724–735. https://doi.org/10.1038/nrn2719.
4. Peruzzotti-Jametti, L., Bernstock, J.D., Willis, C.M., Manferrari, G., Rogall, R., Fernandez-Vizarra, E., Williamson, J.C., Braga, A., van den Bosch, A., Leonardi, T., et al. (2021). Neural stem cells traffic functional mitochondria via extracellular vesicles. PLoS Biol. *19*, e3001166. https://doi.org/10.1371/journal.pbio.3001166.
5. Pellegrini, L., Bonfio, C., Chadwick, J., Begum, F., Skehel, M., and Lancaster, M.A. (2020). Human CNS barrier-forming organoids with cerebrospinal fluid production. Science *369*, eaaz5626. https://doi.org/10.1126/science.aaz5626.
6. Long, K.R., Newland, B., Florio, M., Kalebic, N., Langen, B., Kolterer, A., Wimberger, P., and Huttner, W.B. (2018). Extracellular Matrix Components HAPLN1, Lumican, and Collagen I Cause Hyaluronic Acid-Dependent Folding of the Developing Human Neocortex. Neuron *99*, 702–719.e6. https://doi.org/10.1016/j.neuron.2018.07.013.
7. Sharma, P., Mesci, P., Carromeu, C., McClatchy, D.R., Schiapparelli, L., Yates, J.R., Muotri, A.R., and Cline, H.T. (2019). Exosomes regulate neurogenesis and circuit assembly. Proc. Natl. Acad. Sci. USA *116*, 16086–16094. https://doi.org/10.1073/pnas.1902513116.
8. Long, K.R., and Huttner, W.B. (2019). How the Extracellular Matrix Shapes Neural Development. Preprint at Royal Society Publishing. https://doi.org/10.1098/rsob.180216.
9. Silva, C.G., Peyre, E., and Nguyen, L. (2019). Cell Migration Promotes Dynamic Cellular Interactions to Control Cerebral Cortex Morphogenesis. Preprint at Nature Publishing Group. https://doi.org/10.1038/s41583-019-0148-y.
10. Di Giaimo, R., Penna, E., Pizzella, A., Cirillo, R., Perrone-Capano, C., and Crispino, M. (2020). Cross Talk at the Cytoskeleton–Plasma Membrane Interface: Impact on Neuronal Morphology and Functions. Int. J. Mol. Sci. *21*, 9133. https://doi.org/10.3390/ijms21239133.
11. Gomes, A.R., Sangani, N.B., Fernandes, T.G., Diogo, M.M., Curfs, L.M.G., and Reutelingsperger, C.P. (2020). Extracellular Vesicles in CNS Developmental Disorders. Int. J. Mol. Sci. *21*, 9428. https://doi.org/10.3390/IJMS21249428.
12. Van Niel, G., D'Angelo, G., and Raposo, G. (2018). Shedding Light on the Cell Biology of Extracellular Vesicles. Preprint at Nature Publishing Group. https://doi.org/10.1038/nrm.2017.125.
13. Marzesco, A.M., Janich, P., Wilsch-Bräuninger, M., Dubreuil, V., Langenfeld, K., Corbeil, D., and Huttner, W.B. (2005). Release of extracellular membrane particles carrying the stem cell marker prominin-1 (CD133) from neural progenitors and other epithelial cells. J. Cell Sci. *118*, 2849–2858. https://doi.org/10.1242/JCS.02439.
14. Zhou, J., Benito-Martin, A., Mighty, J., Chang, L., Ghoroghi, S., Wu, H., Wong, M., Guariglia, S., Baranov, P., Young, M., et al. (2018). Retinal progenitor cells release extracellular vesicles containing developmental transcription factors, microRNA and membrane proteins. Sci. Rep. *8*, 2823–2915. https://doi.org/10.1038/s41598-018-20421-1.
15. Zhou, J., Flores-Bellver, M., Pan, J., Benito-Martin, A., Shi, C., Onwumere, O., Mighty, J., Qian, J., Zhong, X., Hogue, T., et al. (2021). Human retinal organoids release extracellular vesicles that regulate gene expression in target human retinal progenitor cells. Sci. Rep. *11*, 21128. https://doi.org/10.1038/s41598-021-00542-w.
16. Fauré, J., Lachenal, G., Court, M., Hirrlinger, J., Chatellard-Causse, C., Blot, B., Grange, J., Schoehn, G., Goldberg, Y., Boyer, V., et al. (2006). Exosomes are released by cultured cortical neurones. Mol. Cell. Neurosci. *31*, 642–648. https://doi.org/10.1016/J.MCN.2005.12.003.
17. Patel, M.R., and Weaver, A.M. (2021). Astrocyte-derived small extracellular vesicles promote synapse formation via fibulin-2-mediated

TGF-β signaling. Cell Rep. *34*, 108829. https://doi.org/10.1016/j.celrep.2021.108829.

18. Schiera, G., Di Liegro, C.M., and Di Liegro, I. (2015). Extracellular Membrane Vesicles as Vehicles for Brain Cell-to-Cell Interactions in Physiological as well as Pathological Conditions. BioMed Res. Int. *2015*, 152926. https://doi.org/10.1155/2015/152926.
19. Takeda, Y.S., and Xu, Q. (2015). Neuronal Differentiation of Human Mesenchymal Stem Cells Using Exosomes Derived from Differentiating Neuronal Cells. PLoS One *10*, e0135111. https://doi.org/10.1371/JOURNAL.PONE.0135111.
20. Kyrousi, C., O'Neill, A.C., Brazovskaja, A., He, Z., Kielkowski, P., Coquand, L., Di Giaimo, R., D' Andrea, P., Belka, A., Forero Echeverry, A., et al. (2021). Extracellular LGALS3BP regulates neural progenitor position and relates to human cortical complexity. Nat. Commun. *12*, 6298. https://doi.org/10.1038/s41467-021-26447-w.
21. Pipicelli, F., Baumann, N., Di Giaimo, R., Forero-Echeverry, A., Kyrousi, C., Bonrath, R., Maccarrone, G., Jabaudon, D., and Cappello, S. (2023). Non-cell-autonomous regulation of interneuron specification mediated by extracellular vesicles. Sci. Adv. *9*, eadd8164. https://doi.org/10.1126/SCIADV.ADD8164.
22. Albacete-Albacete, L., Sánchez-Álvarez, M., and del Pozo, M.A. (2021). Extracellular Vesicles: An Emerging Mechanism Governing the Secretion and Biological Roles of Tenascin-C. Front. Immunol. *12*, 1425. https://doi.org/10.3389/FIMMU.2021.671485/BIBTEX.
23. Rilla, K., Mustonen, A.M., Arasu, U.T., Härkönen, K., Matilainen, J., and Nieminen, P. (2019). Extracellular vesicles are integral and functional components of the extracellular matrix. Matrix Biol. *75–76*, 201–219. https://doi.org/10.1016/J.MATBIO.2017.10.003.
24. Nawaz, M., Shah, N., Zanetti, B.R., Maugeri, M., Silvestre, R.N., Fatima, F., Neder, L., and Valadi, H. (2018). Extracellular Vesicles and Matrix Remodeling Enzymes: The Emerging Roles in Extracellular Matrix Remodeling, Progression of Diseases and Tissue Repair. Cells *7*, 167. https://doi.org/10.3390/CELLS7100167.
25. Davies, O.G., Cox, S.C., Williams, R.L., Tsaroucha, D., Dorrepaal, R.M., Lewis, M.P., and Grover, L.M. (2017). Annexin-enriched osteoblast-derived vesicles act as an extracellular site of mineral nucleation within developing stem cell cultures. Sci. Rep. *7*, 12639. https://doi.org/10.1038/s41598-017-13027-6.
26. Mathieu, M., Martin-Jaular, L., Lavieu, G., and Théry, C. (2019). Specificities of secretion and uptake of exosomes and other extracellular vesicles for cell-to-cell communication. Nat. Cell Biol. *21*, 9–17. https://doi.org/10.1038/s41556-018-0250-9.
27. Théry, C., Amigorena, S., Raposo, G., and Clayton, A. (2006). Isolation and Characterization of Exosomes from Cell Culture Supernatants and Biological Fluids. Curr. Protoc. Cell Biol. *30*, 3.22.1–3.22.29. https://doi.org/10.1002/0471143030.CB0322S30.
28. Théry, C., Witwer, K.W., Aikawa, E., Alcaraz, M.J., Anderson, J.D., Andriantsitohaina, R., Antoniou, A., Arab, T., Archer, F., Atkin-Smith, G.K., et al. (2018). Minimal information for studies of extracellular vesicles 2018 (MISEV2018): a position statement of the International Society for Extracellular Vesicles and update of the MISEV2014 guidelines. J. Extracell. Vesicles *7*, 1535750. https://doi.org/10.1080/20013078.2018.1535750.
29. Men, Y., Yelick, J., Jin, S., Tian, Y., Chiang, M.S.R., Higashimori, H., Brown, E., Jarvis, R., Yang, Y., and Yang, Y. (2019). Exosome reporter mice reveal the involvement of exosomes in mediating neuron to astroglia communication in the CNS. Nat. Commun. *10*, 4136. https://doi.org/10.1038/s41467-019-11534-w.
30. Andreu, Z., and Yáñez-Mó, M. (2014). Tetraspanins in extracellular vesicle formation and function. Front. Immunol. *5*, 442. https://doi.org/10.3389/FIMMU.2014.00442.
31. Cruceanu, C., Dony, L., Krontira, A.C., Fischer, D.S., Roeh, S., Di Giaimo, R., Kyrousi, C., Kaspar, L., Arloth, J., Czamara, D., et al. (2022). Cell-Type-Specific Impact of Glucocorticoid Receptor Activation on the Developing Brain: A Cerebral Organoid Study. Am. J. Psychiatry *179*, 375–387. https://doi.org/10.1176/APPI.AJP.2021.21010095.
32. D'Acunzo, P., Pérez-González, R., Kim, Y., Hargash, T., Miller, C., Alldred, M.J., Erdjument-Bromage, H., Penikalapati, S.C., Pawlik, M., Saito, M., et al. (2021). Mitovesicles are a novel population of extracellular vesicles of mitochondrial origin altered in Down syndrome. Sci. Adv. *7*, eabe5085. https://doi.org/10.1126/SCIADV.ABE5085.
33. van Niel, G., D'Angelo, G., and Raposo, G. (2018). Shedding light on the cell biology of extracellular vesicles. Nat. Rev. Mol. Cell Biol. *19*, 213–228. https://doi.org/10.1038/nrm.2017.125.
34. Lancaster, M.A., and Knoblich, J.A. (2014). Generation of cerebral organoids from human pluripotent stem cells. Nat. Protoc. *9*, 2329–2340. https://doi.org/10.1038/nprot.2014.158.
35. Bagley, J.A., Reumann, D., Bian, S., Lévi-Strauss, J., and Knoblich, J.A. (2017). Fused cerebral organoids model interactions between brain regions. Nat. Methods *7*, 743–751. https://doi.org/10.1038/nmeth.4304.
36. Falk, S., Wurdak, H., Ittner, L.M., Ille, F., Sumara, G., Schmid, M.-T., Draganova, K., Lang, K.S., Paratore, C., Leveen, P., et al. (2008). Brain Area-Specific Effect of TGF-β Signaling on Wnt-Dependent Neural Stem Cell Expansion. Cell Stem Cell *2*, 472–483. https://doi.org/10.1016/j.stem.2008.03.006.
37. Sahu, M.R., and Mondal, A.C. (2021). Neuronal Hippo signaling: From development to diseases. Dev. Neurobiol. *81*, 92–109. https://doi.org/10.1002/DNEU.22796.
38. You, Y., Muraoka, S., Jedrychowski, M.P., Hu, J., McQuade, A.K., Young-Pearse, T., Aslebagh, R., Shaffer, S.A., Gygi, S.P., Blurton-Jones, M., et al. (2022). Human neural cell type-specific extracellular vesicle proteome defines disease-related molecules associated with activated astrocytes in Alzheimer's disease brain. J. Extracell. Vesicles *11*, e12183. https://doi.org/10.1002/JEV2.12183.
39. Nallakumarasamy, A., Jeyaraman, M., Maffulli, N., Jeyaraman, N., Suresh, V., Ravichandran, S., Gupta, M., Potty, A.G., El-Amin, S.F., Khanna, M., and Gupta, A. (2022). Mesenchymal Stromal Cell-Derived Extracellular Vesicles in Wound Healing. Life *12*, 1733. https://doi.org/10.3390/life12111733.
40. Gurung, S., Perocheau, D., Touramanidou, L., and Baruteau, J. (2021). The exosome journey: from biogenesis to uptake and intracellular signalling. Cell Commun. Signal. *19*, 47. https://doi.org/10.1186/s12964-021-00730-1.
41. Hagey, D.W., Ojansivu, M., Bostancioglu, B.R., Saher, O., Bost, J.P., Gustafsson, M.O., Gramignoli, R., Svahn, M., Gupta, D., Stevens, M.M., et al. (2023). The cellular response to extracellular vesicles is dependent on their cell source and dose. Sci. Adv. *9*, eadh1168. https://doi.org/10.1126/SCIADV.ADH1168/SUPPL_FILE/SCIADV.ADH1168_TABLES_S1_TO_S3.ZIP.
42. Ratajczak, J., Miekus, K., Kucia, M., Zhang, J., Reca, R., Dvorak, P., and Ratajczak, M.Z. (2006). Embryonic stem cell-derived microvesicles reprogram hematopoietic progenitors: evidence for horizontal transfer of mRNA and protein delivery. Leukemia *20*, 847–856. https://doi.org/10.1038/sj.leu.2404132.
43. Goetzl, E.J., Boxer, A., Schwartz, J.B., Abner, E.L., Petersen, R.C., Miller, B.L., Carlson, O.D., Mustapic, M., and Kapogiannis, D. (2015). Low neural exosomal levels of cellular survival factors in Alzheimer's disease. Ann. Clin. Transl. Neurol. *2*, 769–773. https://doi.org/10.1002/ACN3.211.
44. Ung, T.H., Madsen, H.J., Hellwinkel, J.E., Lencioni, A.M., and Graner, M.W. (2014). Exosome proteomics reveals transcriptional regulator proteins with potential to mediate downstream pathways. Cancer Sci. *105*, 1384–1392. https://doi.org/10.1111/CAS.12534.
45. Chen, T.Y., Gonzalez-Kozlova, E., Soleymani, T., La Salvia, S., Kyprianou, N., Sahoo, S., Tewari, A.K., Cordon-Cardo, C., Stolovitzky, G., and Dogra, N. (2022). Extracellular vesicles carry distinct proteo-transcriptomic signatures that are different from their cancer cell of origin. iScience *25*, 104414. https://doi.org/10.1016/j.isci.2022.104414.

46. Corbeil, D., Santos, M.F., Karbanová, J., Kurth, T., Rappa, G., and Lorico, A. (2020). Uptake and Fate of Extracellular Membrane Vesicles: Nucleoplasmic Reticulum-Associated Late Endosomes as a New Gate to Intercellular Communication. Cells *9*, 1931. https://doi.org/10.3390/CELLS9091931.

47. Rappa, G., Santos, M.F., Green, T.M., Karbanová, J., Hassler, J., Bai, Y., Barsky, S.H., Corbeil, D., and Lorico, A. (2017). Nuclear transport of cancer extracellular vesicle-derived biomaterials through nuclear envelope invagination-associated late endosomes. Oncotarget *8*, 14443–14461. https://doi.org/10.18632/ONCOTARGET.14804.

48. Kamal, A., and Goldstein, L.S. (2000). Connecting vesicle transport to the cytoskeleton. Curr. Opin. Cell Biol. *12*, 503–508. https://doi.org/10.1016/S0955-0674(00)00123-X.

49. O'Brien, K., Breyne, K., Ughetto, S., Laurent, L.C., and Breakefield, X.O. (2020). RNA delivery by extracellular vesicles in mammalian cells and its applications. Nat. Rev. Mol. Cell Biol. *21*, 585–606. https://doi.org/10.1038/s41580-020-0251-y.

50. Deutsch, E.W., Bandeira, N., Sharma, V., Perez-Riverol, Y., Carver, J.J., Kundu, D.J., García-Seisdedos, D., Jarnuczak, A.F., Hewapathirana, S., Pullman, B.S., et al. (2020). The ProteomeXchange consortium in 2020: enabling "big data" approaches in proteomics. Nucleic Acids Res. *48*, D1145–D1152. https://doi.org/10.1093/nar/gkz984.

51. Perez-Riverol, Y., Csordas, A., Bai, J., Bernal-Llinares, M., Hewapathirana, S., Kundu, D.J., Inuganti, A., Griss, J., Mayer, G., Eisenacher, M., et al. (2019). The PRIDE database and related tools and resources in 2019: improving support for quantification data. Nucleic Acids Res. *47*, D442–D450. https://doi.org/10.1093/nar/gky1106.

52. Rispoli, A., Cipollini, E., Catania, S., Di Giaimo, R., Pulice, G., van Houte, S., Sparla, F., Dal Piaz, F., Roncarati, D., Trost, P., and Melli, M. (2013). Insights in progressive myoclonus epilepsy: HSP70 promotes cystatin B polymerization. Biochim. Biophys. Acta *1834*, 2591–2599. https://doi.org/10.1016/j.bbapap.2013.09.011.

53. Klaus, J., Kanton, S., Kyrousi, C., Ayo-Martin, A.C., Di Giaimo, R., Riesenberg, S., O'Neill, A.C., Camp, J.G., Tocco, C., Santel, M., et al. (2019). Altered neuronal migratory trajectories in human cerebral organoids derived from individuals with neuronal heterotopia. Nat. Med. *25*, 561–568. https://doi.org/10.1038/s41591-019-0371-0.

54. Di Matteo, F., Pipicelli, F., Kyrousi, C., Tovecci, I., Penna, E., Crispino, M., Chambery, A., Russo, R., Ayo-Martin, A.C., Giordano, M., et al. (2020). Cystatin B is essential for proliferation and interneuron migration in individuals with EPM1 epilepsy. EMBO Mol. Med. *12*, e11419.

55. F, C., and J, L. (2012). A method for stable transgenesis of radial glia lineage in rat neocortex by piggyBac mediated transposition. J. Neurosci. Methods *207*, 172–180. https://doi.org/10.1016/J.JNEUMETH.2012.03.016.

56. Lancaster, M.A., Renner, M., Martin, C.A., Wenzel, D., Bicknell, L.S., Hurles, M.E., Homfray, T., Penninger, J.M., Jackson, A.P., and Knoblich, J.A. (2013). Cerebral organoids model human brain development and microcephaly. Nature *501*, 373–379. https://doi.org/10.1038/nature12517.

57. Boyer, L.F., Campbell, B., Larkin, S., Mu, Y., and Gage, F.H. (2012). Dopaminergic differentiation of human pluripotent cells. Curr Protoc Stem Cell Biol *Chapter 1*, Unit1H-6. https://doi.org/10.1002/9780470151808.sc01h06s22.

58. Gunhanlar, N., Shpak, G., van der Kroeg, M., Gouty-Colomer, L.A., Munshi, S.T., Lendemeijer, B., Ghazvini, M., Dupont, C., Hoogendijk, W.J.G., Gribnau, J., et al. (2018). A simplified protocol for differentiation of electrophysiologically mature neuronal networks from human induced pluripotent stem cells. Mol. Psychiatry *23*, 1336–1344. https://doi.org/10.1038/mp.2017.56.

59. Cappello, S., Gray, M.J., Badouel, C., Lange, S., Einsiedler, M., Srour, M., Chitayat, D., Hamdan, F.F., Jenkins, Z.A., Morgan, T., et al. (2013). Mutations in genes encoding the cadherin receptor-ligand pair DCHS1 and FAT4 disrupt cerebral cortical development. Nat. Genet. *45*, 1300–1308.

60. Schneider, C.A., Rasband, W.S., and Eliceiri, K.W. (2012). NIH Image to ImageJ: 25 years of image analysis. Nat. Methods *9*, 671–675. https://doi.org/10.1038/nmeth.2089.

61. Ferrara, E., Cefaliello, C., Eyman, M., De Stefano, R., Giuditta, A., and Crispino, M. (2009). Synaptic mRNAs are modulated by learning. J. Neurosci. Res. *87*, 1960–1968. https://doi.org/10.1002/jnr.22037.

62. Deun, J.V., Roux, Q., Deville, S., Acker, T.V., Rappu, P., Miinalainen, I., Heino, J., Vanhaecke, F., Geest, B.G.D., De Wever, O., et al. (2020). Feasibility of Mechanical Extrusion to Coat Nanoparticles with Extracellular Vesicle Membranes. Cells *9*, 1797–1799. https://doi.org/10.3390/CELLS9081797.

63. Wiśniewski, J.R., Zougman, A., Nagaraj, N., and Mann, M. (2009). Universal sample preparation method for proteome analysis. Nat. Methods *6*, 359–362. https://doi.org/10.1038/nmeth.1322.

64. Tyanova, S., Temu, T., and Cox, J. (2016). The MaxQuant computational platform for mass spectrometry-based shotgun proteomics. Nat. Protoc. *11*, 2301–2319. https://doi.org/10.1038/nprot.2016.136.

65. Prianichnikov, N., Koch, H., Koch, S., Lubeck, M., Heilig, R., Brehmer, S., Fischer, R., and Cox, J. (2020). MaxQuant Software for Ion Mobility Enhanced Shotgun Proteomics. Mol. Cell. Proteomics *19*, 1058–1069. https://doi.org/10.1074/MCP.TIR119.001720.

66. Cernilogar, F.M., Hasenöder, S., Wang, Z., Scheibner, K., Burtscher, I., Sterr, M., Smialowski, P., Groh, S., Evenroed, I.M., Gilfillan, G.D., et al. (2019). Pre-marked chromatin and transcription factor co-binding shape the pioneering activity of Foxa2. Nucleic Acids Res. *47*, 9069–9086. https://doi.org/10.1093/nar/gkz627.

67. Dobin, A., Davis, C.A., Schlesinger, F., Drenkow, J., Zaleski, C., Jha, S., Batut, P., Chaisson, M., and Gingeras, T.R. (2013). STAR: ultrafast universal RNA-seq aligner. Bioinformatics *29*, 15–21. https://doi.org/10.1093/BIOINFORMATICS/BTS635.

68. Love, M.I., Huber, W., and Anders, S. (2014). Moderated estimation of fold change and dispersion for RNA-seq data with DESeq2. Genome Biol. *15*, 550. https://doi.org/10.1186/S13059-014-0550-8.

69. Watanabe K., Taskesen E., van Bochoven A., and Posthuma D. (2017). Functional mapping and annotation of genetic associations with FUMA. Nature Communications 2017 8:1 *8*, 1–11. https://doi.org/10.1038/s41467-017-01261-5.

STAR★METHODS

KEY RESOURCES TABLE

REAGENT or RESOURCE	SOURCE	IDENTIFIER
Antibodies		
Mouse monoclonal Anti-CD63	Santa Cruz	Cat#sc-5275; Lot#I2719; RRID:AB_627877
Mouse monoclonal Anti-CD81	Santa Cruz	Cat#sc-7637; Lot#K0819; RRID:AB_627190
Rabbit polyclonal Anti-KAI 1	Santa Cruz	Cat#sc-1087; Lot#J2814; RRID:AB_2244586
Mouse monoclonal Anti-CD9	Santa Cruz	Cat#sc-59140; Lot#K1220; RRID:AB_1120766
Mouse monoclonal Anti-PDCD6IP (ALIX)	Santa Cruz	Cat#sc-53540; Lot#I1219; RRID:AB_673819
Rabbit polyclonal Anti-SOX2	Abcam	Cat#ab5603; Lot#2682436; RRID:AB_2286686
Chicken polyclonal Anti-MAP2	Abcam	Cat#ab5392; Lot#GR3366474-1; RRID:AB_2138153
Rabbit polyclonal Anti-GFAP	Agilent Dako	Cat#Z0334; Lot#20080613; RRID:AB_10013382
Chicken polyclonal Anti-RFP	Rockland	Cat#600-901-379S; Lot#30253; RRID:AB_10703148
Mouse monoclonal Anti-NESTIN	EMD Millipore	Cat#MAB5326; Lot#3112610; RRID:AB_2251134
Mouse monoclonal Anti-S100β	Sigma	Cat#S2532; Lot#048M4858V; RRID:AB_477499
Guinea pig polyclonal Anti-DCX	EMD Millipore	Cat#AB2253; Lot#3601335; RRID:AB_1586992
Rabbit polyclonal Anti-KI67	Abcam	Cat#AB15580; RRID:AB_443209
Chicken polyclonal Anti-GFP	Rockland	Cat#600-901-215; RRID:AB_1537403;
Mouse monoclonal Anti-RELN	EMD Millipore	Cat#MAB5366 Lot#3601682; RRID:AB_2285132
Mouse monoclonal Anti-LGALS3 (galectin-3)	Santa Cruz	Cat# sc-53127; Lot#K1918; RRID:AB_629514
Mouse monoclonal Anti-ANXA5 (Annexin V)	Santa Cruz	Cat#sc-74438; Lot#I2717; RRID:AB_1118989
Mouse monoclonal Anti-β-Tubulin III	Sigma	Cat# T8660; Lot#097M4835V; RRID:AB_477590
Rabbit polyclonal Anti-FABP7 (BLBP)	EMD Millipore	Cat#ABN14; Lot#3160120; RRID:AB_10000325
Mouse monoclonal Anti-MEIS1/2/3	Santa Cruz	Cat#sc-101850; Lot#H0817; RRID:AB_2143143
Alexa Fluor® 488 Goat Anti-Chicken IgY (H + L)	ThermoFisher Scientific	Cat#A-11039; RRID:AB_2534096
Alexa Fluor® 647 Goat Anti-Guinea Pig IgG (H + L), highly cross-adsorbed	ThermoFisher Scientific	Cat#A-21450; RRID:AB_2535867
Alexa Fluor® 488 Goat Anti-Mouse IgG (H + L) highly cross-adsorbed	ThermoFisher Scientific	Cat#A-21141; RRID:AB_2535778
Alexa Fluor® 546 Goat Anti-Rabbit IgG (H + L), highly cross-adsorbed	ThermoFisher Scientific	Cat#A-11035; RRID:AB_2534093
Alexa Fluor® 647 Goat Anti-Mouse IgG (H + L) cross-adsorbed	ThermoFisher Scientific	Cat#A-21235; RRID:AB_2535804
Chemicals, peptides, and recombinant proteins		
Vybrant™ Multicolor Cell-Labeling Kit	ThermoFisher Scientific	Cat#V22889
NucSpot® Live Cell Nuclear Stains	Biotium	Cat#40081
Smoothened Agonist (SAG)	EMD Millipore	Cat#566660
IWP-2	Sigma-Aldrich	Cat# I0536

(*Continued on next page*)

Continued

REAGENT or RESOURCE	SOURCE	IDENTIFIER
Cyclopamine A	Calbiochem	Cat#239803
Critical commercial assays		
miRCURY Exosome Cell/Urine/CSF Kit	Qiagen	Cat#76743
Lipofectamine™ 3000 Transfection Reagent	ThermoFisher Scientific	Cat#L3000015
Chromium Next GEM Chip G Single Cell Kit	10XGenomics	Cat#PN-1000127
Chromium Next GEM Single Cell 3' GEM, Library & Gel Bead Kit v3.1	10XGenomics	Cat#PN-1000128
Single Index Kit T Set A	10XGenomics	Cat#PN-1000213
SMART-Seq v4 Ultra Low Input RNA Kit	Clontech	Cat#634888
Deposited data		
Mass spectrometry proteomics data	ProteomeXchange Consortium	PXD038760
Single-cell RNA-seq dataset	Gene Expression Omnibus	GSE202874
Bulk RNA-seq dataset	Gene Expression Omnibus	GSE197252
Experimental models: cell lines		
BJ (human newborn foreskin fibroblasts)	ATCC	CRL-2522
C3 Control IPSCs	Prof. Dr. Silvia Cappello	N/A
Recombinant DNA		
pCMV-flag YAP2 5SA	Kunliang Guan	Addgene #27371
pEGFP-C1	Rispoli et al.[52]	N/A
PBCAG-eGFP	Joseph Loturco	Addgene #40973
PBCAG-mRFP	Joseph Loturco	Addgene #40996
Software and algorithms		
ImageJ software	NIH	https://imagej.nih.gov/ij/
Imaris (v9.7.2)	Oxford Instruments	https://imaris.oxinst.com/
MaxQuant computational platform (v1.6.17.0)	Max-Planck-Institute of Biochemistry	https://www.maxquant.org/
R v4.1.0	R Core Team	https://www.r-project.org/
R package DEP (v1.15.0)	Arne Smits, Wolfgang Huber	https://www.bioconductor.org/packages/release/bioc/html/DEP.html
R package Seurat (v3.2)	Satija Lab	https://satijalab.org/seurat/
R package pheatmap (v1.0.12)	Raivo Kolde	https://cran.r-project.org/web/packages/pheatmap/index.html
STAR (v2.6.1d)	Alexander Dobin	https://github.com/alexdobin/STAR
R package DESeq2 (v1.32.0)	Michael Love	https://bioconductor.org/packages/release/bioc/html/DESeq2.html
GraphPad Prism 8	GraphPad, Inc	https://www.graphpad.com/scientific-software/prism/
GENE2FUNC software	Posthuma Lab	https://fuma.ctglab.nl/
Other		
900 μm microgroove barrier microfluidics silicone device	Xona Microfluidics	Cat#SND900

EXPERIMENTAL MODEL AND STUDY PARTICIPANT DETAILS

Cell lines

Control iPSC (C1,[53] male; C3,[54] female) and RFP-labelled control IPSC lines were cultured on Matrigel (Corning/VWR International, 354234) coated plates (Thermo Fisher, Waltham, MA, USA) in mTeSR1 basic medium supplemented with 1x mTeSR1 supplement (Stem Cell Technologies, Vancouver, Canada, 85850) at 37°C, 5% CO_2 and ambient oxygen level. Passaging was done using Accutase solution (Sigma Aldrich, St. Louis, MO, USA, A6964) treatment.

METHOD DETAILS

IPSC generation and maintenance

iPSCs were previously reprogrammed from 1 control line of fibroblasts, line C1[53] and, 1 control line of PBMCs, line C3.[54] For control line C1, fibroblasts were obtained from human newborn foreskin biopsies. On Day 1, fibroblast cultures with 70–80% confluency were dissociated using 0.25% trypsin-EDTA (25200056, Life Technologies), counted and seeded on 2.5 × 10–5 NuFF3-RQ human newborn foreskin feeder fibroblasts (GSC-3404, GlobalStem) at two different densities: 2 × 10–4 cells/well and 4 × 10–4 cells/well. Day 2, medium was changed to Pluriton Reprogramming Medium (00–0070, Stemgent) supplemented with 500 ng/mL carrier-free B18R Recombinant Protein (03–0017, Stemgent). Days 3–18, modified mRNA (mmRNA) cocktail was transfected daily combining OCT4, SOX2, KLF4, LIN28 and C-MYC mmRNAs at a 3:1:1:1:1 stoichiometric ratio and Opti-MEM I Reduced Serum Medium (13778150, Thermo Fisher Scientific) in a total volume of 105 μL with a mix of 92 μL Opti-MEM I Reduced Serum Medium and 13 μL Lipofectamine RNAiMAX Transfection Reagent (31985062, Thermo Fisher Scientific) after incubation at room temperature (RT) for 15 min. Cells were transfected for 4 h, then washed, and fresh reprogramming medium supplemented with B18R was added to the cultures. The mmRNA factors were provided by the RNA CORE of the Houston Methodist Hospital and contained the following modifications: 5-methyl CTP, Pseudo-UTP, ARCA cap and a 150-nucleotide poly-A tail. For control line C3, PBMCs were isolated from human blood from a control 39-year-old woman. On the first day, a minimum number of 5 × 10^6 PBMCs were cultured in a 25-cm^2 flask containing 5 mL Erythroid Expansion Medium (IMDM 49% v/v; Ham's F-12 49% v/v; ITS-X 1% v/v; lipid concentrate 1% v/v; l-Glutamine 1% v/v; l-Ascorbic acid 0.005% w/v; BSA 0.5% w/v; 1-thioglycerol 0.0018% v/v; human stem cell factor (SCF) 100 ng/mL; human IL-3 10 ng/mL; IGF-1 40 ng/mL; Erythropoietin (EPO) 2 units/mL, KMS (Janssen-Cilag); holo-transferrin 0.1 mg/mL; Dexamethasone 1 μM). On the following day, cell suspension was transferred into a new 25-cm^2 flask. On days 2, 4, and 6, cells were transferred into a 15-mL conical tube and centrifuged at 300 × *g* for 5 min. Supernatant was removed, and cells were resuspended in 1 mL fresh Erythroid Expansion Medium and plated in a new 25-cm^2 flask containing 5 mL fresh Erythroid Expansion Medium. Transfection was carried out on day 8: Cells were collected in a 15-mL conical tube, centrifuged at 300 × *g* for 5 min and the cell pellet resuspended in 2 mL fresh Erythroid Expansion Medium. The cell number was determined using the LUNA-II Automated Cell Counter from Logos Biosystems according to the manufacturer's instructions. For each nucleofection, 2 × 10^6 culture-expanded erythroid cells were transferred into a 15-mL conical tube and centrifuged at 300 × *g* for 5 min, the supernatant was carefully removed and cells were resuspended in 100 μL $CD34^+$ Cell Nucleofector Solution (Lonza, VAPA-1003). 4 μg MOS (Addgene, 64120), 4 μg MMK (Addgene, 64121), and 2 μg GBX (Addgene, 64123) were added to the cell suspension and mixed well. Cells were electroporated with the reprogramming vectors using the Lonza Nucleofector 2b and program T-016. The electroporated cells were transferred into 2 mL fresh Erythroid Expansion Medium and plated in one well of a 12-well plate and incubated for 2 days at 37°C and 5% CO_2. On day 10, electroporated cells were collected into a 15-mL conical tube and centrifuged at 200 × *g* for 5 min. The cell pellet was resuspended in 1 mL DMEM (Life Technologies, 41965039) supplemented with 10% FCS (Life Technologies, 10270–106) and transferred to one well of a 12-well plate, coated with vitronectin (Life Technologies, A14700). The sealed plate was centrifuged at 200 × *g* for 30 min at 25°C and incubated at 37°C, 5% CO_2. The following day, the medium was carefully removed from the culture and collected in a 15-mL conical tube, and 0.5 mL E8 medium (Life Technologies, A1517001) supplemented with 0.25 mM n-Butyric Acid Sodium Salt (NaB) (Sigma, B-5887; MW 110.1) were added to each well. The tubes were centrifuged at 300 × *g* for 5 min, the supernatant was carefully removed and the cell pellet was resuspended in 0.5 mL E8 medium supplemented with 0.25 mM NaB and plated back to the same well so that there was 1 mL of E8 medium supplemented with 0.25 mM NaB per well. The medium was replaced with fresh E8 medium supplemented with 0.25 mM NaB and changed every second day until large colonies of iPSCs become visible. The absence of genomic rearrangements (>0.2 Mb) of the iPSCs reprogrammed from PBMCs was confirmed by Copy Number Variation analysis (Danecek et al., 2016) performed on genotype data obtained by genome-wide SNP array (Infinium Global Screening Array-24 v1.0; Illumina). Both IPSC lines were then cultured on Matrigel (Corning/VWR International, 354234) coated plates (Thermo Fisher, Waltham, MA, USA) in mTeSR1 basic medium supplemented with 1x mTeSR1 supplement (Stem Cell Technologies, Vancouver, Canada) at 37°C, 5% CO2 and ambient oxygen level. Passaging was done using Accutase solution (Sigma Aldrich, St. Louis, MO, USA, A6964) treatment.

Generation of RFP-labelled iPSC lines

RFP-labelled iPSC lines were generated by transfection iPSC control lines with piggyBac transposase (1 μg) and PB-RFP (1 μg) nucleofection.[55] Single cells of iPSCs were transfected with the Amaxa Nucleofector 2b (program B-016). RFP-positive colonies were picked and cultured on Matrigel (Corning/VWR International, 354234) coated plates in mTeSR1 basic medium (Stem Cell Technologies, 85850) supplemented with 1× mTeSR1 supplement (Stem Cell Technologies, 85850) at 37°C and 5% CO2.

Generation of unpatterned human cerebral organoids

Reprogrammed iPSCs, line C1[53] and line C3,[54] were used to generate human cerebral organoids (hCOs).[34,56] On day 1, iPSCs grown to 70–80% confluency were dissociated using Accutase solution (Sigma Aldrich, St. Louis, MO, USA, A6964) treatment, counted and plated in a 96-well U-bottom plate at a density of 9,000 live cells per 150 μL in low-bFGF hESC medium with ROCK inhibitor (1:100, final concentration 50 μM) to form Embryoid Bodies (EBs). On day 4–5, EBs were transferred to neural induction medium (DMEM-F12 with 1% (v/v) N2 supplement, 1% (v/v) GlutaMAX supplement and 1% (v/v) MEM-NEAA, heparin (final concentration of 1 μg mL^{-1})) to

promote the induction of primitive neuroepithelia. 4–5 days later, EBs were embedded in Matrigel (Corning/VWR International, 354234) droplets and kept in static culture in differentiation medium without vitamin A containing 1:1 mixture of DMEM/F12 and Neurobasal supplemented with 1:200 N2 supplement (Invitrogen), 1:100 B27 supplement without vitamin A (Invitrogen), 3.5 mL L21 2-mercaptoethanol, 1:4,000 insulin (Sigma), 1:100 Glutamax (Invitrogen), 1:200 MEM-NEAA. 4–5 days following the embedding, organoids were transferred to an orbital shaker in differentiation medium as above, except B27 supplement with vitamin A (Invitrogen) was used. Organoids were kept in 10-cm dishes on a shaker at 37°C, 5% CO2 and ambient oxygen level with medium changes every 3–4 days.

Generation of dorsally- and ventrally- patterned human cerebral organoids

Patterned human cerebral organoids (dorsal and ventral) were generated as previously described.[51] Briefly, embryoid bodies (EBs) were guided to generate ventral and dorsal identities. iPSCs were dissociating into single cells using Accutase (Sigma-Aldrich, A6964), and approximately 9000 cells were transferred to one well of an ultralow-attachment 96-well plate (Corning). Five days later, during the neuronal induction, EBs were treated individually with Smoothened Agonist (SAG) (1:10,000) (Millipore, 566660) and IWP-2 (1:2000) (Sigma-Aldrich, I0536) to promote a ventral identity and with cyclopamine A (1:500) (Calbiochem, 239803) for a dorsal identity. Following 7 days, EBs were embedded in a Matrigel (Corning/VWR International, 354234) droplet. After this point, the patterned organoids were cultured following the same guidelines used for unpatterned organoids (see generation of unpatterned human cerebral organoids).

NPC, neuron and astrocyte cultures

Neural progenitor cells (NPCs) were generated by following Basic Protocol 1,[57] with the exception that FGF8 and SHH were replaced by FGF2 (Peprotech, 100-18b-50) in the neural progenitor medium (NPM). Briefly, iPSCs were cultured in 10 cm plates in neural induction medium (NIM; DMEM/F12 medium base, 1X N2-supplement (100X), 1X B-27 supplement (50X)), for approximately two days, until large, nearly touching colonies developed. Colonies were then detached using collagenase solution (….) and seeded in an ultra-low-attachment plate for the generation of EBs. After 1 week, EBs were transferred to a 10 cm polyornithine/laminin-coated plate in NIM, and 1 week later, EBs containing neural rosettes were manually picked using a 200 μL (P200) pipet tip. These clumps were then cultures in a new polyornithine/laminin-coated plate in NPM (DMEM/F12 medium base, 1X N2-supplement (100X), 1X B-27 supplement (50X), FGF2 (20 ng/mL) and passaged 1:3 weekly for up to 15 passages. NPCs were generated from three control iPSC lines, line C1,[53] line C3,[54] and one RFP-labelled line[21] (see "IPSCs culture" and "Generation of labeled iPSC lines"), which generated a ratio of 60% neurons and 40% astrocytes in accordance with this protocol, providing electrophysiologically mature neurons in a more physiological environment. Neural differentiation was conducted as previously described,[58] which generates a mixture of neuronal types. In summary, 20,000 cells/well were seeded in 24-well plates coated with polyornithine/laminin in neural differentiation media (Neurobasal as medium base, 1X N2-supplement (100X), 1X B-27 supplement (50X)). Astrocytes were isolated from 8-month-old organoids as follows: Organoids were transferred to a 15 mL falcon tube and washed 1 time with 1xPBS. For dissociation, they were placed in Accutase solution (A6964, Sigma Aldrich, St. Louis, MO, USA) pipetted up and down 5–10 times with a P1000 tip, and then placed in the incubator for 10 min at 37°C, followed by 5 times pipetting for a second time. The dissociated cells were then centrifuged at 300 x g for 3 min and resuspended in *NDM+A media* (DMEME/F12+Glutamax and Neurobasal medium in a ratio 1:1 supplemented with 1:100 N2-supplement (100X), 1:100 B-27 supplement (50X), 0.5% of MEM Non-Essential Amino Acids Solution (100X), 0.5% GlutaMAX Supplement, 50 μM of 2-mercaptoethanol (50 mM), antibiotic antimycotic Solution (100×) and Insulin 2.5 μg/mL) for 24 h. The next day, the cells were transferred to Matrigel Basement Membrane Matrix LDEV-free (Corning, 354234) coated plates. One day later the media was changed to Astrocyte media (89% DMEM/F12+Glutamax, 10% fetal bovine serum, 1% Antibiotic-Antimycotic). The astrocytes obtained were characterized by immunostaining and were positive for astrocytic markers such as SOX9, s100B, NFIA, and negative for neuronal markers MAP2 and NeuN. All the cells were kept in an incubator at 37°C, 5% CO2 and ambient oxygen level with medium changes every 2–3 days.

FLAG-YAP1 overexpression and EV exchange

NPCs were transfected with an FLAG-YAP1 plasmid (Addgene #27371,[59]) and a control plasmid (pEGFP-C1 plasmid) using the Lipofectamine 3000 Transfection Reagent (ThermoFisher Scientific, USA) as instructed in the protocol. 72h following the transfection, the conditioned media from the NPCs was collected for EV collection (see EV collection and analysis). The collected EVs carrying FLAG-YAP1 were then added to a new set of NPCs. The cells were prepared for immunofluorescence after 18h of the treatment and imaged using confocal microscopy (see Immunohistochemistry and Imaging). The images were then analyzed using ImageJ.[60]

EV and IV collection and analysis

EVs were collected from conditioned media from COs and 2D cultured cells.[27] EVs collected from NPCs, d15 and d40 COs (unpatterned, dorsal and ventral) were obtained from two different IPSC lines, namely line C1[53] and line C3.[54] Only line C1 was used for all the other time points, for each developmental timepoint, EVs were collected from 4 independent differentiations (batches, biological replicates). For cells in 2D, EVs were pooled from at least 3 independent differentiations (biological replicates). We performed EV collection by the following steps: centrifugation at 300*g* for 10 min, supernatant centrifugation at 2000*g* for 10 min at 4°C, supernatant centrifugation at 10.000*g* for 30 min at 4°C, supernatant centrifugation at 100.000*g* for 90 min at 4°C in a fixed-angle rotor (TH865,

Thermo Fisher Scientific), followed by pellet wash with 1x PBS and centrifugation at 100.000*g* for 90 min at 4°C. Alternatively, miRCURY Exosome Cell/Urine/CSF Kit (Qiagen, 76743) was used to isolate EVs from conditioned medium according to the manufacturer instructions. For NPCs, EVs were collected from three independent cultures of control NPCs. Neuronal EVs were collected from three independent neuronal differentiation cultures at 8 to 10 weeks in cultures. Similarly, astrocyte EVs were collected from three independent cultures of astrocytes. For COs, EVs were collected from conditioned media of 20–30 different COs in culture.

IVs were isolated by subcellular fractionation. Briefly, a pool of 5–7 COs was homogenized and upon removal of nuclei, cell debris and mitochondrial fraction as previously reported,[61] the supernatatant was ultracentrifuged at 100.000 g for 30 min to obtain the cellular fraction (IVs).

For the nanoparticle tracking analysis (NTA), fresh, unfrozen extracellular vesicle suspensions were diluted in PBS and analyzed using a Particle Metrix ZetaView PMX110-Z Nanoparticle Tracking Analyzer (Particle Metrix GmbH, Inning am Ammersee, Germany) equipped with a 520 nm laser. For each measurement, samples were introduced manually, the temperature was set to 24°C, and two cycles were performed by scanning at 11 discrete positions in the cell channel and capturing 60 frames per position (video setting: high). The following recommended parameters were used for the measurement.

Sensitivity:	80.0
Shutter:	70
Frame rate:	30
Minimum Brightness:	20
Minimum Area:	5
Maximum Area:	1000
Maximum Brightness:	255
Tracking Radius2:	100
Minimum Tracelength:	15
nm/class:	5
Classes/decade:	64

After capture, the videos were analyzed for particle size and concentration using the ZetaView Software 8.05.12 SP1.

For immune-electron microscopy, aliquots of extracellular vesicle suspensions were anayzed by Dr Ilkka Miinalainen at Biocenter Oulu/EM laboratory, Finland.[62] Vesicles were deposited on Formvar carbon coated, glow-discharged grids and incubated in a blocking serum containing 1% BSA in PBS. CD81 and LGALS3 primary antibodies and secondary gold conjugates (Zymed, San Francisco, CA, USA) were diluted in 1% BSA in PBS. The blocking efficiency was controlled by performing the labeling procedure in the absence of primary antibody.

EV uptake assay in 2D cell cultures

NPCs, astrocytes and neurons were cultured in 24-well plates (see NPC, neuron and astrocyte cultures). 10–12 mL of conditioned media from at least 3 independent differentiations (biological replicates) were used for EV collection via ultracentrifugation. To fluorescently label the EVs, the conditioned media was treated with 1 μL of 10 mM DiI (1,1′-Dioctadecyl-3,3,3′,3′-Tetramethylindocarbocyanine Perchlorate) for 15 min in the dark before the final washing step in ultracentrifugation. The media of the recipient cells was changed just prior to the addition of the labeled EVs. EVs were then added to three individual coverslips with receiving cells. The cells were fixed 18 h after EV treatment with 4% paraformaldehyde for 15 min at room temperature.

EV uptake assay in sectioned COs

COs (d40) were rinsed in PBS and embedded in low-melting point agarose (Biozym Scientific GmbH, 850080). Embedded organoids were then cut into 250 μm thick sections using a VT1200s vibratome (Leica, Germany), approximately 3–4 sections were obtained per organoid, and 3 organoids were used per condition, Sections were then placed on Falcon Cell Culture Insert with a 0.4 μm pore PET membrane (Falcon, 353090) within a 6-well-plate. After 3 days in culture, fluorescently labeled EVs were added in a drop-wise manner on top of the CO sections and incubated for 18 h. Sections were then prepared for immunohistochemistry (see Immunohistochemistry).

Immunohistochemistry

Monolayer cultures of NPCs, neurons, and astrocytes were fixed with 4% paraformaldehyde for 15 min at room temperature, followed by three times 5 min washing with 1xPBS. Next, cells were blocked against unspecific binding and permeabilized in blocking buffer (10% normal goat serum, 0,02% Triton X- in 1xPBS) for 1 h. Primary antibodies diluted in blocking buffer were then added to the cells in the dilutions specified below (Key resources table) and incubated overnight. On the second day, cells were washed five times for 5 min each in PBS with 0,1% Tween (PBS-T), and then incubated at room temperature for 2 h in secondary antibodies raised

against the host animal of the primary antibody. Secondary antibodies were diluted in blocking buffer and the dilutions used are listed below (Key resources table). DAPI (4′,6-diamidino-2-phenylindole) was added as a nuclear counterstaining. Finally, cells were washed three times with PBS-T and mounted on object slides with Fluoromount-G (ThermoFisher Scientific, 00-4958-02). To validate the specificity of the primary antibodies, experiments were always performed with a secondary antibody-only sample as background control.

15-day-old COs were collected, rinsed in PBS and fixed in 4% paraformaldehyde for 30 min at room temperature. They were then placed in 30% sucrose solution for cryoprotection overnight at 4°C and frozen in O.C.T embedding compound for cryosectioning. 14 μm sections were collected in adhesion slides Superfrost Plus (Carl Roth, Germany) and stored at −20°C. For immunohistochemistry, slides were placed at room temperature for 45 min, rinsed in PBS and then incubated in blocking buffer (10% normal goat serum, 0,02% Triton X- in 1xPBS) for 1 h. Primary antibodies diluted in blocking buffer were then added to the slides in the dilutions specified below (Key resources table) and incubated overnight. The following day, slides were washed three times for 5 min each in PBS, and then incubated at room temperature for 2 h in secondary antibodies raised against the host animal of the primary antibody. Secondary antibodies were diluted in blocking buffer and the dilutions used are listed below (Key resources table). DAPI (4′,6-diamidino-2-phenylindole) was added as a nuclear counterstaining. Finally, the slides were washed three times with PBS and a coverslip was mounted with Fluoromount-G (ThermoFisher Scientific, 00-4958-02).

Imaging

Immunostainings were imaged with confocal microscopy or Stimulated Emission Depletion (STED) microscopy.

Confocal stack images were obtained using a Leica SP8 confocal microscope based on a DMi8 stand (Leica Microsystems, Wetzlar, Germany), equipped with 20x/0.75 (oil), 40x/1.10 (water), and 63x/1.30 (glyc) objectives. Images were then processed using ImageJ.[60]

STED imaging was performed with a TCS SP8 STED 3X FALCON confocal head (Leica Microsystems, Germany) mounted on an inverted microscope (DMi8; Leica Microsystems, Germany). For imaging, a 405 nm diode and a white light laser were used as excitation sources for DAPI, Alexa Flour 594 (ThermoFisher, USA), and ATTO 647N (ATTO-TEC GmbH, Germany) (405 nm, 575 nm, 644 nm lasers lines respectively). Single photons were collected through a 100×/1.4 NA oil-immersion objective and detected on Hybrid Detectors (HyD) (Leica Microsystems) with a 420–500 nm, 590–670 nm, 660–720 nm spectral detection window for DAPI, Alexa Flour 594, and ATTO 647N detection, respectively. For depletion, a 775 nm pulsed laser was used for Alexa Fluor 594 and ATTO 647N. DAPI was not depleted and only imaged with confocal resolution. The image size was set to 1024 × 1024 pixels and a 5-fold zoom factor was applied, giving a pixel size of 0.023 μm and an image size of 23,25 × 23,25 μm. For FLIM, the white light laser delivered 80 MHz repetition rate. Arrival time of single photons was measured with the included FALCON module and 8 frames were acquired at a scanning speed of 200 Hz. Recordings were done sequentially for each dye to avoid crosstalk. Raw STED images were further processed with the τ-STED module of LAS X software (Leica Microsystems, Germany) increasing further the resolution thanks to the lifetime information recorded.

For the live imaging of EV uptake by NPCs, NPCs were seeded in a 24-well-plate at a density of 15,000 cells/well. 48h after seeding, 6 wells of cells were treated with NucSpot 488 Live Cell Nuclear Stain as suggested by the supplier (Biotium, U.S.A). Of the 6 wells, 3 wells were then treated with DiI-labelled EVs collected from 12 mL of media, while 3 wells were treated with diluted DiI as a negative control. The cells were imaged for 24h using a Leica TIRF system and a 100x/1.47 NA objective. The videos obtained were analyzed using ImageJ.[60]

3D image reconstruction was conducted using Imaris v9.7.2 (Oxford Instruments). The fluorescence signal of confocal z-stacks with intervals of 250 nm was represented by surface visualization using the default threshold parameters recommended by the software. Snapshots of the 3D rendered images were then captured.

Microfluidics chamber

A silicone device with a 900 μm microgroove barrier (ref. SND900, Xona Microfluidics, USA) was used to co-culture an RFP-labelled NPC cell line and non-fluorescently labeled neurons in independent chambers. Each cell line was maintained in their corresponding media (see NPC, neuron and astrocyte cultures) and after 7 days of being co-cultured, the cells were fixed, immunostained and imaged using confocal microscopy (see Immunohistochemistry and Imaging).

Proteomic analysis

Sample preparation for mass spectrometry

Purified EVs, collected from the conditioned media of 20–30 COs in culture, and IVs, isolated from a pool of 5–7 COs, were lysed in RIPA buffer (150mM NaCl, 50mM Tris pH8, 0.1% DOC, 0.1% SDS, 0.1% NP40). 10 μg of protein for each sample was subjected to the modified FASP protocol.[63] Briefly, the protein extract was loaded onto the centrifugal filter CO10 kDa (Merck Millipore, Darmstadt, Germany), and detergent were removed by washing five times with 8M Urea (Merck, Darmstadt, Germany) 50mM Tris (Sigma-Aldrich, USA) buffer. Proteins were reduced by adding 5mM dithiothreitol (DTT) (Bio-Rad, Canada) at 37°C for 1 h in the dark. To remove the excess of DTT, the protein sample was washed three times with 8M Urea, 50mM Tris. Subsequently protein thiol groups were blocked with 10mM iodoacetamide (Sigma-Aldrich, USA) at RT for 45 min. Before proceeding with the enzymatic digestion, urea was removed by washing the protein suspension three times with 50mM ammonium bicarbonate (Sigma-Aldrich, Spain).

Proteins were digested first by Lys-C (Promega, USA) at RT for 2 h, then by trypsin (Premium Grade, MS Approved, SERVA, Heidelberg, Germany) at RT, overnight, both enzymes were added at an enzyme-protein ratio of 1:50 (w/w). Peptides were recovered by centrifugation followed by two additional washes with 50mM ammonium bicarbonate and 0.5M NaCl (Sigma-Aldrich, Switzerland). The two filtrates were combined, the recovered peptides were lyophilized under vacuum. Dried tryptic peptides were desalted using C18-tips (Thermo Scientific, Pierce, USA), following the manufacture instructions. Briefly, the peptides dissolved in 0.1%(v/v) formic acid (Thermo scientific, USA) were loaded onto the C18-tip and washed 10 times with 0.1% (v/v) formic acid, subsequently the peptides were eluted by 95% (v/v) acetonitrile (Merck, Darmstadt, Germany), 0.1% (v/v) formic acid. The desalted peptides were lyophilized under vacuum. The purified peptides were reconstituted in 0.1% (v/v) formic acid for LC-MS/MS analysis.

MS data acquisition

Desalted peptides were loaded onto a 25 cm, 75 μm ID C18 column with integrated nanospray emitter (Odyssey/Aurora, ionopticks, Melbourne) via the autosampler of the Thermo Easy-nLC 1000 (Thermo Fisher Scientific) at 60°C. Eluting peptides were directly sprayed onto the timsTOF Pro (Bruker Daltonics). Peptides were loaded in buffer A (0.1% (v/v) formic acid) at 400 nL/min and percentage of buffer B (80% acetonitril, 0.1% formic acid) was ramped from 5% to 25% over 90 min followed by a ramp to 35% over 30 min then 58% over the next 5 min, 95% over the next 5 min and maintained at 95% for another 5 min. Data acquisition on the timsTOF Pro was performed using timsControl. The mass spectrometer was operated in data-dependent PASEF mode with one survey TIMS-MS and ten PASEF MS/MS scans per acquisition cycle. Analysis was performed in a mass scan range from 100 to 1700 m/z and an ion mobility range from 1/K0 = 0.85 Vs. cm-2 to 1.30 Vs. cm-2 using equal ion accumulation and ramp time in the dual TIMS analyzer of 100 ms each at a spectra rate of 9.43 Hz. Suitable precursor ions for MS/MS analysis were isolated in a window of 2 Th for m/z < 700 and 3 Th for m/z > 700 by rapidly switching the quadrupole position in sync with the elution of precursors from the TIMS device. The collision energy was lowered as a function of ion mobility, starting from 45 eV for 1/K0 = 1.3 Vs. cm-2 to 27eV for 0.85 Vs. cm-2. Collision energies were interpolated linear between these two 1/K0 values and kept constant above or below these base points. Singly charged precursor ions were excluded with a polygon filter mask and further m/z and ion mobility information was used for 'dynamic exclusion' to avoid re-sequencing of precursors that reached a 'target value' of 14500 a.u. The ion mobility dimension was calibrated linearly using three ions from the Agilent ESI LC/MS tuning mix (m/z, 1/K0: 622.0289, 0.9848 Vs. cm-2; 922.0097 Vs. cm-2, 1.1895 Vs. cm-2; 1221.9906 Vs. cm-2, 1.3820 Vs. cm-2).

Raw data analysis of MS measurements

Raw data were processed using the MaxQuant computational platform (version 1.6.17.0)[64] with standard settings applied for ion mobility data.[65] Shortly, the peak list was searched against the Uniprot database of Human database (75069 entries, downloaded in July 2020) with an allowed precursor mass deviation of 10 ppm and an allowed fragment mass deviation of 20 ppm. MaxQuant by default enables individual peptide mass tolerances, which was used in the search. Cysteine carbamidomethylation was set as static modification, and methionine oxidation, deamidation and N-terminal acetylation as variable modifications. The match-between-run option was enabled, and proteins were quantified across samples using the label-free quantification algorithm in MaxQuant generating label-free quantification (LFQ) intensities.

Bioinformatic analysis

For the proteomic characterization in IVs and EVs, 7486 proteins were quantified. Proteins that were consistently detected in 2 of the 3 technical replicates per each condition were retained. Downstream analysis was performed using R. The LFQs values were log2-transformed. Missing values were imputed using the R package DEP (version 1.15.0) and replaced by random values of a left-shifted Gaussian distribution (shift of 1.8 units of the standard deviation and a width of 0.3). Differentially expression (DE) analysis was performed on the imputed data using Student's t Test. Proteins with log2 fold change values (log2FC) ≥ 1 and ≤ -1 and with an FDR-corrected q-value <0.05 were considered as differentially expressed (exodevo.psych.mpg.de/app/exodevo).[52]

Validation of proteomic results with automated western blot

EVs samples were collected from independent new cultures of COs and cells. 1 μg of proteins were loaded on automated western blot system (Proteinsimple WES, https://www.proteinsimple.com) with 12–230 kDa (SM-W004) or 66–440 kDa (SM-W006) Jess/Wess Separation Modules according to the molecular weight of the analyzed protein. All the antibodies were diluted 1:50 (Key resources table). Figures S1F, S2J, and S3A show the protein simple profiles and relative quantifications performed using ImageJ Software.

Single-cell RNA-sequencing

Single-cell dissociation was performed on five 60 days old-patterned spheroids randomly selected for each pattern condition. Single cells were dissociated using StemPro Accutase Cell Dissociation Reagent (Life Technologies), filtered through 30 μM and 20 μM filters (Miltenyi Biotec) and cleaned of debris using a Percoll (Sigma, P1644) gradient. Single cells were resuspended in ice-cold Phosphate-Buffered Saline (PBS) supplemented with 0.04% Bovine Serum Albumin at a concentration of 1000 cells per ul. Single cells were loaded onto a Chromium Next GEM Single Cell 3' chip (Chromium Next GEM Chip G Single Cell Kit, 16 rxns 10XGenomics PN-1000127) with the Chromium Next GEM Single Cell 3' GEM, Library & Gel Bead Kit v3.1 (Chromium Next GEM Single Cell 3' GEM, Library & Gel Bead Kit v3.1, 4 rxns 10xGenomics PN-1000128) and cDNA libraries were generated with the Single Index Kit T Set A, 96 rxns (10xGenomics PN-1000213) according to the manufacturer's instructions. Libraries were sequenced using Illumina NovaSeq6000 in 28/8/91bp mode (SP flowcell), quality control and UMI counting were performed by the Max-Planck für molekulare

Genetik (Germany). Downstream analysis was performed using the R package Seurat (version 3.2). Cells with more than 2,500 or less than 200 detected genes or with mitochondrial content higher that 10% were excluded as well as genes that were not expressed in at least three cells. Normalization of gene expression was done using a global-scaling normalization method (“LogNormalize”, scale.factor = 10000) and the 2000 most variable genes were selected (selection method, “vst”) and scaled (mean = 0 and variance = 1 for each gene) before principal component analysis. The “FindNeighbors” and “FindClusters” functions were used for clustering with resolution of 0.5 and UMAP for visualization. Clusters were grouped based of the expression of known marker genes and differentially expressed gene identified with the “FindAllMarkers” function.

Bulk-RNA-sequencing

RNA-seq was performed on 10ng of total RNA collected from 3 independent wells of NPCs from a 24well plate. NPCs were not treated with EVS or treated for 12h with EVs collected by ultracentrifugation from 25 mL of conditioned medium collected from 28 to 37 days in culture COs (control ventral, EPM1 ventral, control dorsal and EPM1 dorsal COs). NPCs were lysed in 1mL Trizol (Qiagen)/well and RNA was isolated employing RNA Clean & Concentrator kit (Zymo Research) including digestion of remaining genomic DNA according to producer’s guidelines. RNA was further processed according to.[66] Briefly, cDNA synthesis was performed with SMART-Seq v4 Ultra Low Input RNA Kit (Clontech cat. 634888) according to the manufacturer’s instruction. cDNA was fragmented to an average size of 200–500 bp in a Covaris S220 device (5 min; 4°C; PP 175; DF 10; CB 200). Fragmented cDNA was used as input for library preparation with MicroPlex Library Preparation Kit v2 (Diagenode, cat. C05010012) and processed according to the manufacturer’s instruction. Libraries were quality controlled by Qubit and Agilent DNA Bioanalyzer analysis. Deep sequencing was performed on a HiSeq 1500 system according to the standard Illumina protocol for 50 bp paired-end reads with v3 sequencing reagents.

RNAseq analysis

Paired end reads were aligned to the human genome version GRCh38 using STAR v2.6.1d[67] with default options "–runThreadN 32 –quantMode TranscriptomeSAM GeneCounts –outSAMtype BAM SortedByCoordinate". Reads-per-gene counts were imported in R v4.1.0. Bioconductor package DESeq2 v1.32.0[68] was used for differential expression analysis. Only genes with read counts>1 were considered. Significantly changed genes were determined through pairwise comparisons using the DESeq2 results function (log2 fold change threshold = 1, adjusted p-value <0.05). Heatmaps with differentially expressed genes were plotted with pheatmap v1.0.12 and RColorBrewer v1.1-2 using rlog-normalized expression values.

QUANTIFICATION AND STATISTICAL ANALYSIS

Quantification of EV markers in cell types

The expression of standard EV markers (CD63, CD81, CD82, CD9 and PDCD6IP) was quantified via immunohistochemistry in monolayer cultures of NPCs, young neurons, mature neurons and astrocytes. Immunohistochemistry was conducted as mentioned above using the antibodies and dilutions stated in Key resources table. Immunoreactivity was quantified using ImageJ.[60] A cell was counted as positive for an EV marker if immunoreactivity was observed within the nucleus or in the cytoplasm of the cell. Since neurons generate long projections which are difficult to image to their full extent, only the somas and proximal neurites were quantified as being positive for each EV marker. In NPCs and astrocytes, a cell was counted as positive for an EV marker if immunoreactivity was detected in the nucleus or in the cytoplasm in close proximity to the nucleus since they are cultured in high confluency and therefore sometimes complicating the discrimination between cells. All the statistical details of this quantification can be found in the figure legend.

Quantification of EV uptake by cell types

The uptake of pEVs, nEVs and aEVs by NPCs, neurons (young and mature) and astrocytes was quantified in three individual coverslips of receiving cells by counting the number of cells which had DiI-positive EVs (see EV uptake assay) in either the nucleus or cytoplasm using ImageJ.[60] Since neurons generate long projections which are difficult to image to their full extent, only the somas and proximal neurites were quantified. In NPCs and astrocytes, a cell was counted as positive for an EV marker if immunoreactivity was detected in the nucleus or in the cytoplasm in close proximity to the nucleus since they are cultured in high confluency and therefore sometimes complicating the discrimination between cells.

The number of particles was also quantified in receiving cells using the option “Analyze particles” available in ImageJ.[60] First, a mask was generated from an image with a cytoplasmic marker to outline the cells. Then, EV images were converted to binary with an automatic threshold, and particles ranging from 100 to 300 nm within the cell outline mask were counted with no filtering done for circularity. All the statistical details of these quantifications can be found in the figure legend.

Quantification of EV uptake by CO sections

Images of EV-treated CO sections were analyzed using ImageJ.[60] First, masks were generated for the progenitor zone using Nestin as a marker, and for the cortical plate using DCX as a marker. Then, the number of particles were counted using the “Analyze

particles'' option within these delimited areas using the masks previously generated. EV images were converted to binary with an automatic threshold, and particles ranging from 100 to 300 nm with no filtering done for circularity. All the statistical details of this quantification can be found in the figure legend.

Proteomic statistical analysis

Missing values were imputed using the R package DEP (version 1.15.0) and replaced by random values of a left-shifted Gaussian distribution (shift of 1.8 units of the standard deviation and a width of 0.3). Differentially expression (DE) analysis was performed on the imputed data using Student's t Test. Proteins with log2 fold change values (log2FC) ≥ 1 and ≤ -1 and with an FDR-corrected q-value <0.05 were considered as differentially expressed (exodevo.psych.mpg.de/app/exodevo).

RNAseq statistical analysis

Bioconductor package DESeq2 v1.32.0[68] was used for differential expression analysis. Only genes with read counts>1 were considered. Significantly changed genes were determined through pairwise comparisons using the DESeq2 results function (log2 fold change threshold = 1, adjusted *p*-value <0.05). Heatmaps with differentially expressed genes were plotted with pheatmap v1.0.12 and RColorBrewer v1.1-2 using rlog-normalized expression values.

Enrichment analysis

GO term analysis of differentially expressed proteins was tested using the FUMA algorithm[69] by inserting the DE protein lists into the GENE2FUNC software (FDR<0.05) (https://fuma.ctglab.nl/) or with STRING (https://string-db.org).

HHS Public Access

Author manuscript

Nat Immunol. Author manuscript; available in PMC 2022 December 01.

Published in final edited form as:

Nat Immunol. 2021 December ; 22(12): 1563–1576. doi:10.1038/s41590-021-01064-3.

Disrupting Roquin-1 interaction with Regnase-1 induces autoimmunity and enhances antitumor responses

Gesine Behrens[1,14], **Stephanie L. Edelmann**[2,14], **Timsse Raj**[1,14], **Nina Kronbeck**[1], **Thomas Monecke**[3], **Elena Davydova**[4], **Elaine H. Wong**[1], **Lisa Kifinger**[2], **Florian Giesert**[5], **Martin E. Kirmaier**[6,7], **Christine Hohn**[1], **Laura S. de Jonge**[2], **Mariano Gonzalez Pisfil**[8], **Mingui Fu**[9], **Sebastian Theurich**[6,7], **Stefan Feske**[10], **Naoto Kawakami**[11], **Wolfgang Wurst**[5,12,13], **Dierk Niessing**[3,4], **Vigo Heissmeyer**[1,2]

[1]Institute for Immunology, Biomedical Center (BMC), Faculty of Medicine, Ludwig-Maximilians-Universität in Munich, Planegg-Martinsried, Germany.

[2]Research Unit Molecular Immune Regulation, Helmholtz Zentrum München, Munich, Germany.

[3]Institute of Pharmaceutical Biotechnology, Ulm University, Ulm, Germany.

[4]Institute of Structural Biology, Helmholtz Zentrum München, Neuherberg, Germany.

[5]Institute of Developmental Genetics, Helmholtz Zentrum München, Neuherberg, Germany.

[6]Cancer and Immunometabolism Research Group at the Gene Center, Ludwig-Maximilians-Universität in Munich, Munich, Germany.

[7]Department of Medicine III, LMU University Hospital, Ludwig-Maximilians-Universität in Munich, Munich, Germany.

[8]Core Facility Bioimaging and Walter-Brendel-Centre of Experimental Medicine at the Biomedical Center, Ludwig-Maximilians-Universität in Munich, Planegg-Martinsried, Germany.

Correspondence and requests for materials should be addressed to Vigo Heissmeyer. vigo.heissmeyer@med.uni-muenchen.de.

Author contributions

G.B., S.L.E, T.R., N. Kronbeck and V.H. conceived the project and designed experiments with input from S.F., D.N. and N. Kawakami. G.B., S.L.E., T.R. and N. Kronbeck performed and analyzed most of the experiments. T.M. performed in vitro pulldown experiments, E.D. performed EMSA experiments and SPR assays and E.W. performed ELISA measurements. L.K. performed NanoBret assays and, together with M.G.P., FLIM/FRET experiments and C.H. contributed to kinetic expression analyses. M.K. and L.D.J. performed seahorse measurements with supervision from S.T. F.G. and W.W. generated mice expressing Roquin-1^{L209Y} and M.F. provided the *Zc3h12a*^{fl} mouse line. The manuscript was written by G.B. and V.H. with critical input from S.F.

Reporting Summary. Further information on research design is available in the Nature Research Reporting Summary linked to this article.

Online content

Any methods, additional references, Nature Research reporting summaries, source data, extended data, supplementary information, acknowledgements, peer review information; details of author contributions and competing interests; and statements of data and code availability are available at https://doi.org/10.1038/s41590-021-01064-3.

Extended data is available for this paper at https://doi.org/10.1038/s41590-021-01064-3.

Supplementary information The online version contains supplementary material available at https://doi.org/10.1038/s41590-021-01064-3.

Competing interests

The authors declare no competing interests.

[9]Department of Basic Medical Science, School of Medicine, University of Missouri-Kansas City, Kansas City, MO, USA.

[10]Department of Pathology, New York University School of Medicine, New York, NY, USA.

[11]Institute of Clinical Neuroimmunology, University Hospital and Biomedical Center, Ludwig-Maximilians-Universität in Munich, Planegg-Martinsried, Germany.

[12]German Center for Neurodegenerative Diseases (DZNE) Site Munich, Munich, Germany.

[13]Technische Universität München, Lehrstuhl für Entwicklungsgenetik c/o Helmholtz Zentrum München, Munich, Germany.

[14]These authors contributed equally: Gesine Behrens, Stephanie L. Edelmann, Timsse Raj.

Abstract

Roquin and Regnase-1 proteins bind and post-transcriptionally regulate proinflammatory target messenger RNAs to maintain immune homeostasis. Either the *sanroque* mutation in Roquin-1 or loss of Regnase-1 cause systemic lupus erythematosus-like phenotypes. Analyzing mice with T cells that lack expression of Roquin-1, its paralog Roquin-2 and Regnase-1 proteins, we detect overlapping or unique phenotypes by comparing individual and combined inactivation. These comprised spontaneous activation, metabolic reprogramming and persistence of T cells leading to autoimmunity. Here, we define an interaction surface in Roquin-1 for binding to Regnase-1 that included the *sanroque* residue. Mutations in Roquin-1 impairing this interaction and cooperative regulation of targets induced T follicular helper cells, germinal center B cells and autoantibody formation. These mutations also improved the functionality of tumor-specific T cells by promoting their accumulation in the tumor and reducing expression of exhaustion markers. Our data reveal the physical interaction of Roquin-1 with Regnase-1 as a hub to control self-reactivity and effector functions in immune cell therapies.

Post-transcriptional control of mRNA stability or translation through RNA-binding proteins (RBPs) represents an important level of gene regulation with crucial impact on immune cell fate decisions. This role becomes evident from combined genetic inactivation of alleles encoding for the Roquin-1 and Roquin-2 proteins with redundant functions in mice or in a human patient who developed a severe hyperinflammatory syndrome due to a homozygous nonsense mutation in the *RC3H1* gene encoding ROQUIN-1 (refs. [1-3]). Moreover, a single amino acid exchange (M199R), called *sanroque* mutation, in the murine Roquin-1 protein causes lupus-like autoimmunity. Regnase-1-deficient mice exhibit a comparable autoimmune phenotype with activated $CD4^+$ and $CD8^+$ T cells, accumulation of plasma cells, hypergammaglobulinemia and autoantibody production[4,5]. In response to T cell activation, Roquin-1, its paralog Roquin-2 and Regnase-1 are similarly regulated by MALT1-dependent proteolytic cleavage[5,6]. All three RBPs share a number of mRNA targets[3,5-7], suggesting potential cooperation[6,8]. Roquin-1/2 proteins repress the expression of Regnase-1 (refs. [6,8]). Mapping of binding sites of overexpressed Regnase-1 crosslinked to cellular mRNAs revealed the sequence determinants of Roquin-recognized stem loops of the constitutive decay element (CDE)[7,9]. Despite an extensive overlap in phenotypes and regulation of these RBPs, they have different functions. Roquin-1 interacts with

components of the mRNA deadenylation and decapping machinery[9-11], whereas Regnase-1 endonuclease cleaves target mRNAs[4,7,12]. Because Roquin-1 and Regnase-1 were found enriched in P bodies and at the endoplasmic reticulum (ER), respectively and differed in their requirements for regulation of reporter mRNAs, it was proposed that Roquin-1/2 and Regnase-1 proteins function in a compartmentalized manner independently of each other[7,13].

Owing to the prominent humoral autoimmunity occurring in mice with the *sanroque* mutation or Regnase-1 inactivation[4,14] and recapitulation of hallmark phenotypes by T cell-specific deletion of Roquin-1/2 or Regnase-1 (refs.[3,5]), previous studies mostly focused on $CD4^+$ helper T cells. Nevertheless, the ubiquitous expression of Roquin-1/2 and the prevalence of individual Regnase-1/2/3/4 paralogs suggest an importance of both RBP families in many types of cells and fate decisions[15-17]. More recently, inactivation of Regnase-1 in tumor-specific $CD8^+$ T cells or chimeric antigen receptor (CAR)-T cells resulted in increased antitumor responses[18,19], whereas an involvement of Roquin paralogs in $CD8^+$ effector T cell responses has not yet been studied. In the context of defining tumor antigen-specific T cell antigen receptors (TCRs) or CARs, current efforts also try to modulate tumor-specific T cells. The aim is to bolster activation, prevent regulatory T (T_{reg}) cell-induced suppression, reprogram metabolism or break tumor-imposed exhaustion and make adoptive cell therapies (ACTs) efficient for different blood cancers as well as solid tumors.

Here we explore how the interaction of Roquin-1 with Regnase-1 affects peripheral tolerance and how this program can be used in ACT. We show that both proteins bind to each other in a ternary complex on RNA. This interaction was important for the regulation of shared targets and controlled $CD4^+$ and $CD8^+$ T cell quiescence, metabolic programs, T cell activation, differentiation and effector functions. Weakening the physical interaction of Roquin-1 with Regnase-1 by introducing mutations into the mouse germline caused humoral autoimmunity but led to enhanced responses of cytotoxic T cells directed toward tumor-expressed antigens in the tumor setting.

Results

Roquin-1/2 and Regnase-1 maintain quiescence of T cells.

To address the functional relationship of Roquin-1/2 and Regnase-1 proteins we analyzed mice with T cell-specific deletion of the genes encoding Regnase-1 (ref. [20]) (*Zc3h12a*$^{fl/fl}$;*Cd4*-Cre, termed KO^T), Roquin-1 and Roquin-2 (refs. [3,21]) (*Rc3h1*$^{fl/fl}$;*Rc3h2*$^{fl/fl}$;*Cd4*-Cre, termed DKO^T) or a combination of all three genes (*Zc3h12a*$^{fl/fl}$;*Rc3h1*$^{fl/fl}$;*Rc3h2*$^{fl/fl}$;*Cd4*-Cre, termed TKO^T). $CD4^+$ and $CD8^+$ T cells from all mutant mice showed a spontaneous reduction of naive T cells ($CD62L^+CD44^{lo}$) and an increase in effector memory T cells ($CD62L^-CD44^{hi}$) (Fig. 1a,b). Accumulation of effector $CD4^+$ and $CD8^+$ T cells was not due to a reduction in T_{reg} cells, which instead increased in frequencies in all knockout mice and also in numbers in KO^T and TKO^T mice (Fig. 1c,d). Reconstituting lethally irradiated CD45.1/2 congenic mice with mixtures of wild-type (CD45.1) and TKO^T (CD45.2) bone marrow (Extended Data Fig. 1a) revealed that the increase in peripheral T_{reg} cells (Fig. 1c,d) was not cell intrinsic, as we found comparable frequencies of wild-type and TKO^T T_{reg} cells in mixed-bone-marrow chimeric

mice that were increased compared to wild-type/wild-type chimeric mice (Extended Data Fig. 1b). The increased T_{reg} cell frequencies in TKO^T but also KO^T and DKO^T mice presumably occurred secondary to tissue inflammation[3,5,6,22], consistent with the observed infiltration of leukocytes into the lung of mutant mice (Extended Data Fig. 1c). We then asked whether the observed activation of conventional $CD4^+$ and $CD8^+$ T cells also occurred in the presence of wild-type T_{reg} cells. We therefore generated mice in which deletion of Roquin-1/2- and Regnase-1-encoding genes, individually or in combination, can be induced by tamoxifen treatment using the Cre-ERt2 transgene[23]. We adoptively transferred $CD3^+$ T cells (CD45.2) from iKO (*Zc3h12a*$^{fl/fl}$;Cre-ERt2), iDKO (*Rc3h1/2*$^{fl/fl}$;Cre-ERt2) or iTKO (*Rc3h1/2*$^{fl/fl}$;*Zc3h12a*$^{fl/fl}$;Cre-ERt2) mice into congenic (CD45.1) wild-type hosts that were then treated with tamoxifen to acutely delete Roquin-1/2- and Regnase-1-encoding alleles (Fig. 1e). $CD45.2^+$ T cells on day 8 after transfer showed increased frequencies of $CD4^+$ and $CD8^+$ T cells for all knockouts (Fig. 1f). We determined a breakdown of quiescence in knockout $CD4^+$ and $CD8^+$ T cells by increased effector-memory phenotypes (Extended Data Fig. 1d) and enhanced proliferation of these cells indicated by Ki67 staining (Fig. 1g and Extended Data Fig. 1e). These effects were observed in all knockouts but were typically more pronounced upon combined inactivation of Roquin-1/2 and Regnase-1 iTKO T cells. We employed extracellular flux (Seahorse) analyses to determine metabolic reprogramming, a hallmark of T cell activation and functional adaptation, addressing whether inactivation of the different RBPs alters metabolic pathways. During restimulation of $CD4^+$ T cells after in vitro deletion by 4′-OH-tamoxifen treatment we found increased glycolytic activities in all three knockouts compared to wild-type T cells, even under glucose-deprived conditions at baseline. Extracellular acidification rates (ECARs) were even more elevated upon glucose addition and glycolytic capacities were higher in all three knockouts, with the strongest effects in iTKO T cells (Fig. 1h and Extended Data Fig. 2a-c). Mitochondrial respiration was also affected by Roquin-1/2 and Regnase-1 deficiencies and, at baseline, oxygen consumption rates (OCRs) were elevated in all knockouts with a highest increase in iTKO T cells. OCR changes were more pronounced than ECARs suggesting that knockout T cells fuel their energetic demands to a main extent from OXPHOS (Fig. 1h and Extended Data Fig. 2d,e). Consecutively, maximal respiration rates and respiratory spare capacities were increased in all knockout genotypes but were highest in iTKO T cells (Extended Data Fig. 2d,e). With regard to mitochondrial respiration, Regnase-1 deficiency contributed stronger to the deregulation of metabolism compared to Roquin-1/2 deficiency. Similar metabolic reprogramming was also observed for knockout $CD8^+$ T cell cultures; however, $iTKO^T$ $CD8^+$ T cells showed variable effects in glycolytic tests, especially in mitochondrial stress tests (Extended Data Fig. 2f,g and Supplementary Table 1). These data show that Roquin-1/2 and Regnase-1 inactivation leads to a general metabolic reprogramming with increased energy generation from mitochondrial respiration and enhanced glycolytic capacity.

Roquin-1/2 and Regnase-1 control humoral autoimmunity.

Cd4-Cre mediated deletion of Roquin-1/2 encoding alleles has been associated with follicular helper T (T_{FH}) cell (PD-1^{hi}Cxcr5^{hi}, $Bcl6^+$) accumulation[3], which we also detected in KO^T and even stronger in TKO^T mice (Fig. 2a). In addition, all mutant mice showed an accumulation of germinal center (GC) B cells ($GL7^+CD95^+$) (Fig. 2b). We combined floxed alleles with an inducible *Cd4*-Cre-ERt2 knock in allele[24,25] and adoptively transferred

naive CD4+ T cells (CD45.2+) from wild-type, iKO, iDKO and iTKO mice into congenic (CD45.1+) wild-type mice that were then treated with tamoxifen (Fig. 2c and Extended Data Fig. 2h). Knockout CD4+ T cells spontaneously differentiated into T_{FH} cells in vivo 6 d after acute gene deletion (Fig. 2d,e). Different from non-inducible deletion, the inducible inactivation of Regnase-1 (iKO^T) showed strongest T_{FH} cell accumulation compared to iTKO and iDKO, suggesting an advantage of this genotype in the adoptive transfer. Indeed, at a late time point, 7 weeks after transfer, we observed significantly increased numbers of iKO T cells compared to wild-type and iDKO T cells, which also occurred, albeit to a lesser extent, in iTKO T cells (Fig. 2f). Considering intermediate frequencies of dividing iKO CD4+ T cells compared to iDKO and iTKO genotypes early after transfer (Fig. 1f), this finding suggested that Regnase-1 deficiency promotes survival of T cells. Associated with their increased persistence, iKO T cells were capable of inducing autoimmunity in wild-type host mice within 7 weeks (Fig. 2g,h). Transfer of iKO T cells into congenic hosts resulted in accumulation of GC B cells and plasma cells (Fig. 2g and Extended Data Fig. 2i,j) and induced anti-nuclear antibodies (ANAs) in the serum of recipient mice (Fig. 2h). This phenotype was consistent with the appearance of autoantibodies in the serum of 6–8-week-old KO^T and TKO^T (but not DKO^T) mice (Fig. 2i and Supplementary Table 1). Together, these data demonstrate that the autoimmunity associated with the absence of Roquin-1/2 and Regnase-1 genes is caused by deviation of helper T cell functions, because autoimmunity can be transferred with CD4+ T cells, develops in the presence of wild-type T_{reg} cells and originates from a normal T cell receptor repertoire.

Roquin-1/2 and Regnase-1 control CD8+ T cell functions.

CRISPR–Cas9-mediated inactivation of Regnase-1 yielded in improved antitumor responses of adoptively transferred CD8+ or CAR-T cells[18,19]. We therefore analyzed CD8+ T cell phenotypes after conditional deletion of the different RBPs by *Cd4*-Cre-mediated deletion (Fig. 3 and Extended Data Fig. 3). The majority of Roquin-1/2-deficient DKO^T CD8+ T cells adopted a short-lived effector cell (SLEC) phenotype with upregulated KLRG1 (Fig. 3a,b) and downregulated TCF-1 expression (Fig. 3c,d). Fewer Regnase-1-deficient (KO^T) CD8+ T cells showed increased KLRG1 expression with a majority of cells maintaining high TCF-1 expression (Fig. 3a-d). This finding is consistent with a previous report on retained TCF-1 expression after CRISPR–Cas9-mediated inactivation of Regnase-1 in CAR-T cells[19]. Notably, the TKO^T genotype was similar to either Regnase-1 or Roquin-1/2-deficiencies as it moderately increased KLRG1 and strongly reduced TCF-1 expression (Fig. 3a-d). Analyzing additional markers of activation, stemness and exhaustion[26,27] (Extended Data Fig. 3a) we found increased expression of ICOS, CTLA-4 and CD38 in all knockouts. Regnase-1 deficiency increased CXCR5, whereas Roquin-1/2 deficiency induced PD-1 and Tim3 expression (Extended Data Fig. 3a). All knockout T cells showed elevated expression of the transcription factor BATF (Extended Data Fig. 3b), as reported before for inactivation of Regnase-1 (ref. [18]). CD8+ T cells from all genotypes showed the capacity to produce tumor necrosis factor (TNF) upon ex vivo stimulation, but only knockout T cells simultaneously produced TNF and interferon (IFN)-γ (Fig. 3e and Extended Data Fig. 3c). Only CD8+ T cells with Regnase-1 deficiency (KO^T or TKO^T) acquired an enhanced ability to produce interleukin (IL)-2 (Fig. 3f and Extended Data Fig. 3d), whereas all knockout T cells had increased granzyme B expression compared to wild-type counterparts (Fig. 3g

and Extended Data Fig. 3e). To quantify cytotoxicity in vitro, we redirected polyclonal $CD8^+$ T cells toward P815 mastocytoma tumor cells in the presence of anti-CD3 (Fig. 3h). All knockout T cells showed enhanced killing in a chromium-release assay, but we observed strongest effects for Roquin-1/2 (DKO^T) compared to Regnase-1 deficiencies (KO^T) and intermediate effects were seen for TKO^T $CD8^+$ T cells. We then addressed whether inactivation of Roquin-1/2 or Regnase-1 leads to increased $CD8^+$ effector responses in a B16-OVA melanoma model by adoptively transferring $CD8^+$ TCR-transgenic OT-I T cells into hosts that had received tumor cells 3 d before (Fig. 3i). Of note, hosts that received PBS or wild-type OT-I T cells showed exponential tumor growth between days 7–21, whereas either Regnase-1 or Roquin-1/2-deficient OT-I T cells suppressed tumor formation resulting in delayed occurrence of measurable tumors and reduced affection rates of recipient mice (Fig. 3j). Together these data show that Roquin-1/2 and Regnase-1 proteins also control shared cellular programs in cytotoxic T cells, but both RBPs have different contributions to the individual phenotypes (Supplementary Table 1).

Roquin-1 and Regnase-1 exhibit functional interaction.

To address post-transcriptional interaction, we tested the contribution of Roquin-1/2 and Regnase-1 to the regulation of ICOS, a well-described target of these RBPs[3,5,10,28]. We performed tamoxifen gavage of mice to acutely delete floxed alleles by *Cd4*-Cre-ERt2 in vivo. Isolated naive $CD4^+$ T cells were stimulated in vitro for 2 d with anti-CD3/CD28 under type 1 helper T (T_H1) cell conditions, as ICOS expression differs among helper T cell subsets[10,29]. Appropriate deletion was confirmed in immunoblots (Fig. 4a). In wild-type T cells Roquin-1, the much lower-expressed Roquin-2, as well as Regnase-1 proteins increased during days 1–2 and consistent with TCR-induced MALT1 activity, accumulated as cleavage products. Upon removal of TCR stimulation (days 3–5) the full-length Roquin-1/2 and Regnase-1 proteins increased and the cleavage product of Regnase-1 disappeared. By contrast, cleaved Roquin-1 persisted, suggesting either a longer half-life or constitutive cleavage of this protein (Fig. 4a). Consistent with the Regnase-1-encoding *Zc3h12a* mRNA being a target of Roquin-1/2 (ref. [6]), the Regnase-1 protein became strongly induced in iDKO T cells, whereas Roquin-1/2 expression was unchanged upon Regnase-1 inactivation (Fig. 4a), in contrast to results obtained in a human T cell line[22]. ICOS protein expression on wild-type T_H1 cells increased during stimulation (days 1–2) and returned to basal expression after stimulation (days 3–5). In iTKO compared to wild-type T cells, ICOS protein expression was strongly de-repressed at all time points starting at the naive stage (day 0) (Fig. 4b). Notably, iTKO cells were almost unable to decrease ICOS protein expression after removal of the TCR stimulus (days 3–5) (Fig. 4b). Inactivation of either Roquin-1/2 (iDKO) or Regnase-1 (iKO) increased ICOS protein expression during (day 1–2) and after stimulation (days 3–5) intermediate to wild-type and iTKO T_H1 cells. Different from the iTKO genotype, iDKO and iKO T_H1 cells were partially able to decrease ICOS protein after stimulation (Fig. 4b). We then tested whether Roquin-1 and Regnase-1 can complement in the absence of each other and whether redundancy existed among Regnase paralogs (Fig. 4c). To address these questions, we reconstituted Regnase-1 (iKO)- or Roquin-1/2 (iDKO)-deficient $CD4^+$ T cells with doxycycline-inducible, green fluorescent protein (GFP)-tagged Roquin-1 or Regnase-1, Regnase-2, Regnase-3 and Regnase-4 proteins (Extended Data Fig. 4a). In these assays we quantified endogenous ICOS and Regnase-1

expression on day 4 of T cell activation. Notably, exogenous GFP–roquin-1 was readily able to decrease Regnase-1 or ICOS expression in iDKO T cells, but was only partially able to downregulate ICOS expression in Regnase-1-deficient (iKO) T cells (Fig. 4c). Endogenous Regnase-1 protein displays strong regulation of *Zc3h12a* mRNA by Roquin and Regnase-1 (Fig. 4a and refs. [6,30]). To distinguish endogenous from overexpressed Regnase-1 protein, we altered the epitope within GFP–regnase-1 that is recognized by the monoclonal antibody used for detection (Extended Data Fig. 4b,c). While becoming invisible to the antibody, GFP–regnase-1^{invis} protein remained fully able to downregulate targets such as CTLA-4 (Extended Data Fig. 4d). The analysis of iKO T cells reconstituted with ectopic Regnase-1^{invis}, Regnase-2, Regnase-3 or Regnase-4 revealed that all four Regnase paralogs were able to downregulate ICOS expression in the absence of endogenous Regnase-1, with only Regnase-4 being slightly less efficient (Fig. 4c and Extended Data Fig. 4e). Ectopic expression of the same Regnase paralogs in Roquin-1/2-deficient T cells showed that neither Regnase-1^{invis} nor Regnase-2, Regnase-3 or Regnase-4 were able to efficiently downregulate endogenous ICOS or Regnase-1 protein expression (Fig. 4c and Extended Data Fig. 4f). Therefore, full regulation of these shared targets required Roquin-1/2 and Regnase-1 proteins.

Molecular determinants of Roquin cooperation with Regnase-1.

To better understand the functional interaction in the regulation of mRNA targets by Roquin and Regnase-1, we searched for a minimal region in Roquin-1 that was able to regulate shared targets. Notably, in iDKO T cells the amino-terminal MALT1 cleavage product of Roquin-1 (Roquin-1$^{aa1\text{-}510}$) showed partial or almost full activity to downregulate ICOS or Regnase-1 expression, respectively, but was unable to repress Ox40 (*Tnfrsf4*), another well-known target[3,5,31] (Extended Data Fig. 5a-c). This truncated version of Roquin-1 exerted a slight dominant–negative effect on Regnase-1 and Ox40 protein expression when we induced its expression in wild-type T cells (Extended Data Fig. 5d). Deletion analyses indicated that the core RNA-binding domain of Roquin-1 containing $HEPN_N$/ROQ/$HEPN_C$ was sufficient to suppress Regnase-1 expression in iDKO T cells (Extended Data Fig. 5e). We then utilized the interdependent regulation of endogenous Regnase-1 as a readout to screen a set of Roquin-1 point mutants. We exchanged residues on the surface of the $HEPN_N$/ROQ/$HEPN_C$ domains of Roquin-1 with mutations that alter physical properties but were predicted not to interfere with folding (Extended Data Fig. 6a) and found residues M199, E201, E202, L209, E212, D213, L217, F225, D322 in the ROQ domain essential for Roquin-1$^{aa1\text{-}510}$-mediated repression of Regnase-1 (Fig. 4d). Projecting these residues onto the ROQ domain structure[32-34] revealed a site of potential interaction between Roquin-1 and Regnase-1 that is different from the RNA interaction surface (Fig. 4e). Notably, amino acid M199 of Roquin-1, which is mutated in *sanroque* mice, is part of this patch of residues in the ROQ domain (Fig. 4e) and overexpression of this mutant in wild-type T cells did not exhibit a dominant–negative effect on Regnase-1 or ICOS expression (Fig. 4f and Extended Data Fig. 6b). Instead, M199R, L209Y and E212K Roquin-1 mutants in the full-length protein were impaired to downregulate ICOS and Regnase-1 in iDKO T cells at the protein and mRNA level (Fig. 4g and Extended Data Fig. 6c,d). However, all mutants were fully active to repress Ox40 (Fig. 4g and Extended Data Fig. 6c,d) and, similar to wild-type GFP–roquin-1 protein, localized to P bodies, as identified by the RNA helicase Rck, a marker of

P bodies[10] (Extended Data Fig. 6e). The *sanroque* mutation (M199R) as well as the newly identified L209Y and E212K mutants therefore create hypomorphic Roquin-1 variants that have impaired co-regulation activity with Regnase-1 of ICOS and Regnase-1-encoding target mRNAs. These mutations did not affect Ox40 regulation, consistent with regulation of this target mRNA being fully dependent on the carboxy terminus of Roquin-1 and its interaction with the CCR4-NOT complex[2]. These data demonstrate that shared mRNA targets can be subject to full (*Zc3h12a*) or partial cooperation (*Icos*) as well as independent (*Tnfrsf4*) modes of regulation by Roquin-1 and Regnase-1.

Roquin and Regnase-1 form a ternary complex on RNA.

To determine whether post-transcriptional co-regulation can be explained by direct interaction of Roquin-1 with Regnase-1, we performed co-immunoprecipitation and Förster Resonance Energy Transfer (FRET) experiments. Roquin-1 could be co-immunoprecipitated with Regnase-1 from lysates of wild-type but not iKO $CD4^+$ T cells (Extended Data Fig. 7a). To obtain spatial information on this interaction in living cells, we used fluorescence lifetime imaging (FLIM) in HeLa cells co-transfected with GFP–regnase-1 and mCherry–roquin-1. In these experiments the reduction of fluorescence lifetime of GFP is caused upon energy transfer from GFP to mCherry and can be used to quantify donor–acceptor interactions. Both fluorescent proteins localized diffusely in the cytoplasm and colocalized with the P-body marker Rck tagged by blue fluorescent protein (BFP) (Fig. 5a). We found enrichment of GFP–regnase-1 at the ER as reported earlier[7], but only in cells that were not co-transfected with Roquin-1 (Extended Data Fig. 7b). Moreover, sucrose gradient centrifugation of T cell extracts showed the majority of endogenous Regnase-1 co-migrating with Roquin-1 in fractions without monosomes or polysomes (Extended Data Fig. 7c). Notably, GFP–regnase-1 interacted with mCherry–roquin-1 as evidenced by the reduced fluorescence lifetime of GFP in the presence of mCherry–roquin-1 (Fig. 5a,c) but not in its absence (Fig. 5b,c). This energy transfer occurred mainly in P bodies but also dispersed in the cytoplasm. Expression of mCherry–roquin-$1^{aa1\text{-}510}$ also reduced the lifetime of GFP–regnase-1 fluorescence, albeit to a lesser extent (Fig. 5c), confirming that the amino terminus of Roquin-1 is sufficient for the interaction. As all four Regnase paralogs were able to downregulate ICOS expression in Regnase-1-deficient iKO T cells (Fig. 4c), we tested the PIN domain of Regnase-1, which is highly conserved among Regnase paralogs[35]. The truncated GFP–regnase-$1^{aa112\text{-}297}$ protein was localized to the cytoplasm and nucleus and, similar to truncated Roquin-$1^{aa1\text{-}510}$, was no longer enriched in P bodies (Extended Data Fig. 7d,e). The truncated form of GFP–regnase-$1^{aa112\text{-}297}$ also exhibited a reduction in fluorescence lifetime mainly in the cytoplasm where it colocalized with mCherry–roquin-$1^{aa1\text{-}510}$ (Extended Data Fig. 7d,e).

To finely map the structural details of this interaction, we introduced the identified mutations (Fig. 4d,g) in NanoLuc–roquin-$1^{aa1\text{-}510}$ fusion proteins and coexpressed them with HaloTag–regnase-1 to perform NanoBRET assays (Fig. 5d). Co-transfected cells were analyzed for energy transfer from nano-luciferase to the HaloTag ligand. We observed a similar BRET signal for wild-type Regnase-1 and Roquin-1 proteins as for the positive controls (p53 and MDM2). Of note, single ROQ domain mutants of Roquin-1 (M199R, L209Y and E212K) as well as double mutants (M199R/L209Y or M199R/E212K)

effectively reduced the BRET signal. Mutations that interfere with Roquin-1 binding to RNA (K220A/K239A/R260A) (ref. [32]) did not reduce the interaction with Regnase-1. To confirm direct protein–protein interaction, we used surface plasmon resonance (SPR) with purified recombinant proteins. By immobilizing Roquin-1$^{aa2\text{-}440}$ on the surface of a Biacore chip and adding Regnase-1$^{aa1\text{-}452}$ protein in solution, we demonstrated formation of a stable binary Roquin-1 and Regnase-1-containing complex at nanomolar affinity (K_D = 417 nM) (Fig. 5e). Next, we used a pulldown assay to quantify how the identified mutations in Roquin-1 affect direct binding of recombinant proteins. A larger, SUMO-tagged wild-type Roquin-1 protein was mixed with a shorter (untagged) version of Roquin-1 harboring different mutations. We quantified the ability of both proteins to compete for interaction with immobilized, GST-fused Regnase-1 full-length protein (Fig. 5f). The ratio of Regnase-1 bound untagged Roquin-1 mutants to the SUMO-tagged wild-type Roquin-1 proteins in these pulldown experiments revealed three- to fourfold weaker interactions for M199R/L209Y or M199R/E212K Roquin-1 mutants (Fig. 5f and Extended Data Fig. 7f). Of note, single M199R, L209Y or E212K mutants only resulted in a twofold reduction of binding (Extended Data Fig. 7g, h). We next analyzed the interaction of Roquin-1 and Regnase-1 in RNA-electrophoretic mobility shift assays (EMSAs). We used the RNA-binding sufficient amino terminus of Roquin-1$^{aa2\text{-}440}$ and the RNase-dead version Regnase-1$^{aa1\text{-}452;\ D141N}$ to avoid RNA degradation[4] and asked whether these proteins can form a ternary complex with the 3′-UTR stem loop of the *Zc3h12a* mRNA (nt194–212) (ref. [30]) (Fig. 5g). Indeed, the stem loop of the *Zc3h12a* mRNA was specifically bound by Roquin-1$^{aa2\text{-}440}$ and increasing Regnase-1 concentrations in these binding reactions decreased the Roquin-specific band and induced a supershift (Fig. 5g). Collectively, these data establish Roquin-dependent recognition of the mRNA stem loop and additional interactions of the RNA-bound Roquin-1 protein with Regnase-1.

Roquin-1 interaction with Regnase-1 prevents autoimmunity.

We then addressed the functional consequences of interfering with Roquin-1 and Regnase-1 interaction in vivo. We introduced two different *Rc3h1* mutations encoding for Roquin-1 L209Y or E212K, exhibiting weaker or stronger inhibition of interaction and cooperative regulation with Regnase-1, into the mouse germline. Homozygous mice expressing *Rc3h1* mutations encoding for E212K, L209Y or M199R increased the frequencies of activated CD44$^+$CD4$^+$ T cells (Fig. 6a,b), increased T cell proliferation (Fig. 6c,d), caused a T_H1 cell bias with increased IFN-γ production of ex vivo-stimulated CD4$^+$ T cells (Fig. 6e,f and refs. [22,36]) and also induced accumulation of effector memory CD8$^+$ T cells compared to wild-type mice, which was strongest for E212K mutant (Fig. 6g,h). E212K mutant mice showed compromised viability so that only two homozygous animals could be analyzed to date. Together, these data suggest that Roquin-1$^{L209Y/L209Y}$ or Roquin-1$^{E212K/E212K}$ expressing mice phenocopy the *sanroque* phenotype.

We then addressed whether the *sanroque* phenotype[14] develops only due to altered T cell functions. As heterozygosity of the *sanroque* allele has no phenotype in young mice[37], we combined one *Rc3h1*^{san} and one *Rc3h1*^{fl} allele with *Cd4*-Cre or Vav-Cre. This allowed us to compare phenotypes of the *sanroque* allele originating from T lymphocytes versus hematopoietic cells (Fig. 6i-k and Extended Data Fig. 8a-c). Vav-Cre-mediated deletion

of the floxed *Rc3h1* allele was much more potent to induce T cell activation (Fig. 6i and Extended Data Fig. 8a) and GC B cell accumulation compared to *Cd4*-Cre (Fig. 6k and Extended Data Fig. 8c), whereas T_{FH} cell differentiation was similarly increased for both Cre lines (Fig. 6j and Extended Data Fig. 8b). This result indicated T cell-extrinsic contributions of the *sanroque* allele to the observed activation of T cells and accumulation of GC B cells.

Similar to the *sanroque* allele, heterozygosity of alleles encoding L209Y/+ or E212K/+ did not induce obvious phenotypes in young mice (Fig. 7). To formally test whether L209Y and E212K induce the same functional impairment in Roquin-1 as the M199R-encoding allele, we generated mice encoding two heterozygous mutations and compared their phenotypes to mice with homozygous M199R-encoding or wild-type alleles. $CD4^+$ T cells from mice carrying mutations encoding Roquin-$1^{M199R/L209Y}$ and Roquin-$1^{M199R/E212K}$ showed a pronounced increase in frequencies of effector memory (Fig. 7a,b) and T_{FH} cells (Fig. 7c,d) compared to wild-type or heterozygous mutant mice with one wild-type allele (Fig. 7a-d). The heterozygous combination with one *sanroque* allele also caused spontaneous formation of germinal centers in the majority of B cell follicles of the spleen (Fig. 7e) and induced GC B cells in the absence of immunization (Fig. 7f,g). Analyzing autoantibodies in the sera of mice at 8–12 weeks of age (Fig. 7h) we found that homozygous *sanroque* mice expressing Roquin-$1^{M199R/M199R}$, different from heterozygous Roquin-$1^{M199R/+}$ mice, showed a wide range of elevated titers of ANAs, which were partially matched by mice expressing the compound Roquin-$1^{M199/E212K}$, Roquin-$1^{L209Y/L209Y}$ and Roquin-$1^{E212K/E212K}$. In fact, mice expressing Roquin-$1^{M199R/E212K}$ showed significantly increased titers of ANAs when compared to mice expressing Roquin-$1^{M199R/+}$. Collectively, our data demonstrate that the Roquin-1 L209Y and E212K mutants induce phenotypes similar to *sanroque* mice. Notably, the heterozygous combination of E212K- and M199R-encoding alleles revealed compound effects and autoimmunity equivalent to homozygous *sanroque* mice expressing the Roquin-1^{M199R} protein.

Roquin-1 interaction with Regnase-1 inhibits antitumor immunity.

Based on our previous findings demonstrating enhanced cytotoxic activities of Regnase-1 or Roquin-1/2-deficient $CD8^+$ T cells, we asked whether the mixed heterozygous Roquin-$1^{M199R/E212K}$ or *sanroque* mouse mutants that showed elevated autoantibody titers would also exhibit enhanced antitumor responses. First, we established that OT-I $CD8^+$ T cells from heterozygous *sanroque* mice (Roquin-$1^{M199R/+}$) were not effective in conferring protection from tumor growth in the B16-OVA model, as they were comparable to $CD8^+$ T cells from OT-I wild-type mice (Fig. 8a). In the OT-I context we determined only a moderately increased effector memory phenotype in T cells expressing Roquin-$1^{M199R/E212K}$ or Roquin-$1^{M199R/M199R}$ proteins (Fig. 8b). Nevertheless, mice receiving OT-I T cells with either of the two mutations were largely protected from tumor growth as compared to control-treated tumor bearing mice (Fig. 8c). Similar to previous observations on Regnase-1 inactivation[18], the frequency of transferred OT-I TCR-transgenic relative to endogenous $CD8^+$ T cells increased more in the tumor than in the spleen for T cells with mutations encoding Roquin-$1^{M199R/E212K}$ or Roquin-$1^{M199R/M199R}$ (Fig. 8d) and these mutant OT-I T cells showed similar upregulation of CD44 but moderately increased

KLRG1 expression compared to wild-type OT-I T cells (Fig. 8e). Of note, analyzing PD-1 or TOX as markers of exhaustion[38] revealed decreased expression on T cells of mice expressing Roquin-1$^{M199R/E212K}$ or Roquin-1$^{M199R/M199R}$ (Fig. 8f-i). Moreover, CD101, which marks terminally exhausted CD8$^+$ T cells in chronic infections[26], was strongly expressed on wild-type OT-I T cells in the tumor, but almost absent from OT-I T cells expressing Roquin-1$^{M199R/E212K}$ or Roquin-1$^{M199R/M199R}$ proteins. Together, these data show that inhibition of Roquin-1 interaction with Regnase-1 promotes the effector function of tumor-specific T cells by increasing their abundance and attenuating their functional inactivation in the tumor.

Discussion

We describe the direct physical interaction of Roquin-1 and Regnase-1 proteins on RNA. Our findings reveal cooperative regulation of *Icos* and *Zc3h12a* (Regnase-1) mRNAs within the shared target set[7,9,39-41] and explain overlapping phenotypes of Roquin-1/2 and Regnase-1 mutant mice[3,5,14]. Conditional inactivation of Roquin-1/2 or Regnase-1 in T cells or germline mutations introducing M199R (*sanroque*), L209Y and E212K substitutions in the ROQ domain of Roquin-1 that similarly interfere with Roquin-1 binding to Regnase-1, caused autoimmunity. This role in peripheral tolerance becomes evident from spontaneous activation of T cells and accumulation of T_{FH} cells and GC B cells in all mouse lines, as well as autoantibody formation in some mouse lines.

Analyzing similar changes induced through acute deletion of RBP-encoding alleles in T cells, we find that the Roquin-1/2 and Regnase-1 proteins are continuously required in naive T cells to maintain quiescence. These proteins silence cell-intrinsic programs of activation and proliferation associated with metabolic reprogramming to increased glycolysis and enhanced oxidative phosphorylation. Although both Roquin-1/2 and Regnase-1 proteins have already been found to be negative regulators of the mTOR pathway, protein biosynthesis and purine metabolism[42,43], it is currently unclear which target(s) are driving the observed metabolic changes and trigger spontaneous activation of T cells. Following activation, CD4$^+$ T cells committed to the T_{FH} cell subset and CD8$^+$ T cells acquired polyfunctionality and enhanced cytotoxic activity. In our phenotypic comparisons, contributions from Roquin-1/2 and Regnase-1 were often comparable and combined inactivation typically showed increased effects. The related phenotypes indicate that these RBPs cooperate in the same pathways. Cooperative post-transcriptional regulation can either be explained by binding in a complex to the same mRNA, as established here. It can also be explained by independent binding of the different RBPs to the same mRNA[44] or independent binding to different molecules of the same mRNA species as suggested previously[7,13,22] or independent binding to different mRNA species that then cooperate in the same pathway. Understanding how cooperation is encoded in the transcripts of *Icos* and *Zc3h12a* but not in *Tnfrsf4* and thereby allows formation of differential messenger ribonucleoproteins will require extensive structural, biochemical and functional analyses. Of note, our data also revealed selective contributions, especially for CD8$^+$ T cells. Regnase-1 deficiency was associated with increased persistence of CD4$^+$ and CD8$^+$ T cells[5,18] and enabled CD8$^+$ T cells to produce copious amounts of IL-2. By contrast, Roquin-1/2 deficiency induced KLRG1 expression in CD8$^+$ T cells, caused downregulation of TCF-1

and strongly increased in vitro cytotoxicity. Nevertheless, inactivation of either Roquin-1/2 or Regnase-1 improved antitumor responses and a comparable improvement resulted from interfering with Roquin-1–Regnase-1 interaction.

Here, we present the interaction of Roquin-1 with Regnase-1 as a molecular mechanism underlying the prevention of autoimmunity and propose that this interaction can become a promising target for improvement of therapeutic approaches with adoptively transferred antigen-specific T cells.

Methods

Mice.

All mice used in this study were on a C57BL/6 background. All animals were housed in a specific-pathogen-free barrier facility under a 12 h/12 h dark/light regime at 20–24 °C and at a humidity of 45–65% in accordance with the Helmholtz Zentrum München and the Ludwig-Maximilians-Universität München institutional, state and federal guidelines. All experimental procedures involving male or female mice were performed in accordance with regulations and were approved by the local government (Regierung von Oberbayern reference nos. 55.2-2532-Vet_02-19-122, 55.2-2532.Vet_02-17-159, 55.2-2532.Vet_02-18-10 and 55.2-2532.Vet_02-19-68). *Rc3h1/2*$^{fl/fl}$ mice are transgenic for the Roquin-1-encoding gene *Rc3h1* (ref. [21]) and the Roquin-2-encoding gene *Rc3h2*[3]. *Zc3h12a*$^{fl/fl}$ mice are transgenic for the Regnase-1-encoding gene *Zc3h12a*[20]. Transgenic *Rc3h1/2*$^{fl/fl}$ mice were crossed to *Zc3h12a*$^{fl/fl}$ mice to reach the final genotype of *Rc3h1/2*$^{fl/fl}$;*Zc3h12a*$^{fl/fl}$, which were crossed with either *Cd4*-Cre[45], Cre-ERt2 (ref. [23]) or *Cd4*-Cre-ERt2 (ref. [24]) transgenic mice. For tumor experiments, OVA-specific transgenic TCR was introduced by crossing mice to the OT-I line[46]. Rc3h1/2$^{fl/fl}$;*Cd4*-cre-ERt2;rtTA-M2 or *Zc3h12a*$^{fl/fl}$;*Cd4*-cre-ERt2;rtTA-M2 mice were generated by crossing mice with respective loxP sites and *Cd4*-cre-ERt2 with Gt(ROSA)26Sortm1(rtTA*M2) Jae mice[47]. The *Rc3h1*^{M199R} mice (*sanroque*) (EM:02168) were obtained from the European Mouse Mutant Archive consortium and mice expressing CD45.1 (*Ptprc*^{a} *Pepc*^{b}/BoyJ), Vav-iCre (Jax no. 00861) as well as Gt(ROSA)26Sortm1(rtTA*M2)Jae mice were obtained from the Jackson Laboratory. Data collection and analysis were not performed blind to the conditions of the experiments. Experimental groups were assigned according to genotype.

Generation of *Rc3h1* mutant mouse lines via CRISPR–Cas9-based gene editing.

The *Rc3h1_E212K* mouse line was generated by Polygene Transgenetics via CRISPR–Cas9 gene editing of the ES cell line and blastocyst injection and the *Rc3h1_L209Y* mouse line via CRISPR–Cas9-based gene editing by electroporation of one-cell embryos. Specific guide RNAs (Rc3h1_L209Y_gRNA: 5′-CAATGCAGAACCATCTTCTA-3′) were used in form of in vitro transcribed single gRNA (EnGen sgRNA Synthesis kit, NEB, E3322). Before electroporation, the specific sgRNA(200 ng μl^{-1}) and single-strand oligonucleotides (ssODN_Rc3h1_L209Y: 5′-TTGTACCATTTTTCCTAGCGATGCAGGAGGAAGCTCTGAAGCTGGTCTTGTATGCTTTAGAAGATGGTTCTGCATTGTCTCGGAAAGTGTTGGTTCTCTTCGTGGTGCAAAGACTGGAGC-3′; 300 ng μl^{-1}) were diluted in Opti-MEM buffer (Thermo Fisher

Scientific) together with recombinant Cas9 protein (200 ng μl^{-1}, IDT) and incubated for 10 min at 20 °C and 10 min at 37 °C to form the active ribonucleoprotein complex. One-cell embryos were obtained by mating C57BL/6N males (Charles River) with C57BL/6N females super-ovulated with 5 U pregnant mare's serum gonadotropin and 5 U human chorionic gonadotropin and electroporated using an NEPA21 electroporator and a CUY501P1-1.5 electrode (Nepa Gene Co). Zygotes were transferred into pseudopregnant CD1 female mice to obtain live pups. Gene-editing events were analyzed on genomic DNA isolated from ear biopsies of founder mice and F1 progeny using the Wizard Genomic DNA Purification kit (Promega, A1120) following the manufacturer's instructions.

Isolation, in vitro cultivation and transduction of primary CD4+ T cells.

Isolation, in vitro deletion of floxed alleles, in vitro cultivation and transduction of primary $CD4^+$ T cells was performed as described[44]. In reconstitution experiments, for induction of pRetro-Xtight-GFP construct expression in rtTA expressing T cells, transduced cells were cultured in the presence of doxycycline (1 $\mu g\ ml^{-1}$) for 16 h before flow cytometry analysis or 6 h before sorting of GFP^+ cells for quantitative PCR with reverse transcription (RT–qPCR).

In vivo deletion of floxed alleles.

Male and female *Cd4*-Cre-ERt2 mice (age 8–16 weeks) with alleles encoding Roquin and Regnase-1 were fed by oral gavage with 5 mg tamoxifen (Sigma) in corn oil per dose on three consecutive days with two doses of tamoxifen on the last day (20 mg total tamoxifen dose per mouse). Mice were killed 3 d after the last gavage and total $CD4^+$ T cells were isolated using the EasySep Mouse T Cell Isolation kit (STEMCELL) according to manufacturers' instructions.

Generation of mixed-bone-marrow chimeric mice.

Bone marrow cells were isolated from femurs and tibias, frozen in FCS containing 10% dimethylsulfoxide and stored at –80 °C until injected into mice. Male and female CD45.1/2 heterozygous recipient mice (age 8–11 weeks) were lethally irradiated with 2 × 5.5 Gy with a XStrahl CIX2 X-ray device. Then, 4×10^6 bone marrow cells were injected intravenously (i.v.) into CD45.1/2 heterozygous recipient mice. Mice were treated for 2 weeks with water supplemented with antibiotics in drinking water (0.04% Baytril) and 9 weeks after irradiation, reconstituted cells were analyzed by flow cytometry.

Adoptive T cell transfer.

Total $CD3^+$ T cells, naive $CD4^+$ T cells or $CD8^+$ T cells were isolated from donor mice using the EasySep Mouse $CD3^+$ Cell Isolation kit, Mouse Naive $CD4^+$ T Cell Isolation kit or Mouse $CD8^+$ Cell Isolation kit (STEMCELL), respectively, according to manufacturers' instructions. Then, 1.5×10^6 cells were injected i.v. into 10-week-old male and female $CD45.1^+$ WT recipient mice. On day 1 and 2 after injection all recipient mice were fed 5 mg tamoxifen by oral gavage twice per day (20 mg total tamoxifen per mouse). Mice were killed on day 8 or day 49 after receiving the first tamoxifen dose.

Ex vivo T cell stimulation.

Total splenocytes were stimulated with 20 nM PMA and 1 μM ionomycin for a total of 4 h. After 1 h of stimulation 10 μg ml^{-1} brefeldin A was added. The reaction was stopped by washing the cells with cold PBS twice before proceeding with antibody staining for flow cytometry.

^{51}Cr-release assay.

Cell-mediated cytotoxicity was determined by a redirected lysis assay. P815 mastocytoma target cells were labeled with 50 μCi ^{51}Cr for 1 h at 37 °C. After washing, 2,000 target cells per 96-well were incubated with effector cells (CD8$^+$ T cells isolated from lymph nodes and spleen) at different effector:target (E:T) ratios in the presence of anti-CD3 (clone (cl.) 145-2C11H, 1 μg ml^{-1}, inhouse production) for 4 h at 37 °C. Subsequently, the amount of radioactivity in the supernatant was measured using a scintillation counter (TopCount NXT).

Melanoma tumor model.

Male and female C57BL/6 wild-type mice were subcutaneously injected with 2×10^5 B16-OVA tumor cells. After 3 d, congenically marked OT-I T cells (1×10^6 i.v.) were adoptively transferred directly after isolation. Tumors were measured manually with a caliper three times per week and tumor size was calculated according to the formula (length × width^2) / 2. Mice were humanely killed if the maximal permitted tumor size of 1,400 mm^3 was reached. Otherwise spleens and tumors were collected not later than 21 d after tumor engraftment, cut into small pieces and passed through a 100-μm diameter filter.

Flow cytometry and data analysis with FlowJo.

Single-cell suspensions were stained with fixable blue viability dye (Thermo Fisher Scientific) for 20 min at 4 °C. For the detection of surface proteins cells were stained with the appropriate antibodies in FACS buffer (2% FCS, 1 mM EDTA in PBS) for 20 min at 4 °C. For intracellular staining of cytokines, Roquin, Regnase-1 or CTLA-4 cells were fixed with 2% formaldehyde at 20 °C for 15 min, washed with saponin permeabilization buffer (0.5% saponin and 1% BSA in PBS) and stained with the appropriate antibodies in saponin buffer for 40 min at 4 °C. For commercially available intracellular antibodies, cells were fixed with Foxp3 Fixation/Perm buffer (eBioscience) according to the manufacturer's protocol for 30 min at 4 °C, permeabilized with Foxp3 permeabilization buffer (eBioscience) and stained with antibodies diluted in Foxp3 permeabilization buffer for 40 min at 4 °C. Cell populations were acquired on BD LSR Fortessa, BD FACSCanto II or Cytoflex (Beckmann Coulter) flow cytometry devices or sorted using BD FACS Aria III. Data were processed using FlowJo software (v.10.6.0, BD Bioscience). An exemplified gating strategy is shown in Extended Data Fig. 9. The following antibodies were used: anti-CD4 (cl. GK1.5, 1:400 dilution), anti-CD8a (cl. 53-6.7, 1:400 dilution), anti-CD38 (cl. 90, 1:200 dilution), anti-CD44 (cl. IM7, 1:200 dilution), anti-CD62L (cl. MEL-14, 1:200 dilution), anti-CD45.1 (cl. A20, 1:200 dilution), anti-CD45.2 (cl. 104, 1:200 dilution), anti-CD45R (B220; cl. RA3-6B2, 1:200 dilution), anti-CD101 (cl. Moushi101, 1:200 dilution), anti-PD-1 (cl. J43, 1:200 dilution), anti-GL7 (cl. GL7, 1:200 dilution), anti-granzyme B (cl. NGZB, 1:150 dilution), anti-IFN-γ (cl. XMG1.2, 1:200 dilution), anti-ICOS (cl. C398.4A, 1:200 dilution),

anti-IL-2 (cl. JES6-5H4, 1:100 dilution), anti-KLRG1 (cl. 2F1, 1:100 dilution), anti-Ox40 (cl. OX-86, 1:200 dilution), anti-CTLA-4 (cl. UC10-4B9, 1:200 dilution), anti-Foxp3 (cl. FJK-16S, 1:100 dilution), anti-Ki67 (cl. SolA15, 1:200 dilution), anti-Tim3 (cl. RMT3-23, 1:200 dilution) and anti-TNF-α (cl. MP6-XT22, 1:100 dilution) all from eBioscience; anti-CD95 (cl. JO2, 1:200 dilution), anti-BATF (cl. S39-1060, 1:40 dilution) and anti-Bcl6 (K112-91, 1:50 dilution) all from BD Bioscience; anti-IL-17A (cl. TC11-18H10.1, 1:100 dilution), anti-CXCR5 (cl. L138D7, 1:50 dilution), anti-CD19 (cl. 6D5, 1:300 dilution), anti-IgD (cl. 11-26c.2a, 1:200 dilution), goat anti-rat antibody (cl. Poly4054, 1:200 dilution) all from BioLegend; and goat anti-rabbit antibody (Invitrogen, 1:200 dilution), anti-CD138 (cl. 281-2, BD Pharmingen, 1:200 dilution), anti-Roquin-1/2 (cl. 3F12, inhouse production, 1:10 dilution), anti-Regnase-1 (cl. 15D11, inhouse production, 1:10 dilution), anti-TCF-1 (cl. S33-966, BD Bioscience, 1:80 dilution), anti-TOX (cl. REA473, Miltenyi Biotech, 1:50 dilution) and anti-Rck (Bethyl).

AMNIS image stream measurements.

Cells were stained as described above and measured using the AMNIS image stream (Millipore).

Immunofluorescence microscopy.

Spleens were frozen in OCT compound (Tissue Tek), cryosections (7 μm) were prepared and fixed in acetone. Slides were stained with anti-IgD-PE (cl. 11-26c.2a, BioLegend) and anti-GL7-Alexa647 (cl. GL7, BioLegend). Images were acquired on an Olympus BX41 fluorescence microscope and processed with Fiji (v.1.0).

Seahorse measurements.

In vitro-deleted and activated $CD4^+$ and $CD8^+$ T cells were starved of IL-2 overnight and restimulated with anti-CD3e and anti-CD28 antibodies (0.5 $\mu g\ ml^{-1}$, BioLegend) for 6–7 h before the seahorse measurement. Cells were washed with PBS, resuspended in seahorse assay medium (XF RPMI, Agilent) containing 2 mM L-glutamine (Thermo Fisher Scientific), with or without 5 mM glucose (Sigma-Aldrich) for glycolytic or mitochondrial stress tests, respectively, and seeded on poly-L-lysine (50 $\mu g\ ml^{-1}$, Sigma-Aldrich) and goat anti-hamster (50 $\mu g\ ml^{-1}$) pre-coated plates at a density of 2–2.2 × 10^5 cells per well. Cells were degassed using a Cytation1 reader (BioTek) at 37 °C for 1 h. ECARs and OCRs were measured on a 96-well XFe Extracellular Flux Analyzer (Agilent). For each treatment three cycles of 3 min mixing and measurement each were performed. For normalization, nuclei stained with 8 μm Hoechst (Thermo Fisher Scientific) were counted in a Cytation1 reader. To assess basal glycolytic activity during the glycolytic stress test, the ECAR response to an acute 5-mM glucose (Sigma-Aldrich) injection was measured, followed by a 1.5μM oligomycin (Sigma-Aldrich) injection to inhibit mitochondrial respiration and induce maximal glycolytic capacity. Nonglycolytic acidification was assessed after injecting 50 mM 2-DG (Sigma-Aldrich). In the mitochondrial stress test 1.5 μM oligomycin was injected to inhibit mitochondrial proton flux. Maximal mitochondrial respiration was induced by injection of 1 μM FCCP (Sigma-Aldrich) and terminated by 0.5 μM rotenone (Sigma-Aldrich) and antimycin A (Sigma-Aldrich) injections.

Sucrose gradient fractionation.

Sucrose gradient fractionation was performed as described[48], with slight modifications. Shortly after, 5×10^7 $CD4^+$ T cells were washed in ice-cold PBS containing cycloheximide (0.1 mg ml^{-1}), resuspended in extraction buffer (20 mM Tris-HCl (pH 7.4), 140 mM KCl, 0.5 mM dithiothreitol (DTT), 5 mM $MgCl_2$, 0.5% Nonidet-P40, 0.1 mg ml^{-1} cycloheximide and protease inhibitor (PI)), incubated for 15 min on ice and centrifuged for 10 min at 12,000*g*. Extracts were layered onto a 4.7-ml sucrose gradient (18–50% sucrose (*w/v*) in 20 mM Tris-HCl, pH 7.4, 140 mM KCl, 0.5 mM DTT, 5 mM $MgCl_2$ and 0.1 mg ml^{-1} cycloheximide) and centrifuged at 4 °C in a SW55Ti rotor (Beckman) at 35,000 r.p.m. for 90 min. Gradients were fractionated into ten 0.5-ml fractions and absorbance profiles at 254 nm were recorded using the Piston gradient fractionator (Biocomp). For further protein analysis, polysome gradient fractions were subjected to TCA precipitation.

Culture of cell lines.

HeLa, HEK293T, P815 and B16-OVA cells were cultured in DMEM (Invitrogen) supplemented with 10% (*v/v*) FCS (Gibco), Pen-Strep (100 U ml^{-1}, each, Thermo Fisher Scientific), 10 mM HEPES, pH 7.2–7.5 (Invitrogen) at 37 °C and 10% CO_2. HEK293T, HeLa, B16-F10 (no. CRL-6475) and P815 (no. TIB-64) cell lines were purchased from ATCC. The B16-F10 cell line was retrovirally transduced with MigR1-OVA-GFP (provided by D. Zehn, TU Munich).

Calcium phosphate transfection for generation of retroviral particles.

HEK293T cells pre-treated with 25 μM chloroquine, were co-transfected with 5 μg of the packaging vector pCL-Eco (Addgene; 12371) and 50 μg of the respective pRetro-Xtight plasmids using calcium phosphate as a transfection reagent. After 6 h cells were washed and cultured in fresh medium for an additional 48 h. Viral particles were filtered (0.45 μM) and mixed with polybrene (10 μg ml^{-1}) before T cell transduction.

Expression plasmids.

For murine T cell reconstitution experiments, the GFP-coding sequence (CDS), the corresponding murine complete CDS or corresponding shortened versions, as indicated, of Roquin-1, Regnase-1, Regnase-2, Regnase-3 or Regnase-4 C-terminally fused to GFP were inserted into the pRetro-Xtight expression plasmid (Clontech) under the control of a Tet-responsive promotor. For FLIM/FRET experiments, murine Roquin-1 CDS fused C-terminally to the mCherry CDS or the Rck CDS C-terminally fused to eBFP2 was inserted into the pdest12.2 backbone (Invitrogen). For NanoBret assays, the complete CDS of Regnase-1 or Roquin-$1^{aa1\text{-}510}$ was inserted downstream of the HaloTag CDS in the pFN21A HaloTag CMV Vector (Promega) or NanoLuc CDS in the pFN31K Nluc CMV-neo Flexi Vector (Promega), respectively. Mutations in the CDS of Regnase-1 or Roquin-1 were inserted via the QuikChange site-directed-mutagenesis procedure (Stratagene). Primer sequences are available on request.

Cell lysis, SDS–PAGE and immunoblotting.

Cell lysis and SDS–PAGE were performed as described[42]. For immunoblotting, proteins were transferred to a PVDF membrane and analyzed using primary antibodies followed by horseradish peroxidase (HRP)-conjugated secondary antibodies (Cell Signaling). For protein detection, Amersham ECL Prime Western Blotting Detection Reagent and X-ray films were used. The following primary antibodies were used: Roquin-1/2 (cl. 3F12, monoclonal, inhouse production), Regnase-1 (cl. 15D11, inhouse production), Roquin-1 (A300-515A, polyclonal, Bethyl), GAPDH (cl. 6C5, Merck Millipore) and Rpl7a (Abcam, ab70753).

RNA isolation and RT–qPCR.

RNA isolation was performed by column-based RNA isolation utilizing the NucleoSpin RNA isolation kit (Macherey-Nagel) according to the manufacturer's protocol. RNA was transcribed into complementary DNA using the Quantitect RT kit (Roche) according to the manufacturer's protocol. To quantify gene expression, the UPL Probe Library System by Roche and the Roche Light Cycler 480 were utilized (Supplementary Table 2).

Co-immunoprecipitation.

To analyze interaction of Roquin and Regnase-1 proteins in T cells, co-immunoprecipitation was performed. T cells were lysed in lysis buffer (20 mM Tris-HCl (pH 7.5), 150 mM NaCl, 0.25% (*v/v*) Nonidet-P40, 1.5 mM $MgCl_2$, 1 mM DTT supplemented with 1× cOmplete, EDTA-free Protease Inhibitor Cocktail (Roche), 1× Halt Phosphatase Inhibitor Cocktail (Thermo Fisher) and 0.2 U μl^{-1} RNase inhibitor (RNasin, Promega)) on ice for 15 min and cleared by centrifugation for 15 min at 12.000*g* and 4 °C. Then, 10 μl Protein-A dynabeads (Invitrogen) were coupled under constant rotation to 10 μg Regnase-1 antibody (R&D systems, no. 604421) in lysis buffer at 4 °C overnight, followed by 1 h at 20 °C. After washing the antibody-coupled beads with phosphate-citrate buffer (24.4 mM citric acid, 65 mM sodium hydrogen phosphate (pH 5), supplemented with 1 mM DTT and PI), washed beads were incubated with 15 mg protein lysate in 900 μl lysis buffer for 4 h at 4 °C while continuously rotating. Then, beads were washed three times with lysis buffer (+ DTT and PI) and resuspended in 40 μl 1× Laemmli buffer. The samples were boiled at 95 °C for 5 min and co-immunoprecipitation was analyzed by SDS–PAGE and immunoblotting with monoclonal antibodies recognizing Regnase-1 (cl. 15D11) and Roquin (cl. 3F12).

NanoBret assay.

NanoBret assays were performed according to the protocol of the NanoBRET Nano-Glo Detection System (Promega). Between 4–6 h after seeding of 1×10^6 HEK293T cells into six-well plates, cells were transfected with 2 μg of HaloTag and 0.02 μg of NanoLuc expression plasmids using FuGENE reagent (Promega) according to the manufacturer's instructions. After 20 h, cells were trypsinized, resuspended in Opti-MEM I Reduced Serum Medium (no phenol red, with 4% FCS, Thermo Fisher Scientific), re-plated into 96-well plates and incubated with HaloTag NanoBRET 618 Ligand (100 nM final concentration) or dimethylsulfoxide as a no ligand negative control for 22 h. After addition of NanoBRET Nano-Glo Substrate the donor emission (460 nm) and acceptor emission (618 nm) was measured using the GloMax Discover System (Promega). The raw donor and acceptor

values were calculated and milliBRET units (mBU) were determined as mBU = acceptor emission (618 nm) / donor emission (460 nm) × 1,000 and afterwards corrected for background signal as mBRET = mean mBU experimental sample – mean mBU no ligand control.

FRET/FLIM experiments.

For confocal microscopy 1 d before analysis HeLa cells were transfected via calcium phosphate precipitation and cells were seeded 6 h before microscopic analysis on eight-well μ-Slides (glass bottom, Ibidi) in Leibovitz's L-15 medium (no phenol red, Thermo Fisher Scientific). For staining of the ER the cells were washed with HBSS (calcium, magnesium and no phenol red, Thermo Fisher Scientific) and incubated for 25 min at 37 °C in prewarmed staining solution (300 μl HBSS containing 0.8 μM ER-Tracker Red dye, Thermo Fisher Scientific). Confocal and FLIM images were performed with a TCS SP8X FALCON confocal head (Leica Microsystems) mounted on an inverted microscope (DMi8; Leica Microsystems). For confocal imaging, a 405-nm diode and a white-light laser were used as excitations sources (488 nm for GFP and 594 nm for mCherry). Single photons were collected through a 93×/1.3 NA glycerin-immersion objective and detected on Hybrid Detectors (HyD) (Leica Microsystems) with a 414–468 nm, 500–550 nm and 610–722 nm spectral detection window for BFP, GFP and mCherry detection, respectively. The image size was set to 512 × 512 pixels and a 2.5-fold zoom factor was applied, giving a pixel size of 0.098 μm and an image size of 50 × 50 μm. For FLIM, the white-light laser delivered 20 MHz repetition rate at 488 nm. Arrival time of single photons was measured with the included FALCON module and 60 frames were acquired at 1.17 Hz for each time-correlated single-photon counting recording, corresponding to a scanning speed of 600 Hz. FLIM image analyses were performed in the LAS X software. A threshold was applied to the lifetime images before analysis to eliminate background noise. Different regions of interest were fitted with a two-exponential decay model. The mean amplitude-weighted fluorescence lifetime of the area was extracted then reported. The FRET efficiency (E_{FRET}) was calculated according to the following formula:

$$E_{FRET} = 1 - (\tau_{DA} / \tau_{D})$$

where τ_{DA} is the lifetime of the donor–acceptor sample and τ_{D} is the lifetime of the donor alone. Lifetime images shown were produced using the phasor approach[49].

ELISA for detection of anti-nuclear antibodies.

Blood taken from hearts of male and female (age 6–12 weeks) mice was directly centrifuged at 10,000*g* for 10 min at 4 °C to collect serum. ANA ELISAs were performed using the mouse ANA total IgG ELISA kit (Alpha Diagnostic) according to the manufacturer's instructions. Optical density at 450 nm was measured on an ELISA reader (Versa Max Microplate reader, Molecular Devices) and concentrations were calculated by using standard serum as a reference.

Prediction of interacting residues on the Roquin surface.

The structures of the ROQ domain bound to RNA (PDB 4QI2) and ROQ-HEPN domain (PDB 4TXA) were superposed using PyMOL and a model of the ROQ-HEPN domain bound to the RNA stem loop was generated. Based on this model, residues on the Roquin surface that are typically involved in protein–protein interactions but not covered by RNA were mutated on the basis of stereochemical and/or electrostatic interference.

Expression and purification of GST–regnase-1^{D141N}.

Full-length GST–regnase-1^{D141N} was expressed from pGEX-6P-3 in *Escherichia coli* Rosetta 2 (DE3) pLysS. Cells were cultured at 37 °C in 2YT containing 50 μg ml^{-1} ampicillin, 35 μg ml^{-1} chloramphenicol and 30 μM $ZnCl_2$. At an optical density (OD_{600}) of 0.8, temperature was reduced to 18 °C and expression was induced by adding isopropyl β-D-1-thiogalactopyranoside (IPTG) to a concentration of 0.7 mM. After 16 h of incubation, cells were collected (5,200*g*, 4 °C, 30 min). Due to the fast degradation of the protein, the whole purification was conducted at 4 °C in one day. Cells were resuspended in lysis buffer (500 mM NaCl, 50 mM HEPES (pH 7.5), 2 mM $MgCl_2$, 30 μM $ZnCl_2$, 2 mM DTT, 1× cOmplete Protease Inhibitor Cocktail (Roche)) and sonicated on ice. After clarification of the lysate (30,000*g*, 4 °C, 30 min), supernatant was applied on a pre-equilibrated GSTrap column (GE Healthcare). After washing steps with high-salt buffer (1 M NaCl, 50 mM HEPES (pH 7.5), 2 mM $MgCl_2$, 30 μM $ZnCl_2$, 2 mM DTT) and re-equilibration in lysis buffer, bound proteins were eluted with lysis buffer containing 30 mM reduced glutathione. Eluted fractions were pooled and immediately loaded onto a heparin column (GE Healthcare) equilibrated in 100 mM NaCl, 20 mM HEPES (pH 7.5), 2 mM $MgCl_2$, 30 μM $ZnCl_2$ and 2 mM DTT and eluted using a linear gradient to 60% high-salt buffer in ten column volumes. Pooled fractions were further purified using a Superdex200 column (GE Healthcare) in gel filtration buffer (150 mM NaCl, 20 mM HEPES (pH 7.5), 2 mM $MgCl_2$, 30 μM $ZnCl_2$, 2 mM DTT). Protein-containing fractions were pooled and concentrated.

Expression and purification of GST–regnase-1$^{aa1\text{-}452;D141N}$.

His_6–GST–regnase-1$^{aa1\text{-}452:D141N}$ with an additional C-terminal His_6 tag was expressed from pOPINJ in *E. coli* Rosetta (DE3) cells. Cells were grown in LB medium with 34 μg ml^{-1} chloramphenicol and 100 μg ml^{-1} ampicillin at 37 °C. Expression of the protein was induced at OD_{600} 0.6 by adding 0.5 mM IPTG and overnight growing conditions changed to 18 °C. Next, cells were collected (6,238*g*, 15 min, 4 °C) and resuspended in lysis buffer (500 mM NaCl, 2 mM DTT, 2 mM $MgCl_2$, 30 μM $ZnCl_2$, PIs and 50 mM HEPES, pH 8) and sonicated on ice. The supernatant of the centrifugation (48,384*g*, 30 min, 4 °C) was applied to GSTrap column. The column was washed with high-salt buffer (1 M NaCl and 50 mM HEPES, pH 8) and the protein eluted using elution buffer (500 mM NaCl, 30 mM glutathione, 2 mM DTT, 2 mM $MgCl_2$, 30 μM $ZnCl_2$, PIs and 50 mM HEPES, pH 8). After changing the buffer to a low-salt buffer (50 mM NaCl, 35 μM $ZnCl_2$, 2 mM DTT, 2 mM $MgCl_2$ and HEPES, pH 8) the protein was loaded onto a heparin column. The bound protein was eluted with a gradient (20 column volumes 0–100%) using the same buffer including 1 M NaCl. Fractions were pooled, concentrated and further purified using a Superdex 75

10/300 GL column (Amersham Pharmacia Biosciences) in 150 mM NaCl, 35 μM $ZnCl_2$, 2 mM DTT and HEPES, pH 7.5 buffer.

Expression and purification of Roquin-1$^{aa2-440}$, SUMO–roquin-1$^{aa2-440}$ and its mutants.

His_6–SUMO–roquin-1$^{aa2-440}$ was expressed from pOPINS3C in *E. coli* BL21 Star (DE3). Roquin-1$^{aa2-440}$ and its mutants (Roquin-1$^{aa2-440;M199R}$, Roquin-1$^{aa2-440;L209Y}$, Roquin-1$^{aa2-440;E212K}$, Roquin-1$^{aa2-440;M199R/L209Y}$ and Roquin-1$^{aa2-440;M199R/E212K}$) were expressed as His_6-tagged proteins from pETM11 or pOPINF in *E. coli* BL21 (DE3) or BL21 Star (DE3). Cells were grown at 37 °C in LB medium with 50 μg ml^{-1} kanamycin (pETM11) or with 100 μg ml^{-1} ampicillin (pOPINS3C or pOPINF). At an OD_{600} of 0.4, cultures were induced by adding 0.5 mM IPTG and overnight growing conditions changed to 20 °C. Cells were collected (6,238*g*, 15 min, 4 °C), resuspended in lysis buffer (300 mM NaCl, 15 mM imidazole, 1 mg ml^{-1} lysozyme, 2 mM DTT, PIs and 50 mM Tris, pH 8) and sonicated on ice. After centrifugation (48,384*g*, 30 min, 4 °C), the supernatant was applied to a HisTrap column (GE Healthcare). Bound protein was eluted, concentrated and further purified using a Superdex 75 10/300 GL column (Amersham Pharmacia Biosciences) in 150 mM NaCl and 50 mM HEPES, pH 7.5 buffer.

Electrophoretic mobility shift assay.

The RNA fragment of Regnase-1 3′-UTR (nt194-212, IBA GmbH) was radioactively labeled using T4 polynucleotide kinase (Thermo Fisher Scientific) and [γ^{32}P] ATP (Hartmann Analytic) at 37 °C for 30 min. The reaction was stopped at 75 °C for 10 min. Sepharose spin columns (NucAway; Invitrogen) were used to separate RNA from free nucleotides. Radioactively labeled RNA (6 nM), proteins (GST–regnase-1$^{aa1-452;D141N}$, Roquin-1$^{aa2-440}$) and tRNA competitor (30 μg ml^{-1}) were incubated in HEPES/NaCl/$MgCl_2$ buffer (10 mM HEPES (pH 7.5), 150 mM NaCl and 2 mM $MgCl_2$) and 4% glycerol in a final volume of 20 μl for 30 min at 20 °C. Samples were resolved by native TBE–PAGE (4% polyacrylamide and 1× TBE buffer) or by gradient NativePAGE 4–16% Bis-Tris (Invitrogen) gels. Gels were analyzed using Fuji imaging plates exposed in the FLA-5100, after 10 min incubation in fixing solution (30% (*v/v*) methanol and 10% (*v/v*) acetic acid) and vacuum drying.

Competition pulldown assays of GST–regnase-1^{D141N} and Roquin variants.

Competition pulldowns were performed using GSTrap beads (GE Healthcare) pre-equilibrated in binding buffer (150 mM NaCl, 30 mM HEPES (pH 7.5), 2 mM $MgCl_2$, 30 μM $ZnCl_2$ and 2 mM DTT). Then, 0.5 nmol human full-length GST–regnase-1^{D141N} was mixed with 150 μl bead slurry and incubated for 10 min on ice. Subsequently, premixes of 1.2 nmol SUMO–roquin-1$^{aa2-440}$ wild-type and 1.2 nmol Roquin-1$^{aa2-440}$ mutant variants were added and incubated for 60 min at 4 °C. After four wash steps (950 μl binding buffer), bound proteins were eluted with 60 μl elution buffer (150 mM NaCl, 30 mM HEPES (pH 7.5), 2 mM $MgCl_2$, 30 μM $ZnCl_2$, 2 mM DTT and 30 mM reduced glutathione). Then, 5% input of individual proteins, wash fractions and elutions were analyzed on 12.5% SDS–PAGE, stained with Coomassie blue and imaged using a ChemiDoc XRS+ (BioRad). Band intensities of Roquin-1$^{aa2-440}$ mutant variants and SUMO–roquin-1$^{aa2-440}$ wild-type of three

independent experiments were quantified and averaged using Image Lab software and their ratio was plotted.

Surface plasmon resonance.

Binding between Roquin-1$^{aa2\text{-}440}$ and GST–regnase-1$^{aa1\text{-}452;D141N}$ was analyzed using BIACORE 3000 instrument (Biacore). Roquin-1$^{aa2\text{-}440}$ was coupled to the CM5 sensor chip (Biacore) at a concentration of 35 μg ml^{-1} in 10 mM sodium-phosphate buffer (pH 5.7). GST–regnase-1$^{aa1\text{-}452;D141N}$ was injected onto the sensor chip using the concentrations 0.032, 0.063, 0.125, 0.25, 0.5 and 1 μM at 30 μl min^{-1} flow rate in running buffer (150 mM NaCl, 35 μM $ZnCl_2$, 0.05% Tween20, 2 mM DTT and 10 mM HEPES, pH 7.5) at 20 °C. Acquired binding curves were double-referenced against the signal in the buffer run and a ligand-free reference channel. The equilibrium dissociation constant (K_D) was calculated from steady-state measurements using the BIAevaluation program (Biacore).

Statistical analysis and experimental design.

Statistical analysis was performed with Prism 5.0b (GraphPad) or Origin. *P* values were calculated with Student's *t*-test or one-way or two-way ANOVA, as indicated. Statistical significance was indicated. Error bars represent mean of all data points ± s.e.m. or mean ± s.d., as indicated. No statistical methods were used to predetermine sample sizes but our sample sizes are similar to those reported in previous publications[3,6,18,19]. Data distribution was assumed to be normal, but this was not formally tested. Experiments did not involve randomization of animals/samples or conditions or blinding of investigators. No animals or data points were excluded from analyses.

Extended Data

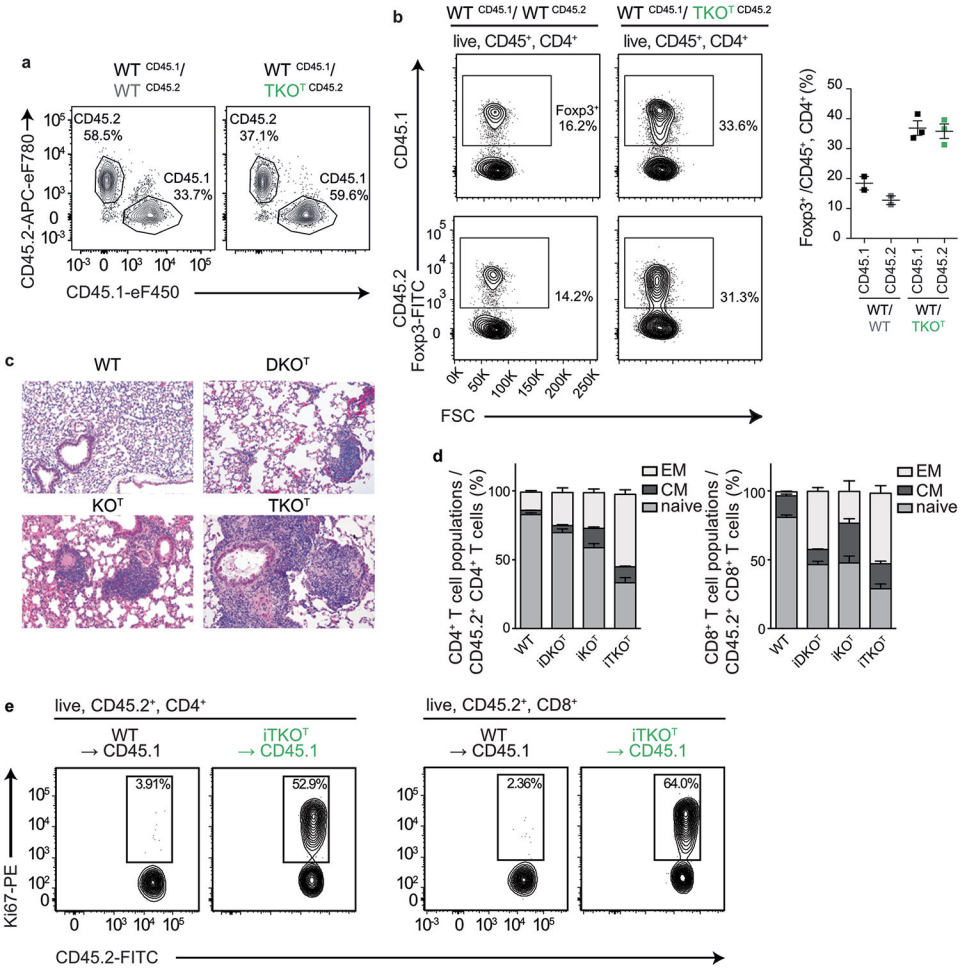

Extended Data Fig. 1 |. Roquin-1/2 and Regnase-1 maintain quiescence of T cells.

(**a**, **b**) Analysis of mixed bone marrow chimeric mice using either WT (CD45.2) and WT (CD45.1) or TKO^T (CD45.2) and WT (CD45.1) bone marrow cells injected into lethally irradiated CD45.1/2 recipient mice. Flow cytometry analysis of CD45.1 and CD45.2 cell populations (**a**) or T_{reg} cells (**b**) in splenocytes from recipient mice 9 weeks after reconstitution (WT CD45.1/WT CD45.2 recipients: n = 2, WT CD45.1/TKO CD45.2 recipients: n = 3, analyzed in one experiment). (**c**) H&E sections of lungs showing alveoli from WT, DKO^T, KO^T and TKO^T mice at the age of 6-8 weeks (Representative data of n ≥3 individual mice). (**d**, **e**) Analysis of CD45.2$^+$ CD3$^+$ T cells from Cre-ERt2 (WT), *Rc3h1/2*$^{fl/fl}$; Cre-ERt2 (iDKO), *Zc3h12a*$^{fl/fl}$; Cre-ERt2 (iKO) and *Rc3h1/2*$^{fl/fl}$; *Zc3h12a*$^{fl/fl}$; Cre-ERt2 (iTKO) mice that were adoptively transferred into WT CD45.1$^+$ mice. Recipient mice were treated with tamoxifen by oral gavage to induce deletion of floxed alleles. On day 8 post transfer, T cells were analyzed for their ability to acquire an effector/memory phenotype (**d**) or to proliferate (**e**) within the host (n = 6 biological replicates).

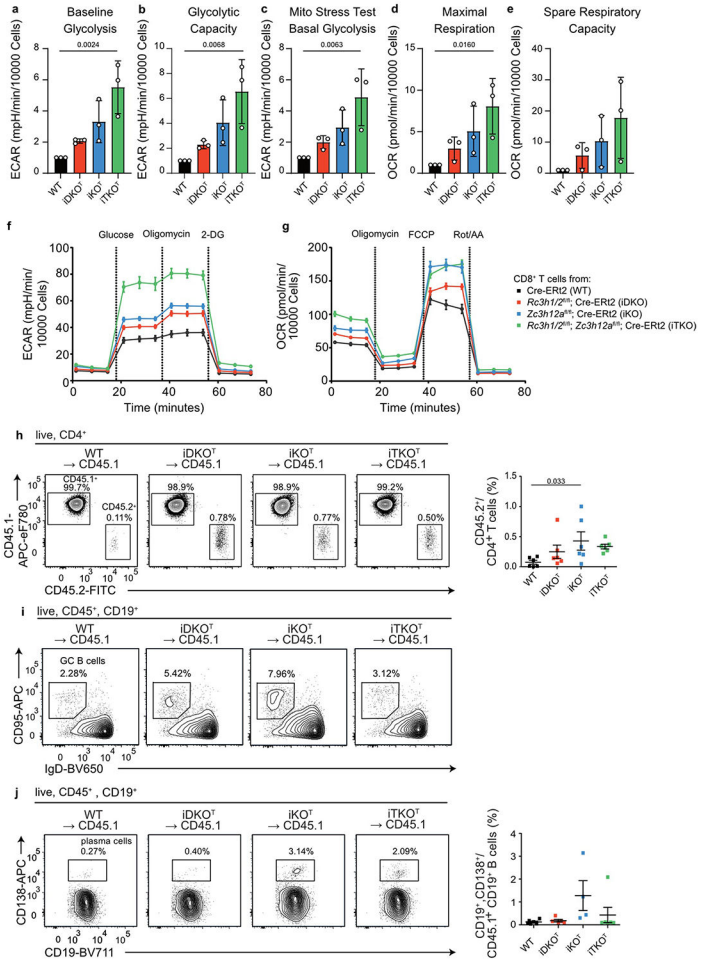

Extended Data Fig. 2 |. Roquin-1/2 and Regnase-1 control metabolism and humoral autoimmunity.

CD4$^+$ (**a–e**) or CD8$^+$ (**f**, **g**) T cells from Cre-ERt2 (WT), *Rc3h1/2*$^{fl/fl}$; Cre-ERt2 (iDKO), *Zc3h12a*$^{fl/fl}$; Cre-ERt2 (iKO) and *Rc3h1/2*$^{fl/fl}$; *Zc3h12a*$^{fl/fl}$; Cd4-Cre-ERt2 (iTKO) were treated with 4′-OH tamoxifen *in vitro* to induce deletion of floxed alleles. T cells were activated *in vitro* and expanded with IL-2 medium for 2d. IL-2 was withdrawn overnight before T cells were restimulated with anti-CD3/28 prior to glycolytic (**a**, **b**, **f**) and mitochondrial stress tests (**c–e**, **g**). Shown are calculated ratios for ECAR (mpH/min/10000 cells) (**a–c**) and OCR (pmol/min/10000 cells) (**d–e**) relative to WT, respectively. Naïve CD45.2$^+$ CD4$^+$ T cells from *Cd4*-Cre-ERt2 (WT), *Rc3h1/2*$^{fl/fl}$; *Cd4*-Cre-ERt2 (iDKO), *Zc3h12a*$^{fl/fl}$; *Cd4*-Cre-ERt2 (iKO) and *Rc3h1/2*$^{fl/fl}$; *Zc3h12a*$^{fl/fl}$; *Cd4*-Cre-ERt2 (iTKO) mice were adoptively transferred into CD45.1$^+$ recipient mice. Mice were treated with tamoxifen by oral gavage to induce deletion of floxed alleles. Adoptively transferred cells were identified by congenic markers on day 8 (**h**) or accumulation of germinal center B (**i**) or plasma cells (**j**) was determined on day 49 after induced deletion. (**a–e**) Data are presented as mean +/− SD of n = 3 biological replicates analyzed over 3 independent experiments, (**f**, **g**) representative of 3 independent experiments, (**h**) n = 6 analyzed mice, or (**i**, **j**) WT: n = 6, iDKO: n = 5, iKO: n = 4, iTKO: n = 6 in 2 independent experiments. Statistical significance was calculated by one-way ANOVA with Dunnett's post-hoc test.

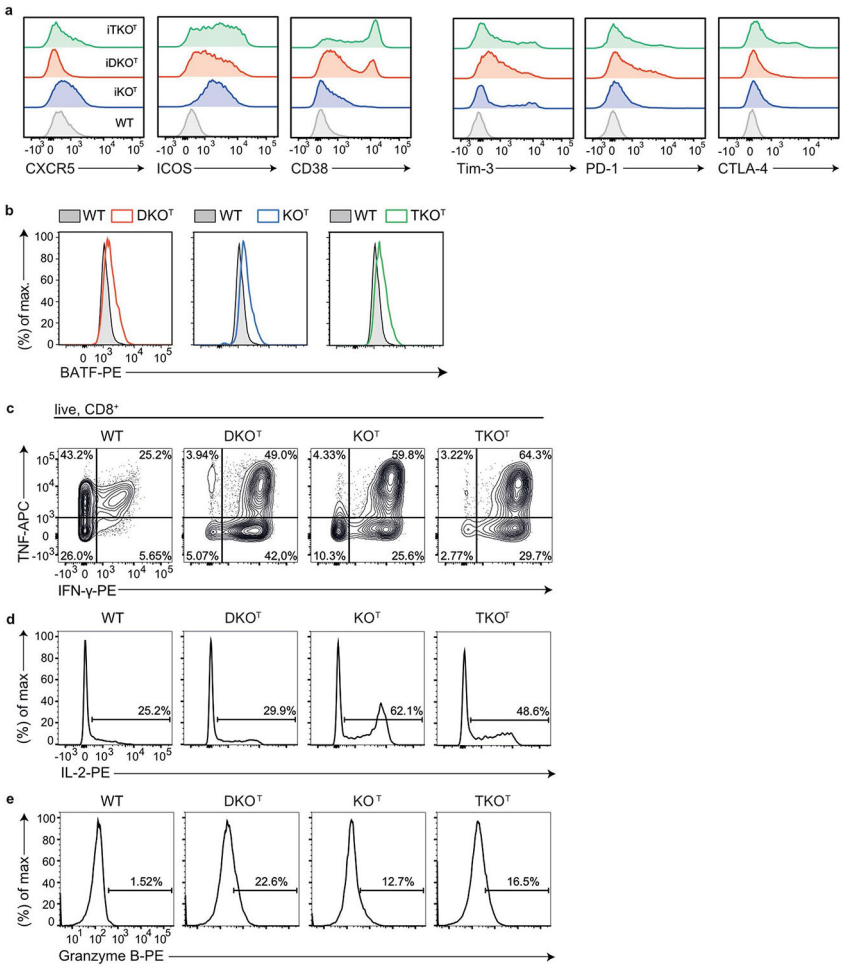

Extended Data Fig. 3 |. Describing phenotypes of DKO^T, KO^T and TKO^T CD8$^+$ T cells.
Flow cytometry analysis of markers of activation and exhaustion (**a**) and BATF transcription factor expression (**b**) in splenic WT, DKO^T, KO^T and TKO^T CD8$^+$ T cells. Data are representative of at least 5 individual 6-12 week old mice per genotype in at least two independent experiments. Flow cytometry analysis to Fig. 3e, f: intracellular cytokine staining of IFN-γ, TNF (**c**) and IL-2 (**d**) after PMA/ionomycin stimulation in CD8$^+$ T cells of splenocytes from WT, DKO^T, KO^T and TKO^T mice for 4 h. Histogram analysis to Fig. 3g: Granzyme B expression in splenic WT, DKO^T, KO^T and TKO^T CD8$^+$ T cells (**e**).

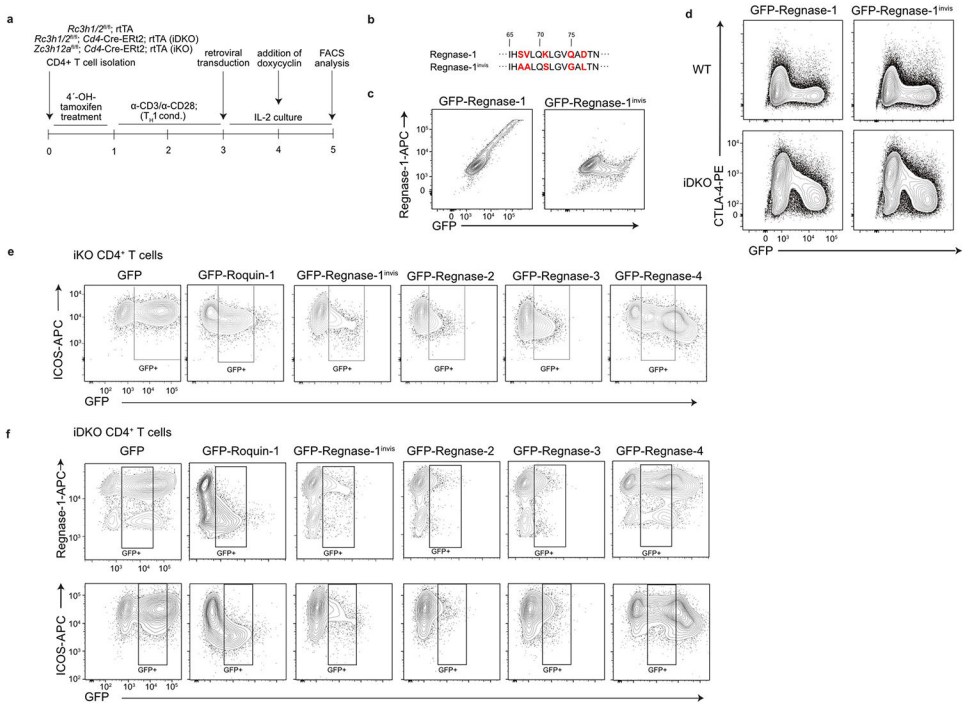

Extended Data Fig. 4 |. Regnase paralogs cannot complement for Roquin loss of function.
(**a**) Workflow of *in vitro* reconstitution experiments. (**b**) Mutations introduced in Regnase-1 coding sequence (marked in red) for the generation of an antibody-invisible GFP-tagged Regnase-1 construct (GFP-Regnase-1^{invis}). (**c**) Flow cytometry analysis of Regnase-1 expression after retroviral transduction of WT CD4$^+$ T cells with GFP-Regnase-1 or GFP-Regnase-1^{invis} constructs. (**d**) WT or iDKO CD4$^+$ T cells were retrovirally transduced with GFP–Regnase-1 or GFP-Regnase-1^{invis}. Contour plots of flow cytometry analysis of CTLA-4 expression in dependence of the GFP expression level. (**e**, **f**) Flow cytometry analysis of ICOS or Regnase-1 expression after retroviral transduction of iKO or iDKO CD4$^+$ T cells with the indicated GFP-fusion protein. Contour plots of histograms shown in Fig. 4c. (**d–f**) Data are representative of n = 3 independent experiments.

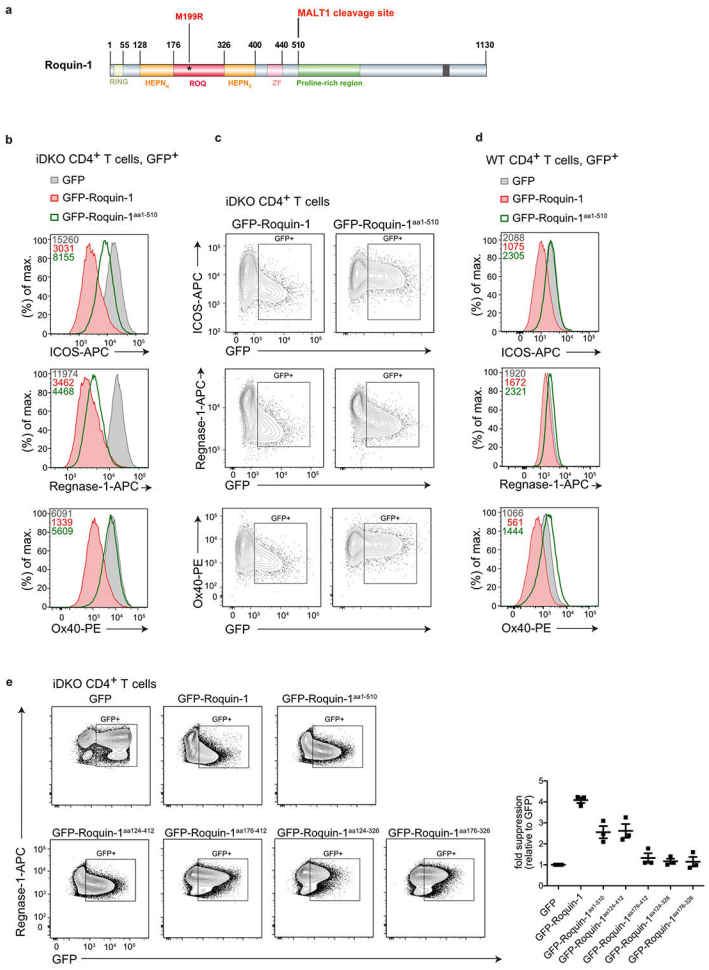

Extended Data Fig. 5 |. Dissecting protein domains of Roquin-1 sufficient for cooperative target regulation with Regnase-1.

(**a**) Schematic representation of Roquin-1 domain organization with indication of M199R mutation. iDKO (**b**, **c**) or WT (**d**) CD4$^+$ T cells were retrovirally transduced with GFP, GFP-Roquin-1 or GFP-Roquin-1$^{aa1\text{-}510}$ constructs. Histograms of flow cytometry analysis of ICOS, Regnase-1 or Ox40 expression, as indicated, in GFP$^+$ cells with indication of respective geometric MFI value. (**c**) Contour plots of histograms depicted in (**b**). (**e**) iDKO CD4$^+$ T cells were retrovirally transduced with the constructs encoding GFP, GFP-Roquin-1 or GFP-Roquin-1 mutant proteins. Flow cytometry analysis of Regnase-1 expression and quantification of fold suppression of Regnase-1 expression level in GFP$^+$ cells relative to cells expressing GFP control construct. (**b–e**) Data are representative of n = 3 independent experiments. (**e**) Data are presented as mean +/− SEM of n = 3 independent experiments.

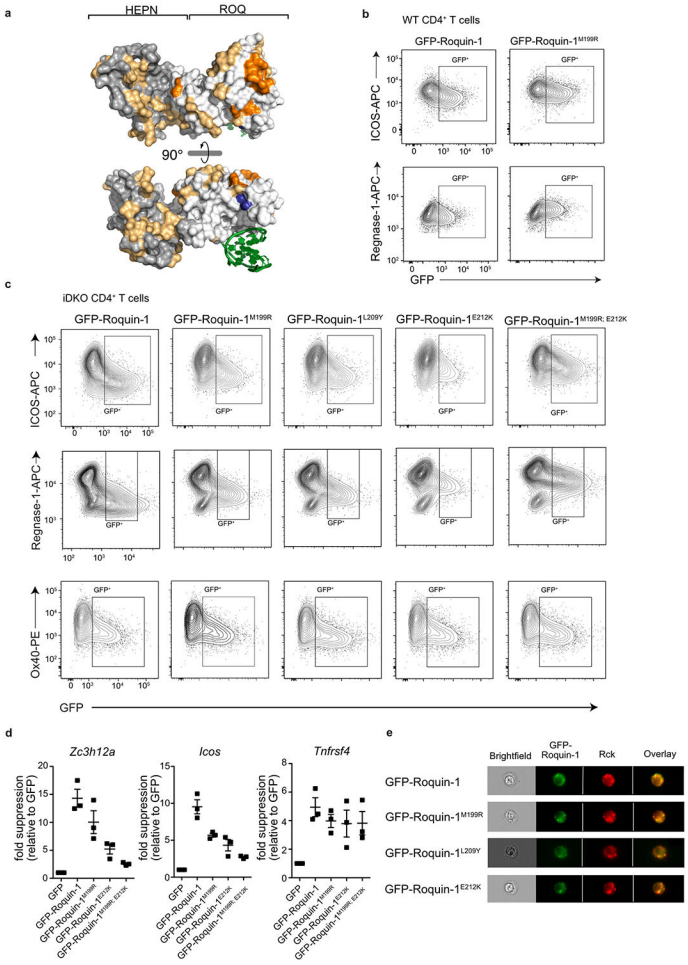

Extended Data Fig. 6 |. Functional validation of point mutations in Roquin-1 that reduce cooperation with Regnase-1.

(**a**) Structure of the Roquin-1 $HEPN_N$/ROQ/$HEPN_C$ domain with a bound RNA stem-loop marked in green. All amino acids tested are colored, essential amino acids for Roquin-1 and Regnase-1 interaction in the ROQ domain are marked in orange, non-essential ones in yellow and amino acid M199 in blue. WT (**b**) or iDKO (**c**) $CD4^+$ T cells were retrovirally transduced with GFP, GFP-Roquin-1 or the indicated GFP-Roquin-1 mutants. Contour plots of flow cytometry measurement of indicated targets in GFP^+ cells after 16 h of doxycycline induction of GFP-tagged constructs. (**b**) Contour plots of histograms shown in Fig. 4f or (**c**) shown in Fig. 4g. (**d**) iDKO $CD4^+$ T cells were retrovirally transduced with GFP, GFP-Roquin-1 or the indicated GFP-Roquin-1 mutants and sorted for GFP^+ cells 6 h after doxycycline induced expression of the respective constructs. The levels of *Zc3h12a*, Icos or *Tnfrsf4* mRNAs in GFP^+ cells were determined via RT-qPCR, normalized to *YWHAZ* and calculated as fold suppression of the respective construct relative to cells expressing the GFP control construct. Data show mean +/− SEM of n = 3 independent experiments. (**e**) Representative images of iDKO $CD4^+$ T cells transduced with the indicated GFP-Roquin-1 WT or mutant proteins, stained with anti-Rck (P-body marker) antibody and analyzed via Image Stream. (**b**, **c**) Data are representative of n = 3 independent experiments or (**e**) n = 2 independent experiments.

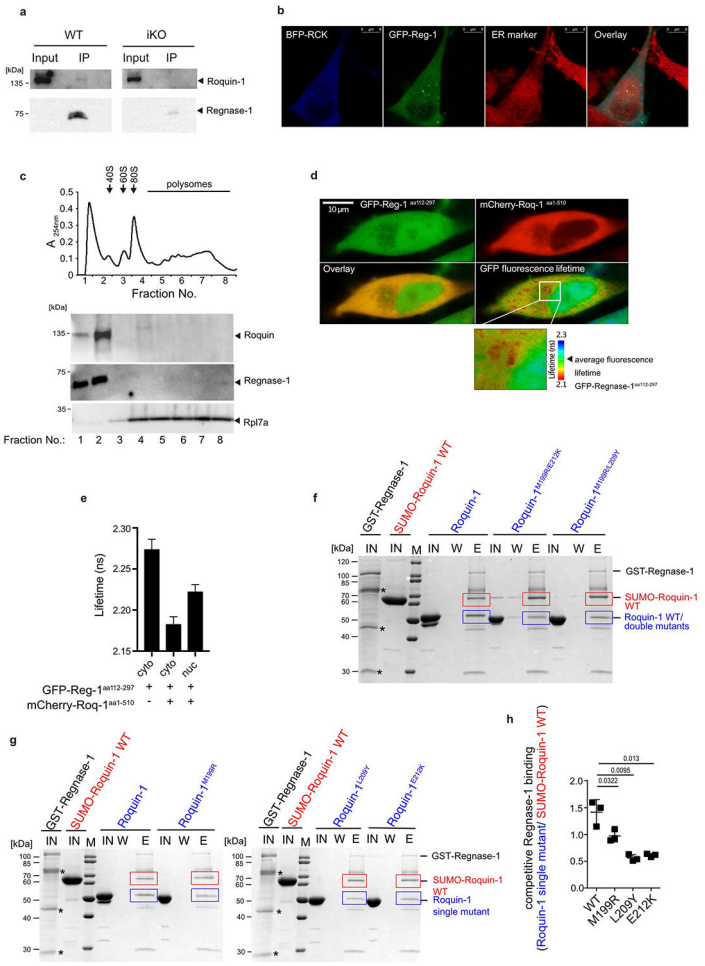

Extended Data Fig. 7 |. Molecular determinants of Roquin-1 interaction with Regnase-1. (**a**) Lysates of WT or iKO CD4$^+$ T cells were subjected to immunoprecipitation (IP) with antibodies against Regnase-1. Input lysates before IP and eluates from beads after IP were analyzed in immunoblots with antibodies against Roquin-1 or Regnase-1. (**b**, **d**) Fluorescence microscopy images of HeLa cells transfected with BFP-Rck and GFP-Regnase-1 (GFP-Reg-1) and stained with ER staining dye (**b**), or of cells transfected with GFP-Regnase-1$^{aa112\text{-}297}$ and mCherry-Roquin-1$^{aa1\text{-}510}$ (**d**). Quantification of GFP fluorescence lifetime in the cytoplasm (cyto) and nucleus (nuc) (**e**) of transfected cells shown in (**d**). (**c**) Cytoplasmic lysates of CD4$^+$ T cells were fractionated after sucrose gradient centrifugation and distribution of Roquin, Regnase-1 and Rpl7a proteins in the individual fractions analyzed via immunoblots, as indicated. Above, representative absorbance profile obtained during fractionation of gradients with indication of localization of 40 S and 60 S ribosomal subunits, 80 S monosomes and polysomes. (**f**, **g**) SDS-PAGE of competitive *in vitro* GST-pulldown experiments using GST-regnase-1^{D141N} and SUMO-roquin-1$^{aa2\text{-}440}$ in combination with the indicated untagged Roquin-1$^{aa2\text{-}440}$ double or single mutants. Purified proteins before pulldown (IN), supernatants of wash steps (W) as well as eluted proteins (E) were loaded. Asterisks mark the migration of degradation products of GST-regnase-1. (**h**) Quantification of eluted mutant Roquin-1$^{aa2\text{-}440}$ relative to SUMO-

roquin-1$^{aa2\text{-}440}$ wild-type protein of *in vitro* GST-pulldown experiments depicted in (**g**). (**b**, **d**, **f**, **g**) Depicted are representative data of n = 3 independent experiments or (**a**, **c**) of n = 2 independent experiments. (**e**) Data are presented as mean +/− SEM or (**h**) mean +/− SD and (**h**) statistical significance was calculated using t tests.

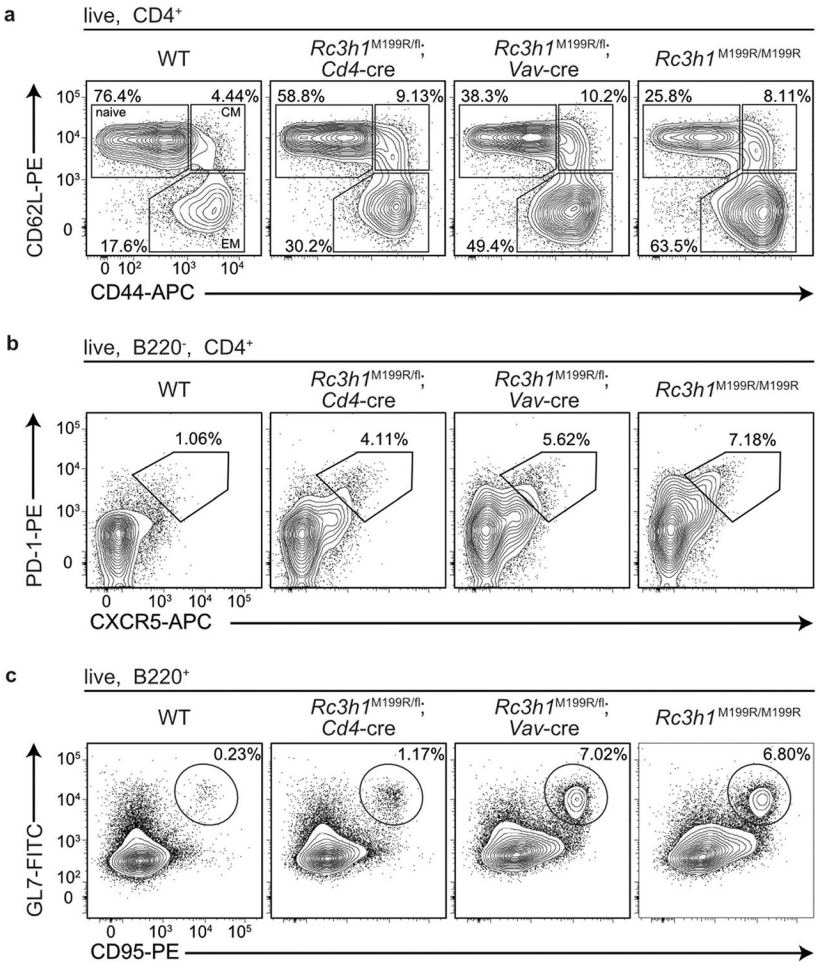

Extended Data Fig. 8 |. Phenotypes of mice with mutations impairing Roquin-1 interaction with Regnase-1.

Contour plots of flow cytometry analysis of CD4+ T cells (**a**), T_{FH} cells (**b**) and GC B cells (**c**) from spleens of 9-14 weeks old WT, *Rc3h1*$^{M199R/fl}$;*Cd4*-Cre, *Rc3h1*$^{M199R/fl}$;*Vav*-Cre and *Rc3h1*$^{M199R/M199R}$ mice. Contour plots are representative of WT, *Rc3h1*$^{M199R/M199R}$: n = 6, *Rc3h1*$^{M199R/fl}$; *Cd4*-Cre, *Rc3h1*$^{M199R/fl}$; *Vav*-Cre: n = 5 (**a**), or WT, *Rc3h1*$^{M199R/M199R}$: n = 8, *Rc3h1*$^{M199R/fl}$; Cd4-Cre: n = 6, *Rc3h1*$^{M199R/fl}$; *Vav*-Cre: n = 7 (**b**, **c**) analyzed mice in at least 3 independent experiments.

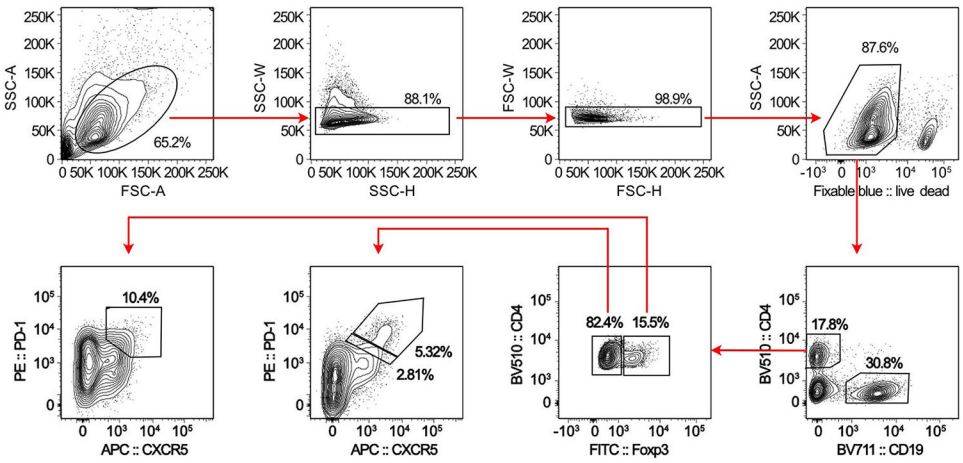

Extended Data Fig. 9 |. Exemplary gating strategy.

Cells were pregated on lymphocytes (FSC-A/SSC-A), single cells (SSC-H/SSC-W and FSC-H/FSC-W) and live cells (Fixable blue -) prior to gating on cell populations of interest.

Supplementary Material

Refer to Web version on PubMed Central for supplementary material.

Acknowledgements

We thank D.H. Busch (TU Munich) for critical reading of the manuscript. We thank C. Keplinger (Helmholtz Zentrum München) and L. Esser and J. Klein (Ludwig-Maximilians-Universität, Munich) for excellent technical support. We thank A. Blutke, J. Kranich and R. Schieweck (Ludwig-Maximilians-Universität, Munich) for support with histology and polysome profiles and the BMC Core Facility (Ludwig-Maximilians-Universität, Munich) for support in flow cytometry and the immunoanalytics platform for their support in chromium release assays (E. Noessner, Helmholtz Zentrum München). For the provision of NanoBret constructs we thank K.-P. Knobeloch (University Clinic Freiburg) and D. Zehn (TU Munich) for providing the MigR1-OVA-GFP retroviral plasmid. The work was supported by the German Research Foundation grants SPP-1935 (to D.N. and V.H.), SFB-TRR338 (projects C02 to V.H. and C05 to S.T.), SFB-1054 (project A03) as well as HE3359/7-1 and HE3359/8-1 to V.H. and under Germany's Excellence Strategy within the framework of the Munich Cluster for Systems Neurology (EXC 2145 SyNergy, ID 390857198 to W.W.) and SFB-870 (project A13 to W.W.) as well as grants from the Wilhelm Sander, Fritz Thyssen, Else Kröner-Fresenius and Krebshilfe foundations to V.H.

Data availability

All data are provided in the article and its supplementary files or from the corresponding author upon reasonable request. For analysis of the Roquin structure the publicly available structural datasets of Roquin-1 ROQ domain bound to RNA (PDB 4QI2) and Roquin-1 ROQ-HEPN domain (PDB 4TXA) were used. Source data are provided with this paper.

References

1. Pratama A et al. Roquin-2 shares functions with its paralog Roquin-1 in the repression of mRNAs controlling T follicular helper cells and systemic inflammation. Immunity 38, 669–680 (2013). [PubMed: 23583642]
2. Tavernier SJ et al. A human immune dysregulation syndrome characterized by severe hyperinflammation with a homozygous nonsense Roquin-1 mutation. Nat. Commun 10, 4779 (2019). [PubMed: 31636267]

3. Vogel KU et al. Roquin paralogs 1 and 2 redundantly repress the Icos and Ox40 costimulator mRNAs and control follicular helper T cell differentiation. Immunity 38, 655–668 (2013). [PubMed: 23583643]
4. Matsushita K et al. Zc3h12a is an RNase essential for controlling immune responses by regulating mRNA decay. Nature 458, 1185–1190 (2009). [PubMed: 19322177]
5. Uehata T et al. Malt1-induced cleavage of regnase-1 in $CD4^+$ helper T cells regulates immune activation. Cell 153, 1036–1049 (2013). [PubMed: 23706741]
6. Jeltsch KM et al. Cleavage of roquin and regnase-1 by the paracaspase MALT1 releases their cooperatively repressed targets to promote $T(_H)17$ differentiation. Nat. Immunol 15, 1079–1089 (2014). [PubMed: 25282160]
7. Mino T et al. Regnase-1 and Roquin regulate a common element in inflammatory mRNAs by spatiotemporally distinct mechanisms. Cell 161, 1058–1073 (2015). [PubMed: 26000482]
8. Jeltsch KM & Heissmeyer V Regulation of T cell signaling and autoimmunity by RNA-binding proteins. Curr. Opin. Immunol 39, 127–135 (2016). [PubMed: 26871597]
9. Leppek K et al. Roquin promotes constitutive mRNA decay via a conserved class of stem-loop recognition motifs. Cell 153, 869–881 (2013). [PubMed: 23663784]
10. Glasmacher E et al. Roquin binds inducible costimulator mRNA and effectors of mRNA decay to induce microRNA-independent post-transcriptional repression. Nat. Immunol 11, 725–733 (2010). [PubMed: 20639877]
11. Sgromo A et al. A CAF40-binding motif facilitates recruitment of the CCR4-NOT complex to mRNAs targeted by *Drosophila* Roquin. Nat. Commun 8, 14307 (2017). [PubMed: 28165457]
12. Mino T et al. Translation-dependent unwinding of stem-loops by UPF1 licenses Regnase-1 to degrade inflammatory mRNAs. Nucleic Acids Res. 47, 8838–8859 (2019). [PubMed: 31329944]
13. Fu M & Blackshear PJ RNA-binding proteins in immune regulation: a focus on CCCH zinc finger proteins. Nat. Rev. Immunol 17, 130–143 (2017). [PubMed: 27990022]
14. Vinuesa CG et al. A RING-type ubiquitin ligase family member required to repress follicular helper T cells and autoimmunity. Nature 435, 452–458 (2005). [PubMed: 15917799]
15. Akira S Regnase-1, a ribonuclease involved in the regulation of immune responses. Cold Spring Harb. Symp. Quant. Biol 78, 51–60 (2013). [PubMed: 24163394]
16. Heissmeyer V & Vogel KU Molecular control of T_{FH} cell differentiation by Roquin family proteins. Immunol. Rev 253, 273–289 (2013). [PubMed: 23550652]
17. von Gamm M et al. Immune homeostasis and regulation of the interferon pathway require myeloid-derived Regnase-3. J. Exp. Med 216, 1700–1723 (2019). [PubMed: 31126966]
18. Wei J et al. Targeting Regnase-1 programs long-lived effector T cells for cancer therapy. Nature 576, 471–476 (2019). [PubMed: 31827283]
19. Zheng W et al. Regnase-1 suppresses $TCF\text{-}1^+$ precursor exhausted T cell formation to limit CAR-T-cell responses against ALL. Blood 138, 122–135 (2021). [PubMed: 33690816]
20. Li Y et al. Central role of myeloid MCPIP1 in protecting against LPS-induced inflammation and lung injury. Signal Transduct. Target Ther 2, 17066 (2017). [PubMed: 29263935]
21. Bertossi A et al. Loss of Roquin induces early death and immune deregulation but not autoimmunity. J. Exp. Med 208, 1749–1756 (2011). [PubMed: 21844204]
22. Cui X et al. Regnase-1 and Roquin nonredundantly regulate T_H1 differentiation causing cardiac inflammation and fibrosis. J. Immunol 199, 4066–4077 (2017). [PubMed: 29127149]
23. Ventura A et al. Restoration of p53 function leads to tumour regression in vivo. Nature 445, 661–665 (2007). [PubMed: 17251932]
24. Sledzinska A TGF-β signalling is required for $CD4^+$ T cell homeostasis but dispensable for regulatory T cell function. PLoS Biol. 11, e1001674 (2013). [PubMed: 24115907]
25. Zeitrag J, Alterauge D, Dahlstrom F & Baumjohann D Gene dose matters: considerations for the use of inducible CD4-CreER(T2) mouse lines. Eur. J. Immunol 50, 603–605 (2020). [PubMed: 32087088]
26. Hudson WH et al. Proliferating transitory T cells with an effector-like transcriptional signature emerge from $PD\text{-}1^+$ stem-like $CD8^+$ T cells during chronic infection. Immunity 51, 1043–1058 (2019). [PubMed: 31810882]

27. McLane LM, Abdel-Hakeem MS & Wherry EJ CD8 T cell exhaustion during chronic viral infection and cancer. Annu Rev. Immunol 37, 457–495 (2019). [PubMed: 30676822]
28. Yu D et al. Roquin represses autoimmunity by limiting inducible T-cell co-stimulator messenger RNA. Nature 450, 299–303 (2007). [PubMed: 18172933]
29. Tan AH, Wong SC & Lam KP Regulation of mouse inducible costimulator (ICOS) expression by Fyn-NFATc2 and ERK signaling in T cells. J. Biol. Chem 281, 28666–28678 (2006). [PubMed: 16880206]
30. Iwasaki H et al. The IκB kinase complex regulates the stability of cytokine-encoding mRNA induced by TLR-IL-1R by controlling degradation of regnase-1. Nat. Immunol 12, 1167–1175 (2011). [PubMed: 22037600]
31. Janowski R et al. Roquin recognizes a non-canonical hexaloop structure in the 3′-UTR of Ox40. Nat. Commun 7, 11032 (2016). [PubMed: 27010430]
32. Schlundt A et al. Structural basis for RNA recognition in roquin-mediated post-transcriptional gene regulation. Nat. Struct. Mol. Biol 21, 671–678 (2014). [PubMed: 25026077]
33. Srivastava M et al. Roquin binds microRNA-146a and Argonaute2 to regulate microRNA homeostasis. Nat. Commun 6, 6253 (2015). [PubMed: 25697406]
34. Tan D, Zhou M, Kiledjian M & Tong L The ROQ domain of Roquin recognizes mRNA constitutive-decay element and double-stranded RNA. Nat. Struct. Mol. Biol 21, 679–685 (2014). [PubMed: 25026078]
35. Suzuki HI et al. MCPIP1 ribonuclease antagonizes dicer and terminates microRNA biogenesis through precursor microRNA degradation. Mol. Cell 44, 424–436 (2011). [PubMed: 22055188]
36. Lee SK et al. Interferon-γ excess leads to pathogenic accumulation of follicular helper T cells and germinal centers. Immunity 37, 880–892 (2012). [PubMed: 23159227]
37. Ellyard JI et al. Heterozygosity for Roquinsan leads to angioimmunoblastic T-cell lymphoma-like tumors in mice. Blood 120, 812–821 (2012). [PubMed: 22700722]
38. Blank CU et al. Defining 'T cell exhaustion'. Nat. Rev. Immunol 19, 665–674 (2019). [PubMed: 31570879]
39. Essig K et al. Roquin targets mRNAs in a 3′-UTR-specific manner by different modes of regulation. Nat. Commun 9, 3810 (2018). [PubMed: 30232334]
40. Murakawa Y et al. RC3H1 post-transcriptionally regulates A20 mRNA and modulates the activity of the IKK/NF-κB pathway. Nat. Commun 6, 7367 (2015). [PubMed: 26170170]
41. Song J et al. Human cytomegalovirus induces and exploits Roquin to counteract the IRF1-mediated antiviral state. Proc. Natl Acad. Sci. USA 116, 18619–18628 (2019). [PubMed: 31451648]
42. Essig K et al. Roquin suppresses the PI3K-mTOR signaling pathway to inhibit T helper cell differentiation and conversion of T_{reg} to Tfr cells. Immunity 47, 1067–1082 e12 (2017). [PubMed: 29246441]
43. Nagahama Y et al. Regnase-1 controls colon epithelial regeneration via regulation of mTOR and purine metabolism. Proc. Natl Acad. Sci. USA 115, 11036–11041 (2018). [PubMed: 30297433]
44. Hoefig KP et al. Defining the RBPome of primary T helper cells to elucidate higher-order Roquin-mediated mRNA regulation. Nat. Commun 12, 5208 (2021). [PubMed: 34471108]

References

45. Lee PP et al. A critical role for Dnmt1 and DNA methylation in T cell development, function, and survival. Immunity 15, 763–774 (2001). [PubMed: 11728338]
46. Hogquist KA et al. T cell receptor antagonist peptides induce positive selection. Cell 76, 17–27 (1994). [PubMed: 8287475]
47. Hochedlinger K, Yamada Y, Beard C & Jaenisch R Ectopic expression of Oct-4 blocks progenitor-cell differentiation and causes dysplasia in epithelial tissues. Cell 121, 465–477 (2005). [PubMed: 15882627]
48. Schieweck R et al. Pumilio2 and Staufen2 selectively balance the synaptic proteome. Cell Rep. 35, 109279 (2021). [PubMed: 34161769]

49. Digman MA, Caiolfa VR, Zamai M & Gratton E The phasor approach to fluorescence lifetime imaging analysis. Biophys. J 94, L14–L16 (2008). [PubMed: 17981902]

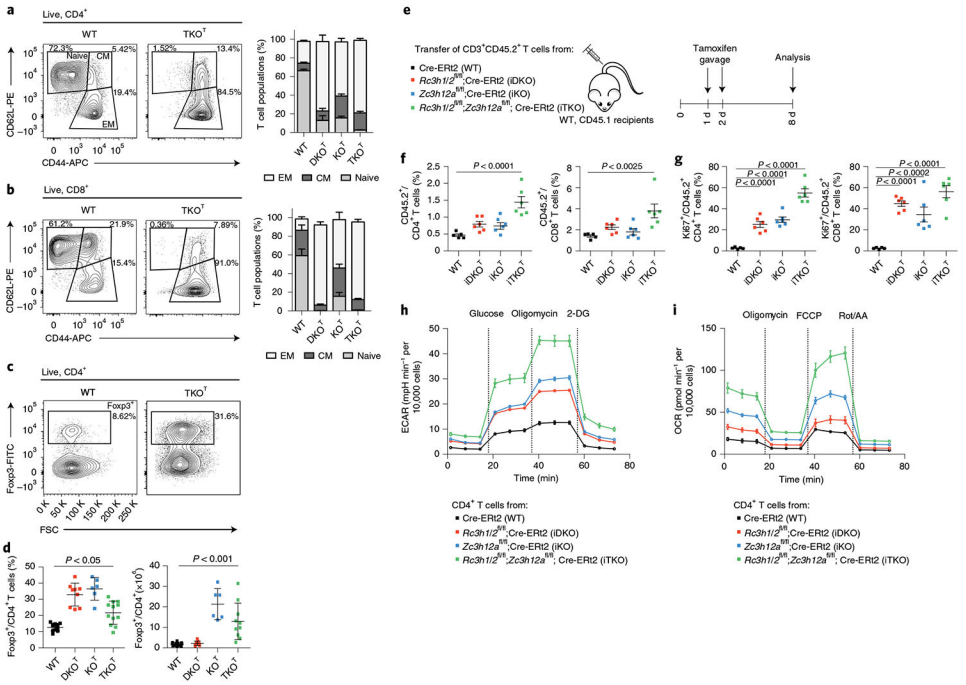

Fig. 1 |. Roquin-1/2 and Regnase-1 maintain quiescence of T cells.

a–d, Flow cytometry analysis of $CD4^+$ (**a**), $CD8^+$ (**b**) subpopulations (WT, $n = 9$; DKO^T and KO^T, $n = 6$; TKO^T, $n = 5$ mice analyzed in at least three independent experiments) and T_{reg} cells (**c**,**d**) (WT, $n = 15$; DKO^T, $n = 9$; KO^T, $n = 6$; TKO^T, $n = 10$ mice analyzed in at least three independent experiments) from spleens of 6–8-week-old WT, DKO^T, KO^T and TKO^T mice. CM, central memory; EM, effector memory; WT, wild type. **e**, $CD45.2^+CD3^+$ T cells from WT, iDKO, iKO and iTKO mice were adoptively transferred into WT $CD45.1^+$ mice. Mice were treated with tamoxifen by oral gavage to induce deletion of floxed alleles. **f**,**g**, Frequency (**f**) and proliferation (**g**) of $CD45.2^+$, $CD4^+$ and $CD45.2^+$, $CD8^+$ T cells were analyzed by flow cytometry on day 8 after transfer ($n = 6$ biological replicates). **h**,**i**, $CD4^+$ T cells from WT, iDKO, iKO and iTKO mice were treated with 4′-OH-tamoxifen in vitro to induce deletion of floxed alleles. T cells were kept under type 1 helper T cell conditions and expanded with IL-2-containing medium for 2 d. IL-2 was withdrawn overnight followed by restimulation with anti-CD3/28 before glycolytic (**h**) and mitochondrial stress testing (**i**) ($n = 3$ independent experiments). 2-DG, 2-deoxyglucose; Rot, rotenone; AA, antimycin. Data are presented as mean ± s.e.m., analyzed by one-way analysis of variance (ANOVA) with Bonferroni (**d**) or Dunnett's (**f**,**g**) post hoc test.

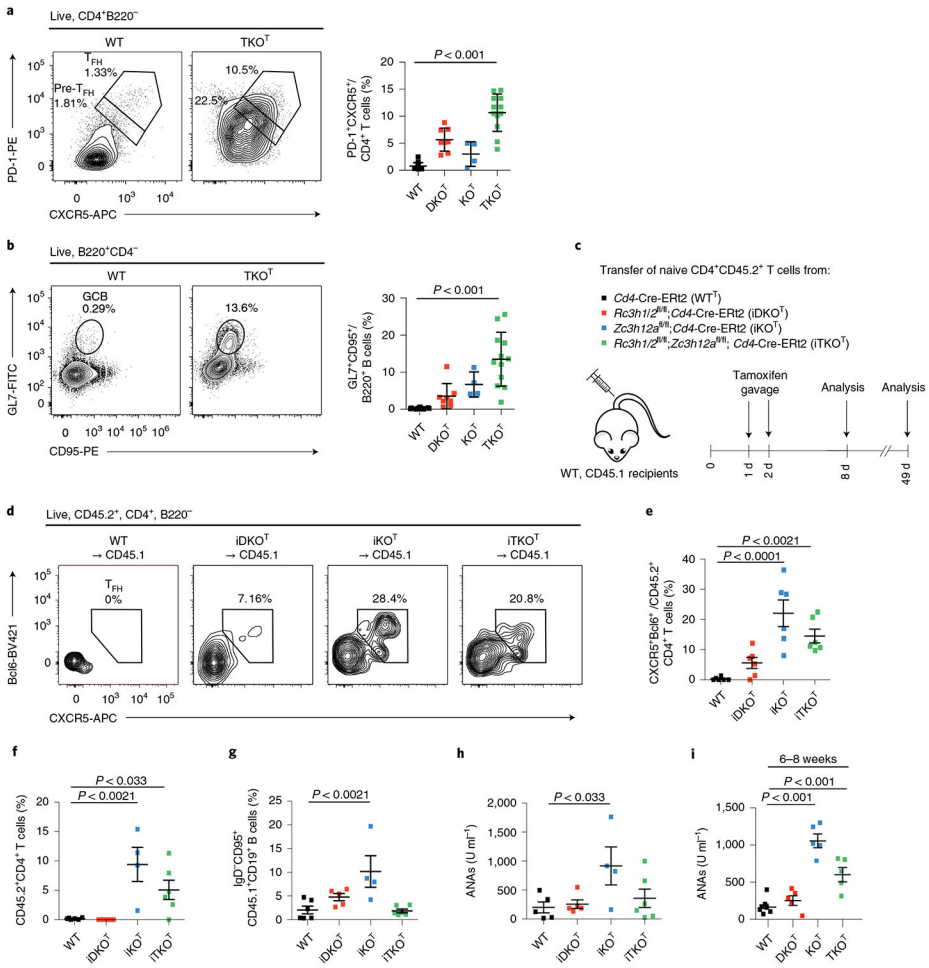

Fig. 2 | Roquin-1/2 and Regnase-1 control T_{FH} differentiation and humoral autoimmunity. **a**,**b**, Flow cytometry analysis of T_{FH} (**a**) and GC B cell (**b**) subpopulations from spleens of 6–8-week-old WT, DKO^T, KO^T and TKO^T mice (WT, $n = 14$; DKO^T, $n = 8$; KO^T, $n = 4$; TKO^T, $n = 12$ analyzed mice in at least three independent experiments). **c**, Naive CD45.2$^+$CD4$^+$ T cells from WT, iDKO, iKO and iTKO mice were adoptively transferred into congenic WT CD45.1 mice. Mice were treated with tamoxifen by oral gavage to induce deletion of floxed alleles. **d**,**e**, Adoptively transferred T cells were analyzed by flow cytometry for markers of T_{FH} cell differentiation on day 8 after transfer ($n = 6$ biological replicates). **f–h**, Frequencies of adoptively transferred WT, iDKO, iKO and iTKO CD45.2$^+$CD4$^+$ T cells (**f**), frequencies of recipient GC B cells (**g**) as well as levels of ANAs in the sera of recipient mice (**h**) were determined on day 49 after transfer (WT, $n = 6$; iDKO, $n = 5$; iKO, $n = 4$; iTKO, $n = 6$). **i**, ANAs in the serum of 6–8-week-old WT, DKO^T, KO^T and TKO^T mice (WT, $n = 7$; DKO^T, KO^T and TKO^T, $n = 5$ analyzed mice in three independent experiments). All data are presented as mean ± s.e.m. Statistical significance was calculated by one-way ANOVA with Bonferroni post hoc test (**a**,**b**) or Dunnett's post hoc test (**e–i**).

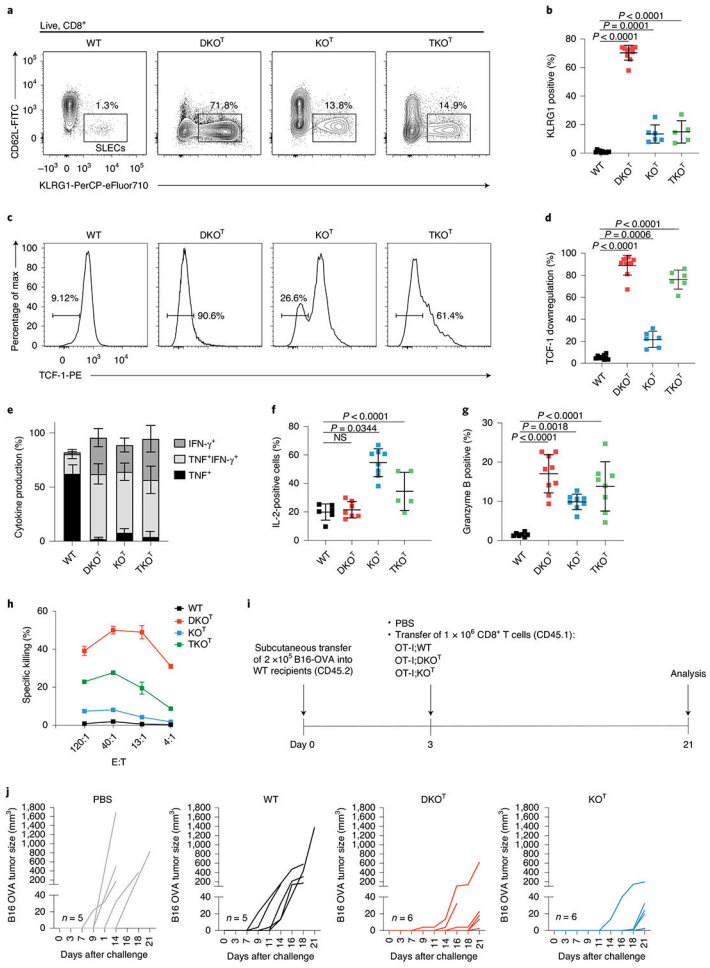

Fig. 3 |. Inactivation of Roquin-1/2 or Regnase-1 in CD8$^+$ T cells enhances cytotoxicity.
a–d, Flow cytometry analysis of splenic WT, DKO^T, KO^T and TKO^T CD8$^+$ T cells for KLRG1 and CD62L expression (**a**), frequencies of SLEC CD8$^+$ T cells (WT, $n = 11$; iDKO, $n = 10$; iKO, $n = 6$; iTKO, $n = 5$ individual mice in three independent experiments) (**b**) and percentage of cells with TCF-1 downregulation (WT, $n = 9$; iDKO, $n = 10$; iKO, $n = 6$; iTKO, $n = 6$ individual mice in three independent experiments) (**c**,**d**). **e**,**f**, Quantification of intracellular cytokine staining of IFN-γ, TNF (WT, $n = 9$; iDKO, $n = 9$; iKO, $n = 11$; iTKO, $n = 5$ individual mice in three independent experiments) (**e**) and IL-2 (WT, $n = 6$; iDKO, $n = 7$; iKO, $n = 8$; iTKO, $n = 5$ individual mice in three independent experiments) (**f**) in CD8$^+$ T cells after PMA/ionomycin stimulation for 4 h. NS, not significant. **g**, Quantification of granzyme B-positive CD8$^+$ T cells (WT, $n = 7$; iDKO, $n = 11$; iKO, $n = 8$; iTKO, $n = 9$ individual mice in four independent experiments) in spleens from WT, DKO^T, KO^T and TKO^T mice. **h**, Chromium-release assay of P815 cells cultivated in effector to target ratios as indicated 4 h after adding splenic CD8$^+$ T cells isolated from WT, DKO^T, KO^T and TKO^T mice ($n = 2$ individual mice in one experiment). **i**, Schematic representation of the experimental set-up of the B16-OVA tumor model. **j**, B16-OVA tumor growth without transfer (PBS control $n = 5$) or after transfer of either WT ($n = 5$), DKO^T or KO^T OT-I

T cells ($n = 6$ individual mice in one experiment). Data are presented as mean ± s.e.m. Statistical significance was calculated by one-way ANOVA with Dunnett's post hoc test.

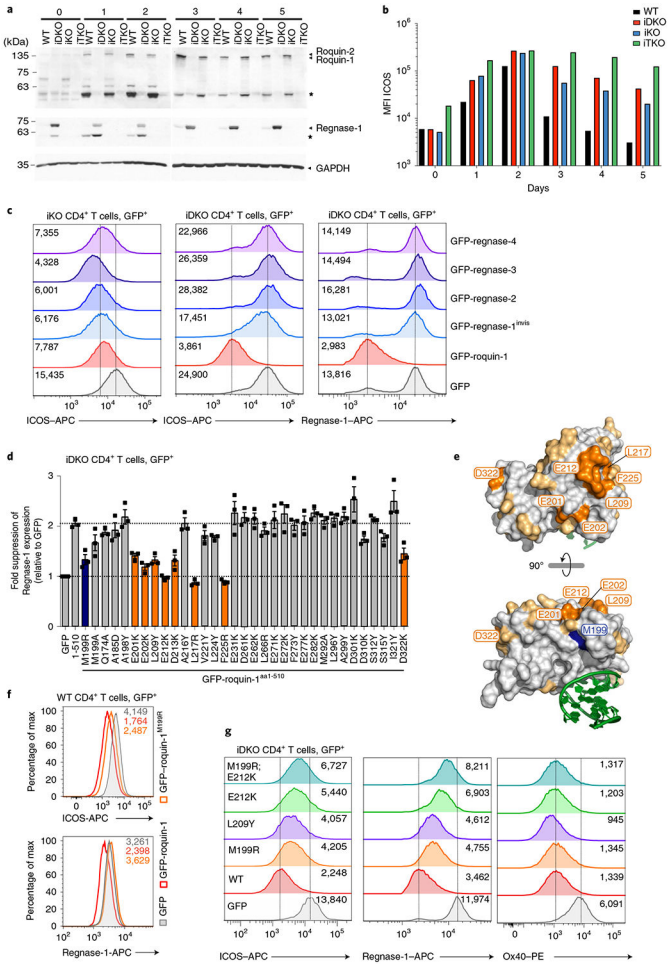

Fig. 4 |. Functional definition of Roquin-1 interaction with Regnase-1.

a,**b**, WT, iDKO, iKO and iTKO CD4$^+$ T cells were deleted in vivo by tamoxifen gavage, activated in vitro with anti-CD3/28 under T_H1 cell conditions (days 0–2) and cultivated in medium containing IL-2 (days 3–5). For each day, expression of Roquin-1/Roquin-2, Regnase-1 and GAPDH (**a**) or ICOS (**b**) was analyzed by immunoblot or flow cytometry, respectively. Asterisks mark MALT1 cleavage fragments of Roquin-1 and Regnase-1 (**a**). MFI, mean fluorescence intensity. **c**,**d** CD4$^+$ T cells of indicated genotypes were retrovirally transduced with GFP, GFP–roquin-1, GFP–regnase-1^{invis}, GFP–regnase-2, GFP–regnase-3, GFP–regnase-4 (**c**) or with GFP, GFP–roquin-1$^{aa1\text{-}510}$ and ROQ mutants introduced into GFP–roquin-1$^{aa1\text{-}510}$ (**d**). Histograms of ICOS and Regnase-1 expression in GFP$^+$ cells with indication of the respective geometric MFI (gMFI) values (**c**) or fold suppression of Regnase-1 expression in GFP$^+$ cells transduced with the indicated construct relative to cells transduced with GFP only calculated using gMFI (**d**). **e**, Structure of the Roquin-1 ROQ domain with a bound RNA stem loop marked in green, amino acid M199 marked in blue, amino acids essential for Roquin-1 and Regnase-1 functional interaction marked in orange and tested nonessential amino acids in yellow. **f**,**g**, WT (**f**) or iDKO (**g**) CD4$^+$ T cells were retrovirally transduced with GFP, GFP–roquin-1 or the indicated GFP–roquin-1 mutants. Histograms of ICOS, Regnase-1 and Ox40 expression in GFP$^+$ cells with indication of the

respective gMFI. Data are representative of $n = 3$ independent experiments (**a–c**,**f**,**g**) and are presented as mean ± s.e.m. of $n = 3$ independent experiments (**d**).

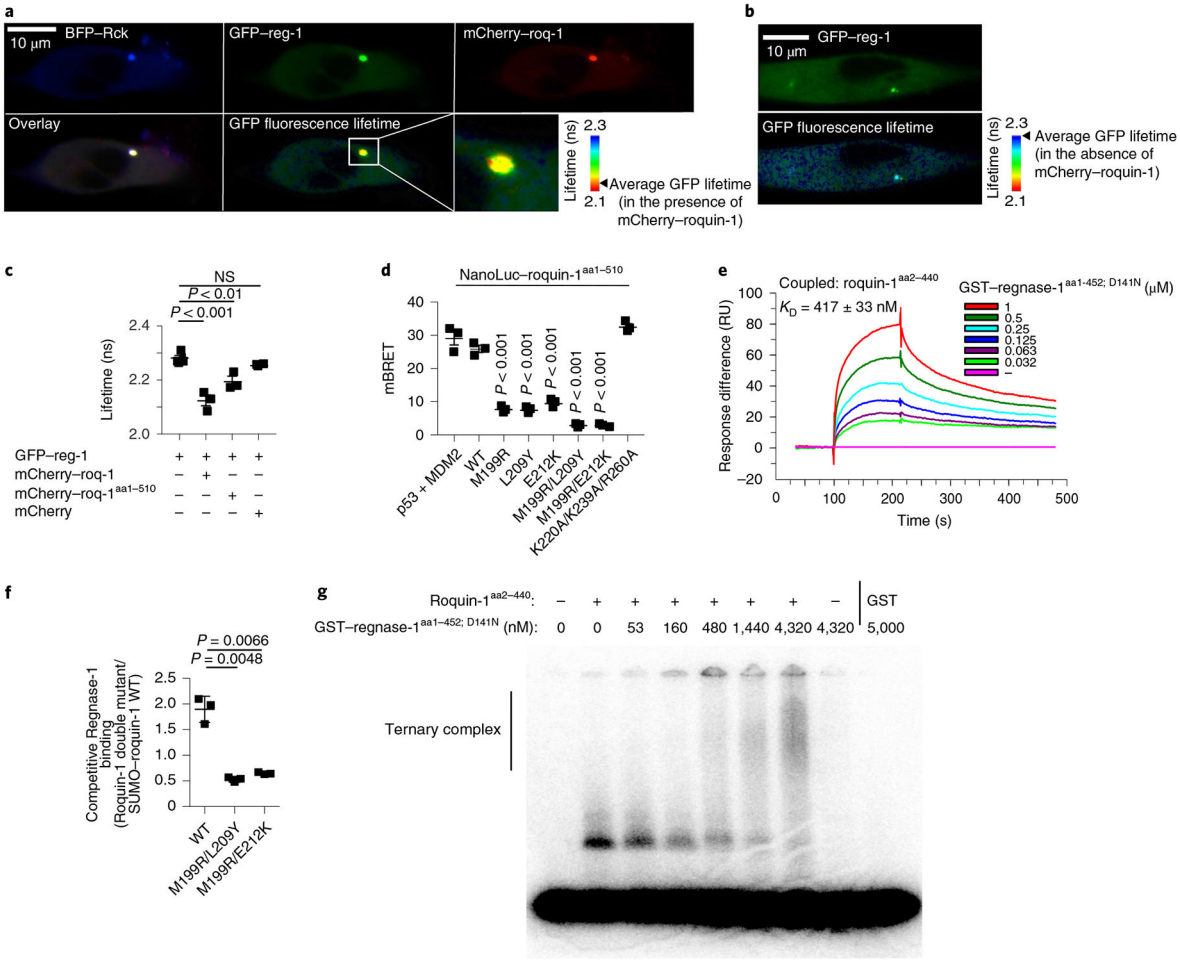

Fig. 5 |. Molecular determinants of Roquin-1 interactions with Regnase-1.

a–c, HeLa cells were co-transfected with BFP–Rck, GFP–regnase-1 (GFP–reg-1) together with mCherry–roquin-1 (mCherry–roq-1), mCherry–roquin-1$^{aa1-510}$ or mCherry (**a**,**c**) or with GFP–regnase-1 alone (**b**). Protein localization (**a**,**b**), FRET efficiency (GFP–regnase-1 in combination with mCherry 0.67%, mCherry–roq-1 6.6% or mCherry–roq-1$^{aa1-510}$ 3.91%) and lifetime of GFP fluorescence (**c**) was analyzed via fluorescence lifetime microscopy. **d**, HEK293T cells were transfected with HaloTag–regnase-1 in combination with the indicated NanoLuc–roquin-1$^{aa1-510}$ expression plasmids and NanoBret ratio (mBRET) was calculated after measuring NanoLuc and HaloTag signals via NanoBret assay. **e**, SPR signals after addition of GST–regnase-1$^{aa1-452;D141N}$ to Biacore-chip-immobilized Roquin-1$^{aa2-440}$. RU, resonance units. **f**, Competitive in vitro GST-pulldown experiment using GST–regnase-1^{D141N} and wild-type SUMO–roquin-1$^{aa2-440}$ in combination with the indicated Roquin-1$^{aa2-440}$ double mutants (untagged). Quantification of eluted Roquin-1$^{aa2-440}$ mutant relative to SUMO–roquin-1$^{aa2-440}$ wild-type protein of SDS–PAGE depicted in Extended Data Fig. 7f. **g**, EMSA using a *Zc3h12a* 3′-UTR RNA fragment (nt194–212), Roquin-1$^{aa2-440}$ (320 nM) in combination with increasing levels of GST–regnase-1$^{aa1-452; D141N}$. Presumably due to inclusion of unlabeled competitor RNA, recognition of the *Zc3h12a* mRNA stem loop by Regnase-1 could not be detected.

Representative data of $n = 3$ independent experiments (**a**,**b**,**e**,**g**). Data are presented as mean ± s.e.m. of $n = 3$ independent experiments (**c**,**d**) or mean ± s.d. of $n = 3$ independent experiments (**f**). Statistical significance was calculated using one-way ANOVA with Bonferroni post hoc test (**c**,**d**) or Student's *t*-tests (**f**).

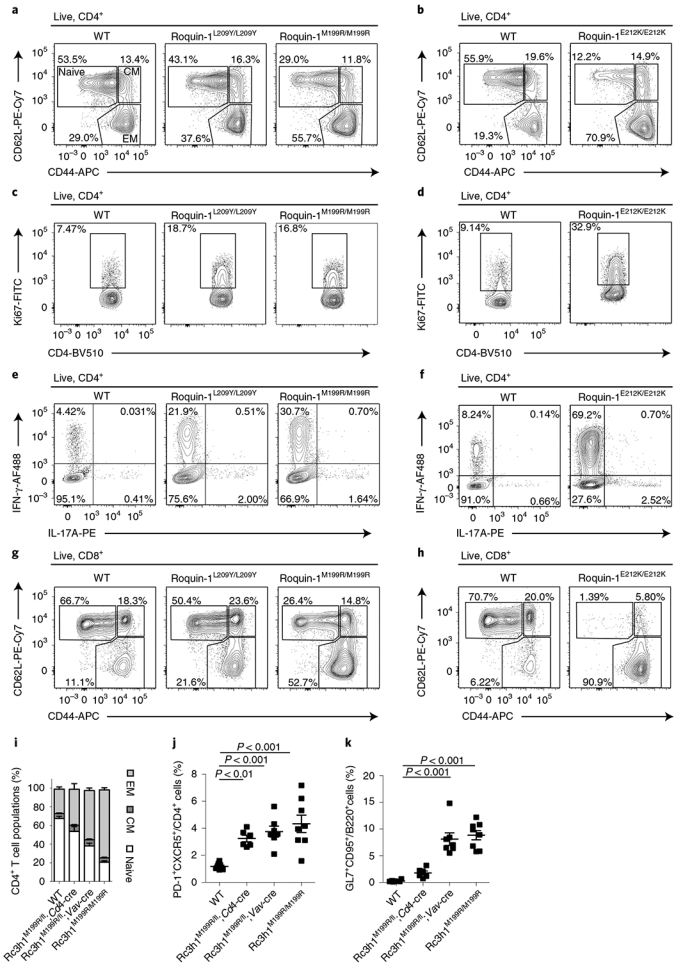

Fig. 6 |. Inhibition of Roquin-1 interaction with Regnase-1 breaks T cell quiescence.

a–h, CD4$^+$ and CD8$^+$ T cells from mice with L209Y and M199R mutations (10–12 weeks old) or from mice with E212K mutations (8 weeks old) in Roquin-1 were characterized. CD4$^+$ effector/memory populations (**a**,**b**), CD4$^+$ T cell proliferation (**c**,**d**), ability of CD4$^+$ T cells to produce IFN-γ and IL-17 after PMA/ionomycin stimulation ex vivo (**e**,**f**) or CD8$^+$ effector/memory populations (**g**,**h**) were compared. **i–k**, Frequencies of CD4$^+$ effector/memory T cell populations (**i**), T_{FH} cells (**j**) and GC B cells (**k**) from spleens of 9–14-week-old WT, *Rc3h1*$^{M199R/fl}$;*Cd4*-Cre, *Rc3h1*$^{M199R/fl}$;*Vav*-Cre and *Rc3h1*$^{M199R/M199R}$ (*sanroque*) mice were determined by flow cytometry. Contour plots are representative of $n = 4$ biological replicates analyzed in at least two independent experiments (**a**,**c**,**e**,**g**) or $n = 2$ biological replicates in two independent experiments (**b**,**d**,**e**,**h**). Data are presented as mean ± s.e.m. of WT, *Rc3h1*$^{M199R/M199R}$, $n = 6$; *Rc3h1*$^{M199R/fl}$, *Cd4*-Cre, *Rc3h1*$^{M199R/fl}$, *Vav*-Cre, $n = 5$ (**i**) or WT, *Rc3h1*$^{M199R/M199R}$, $n = 8$; *Rc3h1*$^{M199R/fl}$, *Cd4*-Cre, $n = 6$; *Rc3h1*$^{M199R/fl}$, *Vav*-Cre, $n = 7$ (**j**,**k**) analyzed mice in at least three independent experiments. Statistical significance was calculated by one-way ANOVA with Bonferroni post hoc test (**j**,**k**).

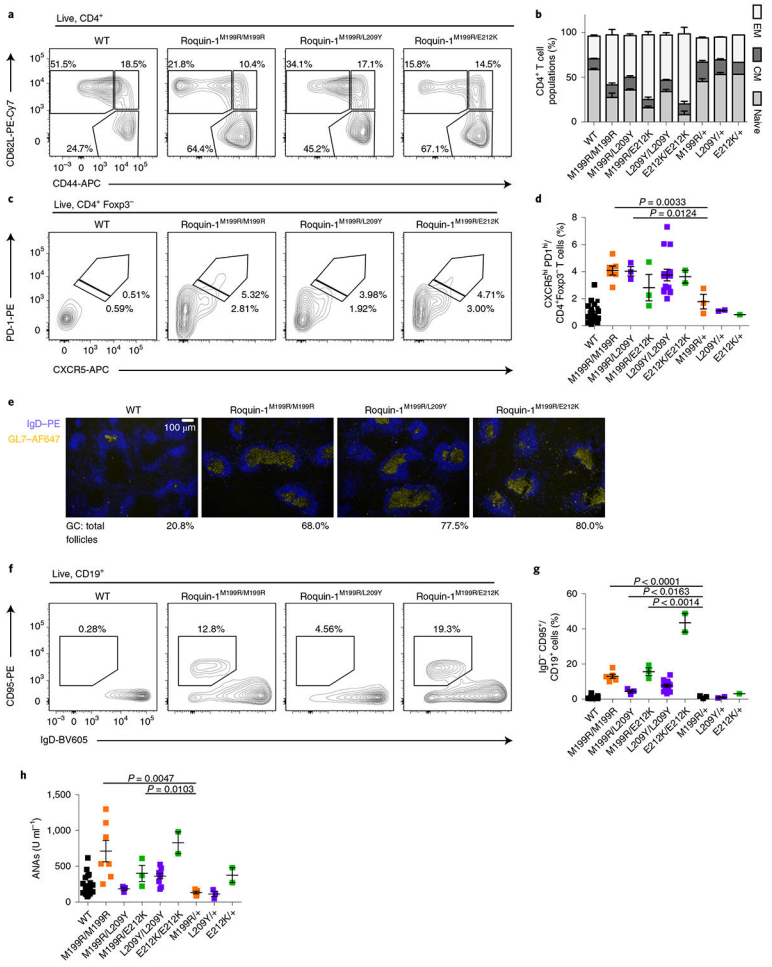

Fig. 7 |. Combined heterozygosity of Roquin-1$^{E212K/M199R}$ shows a synthetic phenotype.
a–d,f–h, T and B cells from 10–12-week-old mice with the M199R mutation in Roquin-1 on one allele and L209Y, E212K or M199R mutations on the other allele were characterized. Frequencies of CD4$^+$ T cell populations (**a**,**b**), T_{FH} cells (**c**,**d**), immunofluorescence of GL7 (blue) and IgD (yellow) in spleen sections (**e**), frequencies of GC B cells (**f**,**g**) and levels of ANAs in sera determined by ELISA (**h**). Contour plots or immunofluorescence microscopy images are representative of at least three individual mice analyzed in at least two independent experiments (**a**,**c**,**e**,**f**). WT, $n = 26$; M199R/M199R, $n = 6$; M199R/L209Y, $n = 3$; M199R/E212K, $n = 3$; L209Y/L209Y, $n = 14$; E212K/E212K, $n = 2$; M199R/+, $n = 3$; L209Y/+, $n = 2$; E212K/+, $n = 1$ (**b**,**d**,**g**,**h**). Data are shown as mean ± s.e.m. Statistical significance was determined using one-tailed Student's *t*-tests. Representative images of $n = 3$ analyzed mice per genotype (**e**).

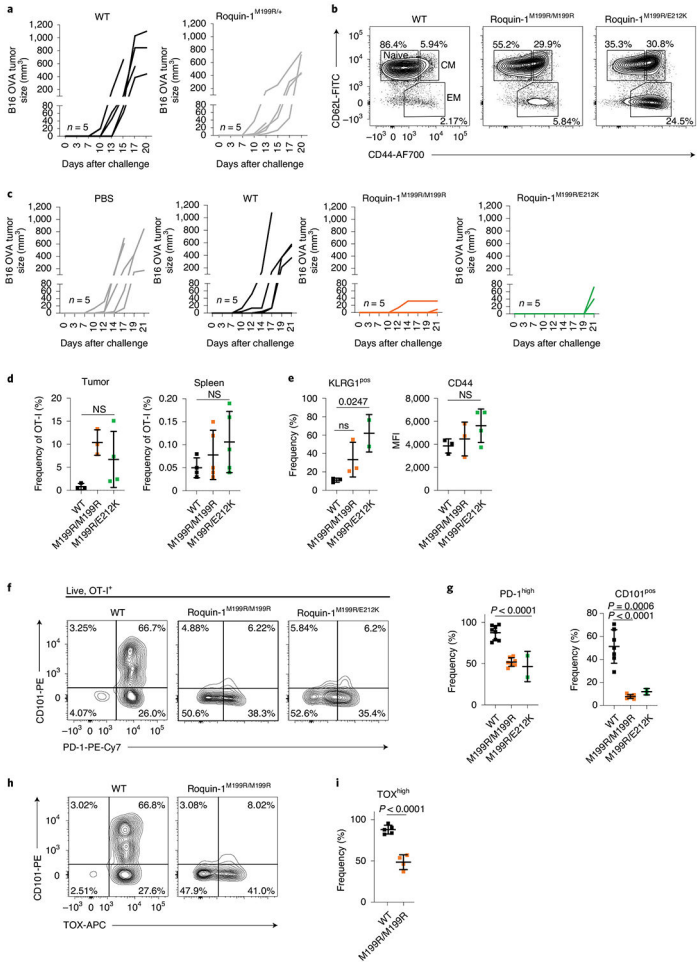

Fig. 8 |. Disrupting Roquin-1 interaction with Regnase-1 improves effector function of tumor-specific T cells.

a,c, Analysis of tumor growth of B16-OVA after transfer of OT-I T cells as described in Fig. 3i and with the indicated genotypes ($n = 5$ individual mice in one experiment, respectively). **b**, Flow cytometry analysis of activation markers CD44 and CD62L on OT-I T cells before transfer. **d**, Frequencies of OT-I T cells relative to all $^{+}$ cells are displayed for tumor and spleen at day 21 after tumor cell transfer. **e–i**, Flow cytometry analysis of KLRG-1, CD44, CD101, PD-1 and TOX on OT-I T cells in the tumor on day 21 after tumor cell transfer. Data are representative of WT, $n = 4$; M199R/M199R, $n = 5$; M199R/E212K, $n = 5$ individual mice analyzed in one experiment (**d**). Data are representative of WT, $n = 3$; M199R/M199R, $n = 3$; M199R/E212K, $n = 2$ or 4 each individual mice analyzed in one experiment (**e**). Data are representative of WT, $n = 7$; M199R/M199R, $n = 7$; M199R/E212K, $n = 2$ individual mice in three independent experiments (**g**). Data are representative of WT, $n = 5$ and M199R/M199R, $n = 4$ individual mice in two independent experiments (**h**). Data are presented as mean ± s.e.m. Statistical significance was calculated by one-way ANOVA with Bonferroni post hoc test (**d**,**e**,**g**) or unpaired one-tailed Student's *t*-test (**i**).

Published in final edited form as:
Nat Struct Mol Biol. 2024 September 01; 31(9): 1331–1340. doi:10.1038/s41594-024-01290-x.

ISWI catalyzes nucleosome sliding in condensed nucleosome arrays

Petra Vizjak[1,2,3], **Dieter Kamp**[4], **Nicola Hepp**[1,2,5], **Alessandro Scacchetti**[2,6], **Mariano Gonzalez Pisfil**[7], **Joseph Bartho**[4,8], **Mario Halic**[9], **Peter B. Becker**[2], **Michaela Smolle**[10,11,12], **Johannes Stigler**[#4], **Felix Mueller-Planitz**[#1]

[1]Institute of Physiological Chemistry, Faculty of Medicine Carl Gustav Carus, Technische Universität Dresden, Fetscherstraße 74, , 01307 Dresden, Germany.

[2]Department of Molecular Biology, Biomedical Center, Faculty of Medicine, Ludwig-Maximilians-Universität München, Großhadernerstr. 9, , 82152 Planegg-Martinsried, Germany.

[4]Gene Center, Department of Biochemistry, Ludwig-Maximilians-Universität München, Feodor-Lynen-Str 25, , 81377 München, Germany.

[7]Core Facility Bioimaging and Walter-Brendel-Centre of Experimental Medicine, Biomedical Center, Ludwig-Maximilians-Universität München, Großhaderner Straße 9, , 82152, Planegg-Martinsried, Germany.

[9]Department of Structural Biology, St. Jude Children's Research Hospital, 262 Danny Thomas Place, , Memphis, TN, 38105, USA.

[10]Department of Physiological Chemistry, Biomedical Center, Faculty of Medicine, Ludwig-Maximilians-Universität München, Großhadernerstr. 9, , 82152 Planegg-Martinsried, Germany.

[11]BioPhysics Core Facility, Biomedical Center, Faculty of Medicine, Ludwig-Maximilians-Universität München, Großhadernerstr. 9, , 82152 Planegg-Martinsried, Germany.

[#] These authors contributed equally to this work.

Correspondence to: Johannes Stigler; Felix Mueller-Planitz.

Correspondence: felix.mueller-planitz@tu-dresden.de, stigler@genzentrum.lmu.de .
[3]Current address: Early Stage Bioprocess Development, Boehringer Ingelheim Pharma GmbH & Co. KG, Biberach an der Riss, Germany
[5]Current address: Department of Clinical Genetics, Rigshospitalet, Copenhagen University Hospital, Blegdamsvej 9, 2100 Copenhagen, Denmark
[6]Current address: Epigenetics Institute & Department of Cell and Developmental Biology, University of Pennsylvania, Perelman School of Medicine, Philadelphia (PA), USA
[8]Current address: European Molecular Biology Laboratory, Meyerhofstraße 1, 69117 Heidelberg, Germany
[12]Current address: ViraTherapeutics GmbH, 6063 Rum, Austria

Author Contributions Statement
Conceptualization: F.M.-P., J.S., P.V.
Methodology and formal analysis: P.V., J.S., M.G.P, N.H., A.S., D.K., M.S.
Investigation: P.V., M.G.P., A.S., J.B., J.S., D.K., N.H., M.S.
Writing of original draft: F.M.-P., P.V., M.G.P, D.K., M.S., A.S., J.B., J.S.
Visualization: P.V., J.S., D.K., M.S., M.G.P.
Funding acquisition: F.M.-P., J.S., P.B.B, M.H.
Writing—Review and Editing: All authors
N.H. and A.S. contributed equally.

Competing Interests Statement
We declare no competing interest.

Europe PMC Funders Author Manuscripts

Abstract

How chromatin enzymes work in condensed chromatin and how they maintain diffusional mobility inside remains unexplored. We investigated these challenges using the *Drosophila* ISWI remodeling ATPase, which slides nucleosomes along DNA. Folding of chromatin fibers did not affect sliding *in vitro*. Catalytic rates were also comparable in- and outside of chromatin condensates. ISWI cross-links and thereby stiffens condensates, except when ATP hydrolysis is possible. Active hydrolysis is also required for ISWI's mobility in condensates. Energy from ATP hydrolysis therefore fuels ISWI's diffusion through chromatin and prevents ISWI from cross-linking chromatin. Molecular dynamics simulations of a 'monkey-bar' model in which ISWI grabs onto neighboring nucleosomes, then withdraws from one before rebinding another in an ATP hydrolysis-dependent manner qualitatively agree with our data. We speculate that 'monkey-bar' mechanisms could be shared with other chromatin factors and that changes in chromatin dynamics caused by mutations in remodelers could contribute to pathologies.

Introduction

Eukaryotes prevent non-specific, cation-induced aggregation of genomic DNA by wrapping their DNA around histones, thereby forming nucleosomes [1,2]. Nucleosomes allow for regulated and reversible condensation of genomic DNA and have evolved as an important medium for epigenetic gene regulation.

Nucleosomal DNA can fold into various higher order structures. In low ionic strength environments, chromatin forms an extended structure referred to as the 10-nm fiber [3,4]. Moderate ionic strength promotes folding into different but defined higher order structures, collectively referred to as '30-nm fibers' [5]. Cellular chromatin, however, appears to assume variable, irregular structures [6]. It may contain interdigitated 10-nm fibers [7,8] and small folded nodules of chromatin, including tri- and tetranucleosomes [9,10].

Recently, it was discovered that reconstituted chromatin can undergo phase separation [11,12]. Phase separation is a property of multivalent polymers incl. many proteins and nucleic acids. They can demix from the solution into polymer-rich condensates and a polymer-depleted solution. Biomolecular condensates harbor distinct chemical environments compared to their surrounding solution. They could, for instance, be enriched or depleted for cellular enzymes or metabolites, providing an additional regulatory layer of cellular processes [13].

Concentrations can massively increase upon condensate formation. For example, sub-micromolar concentrations of soluble nucleosomes form salt-induced condensates that contain ~0.34 mM nucleosomes [11]. Such a high concentration rivals nucleosome concentrations observed in highly condensed metaphase chromosomes *in vivo* (0.52 mM) [14].

Most nuclear processes, including transcription and replication, are thought to be inhibited by the presence of nucleosomes [15]. Intuitively, one would expect that folding of chromatin into various higher-order structures and formation of chromatin condensates could pose additional barriers for nuclear factors. For instance, access to specific DNA sequences may be restricted if they are buried deep inside a folded structure, nucleosomal epitopes may

become unavailable, enzymes may be excluded from condensates, and even if they are not, diffusion through dense nucleosome fibers may become slow and inefficient. Remarkably, many chromatin enzymes are mobile in the nucleus [16]. Since the high concentration of nucleosomes in the nucleus well exceeds the dissociation constants (K_D) of most chromatin-associated enzymes, mechanisms must exist that prevent quantitative binding of the enzymes to chromatin and allow sufficient diffusional mobility.

We address these and other fundamental questions using *Drosophila melanogaster* ISWI as a prototypical nucleosome remodeling enzyme. ISWI slides nucleosomes along DNA in an ATP hydrolysis-dependent fashion (Längst et al., 1999; Hamiche et al., 1999). It can slide internal nucleosomes in reconstituted nucleosome arrays [19–22]. However, if and how fiber folding and condensation have an impact on nucleosome remodeling has not been systematically investigated, despite the physiological importance [23,24]. A dense and folded environment could conceivably obstruct remodeling activity, or possibly enhance it as observed for other enzymes [25].

Intramolecular chromatin folding does not impede remodeling

We reconstituted nucleosomes on DNA with 25 repeats of the Widom '601' nucleosome positioning sequence (Fig. 1a). 13 of these repeats contain a unique restriction site, such as a BamHI site, which becomes exposed during nucleosome remodeling [19,20]. By measuring accessibility with BamHI, we compared remodeling of folded and unfolded chromatin arrays.

After *in vitro* nucleosome reconstitution, three independent quality controls confirmed saturation of array DNA with nucleosomes (Extended Data Fig. 1a). Analytical ultracentrifugation and negative stain electron microscopy showed intramolecular folding of chromatin arrays but no substantial multimerization at Mg^{2+} concentrations of 1.7 mM. (Fig. 1b,c). A lower Mg^{2+} concentration (0.2 mM) served as a loosely folded control. Whereas single particles exhibited structural heterogeneity in both conditions, their Feret´s diameter decreased, and their circularity increased with increasing Mg^{2+} concentration, consistent with Mg^{2+}-induced intramolecular folding (Fig. 1d,e).

Induction of fiber folding by supplementation of Mg^{2+} to 1.7 mM reduced rate constants for remodeling by 2.5±0.2 fold (Fig. 1f,g). Folding however is not the major cause of this drop in activity, as the higher Mg^{2+} concentration also reduced the ATPase activity in presence of non-folding mononucleosomes (Extended Data Fig. 1b).

Internal nucleosomes in nucleosome fibers are more stable and less accessible than external, end-positioned nucleosomes [21,26–28]. To confirm that the effect we observe is not dependent on the linear nucleosome position in an array, we cloned a second version of the 25mer array, in which the positions of the restriction sites are reversed (Extended Data Fig. 1c). Supporting our earlier modeling results [21], ISWI remodeled nucleosomes with identical rate constants regardless of their location in the array (compare Extended Data Fig. 1d,e with Fig. 1f,g). We conclude that Mg^{2+}-induced intramolecular folding of the chromatin fiber does not impede nucleosome remodeling by ISWI.

ISWI slides nucleosomes inside chromatin condensates

Mg^{2+} also promotes intermolecular interactions between array molecules at elevated array concentrations [7]. Spherical condensates formed upon addition of physiologically relevant concentrations of Mg^{2+} (1 mM and 5 mM Mg^{2+}; Fig. 2a) [11,12]. The physical nature of these condensates can range from liquid-to solid-like depending on conditions and nucleosome array length [11,12,29].

Given their high nucleosome concentrations, these condensates could potentially exclude large protein complexes. To determine the size exclusion limit of the condensates, we used a series of fluorophore-labeled dextrans of different molecular weights and determined their partition coefficients (Fig. 2b). Dextrans were progressively excluded from chromatin with increasing molecular mass. Nevertheless, even 500 kDa dextrans, which possess a Stokes radius (15.1 nm) [30] equivalent to a 6 MDa protein complex, were able to enter the condensates. The data suggest that the chromatin condensates are porous or pliable enough to accommodate large particles.

Our dextran results encouraged us to evaluate whether ISWI can also penetrate condensates. We premixed GFP-labeled ISWI with Cy3-labeled chromatin arrays in the absence of nucleotides and induced phase separation by addition of Mg^{2+}. ISWI-GFP was strongly enriched in condensates (Fig. 2c). Control experiments proved that GFP or ISWI-GFP did not form condensates by themselves and that GFP on its own does not enrich in chromatin condensates (Fig. 2c and Extended Data Fig. 2a). Importantly, order of addition experiments showed that ISWI-GFP could penetrate condensates even after their formation with similar efficiency (Fig. 2c). ISWI reached a concentration of ~4 μM in condensates (Extended Data Fig. 2b).

The intermolecular interactions between nucleosomes in condensates could conceivably prevent ISWI-mediated sliding of nucleosomes. Using the restriction enzyme accessibility assay, we clearly detected remodeling under condensate conditions (5 mM Mg^{2+}; Fig. 2d and Extended Data Fig. 2c). The observed rate constant for sliding was reduced about eight-fold at the higher Mg^{2+} concentration. Condensation, however, is not the major cause of this drop in the activity, as the higher Mg^{2+} concentration also reduced the ATPase activity in presence of mononucleosomes to a similar extent (Extended Data Fig. 1b).

To test if remodeling takes place inside of condensates, we developed an imaging-based nucleosome sliding assay (Fig. 3a). We employed double-fluorophore labeled mononucleosomes that can report on nucleosome sliding via changes in FRET [31]. These FRET nucleosomes readily partitioned into condensates (Extended Data Fig. 3a). FRAP of individual condensates showed little exchange of the FRET nucleosomes between the condensate and the surrounding dilute phase (Extended Data Fig. 3b). Fluorescence lifetime imaging (FLIM) then allowed us to image FRET levels in- and outside of condensates. The donor lifetime of FRET nucleosomes was quenched compared to nucleosomes that were only labeled with the donor fluorophore or whose acceptor fluorophore was bleached, confirming FRET (Fig. 3b and Extended Data Fig. 3c,d). Importantly, addition of ISWI and Mg-ATP to FRET nucleosomes, but not to donor-only nucleosomes, increased the

donor lifetime, indicative of nucleosome sliding (Fig. 3b and Extended Data Fig. 3c). Time course measurements after flowing in Mg-ATP to ISWI-containing condensates reveal a steady increase in the fluorescence lifetime (Fig. 3c, Movie S1). No lifetime changes were recordable after addition of the non-hydrolyzable ATP analog Mg-AMPPNP as a negative control (Fig. 3c, Movie S2). We conclude that FLIM-FRET is a sensitive technology to visualize nucleosome sliding with spatial resolution.

To quantify if and to what extent condensates pose a barrier for remodeling, we determined the initial velocities for nucleosome sliding inside condensates (0.77±0.06 s^{-1}) and compared it to remodeling in solution (2.15±0.15 s^{-1}). We obtained the latter by using mononucleosomes that do not phase separate under these conditions at equivalent bulk concentrations (1.2 μM) under otherwise identical conditions (Fig. 3d). Use of five times higher Mg-ATP concentrations gave similar results (Extended Data Fig. 3e), arguing that Mg-ATP was saturating both in solution and condensates. ISWI concentrations inside condensates were substoichiometric, reaching 4.7 ± 0.6 μM (Extended Data Fig. 2b), which is well below the nucleosome concentration in condensates (225 ± 59 μM; see below). In summary, condensates slowed down remodeling by 2.6-fold, suggesting that condensation poses no substantial barrier for remodeling; instead, it may fine tune the remodeling activity.

ISWI uses ATP hydrolysis to diffuse through condensates

Nucleosome concentrations inside of condensates reach remarkably high levels, 225 ± 59 μM, equivalent to ~45 g/l, as determined by holotomography (Fig. 4a), a label-free methodology that can determine concentrations from the refractive index. Our measurement using 25mer arrays agreed well with previous estimates that employed 4- and 12-mer nucleosome arrays (195 to 550 μM) using electron tomography and fluorescence microscopy [11,32]. A broad range of conditions (array length and buffer conditions) thus leads to relatively static nucleosome densities in condensates. Of note, *in vivo* nucleosome concentrations fall into the same regime (100 μM to 500 μM) [14,33], making *in vitro* condensates a model for studying challenges encountered by chromatin enzymes in the crowded nucleus.

At such a high concentration, well above the dissociation constant of ISWI (<1 μM; (Leonard & Narlikar, 2015)), the enzyme would be expected to be constantly bound to nucleosomes, presumably limiting its mobility. Yet, we found above that condensates do not abrogate remodeling, suggesting a certain mobility of the enzyme.

To probe ISWI´s dynamics inside condensates, we performed FRAP of GFP-labeled ISWI. After bleaching the central area of condensates, there was a poor recovery in the absence of nucleotides and with saturating concentrations of Mg-ADP or Mg-AMPPNP (Fig. 4b and Extended Data Fig. 4a,b), consistent with the expectation that ISWI is highly immobile in condensates. Strikingly, however, Mg-ATP addition rendered ISWI strongly dynamic, suggesting that active ATP hydrolysis is required not only for productive remodeling, but also to ensure rapid diffusion of ISWI within condensates.

ATP hydrolysis prevents ISWI from hardening condensates

An intriguing model to explain the mobility of ISWI through condensates in the presence of ATP would be that chromatin remodeling by ISWI makes the condensate more fluid. ISWI would essentially act as a 'molecular stir bar' [35]. However, fluorophore-labeled nucleosome arrays were not mobile, as assessed by FRAP, even after prolonged incubation with ISWI and Mg-ATP (60 min; Extended Data Fig. 4c). We conclude that enhanced fluidity of chromatin upon remodeling is unlikely to explain efficient diffusion of ISWI in presence of ATP.

ISWI has two known DNA binding domains, its ATPase domain and its HSS domain [36], allowing it to bind two nucleosomes [37–39] potentially on neighboring DNA fibers. ISWI-mediated bridges between neighboring fibers would alter mechanical properties of condensates. To test this prediction, we employed optical tweezers to fuse condensates in a controlled manner (Fig. 5a) and recorded the fusion velocity (Extended Data Fig. 5a), which depends on the viscoelastic properties of condensates [40]. The number of fusion events decreased with the length of the nucleosome array, consistent with a recent report [41], and with increased Mg^{2+} concentration (Extended Data Fig. 5b). Higher ISWI concentrations also slowed down the fusion velocity (Extended Data Fig. 5c), which, at least partially, can be explained by an increase in viscosity (Extended Data Fig. 5d). For these reasons, the following experiments were performed with 13mer arrays in 1 mM $MgCl_2$ and substoichiometric ISWI amounts, typically 1:5 ISWI to nucleosomes.

Compared to nucleotide-free ISWI, the fusion velocities drastically slowed down when we added Mg-AMPPNP, Mg-ADP-BeF_x or Mg-ADP to ISWI-containing condensates (Fig. 5b; Movie S3). The presence of ISWI's HSS domain was required for this effect (Fig. 5c). Fusion velocities also shrank when we added Mg-ATP to an ATP hydrolysis-defective ISWI mutant ($ISWI_{E257Q}$; Fig. 5d). Strikingly, however, Mg-ATP did not slow down fusion when we employed wild-type ISWI (Fig. 5b,d; Movie S4). In control experiments, we ruled out that nucleotides or excess Mg^{2+} that is added together with nucleotides caused strong effects on fusion independent of ISWI (Extended Data Fig. 5e).

We conclude that ISWI, when stuck in individual nucleotide states, stiffens condensates. The HSS domain participates in this process, likely by forming bridges to a neighboring nucleosome. It is active hydrolysis, in other words the active cycling through all nucleotide states, that prevents ISWI from stably bridging nucleosomes.

Model to describe ISWI diffusion in condensed chromatin

We next derived a theoretical framework for ISWI-chromatin interactions in condensates. The two DNA binding domains of ISWI, the ATPase and the HSS domain, are flexibly linked [42] and undergo large conformational changes during the ATPase cycle [34,43]. These conformational changes might allow ISWI to make and break interactions with neighboring nucleosomes during the ATPase cycle.

When ISWI binds two nucleosomes on different DNA fibers at once, nucleosome condensates should stiffen, leading to slower condensate fusion. The drastically slower

fusion velocities that we observed when ISWI was bound to ADP, AMPPNP or ADP-BeF_x therefore indicate that ISWI can bridge nucleosomes in these nucleotide states (Fig. 5b,c). Of note, bridge formation is nucleotide-state dependent. Addition of nucleotide-free ISWI to condensates had only a modest impact on fusion velocity, suggesting that nucleotide-free ISWI only forms unstable bridges. Yet, it is still stably bound to chromatin as suggested by FRAP (Extended Data Fig. 4a). Taken together, the results indicate that only one of ISWI's domains interacts with chromatin in the nucleotide-free state.

ISWI FRAPs slowly in its AMPPNP, ADP-BeF_x and ADP-bound states, suggesting that ISWI interacts with nucleosomes with at least one of its binding domains in all these states. Intriguingly, ISWI FRAPs rapidly in the presence of ATP. It is thus the progression through ISWI's ATPase cycle that repeatedly modulates the binding affinities of both binding domains. Hydrolysis-powered conformational changes would also repeatedly break up nucleosome-nucleosome bridges, explaining why addition of ATP prevents stiffening of condensates in condensate fusion experiments. We refer to this model as a "monkey bar" mechanism [44] as it results in an alternating release of one or the other binding site during the ATPase cycle (Fig. 6a).

ADP-bound and nucleotide-free ISWI display different behavior in fusion and FRAP experiments. ISWI in both states FRAPs slowly, whereas ISWI in the ADP but not the nucleotide-free state stiffens condensates. This difference suggests that the two interaction sites have individual nucleotide state-dependent binding affinities for nucleosomes. In both ADP-bound and nucleotide-free ISWI, one domain has a higher binding affinity than the other. The FRAP rate will be dominated by the higher affinity interaction. The fusion speed, on the other hand, also relies on the strength of the weaker affinity of the other domain. In the ADP-bound state, the weaker interaction domain therefore likely possesses an affinity that is higher than in the nucleotide-free state.

We formalized these findings in terms of a simple kinetic model (Extended Data Fig. 6a). In the ATP state, ISWI stably binds with both domains to two nucleosomes. Upon hydrolysis, a conformational change weakens one of the interactions and leads to the release of one nucleosome. Subsequent ADP release switches the strengths of the two interactions, leading to rebinding of the first domain to a nucleosome, while releasing the second nucleosome. This alternating binding and unbinding of the two domains would enable ISWI to actively move through a dense mesh of nucleosomes and prevent ISWI from stably crosslinking neighboring fibers.

To test if such a simple, idealized model could recapitulate our observation that ATP hydrolysis allows fast FRAP and prevents condensate hardening in fusion experiments, we performed molecular dynamics simulations using Rouse chains to model chromatin arrays and describing all other interactions using Lennard-Jones potentials (Extended Data Fig. 6b-d). Different nucleotide states of the remodeler were modeled by changing the depth of the respective interaction potentials.

In ISWI FRAP simulations (Fig. 6b, Movie S5), we observed enhanced recovery of the remodeler in the case of active ATP hydrolysis compared to remodeler that was stalled in

any other nucleotide state (Fig. 6c). Like experiments, simulations of fusion (Fig. 6d, Movie S6) show no significant difference between ATP and nucleotide free conditions (Fig. 6e). The ADP and AMPPNP conditions are noticeably slower and do not reach full circularity within the simulated time. This again hints at the formation of ISWI-mediated stably bridged chromatin networks in the condensates that leads to a decrease in condensate fluidity.

Discussion

One major result of our study is that the nucleosome remodeling enzyme ISWI can work largely unimpeded in folded and condensed nucleosome environments. This conclusion likely extends to other remodeling complexes given that their remodeling activities were minimally affected by histone hyperacetylation or trypsinization [23,24]. Our findings imply that all nucleosomes are similarly accessible for the enzyme in condensed arrays. As nucleosome sliding takes place in 1 bp increments [45], each bp movement induces a rotation of the nucleosome by ~36° relative to other nucleosomes. Sliding inside condensed arrays, therefore, necessitates that the chromatin structure is highly fluid and readily accommodates large, local structural changes imposed by nucleosome sliding.

ISWI critically depends on interactions to the H4 N-terminal tail and the nucleosome acidic patch for catalysis [46–48]. Incidentally, both these epitopes are also suggested to be important for array folding [49]. The fact that catalysis is not strongly impaired in condensed nucleosomes suggests that these epitopes are still dynamically available for ISWI.

Nucleosome concentrations in condensates reach ~0.2 mM, a regime that nuclear enzymes also encounter *in vivo* [14,33]. Despite this high concentration, condensates remain viscoelastic materials and can accommodate dextrans with a Stokes radius equivalent to a 6 MDa protein complex. Thus, even large remodeling complexes and other nuclear machines retain a chance to enter condensed chromatin, consistent with prior literature [32,50–52].

The biophysical properties of nucleosome condensates varied with ambient conditions. Increasing Mg^{2+} concentrations, for instance, drastically stiffened condensates. As free Mg^{2+} increases during mitosis [53], stiffening of chromatin could facilitate sister chromatid condensation (Shimamoto *et al.*, 2017). Moreover, changes in the extracellular milieu could rapidly elicit cellular responses through changes in viscoelastic properties of cellular components including chromatin [54,55].

Biomolecular condensates are suggested to affect enzyme activities through their unique chemical environments (Zhang et al., 2021). Performing enzyme kinetics in non-homogeneous solutions is a challenge. Here, we have developed a FLIM-FRET nucleosome sliding assay to overcome such limitations. Its spatial resolution allows us to compare nucleosome sliding in- and outside of condensates. We predict that this kind of technology could become beneficial in the future for tracking enzymatic processes in cellular condensates in real time.

Enzymatic reactions inside biological condensates were suggested to benefit from high concentration of components (Zhang et al., 2021). However, rate enhancements would be expected for enzymes that have to work at subsaturating substrate concentrations. This is not

the case for remodelers, which face nucleosome concentrations in the nucleus far above their K_D, explaining why ISWI did not experience rate enhancements upon condensate formation.

The mode and extent of chromatin phase separation occurring *in vivo* is still debated [56–61]. Generally, a straightforward answer is difficult, not least because chromatin *in vivo* is neither homogenous nor isolated from the proteins that interact with it. Our controlled *in vitro* study shows a direct example of this: We demonstrate that short nucleosome arrays solidify upon sequestration of ISWI under non-hydrolyzing conditions, likely by cross-linking neighboring fibers. Thus, remodelers like ISWI could also serve structural purposes in chromatin [62]. ISWI itself probably does not form a condensate inside chromatin. We show that the timescales of chromatin rearrangement within droplets are slow compared to ISWI movement, such that the movement of ISWI within condensed chromatin arrays could be approximated by interactions with spatially clustered binding sites (ICBS) [63], albeit with the difference that ISWI is not propelled by a passive association-dissociation mechanism but by an ATP-coordinated release mechanism as formalized in the monkey bar model.

We view nucleosome condensates as useful model systems to study challenges enzymes face at the enormously high nucleosome concentrations in the nucleus. Given that nucleosome concentrations generally far exceed K_D-values of chromatin enzymes, almost all enzyme molecules would be expected to be bound to chromatin at equilibrium. In fact, the high nucleosome concentration would drive both nucleosome binding domains of ISWI to interact with nucleosomes, even allowing them to contact nucleosomes in unproductive conformations [20]. Multivalent nucleosome interactions further reduce the likelihood that ISWI can dissociate from nucleosomes and diffuse away. Our FRAP data support that notion, showing that ISWI becomes stuck in condensates if ATP cannot be turned over. This finding also helps explain why ATPase-dead variants of ISWI are easier to ChIP [64,65] even though nucleotides only weakly modulate affinities [34].

Given its propensity to stick to chromatin, how can ISWI be mobile enough to fulfill its functions *in vivo*? ISWI could mobilize ("stir up") chromatin by shuffling nucleosomes around, but we found no evidence in support of this possibility. Instead, we propose the existence of a novel functionality of ISWI's ATPase activity: besides nucleosome sliding, ATP hydrolysis may power conformational changes that pull the nucleosome binding domains of ISWI away from nucleosomes, leading to dissociation and subsequent re-association to other nucleosomes. Non-productive ISWI-nucleosome interactions could be dissolved in this fashion, and we speculate that some of the frequent pauses that ISWI remodelers take during sliding could be caused by unproductive binding [45,66]. According to this mechanism, ISWI effectively remains bound to nucleosomes at any time, yet active ATP hydrolysis fuels its diffusion through chromatin. At the same time, hydrolysis prevents ISWI from crosslinking and thereby solidifying condensates. This mechanism may be shared with other fly and yeast remodelers, which also become more dynamic in presence of ATP [16,67]. The mechanism however may not extend to Snf2H and Snf2L transfected into human cells, which were mobile before and after ATP depletion (Erdel et al., 2010). These remodelers may rely on a different mechanism, perhaps due to heteromerization [69].

Our findings add another facet to why loss of function mutations can induce dominant negative phenotypes or be cancer-associated [70]. Half of SMARCA4 mutations in cancers map to the ATP cleft and these mutants show slower FRAP[71]. Expression of ATPase-dead BRM in *Drosophila* caused peripheral nervous system defects, homeotic transformations, and decreased viability [72]. All phenotypes were dominant negative [71,72] and might be caused in part by changes in chromatin dynamics, and not exclusively by disruption of canonical remodeler functions. Changed dynamics of biomolecular condensates may in turn disturb biological functions (Li et al., 2020; Shi et al., 2021). It is our hope that our tools and concepts will help open new avenues for mechanistic dissections and development of therapeutics.

Methods

Cloning

Cloning of GST-sfGFP and 6xHis-TEV-ISWI-3C-STREP-sfGFP: Full length super folder GFP [77] was amplified from a plasmid pFMP248 provided by the Ökten group at TU Munich and cloned into pET41b(+) with *BgIII* and *EcoRI* to yield a GST-sfGFP construct (pFMP241). A 6xHis-TEV-ISWI-3C-STREP-sfGFP construct (pFMP244) was constructed by first subcloning the sfGFP sequence into pUC57 encoding the tag 3C-STREP-KKCKK-GFP1-11 (pFMP249) before cloning the 3C-STREP-KKCKK-sfGFP tag into pFMP210 to yield pFMP244. Correct sequences were confirmed by Sanger sequencing.

Protein expression and purification

GFP expression and purification: GST-GFP was purified from *E.coli* BL21 (DE3) after induction with 0.2 mM IPTG overnight at 20 °C. Pellet from 0.5 l culture was resuspended in 20 mL of GST binding buffer (25 mM Tris-HCl pH=7.5, 150 mM NaCl, 1 mM EDTA, 0.5 mM DTT, 20 mM imidazole, 1 mM PMSF and one tablet Complete EDTA-free protease inhibitor cocktail (Roche). Cells were disrupted by French press and sonication. and the extract clarified (SS34 rotor, 43100 x g, 30 min, 4 °C). 1 mL of 1:1 slurry of prewashed GST-beads were added to the supernatant and incubated for 90 min at 4 °C. Beads were washed five times with 10 ml binding buffer. Protein was eluted with 1.5 mL elution buffer (50 mM Tris-HCl pH=8.0, 10 mM reduced glutathione, 5% glycerol) for 30 min at 4 °C and stored at -80 °C.

Expression and purification of ISWI, ISWI-GFP, ISWI$_{\Delta HSS}$ and ISWI E257Q: Plasmids containing *D. melanogaster* ISWI (pFMP210 for 6xHis-TEV-ISWI, pFMP244 for 6xHis-TEV-ISWI-3C-STREP-sfGFP, pFMP114 for 6xHis-TEV-ISWI26–648 (*ISWI$_{\Delta HSS}$*), pFMP110 for 6xHis-TEV-ISWI E257Q) were freshly transformed. The bacterial lawn from one plate was used to inoculate two l of LB. Expression and purification was essentially as described [20,43], entailing Nickel affinity chromatography (5 mL, Cytiva), TEV cleavage, MonoS chromatography (5/50 GL GE Healthcare 1 mL), and HiLoad Superdex200 (GE Healthcare, 120 mL) size exclusion chromatography with the difference that bacteria were cracked with six runs on Microfluidizer LM10 at 1200 bar.

Expression and purification of histones: *D. melanogaster* histones were expressed and purified as described [78] from the following plasmids: pFMP128 for H2A, pFMP129 for H2B, pFMP186 for H3, pFMP187 for H4, pFMP269 for H2AK119C, pFMP270 for H3C111A, pFMP268 for H4T1C. Bacterial lawns from one plate were used to inoculate two liters of LB media. Cells were resuspended in SA buffer (40 mM NaOAc pH=5.2, 1 mM EDTA pH=8, 10 mM lysine) supplemented with 6 M urea, 200 mM NaCl, 1 mg/mL aprotinin, 1 mg/mL leupeptin, 1 mg/mL pepstatin, 1 mM PMSF and 5 mM β-mercaptoethanol. Benzonase (Merck Millipore 1016540001 100000; 5 μl per liter of culture) and lysozyme (tip of a spatula) were added, and the suspension was sonicated on ice (Branson sonifier, 15 seconds on, 30 seconds off, amplitude 30%, effective sonication time 20 minutes). Bacteria were cracked with six runs on Microfluidizer LM10 with 1200 bar.

Assembly and purification of octamers: Lyophilized histone aliquots were dissolved in an unfolding buffer (20 mM Tris-HCl, 7 mM guanidinium-HCl, 20 mM DTT) to 4 mg/ml for 10 minutes in a thermoblock (24 °C, 600 rpm). Solutions were spun down in table top centrifuge (10 minutes, full speed, 4 °C), and supernatants transferred to fresh tubes and kept on ice until dialysis. Histone concentrations were remeasured in unfolding buffer by measuring OD280 and corrected for purity as assessed from SDS-PAGE gel. Histones were mixed in molar ratio H2A:H2B:H3:H4=1.4:1.4:1:1. The histone mixture was transferred into dialysis membranes (Roth E658.1 MWCO: 4000-6000) which were pre-soaked in water for one hour and rinsed with refolding buffer (10 mM Tris-HCl pH=7.5, 2 M NaCl, 1 mM EDTA, 5 mM β-mercaptoethanol). The mixture was then dialyzed three times against 1 L of refolding buffer, with the second dialysis step being overnight. Lastly, octamers were purified by size exclusion chromatography (HiLoad 16/60 Superdex 200 prep grade), concentrated to 4 mg/mL (Amicon 15 mL 30 kDa), aliquoted, flash frozen in liquid nitrogen and stored at -80 °C.

Histone labeling (H2AK119C-atto565, H4T1C-cy3): Lyophilized histone aliquots were dissolved in a labeling buffer (7 M guanidinium-HCl, 20 mM Tris-HCl pH=7.5, 5 mM EDTA, 0.7 mM TCEP) to final concentration 0.2 mM and incubated two hours to reduce all cysteines. Cyanin-3-maleimide (Lumiprobe) was dissolved in DMSO to final concentration 100 mM and added to solution in 5.7-fold excess. Atto-565 maleimide (Atto-tec) was dissolved in DMF to final concentration 100 mM and added to solution in 13.2-fold excess. Histones were incubated with the dye for 14 hours (3 hours for cy3 labeling) on rotating wheel at room temperature covered with aluminum folium. To stop the labeling reaction, β-mercaptoethanol was added to final concentration to 340 mM. For cy3 labeling, reaction was stopped by adding DTT to final concentration 20 mM. Unreacted dye was partially removed by several rounds of ultrafiltration (15 mL 10K Amicon, Millipore) and successive dilutions with labeling buffer (this step was omitted for Cy3 labeling). The labeling efficiency was assessed with SDS-PAGE and fluorescence imaging.

Synthesis of DNA for nucleosome arrays: To distinguish remodeling of individual nucleosomes in a nucleosome array, we previously cloned a DNA with unique restriction sites in 13 of 25 Widom-601 positioning sequences with a 197 bp repeat length (pFMP233) [19] (Extended Data Fig. 1c). Here we cloned a second variant of this DNA by placing the

13 unique restriction sites on the other end of the canonical 601 sites, essentially inverting the unique restriction sites with regards to their positioning inside of the array, yielding pFMP232 (Fig. 1a). To this end, thirteen 601 repeats were synthesized (GenScript) in which naturally occurring AvaI and AluI sites in the canonical 601 sequenced were replaced with unique restriction sites (pFMP226). A unique AvaI restriction site was added to the 3´-end (pFMP226). The 13mer was extended to a 25mer as follows. pFMP226 was completely digested with XbaI, EcoRI and AseI in buffer II (NEB) and the insert was subcloned into pUC18, which was fully digested with XbaI and EcoRI, yielding pFMP236. A plasmid containing 25x197 bp canonical Widom-601 repeats (pFMP166) was subjected to partial AvaI digestion. The band corresponding to a 12mer repeat (2354 bp) was gel purified and cloned via ligation into AvaI digested pFMP236, yielding pFMP232 (Fig. 1a).

Preparation of DNA for nucleosome arrays: 25mer and 13mer nucleosome arrays were prepared as published previously [19]. Briefly, plasmids carrying 25 (pFMP232, pFMP233) or 13 (pFMP226) consecutive copies of 197 bp with modified 601 sequence were purified from 4 l cultures of DH5α *Escherichia coli* using Nucleobond® PC 10000 (Macherey-Nagel). Three mg of the plasmids were digested with EcoRI HF (0.25 U/μg DNA) and HincII (0.6 U/μg DNA) in CutSmart Buffer at 37°C for 3 h to cut out the arrays from the plasmids. Restriction enzymes were heat-inactivated at 65°C for 20 min. Tubes were put on ice before AseI was added (0.5 U/ μg DNA) and then incubated at 37 °C for four h. DNA was purified via phenol/chloroform extraction and ethanol precipitated in presence of NaOAc.

Preparation of DNA for mononucleosomes: DNA fragments containing the 601 sequences were amplified by large-scale PCR [31]. The following primers were obtained from Sigma: oFMP839, GCTTGCATGCCTGCAGGTCG, to PCR ON60 fragment used for ATPase assays; oFMP864, CTGGAGAATCCCGGTGCCG, to PCR ON60 fragment used for ATPase assays and 0N60-EcoRI fragment used for FLIM-FRET; oFMP1260, TAAGCAGAATTCGCTTGCATGCCTGCAGGTCG, to PCR [atto647N]0N60-EcoRI fragment used for FLIM-FRET; oFMP1261, [ATTO647N]CTGGAGAATCCCGGTGCCG, to PCR [atto647N]0N60-EcoRI fragment used for FLIM-FRET and 0N60-EcoRI fragment used for FLIM-FRET. The plasmid template was precipitated by addition of ½ of volume 30% PEG 8000 (w/w) in 30 mM $MgCl_2$. The PCR product was then precipitated by adding the same volume of propan-2-ol, washed with 70% (v/v) cold ethanol, and resuspended in TE buffer (10 mM Tris-HCl pH=7.6, 1 mM EDTA pH=8).

Chromatin assembly and purification

Assembly of 25- and 13mer arrays: Preparative assemblies were performed as described [19]. They contained 100-500 μg digested plasmid (100 ng/μL of 601-array DNA, which corresponds to 150 or 200 ng/μL of total digested plasmid containing 25mer or 13mer, respectively). Salt gradient dialysis was performed by pumping 3 L of low salt buffer (50 mM NaCl, 10 mM Tris-HCl pH=7.6, 1 mM EDTA pH=8, 1 mM DTT) into 1 L of high salt buffer (2 M NaCl, 10 mM Tris-HCl pH=7.6, 1 mM EDTA pH=8, 1 mM DTT) containing the dialysis bag over a period of 24 hours. Assemblies were then dialyzed against 1 L of low salt buffer before they were precipitated by addition of equal volume of

precipitation buffer (10 mM Tris–HCl pH 7.6, 7 mM or 10 mM $MgCl_2$ for 25mer or 13mer, respectively). Pellets were resuspended in TE buffer and quality controls of chromatin array were performed as described [19] (Extended Data Fig. 1a). Chromatin concentrations were approximated by UV assuming that 1 OD at 260 nm equals 50 ng/μL of DNA.

Mononucleosomes: Preparative assemblies contained DNA (200 ng/μL), purified octamers, 2 M KCl, 20 mM Tris-HCl pH=7.7, 10 mM DTT. Reactions were transferred into Slide-A-lyzer 7k Mini (Thermo Scientific) and underwent salt gradient dialysis in 200 mL of Mono2000 buffer (2 M KCl, 20 mM Tris-HCl pH=7.7, 0.1 mM EDTA pH=8, 1 mM DTT) to which 1 L of Mono0 buffer was pumped (20 mM Tris-HCl pH=7.7, 0.1 mM EDTA pH=8, 1 mM DTT) over 24 hours. To maintain constant volume, buffer was simultaneously pumped out with the same speed. Assemblies were dialysed against Mono0 buffer and purified over 10-30% (w/w) glycerol gradient. Concentrations were determined as above for arrays.

Quality controls of assembled chromatin

Agarose gel of nucleosome arrays: 200 ng of before and after Mg-precipitation was analyzed by agarose gel electrophoresis (0.7%).

NotI digestion of nucleosome array: 200 ng of arrays were digested in EX50 buffer (10 mM Hepes–KOH pH 7.6, 50 mM KCl, 1.5 mM $MgCl_2$, 0.5 mM EGTA) with Not1 (20 U/μL) in total volume of 15 μL for three hours at 26 °C. Digestion was analyzed on 1.1% agarose.

BsiWI digestion of nucleosome array: 250 ng of an arrays were digested in buffer (25 mM Hepes–KOH pH 7.6, 0.1 mM EDTA, 50 mM NaCl, 10% glycerol, 2 mM $MgCl_2$) with BsiWI (10 U/μL) for 1 hour at 26 °C in total volume of 20 μL. The digestion was stopped with addition of SDS (final concentration 0.4%) and EDTA (final concentration 20 mM) followed by Proteinase K (1 mg/mL) treatment in total volume of 30 μL for three hours at 65 °C or overnight at 37 °C. DNA was ethanol precipitated and analyzed on 1% agarose gel.

Analytical ultracentrifugation

Sedimentation velocity (SV) experiments were conducted at 20 °C in a Beckman Coulter ProteomeLab XL-I analytical ultracentrifuge (Palo Alto, CA) using an An-50 Ti rotor. Data was recorded with the instrument's AUC controller version 6.2. Samples contained 21.6 ng/μL (6.9 nM) of 25mer in 1 mM Tris-HCl pH 8.0, 0.01 mM EDTA pH 8.0, 0.01 mM DTT, 50 mM NaCl, 0.2 mM or 1.7 mM $MgCl_2$. Samples (360 μl) were loaded into 12 mm charcoal-filled epon double sector centerpieces. A rotor speed of 22,000 rpm was selected and absorbance optics scans at a wavelength of 258 nm were collected every second until sedimentation was complete. Data were analyzed using the c(s) model in SEDFIT 16 which directly models the sedimentation boundary as a continuous distribution of discrete, non-interacting species [79]. Buffer density and viscosity as well as sample partial specific volumes were calculated using UltraScan III version 6005[80].

Negative stain electron microscopy

Quantifoil R2/1 Cu200 C2 grids were plasma cleaned for 20 s at 20 mA (GloCube, Quorum). 3.5 μL of sample containing 1-4 ng/μL (0.3-1.3 nM) of 25mer in buffer (3 mM Tris-HCl pH 8.0, 0.03 mM EDTA pH 8.0, 0.03 mM DTT, 50 mM NaCl, 0.2/1.7 $MgCl_2$) was applied, incubated 30 s, then hand blotted. Grids were negative stained with 2x 3.5 μL of 2% uranyl acetate, and hand blotted after 30 s for each stain application. Images were collected using an FEI Morgagni 100 keV TEM with a SIS Megaview III 1k CCD, at a nominal magnification of 56,000x with the acquisition software iTEM 5.0.

Analysis of electron micrographs: Outlines of single particles were determined with a trainable Weka segmentation in ImageJ (Fiji; v1.52f-1.54f). Feret´s diameter (the maximum distance between two parallel tangential lines), and circularity were calculated for this outline using equation 1.

$$circularity = \frac{4\pi \times area\,2}{perimeter\,2} \quad \text{(Eq. 1)}$$

Restriction based nucleosome sliding assay

Remodeling assays contained 4 nM 25mer arrays (100 nM total nucleosome concentration), 200 nM ISWI, ATP regeneration system (6 mM phosphoenolpyruvate, 15.5 U/mL pyruvate kinase/lactate dehydrogenase, 1 mM DTT), indicated magnesium concentration and 5 μM Mg-ATP in remodeling buffer RB (25 mM Hepes pH=7.6, 0.1 mM EDTA, 50 mM NaCl, 10% (v/v) glycerol, 0.2 mg/mL BSA). Beforehand, chromatin arrays were dialyzed overnight into 10 mM Tris pH=7.6 at 4 °C. The reaction was started with addition of ISWI and incubated at 26 °C. At different time points, 20 μL aliquots were taken and remodeling was quenched with apyrase (50 mU, 1 min, 26 °C). The Mg^{2+} concentration was supplemented to a final concentration of 1.7 mM $MgCl_2$ for all samples. Samples were digested with 10 U/125 ng array of BamHI for 90 min at 26 °C. The digestion was stopped with addition of 20 mM EDTA and 0.5% SDS, followed by Proteinase K (final concentration 0.5 mg/mL) treatment for three hours at 37 °C. Samples were ethanol precipitated and separated on an agarose gel (0.7% to 0.9% in 0.5xTBE, 20 cm). Gels and running buffers contained 0.5 μg/mL EtBr. The bands were analyzed with *AIDA Image Analyzer Software* (Raytest, version 4.27) and the percentage of *Cut*-DNA calculated. The dependence of percentage of Cut-DNA versus time was fitted in R into to a single exponential function (Eq.2):

$$\%cut = \%cut_{\max} \times \left(1 - e^{-k_{obs} \times t}\right) \quad \text{(Eq. 2)}$$

ATPase assay

A NADH-oxidation coupled ATPase assay was performed as described [20]. Briefly, 30 μl reactions were assembled on a 384-well plate (Greiner, 781101), containing 100 nM ISWI and 0.1/0.5/1.33 μM mononucleosomes (0N60) in remodeling buffer supplemented with

ATP-regeneration system and 0.6 mM NADH. Each sample was measured in technical triplicates, which were then averaged. Measurements were independently replicated. Reactions were started by addition of 1 mM Mg-ATP and NADH absorbance was monitored at 340 nm in a plate reader (Biotek PowerWave HT with Gen5 v.1.11 software) at 26°C. Absorbance readings between ten and 20 minutes were fit to a linear function.

Phase separation of nucleosome arrays and imaging of nucleosome condensates

All phase separation experiments were performed in phase separation buffer (PSB) (25 mM Hepes-KOH pH 7.6, 0.1 mM EDTA, 50 mM NaCl, 10% glycerol, 1 mM DTT, 0.2 g/L BSA) supplemented with 1 mM $MgCl_2$ (PSB1) or 5 mM $MgCl_2$ (PSB5). Phase separation was induced by mixing equal volumes of nucleosome arrays diluted in TE buffer with 2x PSB. The formed chromatin condensates (4-10 μL of sample) were incubated at room temperature for a minute and then loaded onto the imaging chamber made out of double-sided tape. Double-sided tape was pierced with a hole puncher before and sample was deposited into the hole. Cover slips were pretreated with 20 μL of BSA solution (25 mM Hepes-KOH pH 7.6, 0.1 mM EDTA, 50 mM NaCl, 10% glycerol, 1 mM DTT, 100 mg/mL BSA) for one minute. The imaging chamber was sealed with nail polish, and unless stated otherwise, spun onto the cover slip (1 min, 1000g, room temperature). Samples we then imaged on a widefield microscope (Zeiss Axiovert).

Analysis of phase diagram: Condensates were detected by Trainable Weka segmentation in ImageJ, their surface was calculated as a percentage of a total field of view surface and plotted in form of a heatmap in R.

Confocal imaging

Confocal and FLIM images were performed with a TCS SP8 X FALCON confocal head (Leica Microsystems, Wetzlar, Germany) mounted on an inverted microscope (DMi8; Leica Microsystems). For confocal imaging, a white light laser was used as excitation source (561 nm or 633 nm as necessary). Single photons were collected through a 40×/1.3 NA oil-immersion objective and detected on Hybrid Detectors (HyD) (Leica Microsystems) with a 570 – 610 nm, and 650 – 707 nm spectral detection window as necessary. Sequential excitation was performed to avoid potential crosstalk between the fluorophores. Data acquisition with software LAS X Version 3.5.7.23225 and for FLIM imaging together with the LAS X FLIM/FCS Version 3.5.6 module.

FITC-dextran partitioning in chromatin condensates

Condensates were formed in a solution containing 100 nM 13mer (final concentration 90 nM), PSB2 supplemented with 2.5 mM DTT and incubated for five minutes at room temperature when the FITC-dextrans (Sigma) diluted in water were added to final concentration of 0.1 mg/mL. Samples were prepared as described above and imaged on Leica laser scanning confocal microscope after 1 h incubation at room temperature.

Images were analyzed in ImageJ, where the dextran partitioning coefficient was determined for individual condensates as a ratio of fluorescence inside the condensate and background

fluorescence. Molecular weights of dextrans were converted into Stokes radii with an online tool (https://www.fluidic.com/toolkit/hydrodynamic-radius-converter/).

ISWI colocalization experiment

Chromatin and ISWI colocalization experiment was performed with 40 nM of unlabeled 25mer, 10 nM of 25mer-Cy3 and 1.125 μM ISWI-GFP/GFP-GST in PSB5. Condensates were induced by adding Mg^{2+} (5 mM) either after or before addition of GFP-GST or ISWI-GFP.

A standard curve for mean Gray value dependence on ISWI-GFP concentration was obtained from ISWI-GFP dilutions in PSB5. Different microscope settings were used to image lower and higher dilutions. ISWI-GFP concentration was then determined inside condensates and in a surrounding solution for 90 nM 13mer, 234 nM ISWI-GFP, 1 mM Mg-ATP, ATP-regeneration system, PSB1 and for 45 nM 25mer, 125 nM 0N60 mononucleosomes, 625 nM ISWI-GFP, 1 mM Mg-ATP, ATP-regeneration system, PSB5.

Restriction enzyme accessibility nucleosome sliding assay adapted to chromatin condensates

A *KpnI* site was used to compare nucleosome sliding in 25mer arrays fully dissolved or after condensate separation. A remodeling assay contained 15 nM 25mer, 750 nM ISWI, ATP regeneration system and 1 mM Mg-ATP in PSB0.2/5, in total reaction volume of 20 μL. Reaction was started with 2 μL of ISWI (Fig. 2d) or ATP (Extended Data Fig. 2c) and incubated at 26 °C. Before the reaction was started, 6 μL of the reaction mixture were checked under the microscope for chromatin condensates. At different time points, 1 μL of reaction was quenched with 45 μL of quenching solution (10 mU/μL apyrase in apyrase reactions buffer (New England Biolabs)), supplemented with additional 1.8 μL 2 mM $MgCl_2$ for low magnesium samples), incubated at 26 °C for 15 min, then on ice. After all time points were quenched, the the presence of condensates was confirmed by microscopy. To each tube, 2.5 μL of *KpnI* (New England Biolabs; R3142L) was added and incubated at 26 °C for 30 min. Cleavage was detected as above for the restriction-based nucleosome sliding assay, except that ImageJ was used for quantification.

FLIM-FRET

Slide preparation: For end point assays (Fig. 3b), 45 nM 25mer (1125 nM nucleosome concentration), 125 nM labeled mononucleosomes, 625 nM ISWI, ATP regeneration system and 1 mM Mg-ATP were mixed in PSB5 in total volume of 10 μL. Samples were incubated at room temperature for 15 minutes, 6 μL was transferred on a slide prepared and spun as above, and imaged after four h. For time lapse assays (Fig. 3c), 40 μL of the reaction mixture was loaded into the channel of imaging chamber (Ibidi μ-Slide $VI^{0.5}$ Glass Bottom 80607). The imaging chamber was spun down and mounted on the microscope. Lifetimes were measured for two min before addition nucleotides. Then, 120 μL of 1 mM Mg-ATP or 1 mM Mg-AMPPNP solution, dissolved in identical buffer and supplemented with ATP regeneration system, was filled into one of the reservoirs without removing the chamber from the microscope or stopping the imaging. Nucleotide solution then replaced solution above the condensates by gravity flow. Time lapses were recorded for two h.

Finally, time lapses in Fig. 3d and Extended Data Fig. 3e contained 1125 nM unlabeled mononucleosomes or 45 nM 25mer, 125 nM FRET mononucleosomes and ATP regeneration system in PSB5 in total volume of 18 μL. Two μL of 10x Mg-ATP solution were added to a final concentration 1 or 5 mM, the mixture was loaded into a channel of the imaging chamber and imaged two to four min after ATP addition.

Image acquisition: For FLIM, the same system described in "Confocal Imaging" was used. The white light laser delivered 80 MHz repetition rate at 561 nm. Arrival time of single photons was measured with the included FALCON module. The FLIM acceptor photobleaching image kept the same parameters as the confocal one with 12 frames accumulations instead. The other FLIM images and movies size was set to 256 × 256 pixels. A 3-fold zoom factor was applied, giving a pixel size of 0.380 μm and an image size of 97 × 97 μm. Pixels number was decreased to favor imaging speed in the time-lapses. Because the statistical determination of the distribution of single photon arrival times requires a minimum number of photons, 60 frames were acquired at 2.34 Hz for each TCSPC recording, for a total time of around 26 s. Corresponding to a scanning speed of 600 Hz. Time-lapses were recorded for at least 15 min with a time point every 2 min.

Analysis: FLIM image analyses were performed in the LAS X Version 3.5.7.23225 with LAS X FLIM/FCS Version 3.5.6 software and with custom MatLab code using Matlab R2021a. Lifetime calculations were based on the Phasor approach [75]. Phase and modulation lifetimes were calculated using the Fourier sine and cosine transforms of the lifetime images. The FRET efficiency (E_{FRET}) was calculated according to Eq. 3:

$$E_{FRET} = 1 - \frac{\tau_{DA}}{\tau_D} \quad \text{(Eq. 3)}$$

where τ_{DA} is the lifetime of the donor-acceptor sample, and τ_D is the lifetime of the donor alone. Results were expressed as mean ± SD. Lifetimes images shown were done using the phasor approach to maximize the number of photons while keeping a good image resolution. For the time lapse, the linear part of lifetime changes was fitted to a linear function to obtain initial velocity.

Holotomography

Slide with 25mer condensates containing ISWI in PSB5 buffer was prepared as described above. Refractive index images were collected on 3D Cell Explorer-fluo (Nanolive) equipped with dry objective (60x magnification, 0.8 numerical aperture) and low power laser (λ = 520 nm, sample exposure 0.2 mW/mm$_2$). 96 slices were collected for a field depth of 30 μm. Software STEVE v.1.6.3496 (Nanolive) was used to collect, view and export images. Data were exported as tiff files (floating values of RI) and further processed in ImageJ (Fiji). Eq. 4 was used to calculate chromatin mass concentration in condensates, where n = refrective index, c = mass concentration and dn/dc is a refractive index increment. We assumed $c_{condensate} >> c_{solution}$ and dn/dc to be 0.185 mL/g.

$$n_{condensate} - n_{solution} = \frac{dn}{dc} \times (c_{condensate} - c_{solution})$$

(Eq. 4)

ISWI-GFP and 25mer-Cy3 FRAP

Four μL of 2.5x mixture of unlabeled chromatin, labeled chromatin and ISWI-GFP were mixed with six μL 1.7xPSB5 containing 1.7xnucleotide. Final experimental conditions were: 76 nM 25mer, 1.75 nM Cy3-25mer, 1 μM ISWI-GFP, 0.77 mM Mg-nucleotide, PSB5, ATP regeneration system (Fig. 4b); 15 nM 25mer-Cy3, 375 nM ISWI-GFP, PSB5, 1 mM Mg-ATP/no nucleotide (Extended Data Fig. 4a); 100 nM 25mer, 4.5 nM 25mer-Cy3, 1.3 μM ISWI-GFP, PSB5, ATP regeneration system, 1 mM Mg-ATP (Extended Data Fig. 4b). The sample was incubated for 1 min and then loaded onto the slide, spun, sealed as above and imaged within 30 minutes of preparation.

Images were acquired at 26°C with a 63X glycerol immersion objective on a Leica Sp5 confocal microscope equipped with Argon 488 nm and DPSS 561 nm lasers. For ISWI-GFP FRAP, 10 frames (512x512 pixel) at 1.2 s intervals were taken as a pre-bleach reference, followed by a single 1.2 s bleaching pulse targeted to a circular region within ≥ 3 droplets at once. After bleaching, 89 frames were taken at 1.2 s intervals to measure fluorescence recovery. For H4-Cy3 FRAP, 10 frames (512x512 pixel) at 1.2 s intervals were taken as pre-bleach reference, followed by four 1.2 s bleaching pulses targeted to a circular region within ≥ 3 droplets at once. After bleaching, 20 frames were taken at 30 s intervals to measure fluorescence recovery. For both cases, brightfield images were also collected in parallel.

All images were processed using Fiji [81]. First, drift was corrected using MultiStackReg package (https://biii.eu/multistackreg) by calculating transformation matrices from brightfield images (code available on request). Bleach, control (within droplet but outside the bleached region) and background Region Of Interest (ROIs) were manually defined, and average fluorescence intensity was measured. Intensities were normalized using the easyFRAP web tool [82] to generate FRAP curves with full scale normalization.. Plots were generated using R – version 4.2.1 (https://www.R-project.org/) [83].

Controlled condensate fusion with optical tweezers

Four μL of chromatin ISWI mixture (225 nM 13mer, 585 nM ISWI, volume was made up with TE) was gently mixed with 6 μL 1.7xPSB1 containing 1.7xnucleotide. Final experimental conditions were: 90 nM 13mer, 234 nM ISWI, 1 mM Mg-nucleotide and ATP regeneration system in 1xPSB1. Data on fusion velocity with different ISWI concentrations (Extended Data Fig. 5c) were collected in 1xPSB1 supplemented with 5 mM DTT. Of note, with an ATP-regeneration system present, slow fusion was detected with AMPPNP and ADP-BeF_x, presumably due to ADP contamination present in nucleotide preparations. Samples were incubated for 1 min and then loaded onto prepared slides. Optical tweezer experiments were carried out on a dual-trap C-Trap (Lumicks, Amsterdam; acquisition software Bluelake 2.3.2). For controlled fusion of condensates, a single condensate was

Europe PMC Funders Author Manuscripts

trapped in each of the optical traps at minimal laser power, resulting in trap stiffnesses on the order of ~0.001 pN/nm. The traps were approached in 20 nm steps until the condensates touched and fusion started which was determined by observation of a rapid drop in the force signal (Extended Data Fig. 5a). During fusion, the trap distance was then held constant. Fusion was further monitored by brightfield microscopy. Events in which fusion was not complete after 30 s were counted as non-fusing and assigned a fusion velocity of 0.

Analysis was performed using custom written code for the IGOR Pro 8 software (WaveMetrics, USA). Fusion velocity was determined by fitting a generalized logistic function (Eq. 5) to the differential force data along the x-axis. With F(start) and F(finish) the differential forces before fusion onset and after finished fusion, respectively.

$$F(x) = F(\,finish\,) + \frac{F(\,start\,) - \mathrm{F}(\,finish\,)}{1 + e^{\left(\frac{t - t_0}{\tau}\right)^{\gamma}}} \quad \text{(Eq. 5)}$$

The force was then normalized so that F(start) = 0 and F(finish) = 1. The fusion velocity was determined as the slope at the inflection point of the fitted function. As the fusion velocity is inversely proportional to the size of the condensates, the obtained velocity was normalized using the mean size of the two fused condensates which was obtained using radial profiling of the brightfield videos pre-fusion. For comparison between conditions, velocities were transformed into the log10-fold change relative to the mean of the chromatin only condition.

ThT fluorescency measurment

Thioflavin T (ThT) fluorescence intensity was measured with increasing ISWI concentrations with 90 nM 13mer in modified PSB (supplemented with 2 mM $MgCl_2$, 2.5 mM DTT and 40 μM ThT).

Molecular dynamics simulations

Molecular dynamics simulations were performed using custom written software in C++ 11 and CUDA SM 6.1. Chromatin arrays were described as Rouse chains with an equilibrium distance between nucleosomes of 16 nm and a spring constant of 15 pN/nm. All nucleosomes further interacted with each other via truncated Lennard-Jones potentials. The remodeler was modeled as single particles that repel each other and can form two independent interactions with nucleosomes (Extended Data Fig. 6a). All attractive interactions were described as truncated Lennard-Jones potentials with an equilibrium distance of 16 nm and a cutoff distance of 48 nm. Between 32 and 48 nm the potential was simplified using a linear approximation (Extended Data Fig. 6c). The strength of the remodeler-nucleosome interactions was modulated based on the remodeler's nucleotide state. The first interaction site switched from a remodeler off-rate of $2.5*10^{-6}$ $timestep^{-1}$ in the nucleotide-free state to an off-rate of $1.25*10^{-7}$ $timestep^{-1}$ in the ATP and ADP bound states. The second interaction site had a remodeler off-rate of $1.25*10^{-6}$ $timestep^{-1}$ in the ADP bound state and $1.25*10^{-7}$ $timestep^{-1}$ in the ATP bound state and without bound nucleotide. Condensates were formed from 169 Rouse chains of length 13 and

Europe PMC Funders Author Manuscripts

440 remodeler particles that were equilibrated in their respective nucleosome condition for $4*10^7$ timesteps before use in FRAP or fusion simulations. Particle motion was simulated using Langevin dynamics with a diffusion coefficient of 0.02 nm^2/timestep ($8*10^5$ nm^2/s) corresponding to remodeler diffusion *in vivo* (Kim *et al.*, 2021) in timesteps of 20 ns.

Apart from simplifications due to coarse-graining, the prime reason why we achieve only qualitative, rather than quantitative agreement between the coarse-grained simulations and experiments lies in technical constraints required for computational performance. To keep thesimulation tractable, typical simulated droplet sizes are approximately an order of magnitude smaller than their experimental counterparts. Even in the model of ISWI being a stable crosslinker, a small shape change during droplet fusion may be expected from the stretching of arrays. This relative change is much more pronounced for the smaller simulated droplets, compared to the experimental droplets. In addition, simulated fusion trajectories have a well-defined endpoint (circularity=1), such that we were able to determine a fusion velocity for all simulation trajectories. In contrast, the fusion velocity for experimental trajectories could only be determined for events which completed fusion (see previous section).

Simulated FRAP

For the simulation of FRAP experiments, remodeler particles in one half of the condensate were marked as bleached. Mixing was determined using the distances between particles. Pairwise distances either between all particles of one type ($dist_{all}$) or only between bleached and non-bleached particles ($dist_{cross}$) were determined.

The pairwise distances were binned, and mixing (M) was quantified with Eq.6

$$M = \sum \frac{(dist\ cross\ - dist\ all)^2}{dist\ all} \quad \text{(Eq. 6)}$$

every $2.5*10^6$ timesteps. The resulting values were normalized between 0 and 1. For each condition three simulations were performed.

Simulated fusion

For the simulation of condensate fusion, two preequilibrated condensates were positioned in close proximity. Fusion progress was then measured using the sphericity of the system over time which approaches 1 as fusion progresses and was fitted with the same generalized logistic function as the force response in experiments. Three simulations were performed for each condition. Relative fusion velocities were calculated with respect to the mean of the nucleotide free condition.

Europe PMC Funders Author Manuscripts

Extended Data

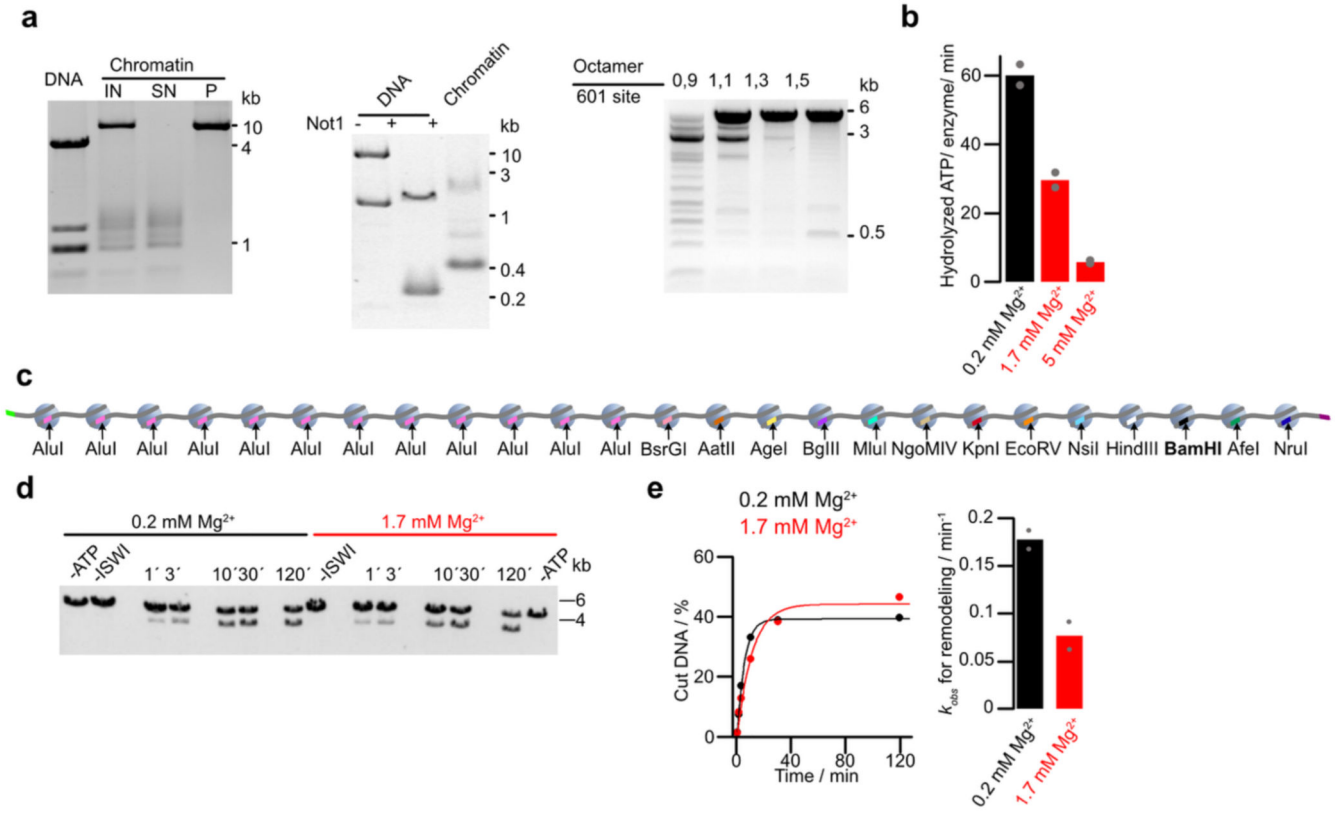

Extended Data Fig. 1. Catalytic activity of ISWI for varying Mg-concentrations.

a, Quality controls for 25mer nucleosome arrays. Left: agarose gel after magnesium precipitation of assembled arrays and the resolubilized pellet. IN, input; SN, supernatant; P, pellet. Competitor DNA derived from the plasmid backbone (< 1 kb) was excluded from P. Middle: Not1 digestion (a Not1 site is present in each linker) liberated mostly mononucleosomes, running around 400 bp, but little 197 bp fragments, confirming saturation of most 601 repeats with octamers. Right: BsiWI digestion (all nucleosomes occlude a BsiWI restriction site) for arrays assembled with different octamer amounts. As 601 sites become saturated, digestion is hindered. Arrays were reconstituted 16 times with similar results. **b**, Increasing Mg^{2+}-concentrations reduce mononucleosome-stimulated ATP hydrolysis rates. Saturating concentrations of ATP (1 mM) and mononucleosomes were used (1.33 μM). Control experiments with three times lower mononucleosome concentrations gave the analogous results. **c**, Nucleosome array as in Fig. 1a but with different orientation of restriction sites such that the BamHI site is now more peripheral. **d**, BamHI accessibility assay as in Fig. 1f but for the array shown in *c*. **e**, Left: quantification of gel in *d* and exponential fits of time courses. Right: rate coefficients from single exponential fits. Bars in *b* and *e* are mean values of two independent experiments (dots).

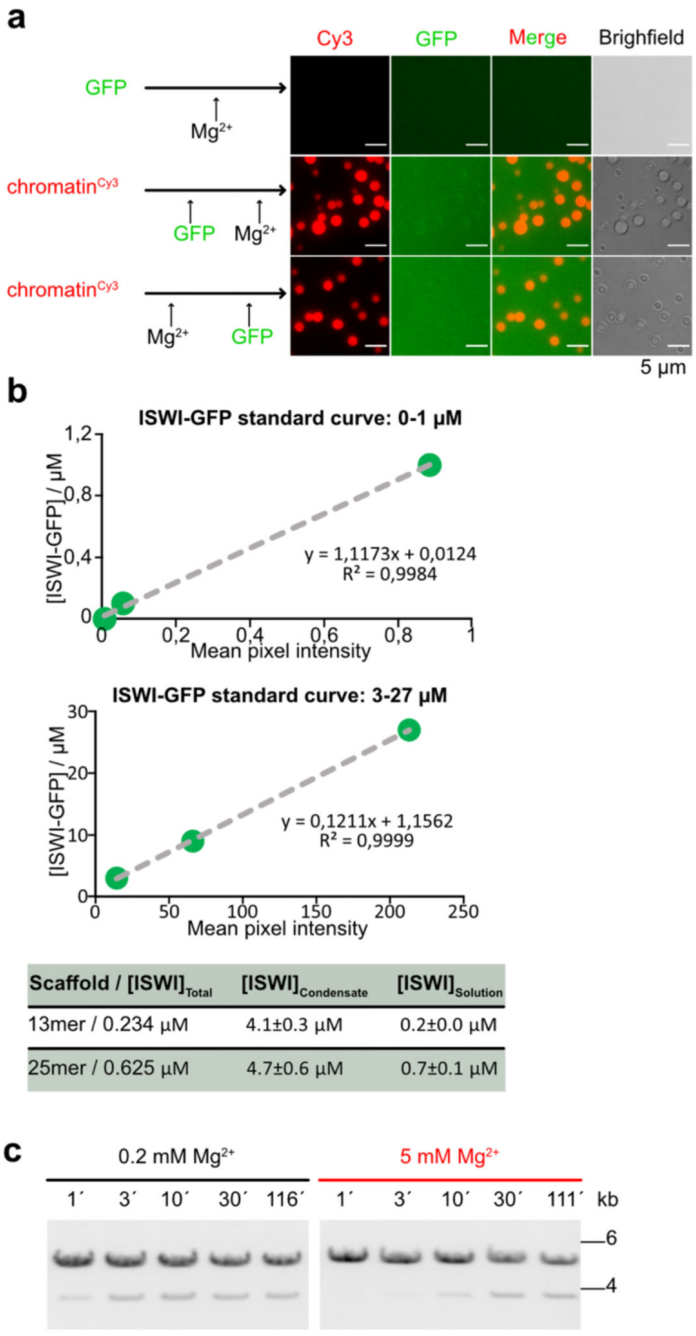

Scaffold / $[ISWI]_{Total}$	$[ISWI]_{Condensate}$	$[ISWI]_{Solution}$
13mer / 0.234 µM	4.1±0.3 µM	0.2±0.0 µM
25mer / 0.625 µM	4.7±0.6 µM	0.7±0.1 µM

Extended Data Fig. 2. ISWI-GFP partitions into condensates.

a, GST-labeled GFP does not partition into chromatin condensates. The colocalization experiment was performed with 40 nM of unlabeled 25mer, 10 nM of 25mer-Cy3 and 1.125 μM of GFP-GST. N = 2, with similar results. **b**, ISWI-GFP concentrations were determined inside condensates and, after centrifugation, in the surrounding solution (bottom) from fluorescence intensities using calibration curves with ISWI-GFP dilutions (top). Two different microscope settings were used to image lower and higher dilutions. Means and SD of two independent replicates are shown. **c**, Nucleosome sliding time courses as in Fig. 2d.

Conditions were identical except that reactions were started by addition of Mg-ATP, not by enzyme. N = 1.

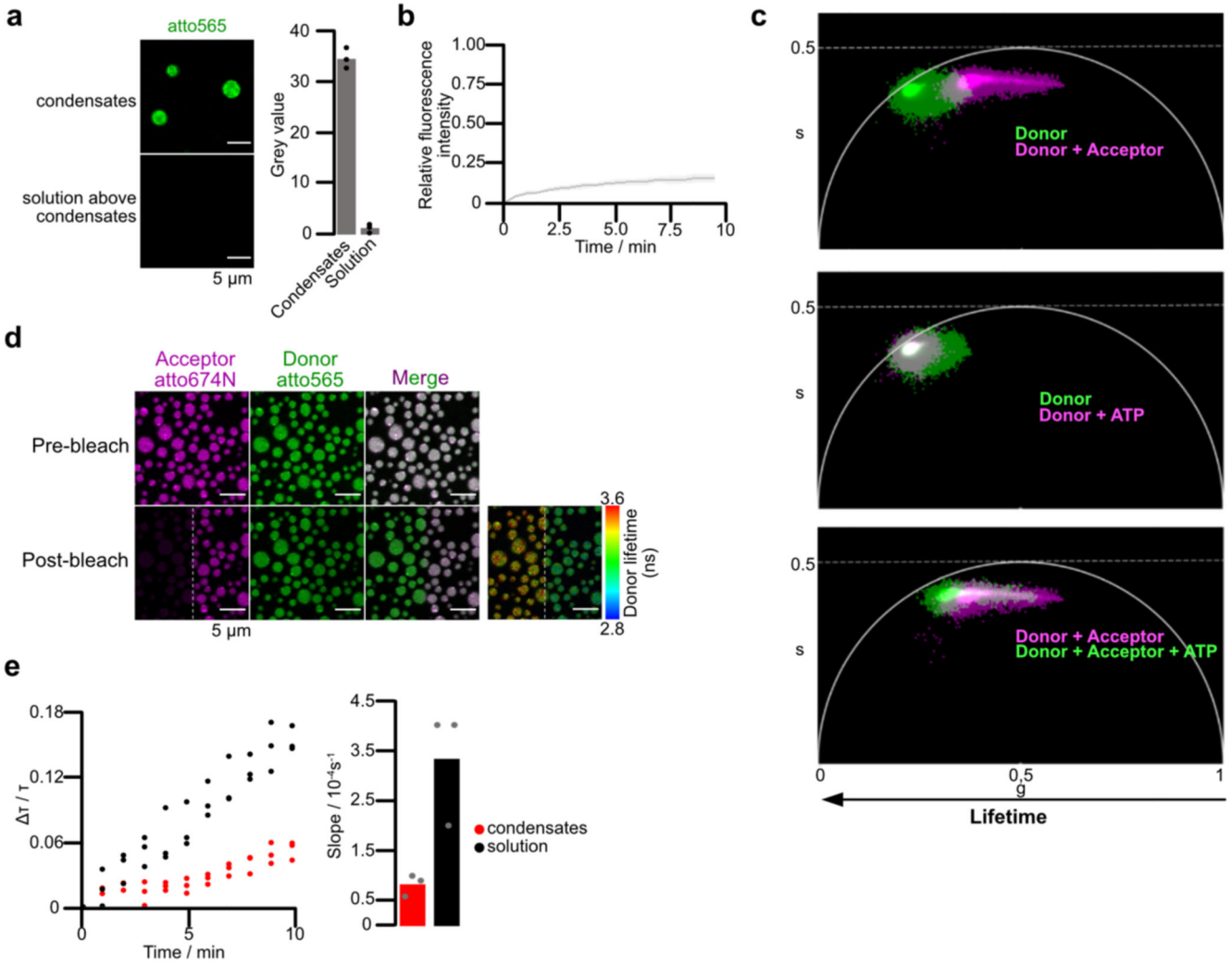

Extended Data Fig. 3. FLIM-FRET controls.

a, Enrichment of labeled 0N60 mononucleosomes in chromatin condensates. N = 3 biological replicates; bars are averages. The mononucleosome concentration in solution was determined from z-plane above the condensates. **b**, Whole condensate FRAP of FRET-0N60 nucleosomes to assess their exchange between condensate and solution. Line is an average and shadow SD of eight bleached condensates. One of two independent replicates with similar results is shown. **c**, Phasor representation of data in Fig. 3b. Upon introduction of the acceptor, the donor's lifetime distribution moves away from the universal circle line (single exponential lifetimes), consistent with at least two donor populations in different FRET states. The phasor representation makes no assumptions on the number of decay rates nor on specific decay model [75]. **d**, Acceptor bleaching enhances donor fluorescence and lifetime, indicative of FRET. Imaging of FRET-0N60 nucleosomes in chromatin condensates. The acceptor fluorophore was bleached in the left half of the field of view, leading to an

Europe PMC Funders Author Manuscripts

increase in donor fluorescence and donor lifetime (right most panel). N = 1. **e**, FLIM-FRET measurements as in Fig. 3d, but with 5 mM Mg-ATP. Bars are averages of three independent experiments (dots).

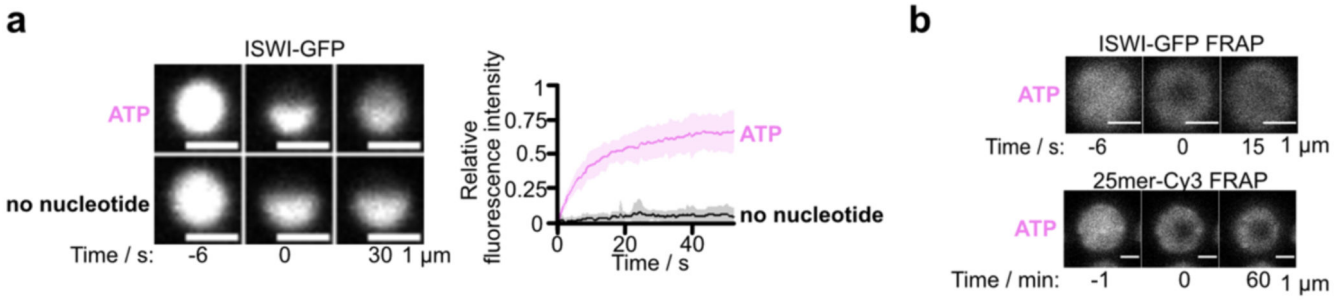

Extended Data Fig. 4. ISWI and nucleosome array mobility inside condensates.

a, Intra-condensate mobility of ISWI-GFP measured by partial-condensate FRAP. Half of a condensate was bleached in presence and absence of Mg-ATP (1 mM). Line is an average and shadow SD of 15 bleached condensates for each condition. N = 4 biological replicates. **b**, Independent replicate of Fig. 4b. Partial-condensate FRAP of ISWI-GFP in presence of indicated nucleotides (all 0.77 mM), at 50% of total chromatin and ISWI concentration as compared to Fig. 4b. **c**, ISWI-GFP is more mobile than chromatin in condensates. Dual FRAP of ISWI-GFP and Cy3-labeled condensates formed by 25mer arrays in presence of Mg-ATP (1 mM) and ISWI (100 nM). Four independent replicates show similar results.

Europe PMC Funders Author Manuscripts

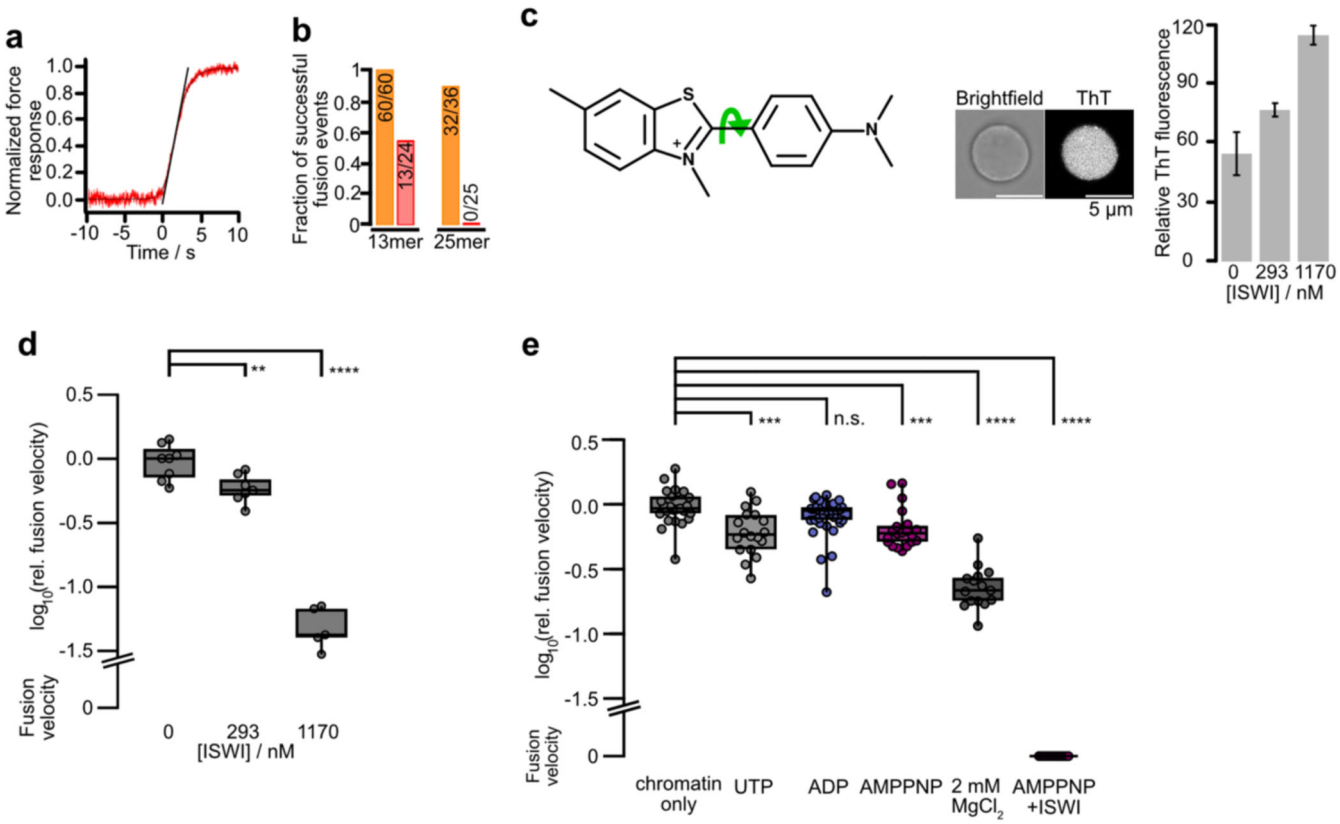

Extended Data Fig. 5. ISWI and Mg^{2+} affect biophysical properties of condensates.

a, Optical tweezer force readout during condensate fusion. The fusion velocity was determined as the slope of the normalized force data at the inflection point. Incurred forces during fusion were on the order of 1 pN (see Methods). **b**, Fraction of successful fusion events in 1 mM $MgCl_2$ (orange) and 5 mM $MgCl_2$ (red). Nucleosome concentration: 1170 nM. **c**, ISWI increased viscosity of condensates as reported by enhanced fluorescence of the molecular rotor thioflavin T (ThT). In a high viscosity medium, rotation around the C-C bond (green arrow) is constrained, and the excitation energy is released as fluorescence. Bars: average ThT fluorescence intensities relative to outside medium; error: SD. Six condensates were analyzed for 0 nM and 293 nM ISWI, five for 1170 nM ISWI red circles). One of two independent replicates with similar results is shown. **d**, Fusion velocities of condensates measured by optical tweezers containing indicated ISWI concentrations. Data was obtained from the indicated number of independent condensates measured in one experiment. Statistical significance was determined by two-sided t-test (p-values: 293 nM: 0.02, 1170 nM: 9.8e-7). **e**, Fusion between condensates without ISWI measured by optical tweezers. Nucleotides (1 mM) and 2 mM instead of 1 mM free Mg^{2+} show only modest effects on fusion velocities compared to ISWI-AMPPNP. Data were obtained from the indicated number of independent condensates derived from two experiments conducted on different days. Statistical significance was determined by two-sided t-test (p-values: UTP: 3.5e-4, AD: 0.053, AMPPNP: 4.6e-4, 2 mM $MgCl_2$: 1.4e-12, AMPPNP + ISWI: 2.3e-14). Box plots in *d* and *e* show medians and the 25^{th}/75^{th} percentiles, whiskers the 9^{th} and 91^{st}

Europe PMC Funders Author Manuscripts

percentiles**;** asterisks indicate significance levels (n.s.: $p > 0.05$, *: $p \leq 0.05$, **: $p \leq 0.01$, ***: $p \leq 0.001$, ****: $p \leq$ 1e-4).

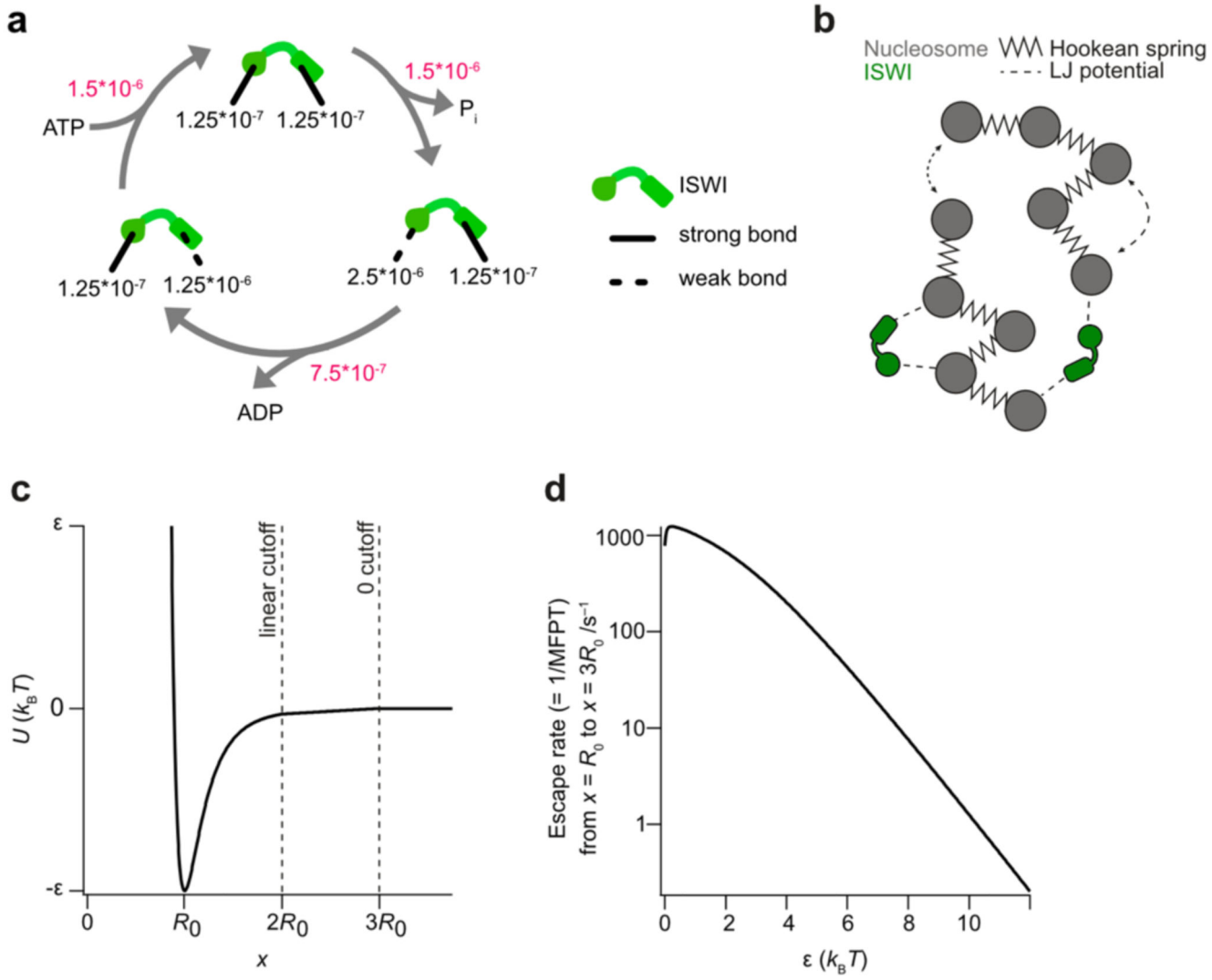

Extended Data Fig. 6. Mechanistic details of the simulated monkey bar mechanism.

a, A model for the independent switching of the strengths of the two nucleosome interaction sites during ISWI´s ATPase cycle. Escape rates (black) and transition rates (red) in timestep^{-1} are indicated. **b**, Schematic representation of the implementation of the model in Fig. 6a for molecular dynamics simulations. **c**, Modified Lennard-Jones potential used in simulations. Below distances of $2R_0$ a regular Lennard-Jones potential is used. Between $2R_0$ and $3R_0$ the potential is described using a linear approximation, while interactions with range above $3R_0$ are set to 0. **d**, Conversion of the strength of the modified Lennard-Jones potential to escape rates based on the mean first passage time of potential escape [76].

Europe PMC Funders Author Manuscripts

Supplementary Material

Refer to Web version on PubMed Central for supplementary material.

Acknowledgements

We thank the following members of the Mueller-Planitz lab: Sabrina Albig, Madhura Khare and Silvia Härtel for histone purification, Ameli Lentz for purifying GFP and cloning ISWI-GFP. We thank Marlies Muernseer (Nanolive) for collecting holotomography data and the Ökten group (TU Munich) for providing sfGFP plasmid. P.V. acknowledges support from the IRTG SFB 1064. F.M.-P. acknowledges financial support from the Deutsche Forschungsgemeinschaft (SFB1064 A07, MU3613/3-1, MU3613/8-1); J.S. from the LMU Center for Nanoscience CeNS, a DFG Emmy Noether grant (STI673/2-1) and an ERC Starting Grant (758124); P.B.B from SFB1064 A01 and BE1140/6-1; and M.H. by St. Jude Children's Research Hospital, the American Lebanese Syrian Associated Charities and NIH awards R01GM141694 and R01GM135599. The funders had no role in study design, data collection and analysis, decision to publish or preparation of the manuscript.

Data availability statement

Source data are included in the supplementary information. Large data files that exceed the size limitations or data that underly more peripheral parts of the study are available upon request from the corresponding authors.

Code availability statement

Code available from https://github.com/StiglerLab/Vizjak_2023.

References

1. Burak Y, Ariel G, Andelman D. Onset of DNA aggregation in presence of monovalent and multivalent counterions. Biophys J. 2003; 85: 2100–2110. DOI: 10.1016/s0006-3495(03)74638-4 [PubMed: 14507678]
2. Post CB, Zimm BH. Theory of DNA condensation: Collapse versus aggregation. Biopolymers. 1982; 21: 2123–2137. [PubMed: 7171729]
3. Woodcock CLF. Ultrastructure of inactive chromatin. Journal of Cell Biology. 1973; 59 A368
4. Olins AL, Olins DE. Spheroid chromatin units (v bodies). Science (1979). 1974; 183: 330–332. [PubMed: 4128918]
5. Finch JT, Klug A. Solenoidal model for superstructure in chromatin. Proc Natl Acad Sci U S A. 1976; 73 1897 doi: 10.1073/pnas.73.6.1897 [PubMed: 1064861]
6. Ou HD, et al. ChromEMT: Visualizing 3D chromatin structure and compaction in interphase and mitotic cells. Science (1979). 2017; 357 doi: 10.1126/science.aag0025 [PubMed: 28751582]
7. Maeshima K, et al. Nucleosomal arrays self-assemble into supramolecular globular structures lacking 30-nm fibers. EMBO J. 2016; 35: 1115–1132. DOI: 10.15252/embj.201592660 [PubMed: 27072995]
8. Adhireksan Z, Sharma D, Lee PL, Davey CA. Near-atomic resolution structures of interdigitated nucleosome fibres. Nature communations. 2020; doi: 10.1038/s41467-020-18533-2 [PubMed: 32958761]
9. Hsieh THS, et al. Mapping nucleosome resolution chromosome folding in yeast by Micro-C. Cell. 2015; 162: 108. doi: 10.1016/j.cell.2015.05.048 [PubMed: 26119342]
10. Ricci MA, Manzo C, García-Parajo MF, Lakadamyali M, Cosma MP. Chromatin fibers are formed by heterogeneous groups of nucleosomes in vivo. Cell. 2015; 160: 1145–1158. [PubMed: 25768910]
11. Gibson BA, et al. Organization of Chromatin by Intrinsic and Regulated Phase Separation. Cell. 2019; 179: 470–484. e21 doi: 10.1016/j.cell.2019.08.037 [PubMed: 31543265]

12. Strickfaden H, et al. Condensed Chromatin Behaves like a Solid on the Mesoscale In Vitro and in Living Cells. Cell. 2020; 183: 1772–1784. e13 [PubMed: 33326747]
13. Zhang Y, Narlikar GJ, Kutateladze TG. Enzymatic Reactions inside Biological Condensates. J Mol Biol. 2021; 433 doi: 10.1016/j.jmb.2020.08.009 [PubMed: 32805219]
14. Hihara S, et al. Local Nucleosome Dynamics Facilitate Chromatin Accessibility in Living Mammalian Cells. Cell Rep. 2012; 2: 1645–1656. [PubMed: 23246002]
15. Kornberg RD, Lorch Y. Primary Role of the Nucleosome. Mol Cell. 2020; 79: 371–375. [PubMed: 32763226]
16. Kim JM, et al. Single-molecule imaging of chromatin remodelers reveals role of atpase in promoting fast kinetics of target search and dissociation from chromatin. Elife. 2021; 10 doi: 10.7554/eLife.69387 [PubMed: 34313223]
17. Corona DFV, et al. ISWI is an ATP-dependent nucleosome remodeling factor. Mol Cell. 1999; 3: 239–245. [PubMed: 10078206]
18. Hamiche A, Sandaltzopoulos R, Gdula DA, Wu C. ATP-dependent histone octamer sliding mediated by the chromatin remodeling complex NURF. Cell. 1999; 97: 833–842. [PubMed: 10399912]
19. Ludwigsen J, Hepp N, Klinker H, Pfennig S, Mueller-Planitz F. Remodeling and repositioning of nucleosomes in nucleosomal arrays. Methods in Molecular Biology. 2018. [PubMed: 29971727]
20. Mueller-Planitz F, Klinker H, Ludwigsen J, Becker PB. The ATPase domain of ISWI is an autonomous nucleosome remodeling machine. Nat Struct Mol Biol. 2013. [PubMed: 23202585]
21. Schram RD, Klinker H, Becker PB, Schiessel H. Computational study of remodeling in a nucleosomal array. European Physical Journal E. 2015; 38 [PubMed: 26248702]
22. Klinker H, et al. ISWI remodelling of physiological chromatin fibres acetylated at lysine 16 of histone H4. PLoS One. 2014; 9 doi: 10.1371/journal.pone.0088411 [PubMed: 24516652]
23. Boyer LA, et al. Functional delineation of three groups of the ATP-dependent family of chromatin remodeling enzymes. Journal of Biological Chemistry. 2000; 275: 18864–18870. [PubMed: 10779516]
24. Logie C, Tse C, Hansen JC, Peterson CL. The Core Histone N-Terminal Domains Are Required for Multiple Rounds of Catalytic Chromatin Remodeling by the SWI/SNF and RSC Complexes†. Biochemistry. 1999; 38: 2514–2522. [PubMed: 10029546]
25. Peeples W, Rosen MK. Mechanistic dissection of increased enzymatic rate in a phase-separated compartment. Nat Chem Biol. 2021; doi: 10.1038/s41589-021-00801-x [PubMed: 34035521]
26. Poirier MG, Bussiek M, Langowski J, Widom J. Spontaneous Access to DNA Target Sites in Folded Chromatin Fibers. J Mol Biol. 2008; 379: 772–786. DOI: 10.1016/j.jmb.2008.04.025 [PubMed: 18485363]
27. Poirier MG, Oh E, Tims HS, Widom J. Dynamics and function of compact nucleosome arrays. Nat Struct Mol Biol. 2009; 16: 938–944. DOI: 10.1038/nsmb.1650 [PubMed: 19701201]
28. Hagerman TA, et al. Chromatin stability at low concentration depends on histone octamer saturation levels. Biophys J. 2009; 96: 1944–1951. DOI: 10.1016/j.bpj.2008.10.070 [PubMed: 19254554]
29. Gibson BA, et al. In diverse conditions, intrinsic chromatin condensates have liquid-like material properties. Proc Natl Acad Sci U S A. 2023; 120 doi: 10.1073/pnas.2218085120 [PubMed: 37094140]
30. Goins AB, Sanabria H, Waxham MN. Macromolecular crowding and size effects on probe microviscosity. Biophys J. 2008; 95: 5362–5373. DOI: 10.1529/biophysj.108.131250 [PubMed: 18790853]
31. Yang JG, Narlikar GJ. FRET-based methods to study ATP-dependent changes in chromatin structure. Methods. 2007; 41: 291–295. DOI: 10.1016/j.ymeth.2006.08.015 [PubMed: 17309839]
32. Zhang M, et al. Molecular Organization of the Early Stages of Nucleosome Phase Separation Visualized by Cryo-Electron Tomography. Mol Cell. 2022; 82: 3000. doi: 10.1016/j.molcel.2022.06.032 [PubMed: 35907400]
33. Weidemann T, et al. Counting nucleosomes in living cells with a combination of fluorescence correlation spectroscopy and confocal imaging. J Mol Biol. 2003; 334: 229–240. [PubMed: 14607115]

34. Leonard JD, Narlikar GJ. A Nucleotide-Driven Switch Regulates Flanking DNA Length Sensing by a Dimeric Chromatin Remodeler. Mol Cell. 2015; 57: 850–859. DOI: 10.1016/j.molcel.2015.01.008 [PubMed: 25684208]
35. Larson AG, Narlikar GJ. The Role of Phase Separation in Heterochromatin Formation, Function, and Regulation. Biochemistry. 2018; 57: 2540–2548. DOI: 10.1021/acs.biochem.8b00401 [PubMed: 29644850]
36. Grüne T, et al. Crystal structure and functional analysis of a nucleosome recognition module of the remodeling factor ISWI. Mol Cell. 2003; 12: 449–460. [PubMed: 14536084]
37. Bhardwaj SK, et al. Dinucleosome specificity and allosteric switch of the ISW1a ATP-dependent chromatin remodeler in transcription regulation. Nat Commun. 2020; doi: 10.1038/s41467-020-19700-1 [PubMed: 33219211]
38. Yamada K, et al. Structure and mechanism of the chromatin remodelling factor ISW1a. Nature. 2011. [PubMed: 21525927]
39. Li L, et al. Structure of the ISW1a complex bound to the dinucleosome. bioRxiv. 2023. [PubMed: 38177688]
40. Wang J, et al. A Molecular Grammar Governing the Driving Forces for Phase Separation of Prion-like RNA Binding Proteins. Cell. 2018; 174: 688–699. e16 doi: 10.1016/j.cell.2018.06.006 [PubMed: 29961577]
41. Muzzopappa F, Hertzog M, Erdel F. DNA length tunes the fluidity of DNA-based condensates. Biophys J. 2021; 120: 1288–1300. DOI: 10.1016/j.bpj.2021.02.027 [PubMed: 33640380]
42. Ludwigsen J, Klinker H, Mueller-Planitz F. No need for a power stroke in ISWI-mediated nucleosome sliding. EMBO Rep. 2013; 14: 1092–1097. DOI: 10.1038/embor.2013.160 [PubMed: 24113208]
43. Harrer N, et al. Structural Architecture of the Nucleosome Remodeler ISWI Determined from Cross-Linking, Mass Spectrometry, SAXS, and Modeling. Structure. 2018; 26: 282–294. e6 [PubMed: 29395785]
44. Rudolph J, Mahadevan J, Dyer P, Luger K. Poly(ADP-ribose) polymerase 1 searches DNA via a 'monkey bar' mechanism. Elife. 2018; 7 doi: 10.7554/eLife.37818 [PubMed: 30088474]
45. Deindl S, et al. ISWI Remodelers Slide Nucleosomes with Coordinated Multi-Base-Pair Entry Steps and Single-Base-Pair Exit Steps. Cell. 2013; 152: 442–452. DOI: 10.1016/j.cell.2012.12.040 [PubMed: 23374341]
46. Gamarra N, Johnson SL, Trnka MJ, Burlingame AL, Narlikar GJ. The nucleosomal acidic patch relieves auto-inhibition by the ISWI remodeler SNF2h. Elife. 2018; 7 doi: 10.7554/eLife.35322 [PubMed: 29664398]
47. Dann, geoffrey P; , et al. ISWI chromatin remodellers sense nucleosome modifications to determine substrate preference. 2017; doi: 10.1038/nature23671 [PubMed: 28767641]
48. Clapier CR, Corona DF, Becker PB, Nightingale KP, Programme I. Critical Role for the Histone H4 N Terminus in Nucleosome Remodeling by ISWI. Mol Cell Biol. 2001; 21: 875–883. DOI: 10.1128/MCB.21.3.875-883.2001 [PubMed: 11154274]
49. Schalch T, Duda S, Sargent DF, Richmond TJ. X-ray structure of a tetranucleosome and its implications for the chromatin fibre. Nature. 2005; 436: 138–141. [PubMed: 16001076]
50. Verschure PJ, et al. Condensed chromatin domains in the mammalian nucleus are accessible to large macromolecules. EMBO Rep. 2003; 4: 861–866. DOI: 10.1038/sj.embor.embor922 [PubMed: 12947417]
51. Beaudouin J, Mora-Bermúdez F, Klee T, Daigle N, Ellenberg J. Dissecting the contribution of diffusion and interactions to the mobility of nuclear proteins. Biophys J. 2006; 90: 1878–1894. DOI: 10.1529/biophysj.105.071241 [PubMed: 16387760]
52. Erdel F, Baum M, Rippe K. The viscoelastic properties of chromatin and the nucleoplasm revealed by scale-dependent protein mobility. Journal of Physics: Condensed Matter. 2015; 27 064115 [PubMed: 25563347]
53. Maeshima K, et al. A Transient Rise in Free Mg2+ Ions Released from ATP-Mg Hydrolysis Contributes to Mitotic Chromosome Condensation. Current Biology. 2018; 28: 444–451. e6 [PubMed: 29358072]

54. Kroschwald S, et al. Different Material States of Pub1 Condensates Define Distinct Modes of Stress Adaptation and Recovery. Cell Rep. 2018; 23: 3327–3339. [PubMed: 29898402]
55. Munder MC, et al. A pH-driven transition of the cytoplasm from a fluid-to a solid-like state promotes entry into dormancy. Elife. 2016; 5 doi: 10.7554/eLife.09347 [PubMed: 27003292]
56. Erdel F, Rippe K. Formation of Chromatin Subcompartments by Phase Separation. Biophys J. 2018; 114: 2262–2270. DOI: 10.1016/j.bpj.2018.03.011 [PubMed: 29628210]
57. Schneider MWG, et al. A mitotic chromatin phase transition prevents perforation by microtubules. Nature. 2022; 609: 183. doi: 10.1038/s41586-022-05027-y [PubMed: 35922507]
58. Keizer VIP, et al. Live-cell micromanipulation of a genomic locus reveals interphase chromatin mechanics. Science (1979). 2022; 377: 489–495. [PubMed: 35901134]
59. Erdel F, et al. Mouse Heterochromatin Adopts Digital Compaction States without Showing Hallmarks of HP1-Driven Liquid-Liquid Phase Separation. Mol Cell. 2020; 78: 236–249. e7 doi: 10.1016/j.molcel.2020.02.005 [PubMed: 32101700]
60. Irgen-Gioro S, Yoshida S, Walling V, Chong S. Fixation can change the appearance of phase separation in living cells. Elife. 2022; 11 doi: 10.7554/eLife.79903 [PubMed: 36444977]
61. Hansen JC, Maeshima K, Hendzel MJ. The solid and liquid states of chromatin. Epigenetics Chromatin. 2021; 14 doi: 10.1186/s13072-021-00424-5 [PubMed: 34717733]
62. Korber P, Becker PB. Nucleosome dynamics and epigenetic stability. Essays Biochem. 2010; 48: 63–74. [PubMed: 20822486]
63. Muzzopappa F, et al. Detecting and quantifying liquid–liquid phase separation in living cells by model-free calibrated half-bleaching. Nature Communications. 2022; 13: 1–15. doi: 10.1038/s41467-022-35430-y [PubMed: 36526633]
64. Whitehouse I, Rando OJ, Delrow J, Tsukiyama T. Chromatin remodelling at promoters suppresses antisense transcription. Nature. 2007; 450: 1031–1035. [PubMed: 18075583]
65. Gelbart ME, Bachman N, Delrow J, Boeke JD, Tsukiyama T. Genome-wide identification of Isw2 chromatin-remodeling targets by localization of a catalytically inactive mutant. Genes Dev. 2005; 19: 942. doi: 10.1101/gad.1298905 [PubMed: 15833917]
66. Blosser TR, Yang JG, Stone MD, Narlikar GJ, Zhuang X. Dynamics of nucleosome remodelling by individual ACF complexes. Nature. 2009; 1022–1027. DOI: 10.1038/nature08627 [PubMed: 20033040]
67. Tilly BC, et al. In vivo analysis reveals that ATP-hydrolysis couples remodeling to SWI/SNF release from chromatin. Elife. 2021; 10 doi: 10.7554/eLife.69424 [PubMed: 34313222]
68. Erdel F, Schubert T, Marth C, Längst G, Rippe K. Human ISWI chromatin-remodeling complexes sample nucleosomes via transient binding reactions and become immobilized at active sites. Proc Natl Acad Sci U S A. 2010; 107: 19873–19878. DOI: 10.1073/pnas.1003438107 [PubMed: 20974961]
69. Oppikofer M, et al. Expansion of the ISWI chromatin remodeler family with new active complexes. EMBO Rep. 2017; 18: 1697–1706. DOI: 10.15252/embr.201744011 [PubMed: 28801535]
70. Clapier CR, Verma N, Parnell TJ, Cairns BR. Cancer-Associated Gain-of-Function Mutations Activate a SWI/SNF-Family Regulatory Hub. Mol Cell. 2020; 80: 712–725. e5 doi: 10.1016/j.molcel.2020.09.024 [PubMed: 33058778]
71. Hodges HC, et al. Dominant-negative SMARCA4 mutants alter the accessibility landscape of tissue-unrestricted enhancers. Nat Struct Mol Biol. 2018; 25: 61–72. DOI: 10.1038/s41594-017-0007-3 [PubMed: 29323272]
72. Elfring LK, et al. Genetic analysis of brahma: The drosophila homolog of the yeast chromatin remodeling factor SWI2/SNF2. Genetics. 1998; 148: 251–265. DOI: 10.1093/genetics/148.1.251 [PubMed: 9475737]
73. Li W, et al. Biophysical properties of AKAP95 protein condensates regulate splicing and tumorigenesis. Nat Cell Biol. 2020; 22: 960–972. DOI: 10.1038/s41556-020-0550-8 [PubMed: 32719551]
74. Shi B, et al. UTX condensation underlies its tumour-suppressive activity. Nature. 2021; 597: 726–731. DOI: 10.1038/s41586-021-03903-7 [PubMed: 34526716]

75. Digman MA, Caiolfa VR, Zamai M, Gratton E. The phasor approach to fluorescence lifetime imaging analysis. Biophys J. 2008; 94: 14–16. DOI: 10.1529/biophysj.107.120154 [PubMed: 17827229]

76. Gray TH, Yong EH. An effective one-dimensional approach to calculating mean first passage time in multi-dimensional potentials. J Chem Phys. 2021; 154 084103 [PubMed: 33639738]

77. Pédelacq J-D, Cabantous S, Tran T, Terwilliger TC, Waldo GS. Engineering and characterization of a superfolder green fluorescent protein. 2006. [PubMed: 16369541]

78. Klinker H, Haas C, Harrer N, Becker PB, Mueller-Planitz F. Rapid purification of recombinant histones. PLoS One. 2014; 9 doi: 10.1371/journal.pone.0104029 [PubMed: 25090252]

79. Schuck P. Size-distribution analysis of macromolecules by sedimentation velocity ultracentrifugation and Lamm equation modeling. Biophys J. 2000; 78: 1606–1619. DOI: 10.1016/S0006-3495(00)76713-0 [PubMed: 10692345]

80. Demeler, B, Gorbet, GE. Analytical Ultracentrifugation. Uchiyama, S, Arisaka, F, Stafford, W, Laue, T, editors. Springer; 2016. 119–143.

81. Schindelin J, et al. Fiji: an open-source platform for biological-image analysis. Nat Methods. 2012; 9: 676–682. DOI: 10.1038/nmeth.2019 [PubMed: 22743772]

82. Koulouras G, et al. EasyFRAP-web: a web-based tool for the analysis of fluorescence recovery after photobleaching data. Nucleic Acids Res. 2018; 46: 467–472. DOI: 10.1093/nar/gky508 [PubMed: 29901776]

83. R Core Team. R: A Language and Environment for Statistical Computing. 2022. Preprint at

Europe PMC Funders Author Manuscripts

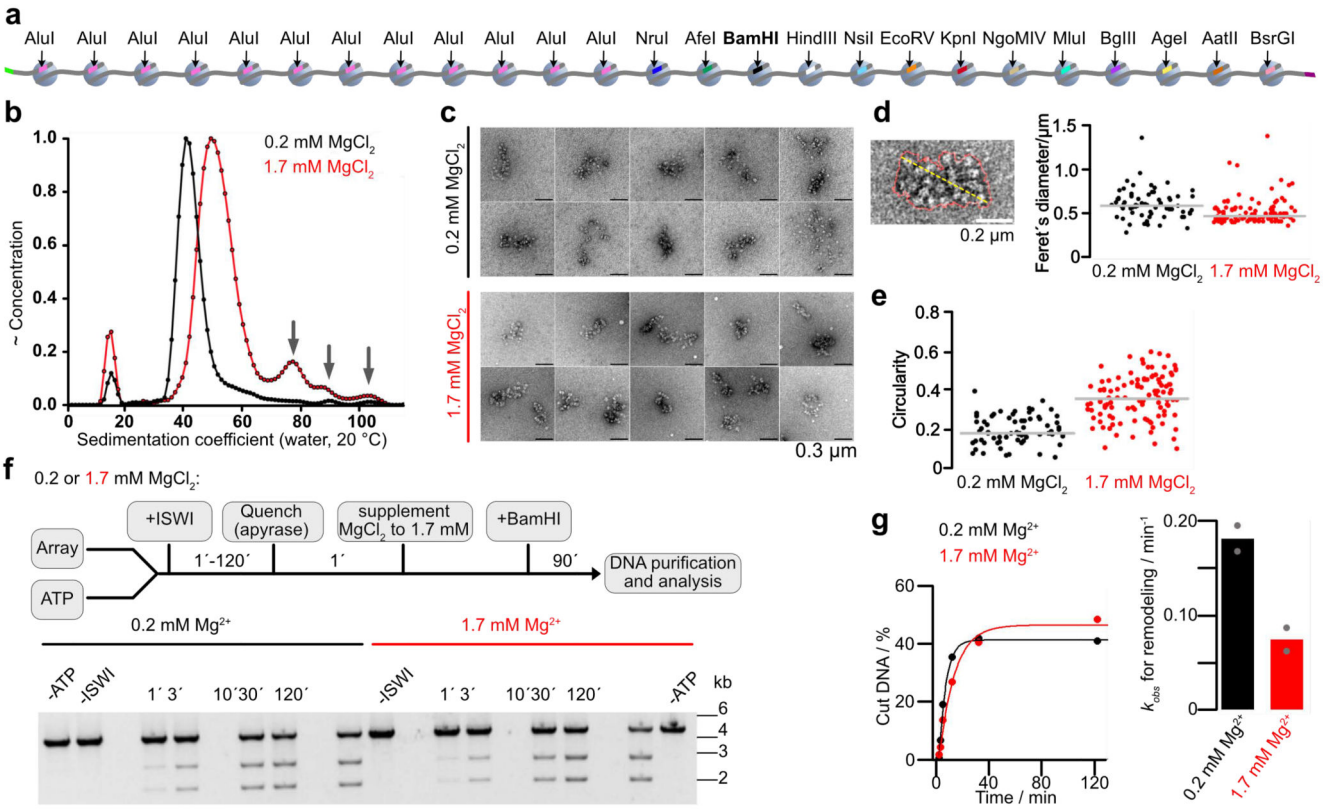

Figure 1. Intramolecular chromatin fiber folding does not impede remodeling.

a, A 25mer nucleosome array assembled on 25 repeats of 197 bp long Widom-601 DNA derivatives. 13 repeats contain unique restriction enzymes sites. **b**, Sedimentation velocity analysis of 25mer arrays in a buffer supplemented with 0.2 mM (black; peak at 42.4 S) or 1.7 mM $MgCl_2$ (red; peak at 51.3 S). The larger S value at the higher Mg^{2+}-concentration indicated stronger compaction of arrays without substantial oligomer formation (arrows). **c**, Representative micrographs of 25mer arrays from negative stain electron microscopy dissolved in a buffer supplemented with indicated $MgCl_2$ concentrations. **d, e**, Single-particle analysis of negative stain EM micrographs. N = 67 (0.2 mM $MgCl_2$); N = 107 (1.7 mM $MgCl_2$). Outlines of single particles (red line) were determined with a trainable Weka segmentation in ImageJ. Feret´s diameter (the maximum distance between two parallel tangential lines, yellow line) and circularity were calculated for all outlines. **f**, Top: Schematic of the BamHI accessibility assay. Bottom: Gel analysis of remodeling time courses. Reactions contained 4 nM arrays and 5 μM Mg-ATP and were started by addition of 200 nM ISWI. **g**, Left: quantification of gel in *f* and exponential fits of the time courses. Right: rate coefficients from single exponential fits. Bars are mean values of two independent experiments (dots).

Europe PMC Funders Author Manuscripts

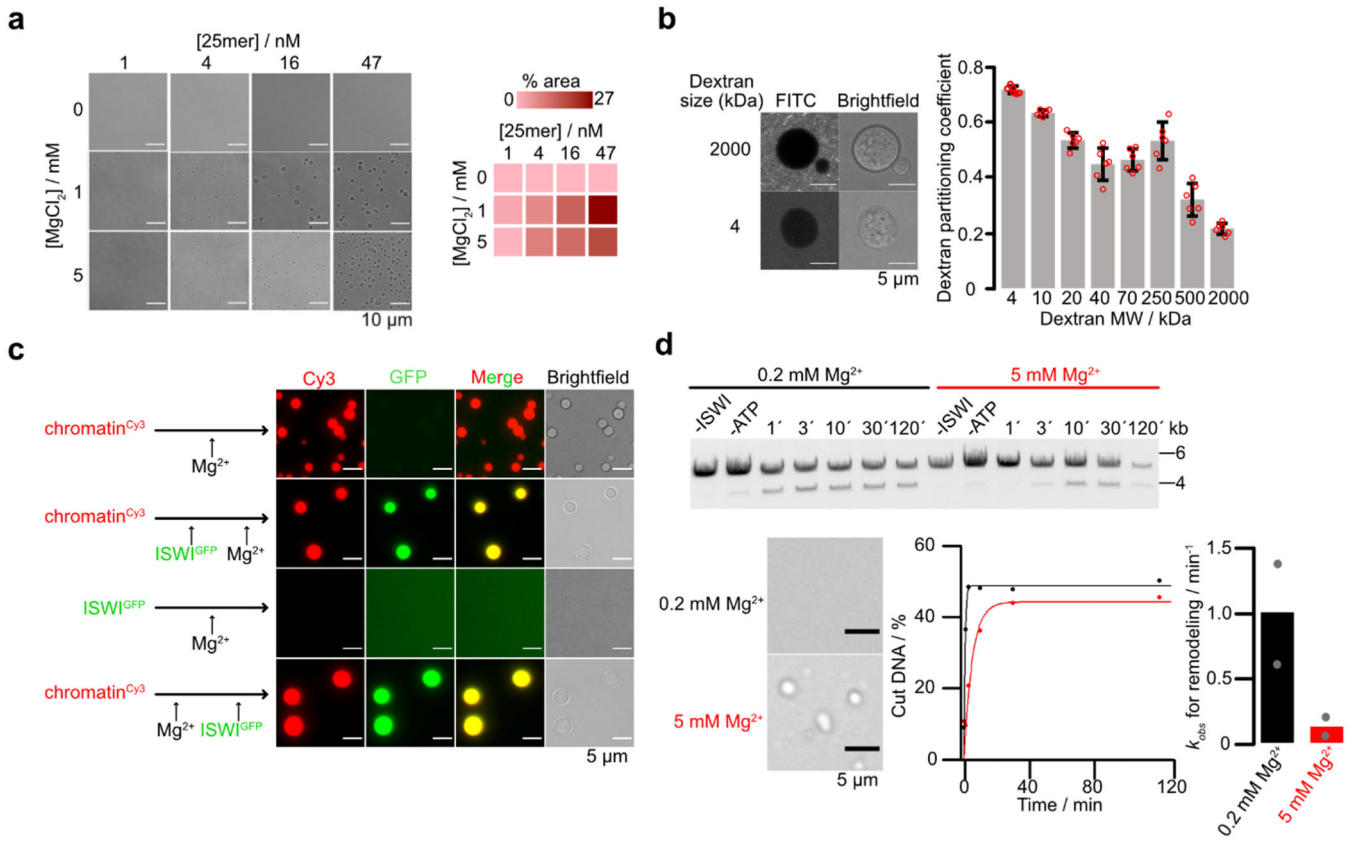

Figure 2. ISWI partitions into condensates and slides nucleosomes under condensate-forming conditions.

a, Condensate formation depends on nucleosome and $MgCl_2$ concentrations. Left: Condensate formation for different $MgCl_2$ and 25mer array concentrations. Right: Percentage of the field of view occupied by condensates. The experiment was independently repeated twice with similar results. **b**, Partition coefficient of FITC-labeled dextrans of indicated molecular weights. Bars are averages from six condensates for each dextran, errors are SD. **c**, Colocalization experiments with GFP-ISWI (1.1 μM) and Cy3-labeled condensates (0.05 μM 25mers). Condensates were induced by addition of Mg^{2+} (5 mM) either before or after addition of GFP-ISWI. The experiment was independently repeated twice with similar results. **d**, Nucleosome sliding time courses (top and bottom left) in absence and presence of condensates (bottom right). Sliding was measured by KpnI accessibility of 25mer arrays (15 nM) with 1 mM Mg-ATP. Reactions were started by addition of 750 nM ISWI. Bars are mean values of two independent experiments (dots).

Europe PMC Funders Author Manuscripts

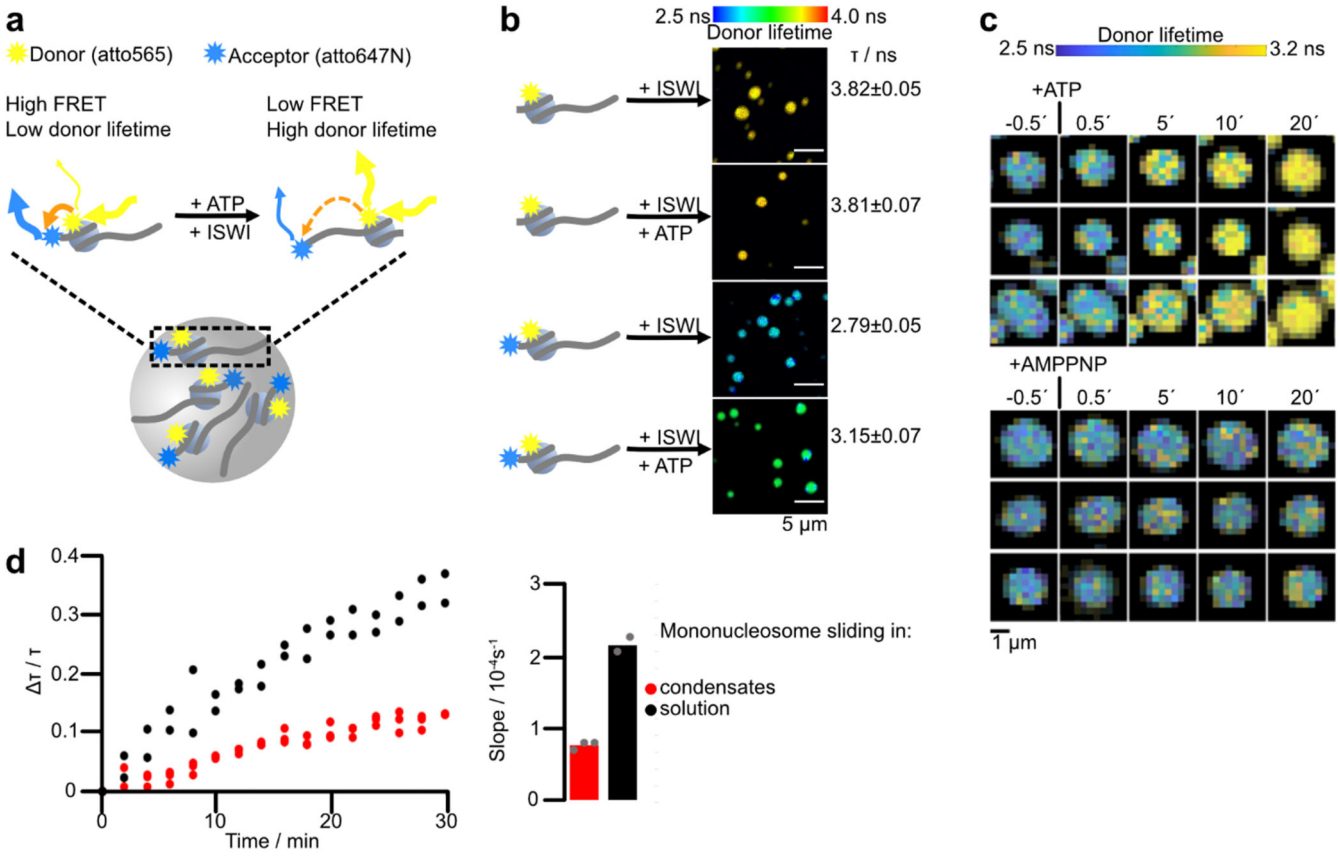

Figure 3. Nucleosome sliding in condensates visualized by FLIM-FRET.

a, Principle of the FLIM-FRET sliding assay. FRET nucleosomes with a donor dye (atto565) coupled to H2A K119C and an acceptor dye (atto647) attached to the octamer-proximal end of 207 bp Widom-601 DNA were spiked to array condensates. Upon nucleosome sliding, the FRET efficiency decreases, prolonging the donor fluorescence lifetime. **b**, The donor lifetime of FRET-nucleosomes in condensates increased after addition of ISWI and Mg-ATP but not in negative controls (donor-only nucleosomes, or without Mg-ATP). One out of two independent replicates with similar results is shown. Averages and SD of lifetimes across ten fields of view of the same sample, with each field of view imaged 30 times, totaling 300 images per condition. Reactions contained 45 nM 25mers, 125 nM FRET nucleosomes, 625 nM ISWI and were imaged four hours after addition of Mg-ATP. **c**, FLIM time lapse microscopy. Mg-ATP or Mg-AMPPNP (both 1 mM) were flown into the imaging chamber at t = 0. Individual condensates are pictured. One of two independent replicates with similar results is displayed. **d**, Left: FLIM-FRET time courses in condensates and solution from N=3 and N=2 independent experiments, respectively. Condensate reactions contained 45 nM 25mers, 125 nM FRET nucleosomes, and 625 nM ISWI and were started with 1 mM Mg-ATP. Solution reactions contained 1125 nM unlabeled 0N60 nucleosomes instead of arrays under otherwise identical conditions. Right: Initial velocities of time courses obtained from linear fits of the time courses on the left. Bars are mean values of independent experiments (dots).

Europe PMC Funders Author Manuscripts

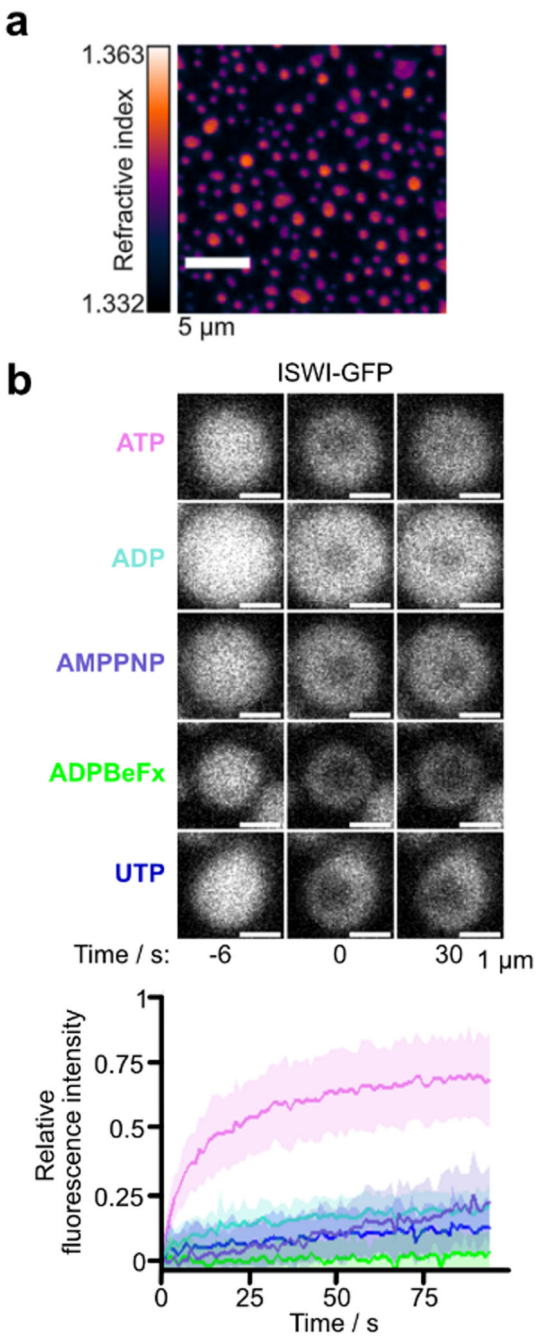

Figure 4. ATP hydrolysis powers mobility of ISWI in condensates.

a, Holotomogram of chromatin condensates. The average nucleosome concentration (225 ± 59 μM) was determined from the refractive index. One of two independent replicates is depicted. **b**, Top: Partial-condensate FRAP of ISWI-GFP in presence of indicated nucleotides (all 0.77 mM). Only addition of ATP allowed a fast recovery. Bottom: Quantification of FRAP time courses. Lines are averages, shaded areas SD of 20 condensates for AMPPNP and UTP, 15 for ADP, 25 for ADP-BeF_x and 30 for ATP.

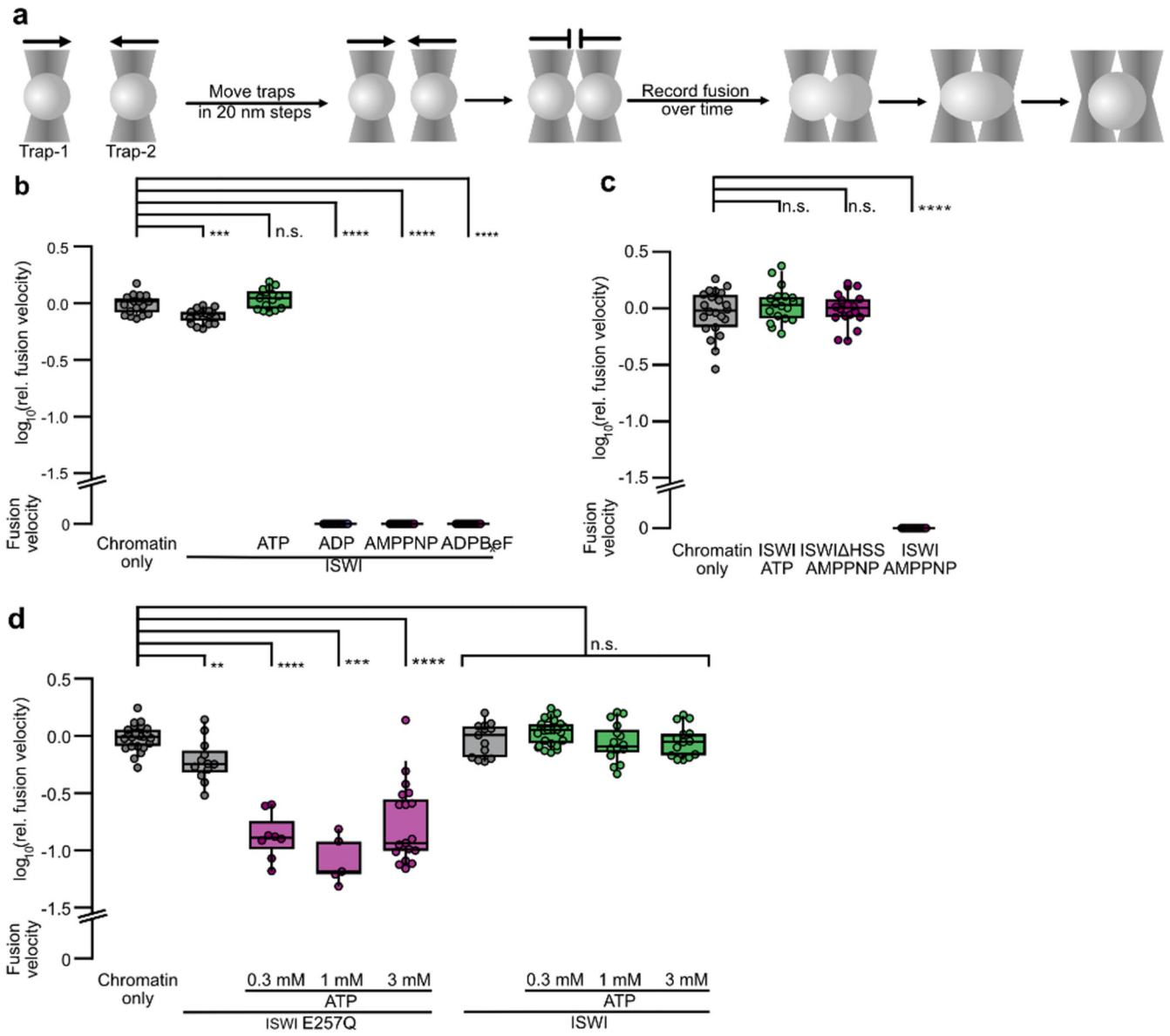

Figure 5. ATP hydrolysis prevents ISWI-mediated hardening of condensates.

a, Schematic of condensate fusion experiments with optical tweezers. **b**, Fusion velocities of condensates measured by optical trapping. ISWI in presence of non-hydrolysable nucleotides but not of ATP slowed down fusion. p-values of pairwise two-sided t-tests with the chromatin only condition: nucleotide-free: 3e-4, ATP: 0.12, ADP: 1.3e-14, AMPPNP: 1.3e-14, ADP-BeF_x: 1.3e-14. **c**, AMPPNP did not slow down fusion when ISWI lacked its HSS domain. p-values of pairwise two-sided t-tests with the chromatin only condition: ISWI-ATP: 0.21, $ISWI^{\Delta HSS}$-AMPPNP: 0.5, ISWI-AMPPNP: 4.5e-7. **d**, Addition of ATP to an ATPase-dead mutant (E257Q) but not to wild-type ISWI slowed down condensate fusion. p-values of pairwise two-sided t-tests with the chromatin only condition: ISWI: 0.70, ISWI + 0.3 mM ATP: 0.14, ISWI + 1 mM ATP: 0.34, ISWI + 3 mM ATP: 0.46, $ISWI^{E257Q}$: 0.003, $ISWI^{E257Q}$ + 0.3 mM ATP: 1.4e-6, $ISWI^{E257Q}$ + 1 mM ATP: 1.9e-4, $ISWI^{E257Q}$ + 3

mM ATP: 8.4e-9. Data are changes in velocities relative to the mean of the chromatin only condition. Box plots in *b–d* show medians and the 25th/75th percentiles, whiskers the 9th and 91st percentiles. Asterisks indicate significance levels (n.s.: $p > 0.05$, *: $p \leq 0.05$, **: $p \leq 0.01$, ***: $p \leq 0.001$, ****: $p \leq$ 1e-4). Data are from the indicated number of independent condensates (n). Chromatin-only and nucleotide-free ISWI datapoints in *b* came from three, all others from two experiments conducted on different days.

Europe PMC Funders Author Manuscripts

Europe PMC Funders Author Manuscripts

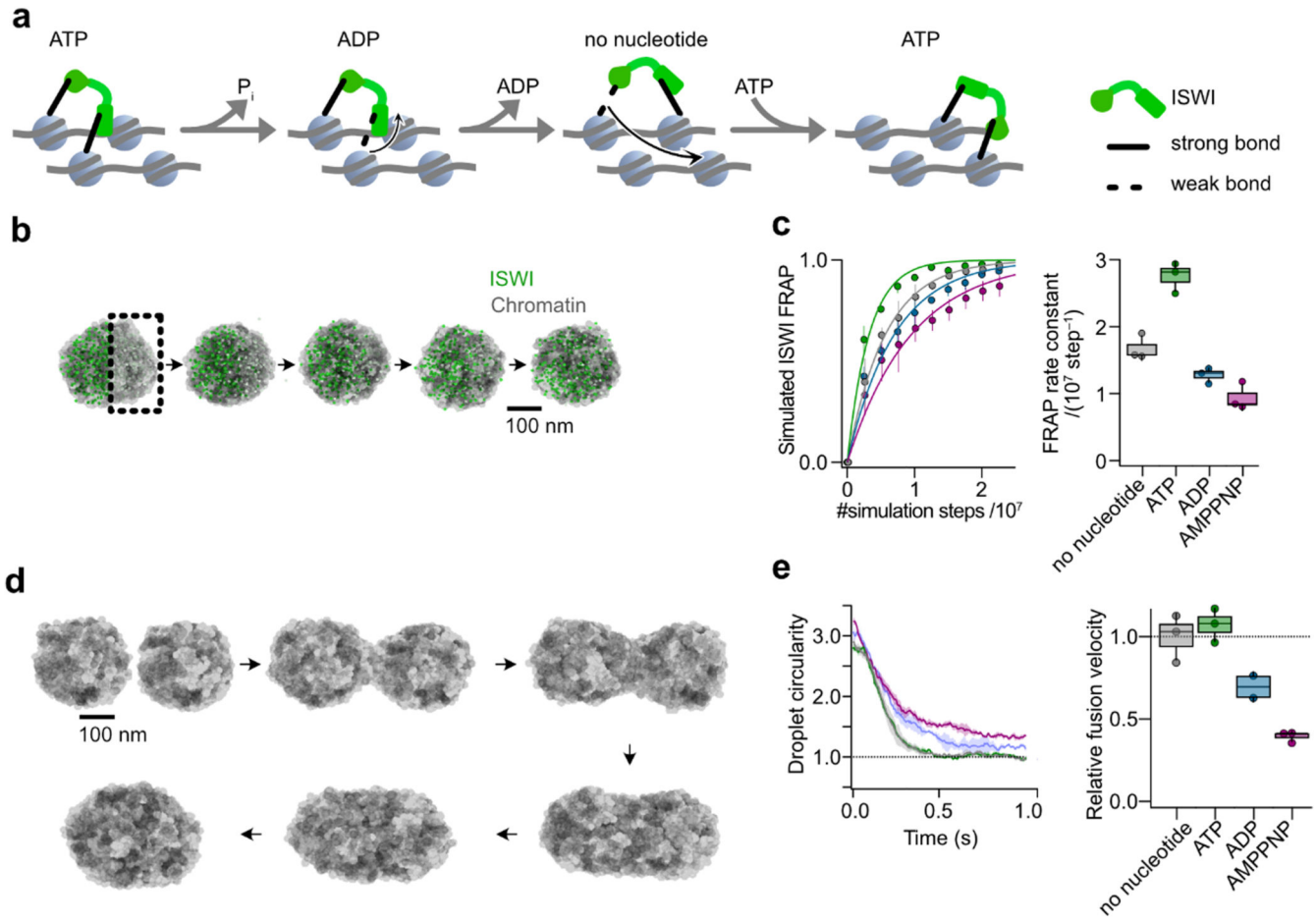

Figure 6. A simple model qualitatively explains experimental observations.

a, ISWI possesses two nucleosome-interacting domains, which can bridge neighboring nucleosomes in dense chromatin. Via large nucleotide-induced conformational changes (not depicted), the domains cycle through high and low affinity states towards nucleosomes, allowing ISWI to actively translocate through chromatin. **b**, Representation of a molecular dynamics simulation of ISWI FRAP in a chromatin condensate. ISWI particles on one side of an equilibrated condensate are switched to a bleached state at t=0 (square). Particle dynamics are then simulated to observe mixing of the two ISWI populations. **c**, ISWI FRAP was simulated as in b for $2.25*10^7$ timesteps in different nucleotide conditions with three independent simulations per condition. Left: Averaged traces of ISWI FRAP in different nucleotide conditions with SD derived from three replicates. Right: Rate constants of the simulated FRAP traces. **d**, Representation of simulated fusion experiments. Two equilibrated condensates were brought into proximity and allowed to fuse. For visual clarity only nucleosomes are shown here. **e**, Simulations of three independent fusion events for each nucleotide condition. Left: Averaged fusion traces with SD. Right: Relative fusion velocities of the simulated traces. Boxplots in c and e show medians and the $25^{th}/75^{th}$ percentiles, whiskers the standard deviation.